Reshaping, intermixing, and coarsening of metallic nanoclusters: Non-equilibrium statistical mechanical and coarse-grained modeling

King C. Lai,[1,2] Yong Han,[1,3] Peter Spurgeon,[4] Wenyu Huang,[4] Patricia A. Thiel,[3,4,5] Da-Jiang Liu,[2] and James W. Evans[1,2]

[1]Department of Physics & Astronomy, Iowa State University, Ames, Iowa 50011
[2]Division of Chemical & Biological Sciences, Ames Laboratory – USDOE, Iowa State University, Ames, Iowa 50011
[3]Division of Materials Science & Engineering, Ames Laboratory – USDOE, Iowa State University, Ames, Iowa 50011
[4]Department of Chemistry, Iowa State University, Ames, Iowa 50011
[5]Department of Materials Science & Engineering, Iowa State University, Ames, Iowa 50011

ABSTRACT Self-assembly of ensembles of supported 2D or 3D nanoclusters (NCs) by surface deposition, and of unsupported 3D NCs by solution-phase synthesis, produces intrinsically non-equilibrium systems. Individual nanoclusters can have far-from-equilibrium shapes and composition profiles. The free energy of the ensemble can be lowered by coarsening which can involve Ostwald ripening or Smoluchowski ripening (NC diffusion and coalescence). Preservation of individual NC structure and inhibition of coarsening is key for, e.g., avoiding catalyst degradation. In this review, we focus on crystalline metallic NCs. Atomistic-level modeling of equilibration processes typically utilizes stochastic lattice-gas models to access appropriate time- and length-scales. However, predictive modeling requires incorporation of realistic rates for relaxation mechanisms, e.g., periphery diffusion and intermixing, in numerous local environments (rather than the use of generic prescriptions). Alternative coarse-grained modeling must also incorporate appropriate mechanisms and kinetics. At the level of individual NCs, we present analyses of reshaping, including sintering and pinch-off, and of compositional evolution. We also discuss modeling of coarsening including diffusion and decay of individual NCs, and unconventional coarsening processes. We describe high-level modeling integrated with STM studies for 2D epitaxial NCs, and developments in modeling for supported and unsupported 3D NCs motivated by in situ TEM studies.

CONTENTS

1. INTRODUCTION

Nanostructured materials, and specifically crystalline nanoclusters or ensembles thereof, can have unique and desirable properties relative to macroscale crystals.[1,2] However, these systems tend to be intrinsically unstable which can limit their utility for applications including catalysis, plasmonics, and energy storage and conversion. The lack of stability derives from two features. First, the synthesis process either in the solution-phase or by deposition onto surfaces can generate far-from-equilibrium nanoscale structures. For example, shapes or morphologies for individual metallic nanoclusters can deviate dramatically from the equilibrium forms (e.g., dendrites and diverse geometric growth shapes which are distinct from the equilibrium Wulff polyhedra), as can composition profiles (e.g., core-shell versus intermixed alloy structures).[3-9] Second, the nanostructured nature of the system means that there is a high free energy cost associated with the large amount of interface area. Thus, there is a natural tendency for coarsening which has the effect of increasing the characteristic length scale, thereby reducing the overall interface area and thus reducing the excess free energy.[10-15] For nanocluster ensembles, coarsening corresponds to increasing the mean size of the nanoclusters while reducing their number (or density).

In this review, we focus on ensembles of metallic nanoclusters or nanocrystals (NCs) each of which has a defect-free crystalline structure. These systems are of particular relevance to catalysis for both single-component and multi-component (e.g., bimetallic) NCs.[16-19] However, other prominent applications relate to plasmonics and related Surface Enhanced Raman Spectroscopy (SERS), nanomagnetism, etc. Thus, many concepts and issues considered in this review will have general applicability and interest. Three different subclasses of systems are considered: (i) 2D supported epitaxial metal NCs, where often the supporting substrate is a crystalline metal with little or no lattice-mismatch;[7-9] (ii) 3D supported metal NCs where the substrate could be a crystalline metal, but is often non-metallic (including oxides, graphite, and graphene);[18,20-22] both 2D and 3D supported NCs are typically formed by vapor deposition; (iii) 3D unsupported metal NCs generally formed by solution-phase nanosynthesis from metal-containing precursors in the presence of capping agents which guide crystal growth and inhibit aggregation.[3,15]

Our presentation will include extensive discussion of 2D epitaxial metal NCs for the following reasons. First, detailed experimental data, particularly from Scanning Tunneling Microscopy (STM) studies from as early as the late 1980's, is available for NC formation and subsequent evolution under well-controlled ultra-high-vacuum (UHV) conditions.[7-9,13,14] To develop a reliable understanding of fundamental behavior, the UHV environment is important since even trace amounts of impurities can dramatically impact NC formation and evolution. Second, high-fidelity modeling,[8,9,14] including predictive atomistic-level models based on ab-initio energetics for both thermodynamics and kinetics,[23-27] is most advanced for these systems. Various insights from this close integration of experimental and high-level theoretical studies should carry over to other systems, particularly 3D supported and unsupported NCs, where the same level of understanding and predictive modeling capability has yet to be achieved.

Actually, there exists extensive historical analysis of 3D supported NCs originally driven by Scanning Electron Microscopy (SEM) and Transmission Electron Microscopy

(TEM) experiments since the 1960's, the availability of which long predated STM.[20] Here, primarily coarse-grained modeling and theory was implemented, which did not capture atomistic-level details of the relevant kinetics. There has been extensive interest in characterizing coarsening kinetics for these 3D supported NC system motivated in part by the challenge of mitigating catalyst degradation.[18,28-30] Finally, there have been immense advances since the 1990's in the capabilities of solution-phase synthesis to enable control of NC shape and composition profiles.[3] Also more recently, in-situ liquid-cell TEM is providing detailed insights into NC dynamics.[31-36] However, the view is still expressed that the field is more of an art than a science.[3] We should note that there exists extensive rate equation and related modeling for solution-phase NC formation and coarsening[15,37-39] with recent interest in unconventional pathways.[40-44] Also, coarse-grained modeling of growth shapes has been developed.[5,45,46] Higher-level realistic atomistic modeling with predictive capability is currently limited, although recent efforts have produced significant advances.[47-51]

The goal of this review is to highlight advances and remaining challenges with a focus on stochastic atomistic-level modeling, but also describing coarse-grained modeling. One aim is also to illustrate the insights that have been gained by close integration of such modeling efforts with experimental microscopy studies. We will emphasize the importance of a realistic and precise atomistic-level treatment of the relevant local environment-dependent kinetics in stochastic lattice-gas modeling, as this is essential for a predictive description of evolution far-from-equilibrium.[9,25] Such treatment necessarily incorporates a correspondingly precise treatment of system thermodynamics through detailed-balance constraints. This requirement for reliable kinetics applies both to the evolution of the structure (shape and composition profiles) of individual NCs, and also to the selection of the overall coarsening pathway for NC ensembles. Common generic Metropolis-type or bond-counting-type Initial Value Approximation (IVA) prescriptions of kinetics in atomistic-level modeling[52,53] do evolve to correct equilibrium, given that detailed-balance is satisfied. However, they do not generally capture correct nanoscale evolution or mesoscale coarsening pathways.

Extensive focus will be on behavior at the level of individual NC's, and in the context we will review the current capabilities of predictive modeling for: reshaping of NCs synthesized with far-from-equilibrium shapes; the coalescence or sintering of pairs of NCs upon collision; and also the diffusion for supported NCs. In addition, for multicomponent NC's, we describe the current status of analysis of compositional evolution. These studies assess, e.g., the stability of core-ring or core-shell structures against intermixing, and also to explore issues related to more complicated nanoscale Kirkendall voiding.[54,55] At the ensemble level, we review classic treatments of Ostwald ripening and Smoluchowski ripening (cluster diffusion and coalescence),[10-12,14] but still with a focus on the evolution of individual NCs. Also, we describe recent observations "anomalous" Ostwald ripening with non-equilibrated shapes of individual NCs in contrast to the classical theory.[56,57] We also describe examples of dramatic additive-enhanced ripening where mass transport is facilitated by metal-additive complex formation, a process long speculated to facilitate degradation of supported NC catalysts.[58,59]

In Sec.2, we provide a brief synopsis of key aspects of the synthesis via self-assembly of metallic NCs and their subsequent evolution and coarsening. This discussion covers both 2D and 3D supported NCs, as well as unsupported solution-

phase NCs. Detail understanding and theoretical description of these systems is provided by stochastic atomistic-level modeling as described in Sec.3. As noted above, a key requirement is the realistic description of system kinetics as well as thermodynamics. In Sec.5, we describe coarse-grained continuum modeling which provide a complementary strategy and additional insight to atomistic-level modeling. Continuum formulations are also traditional applied to describe coarsening, particularly Ostwald ripening. The remainder of the review focuses on examples from a diversity of specific systems of post-synthesis evolution of metallic NCs with most emphasis on behavior for individual NCs. In Sec.5, we describe shape evolution for single-component epitaxial NCs, and in Sec.6 describe corresponding evolution for both supported and unsupported 3D NCs. Here shape evolution includes equilibration of NCs with simple convex geometric initial shapes, sintering or coalescence of pairs of NCs, and pinch-off of elongated nanorod NCs. Compositional evolution in multicomponent (typically bimetallic) NCs is described in Sec.7 including behavior associated with the Kirkendall effect. Diffusion of supported NCs underlying Smoluchowski Ripening, and decay of individual NCs associated with Ostwald Ripening, are described in Sec.8. A summary is provided in Sec.9.

2. SYNOPSIS OF SELF-ASSEMBLY AND COARSENING FOR METALLIC NC SYSTEMS

This section provides an overview of key concepts and phenomena without the inclusion of extensive theoretical or mathematical formalism. A more detailed technical formulation is provided in Sec.3 and Sec.4, and also in later sections.

2.1. Basics of NC self-assembly

There are two key ingredients generally operative for the formation of nanocluster (NC) ensembles:[60] (i) presence of mobile species which facilitates aggregation; and (ii) some degree of relaxation of species within the aggregated state, a process which plays a critical role in determining the structure of individual NCs. As eluded to by the first requirement, two standard scenarios for self-assembly are: (a) deposition on flat single-crystal surfaces; (b) solution-phase synthesis, both of which will be considered in this review. In general, one anticipates non-equilibrium or even far-from-equilibrium structures of individual NCs will be manifested if the characteristic time scale for growth (i.e., for aggregation and incorporation of species) is shorter than the characteristic time for relaxation within the NC (by periphery diffusion, detachment-reattachment, etc.)

Another generic characterization of types of classes of aggregation phenomena relates to the detailed nature of transport to and the ease of attachment to or incorporation into the growing cluster. First, consider the extreme case where there is no relaxation upon aggregation, which is illustrated in Figure 1. If transport to the cluster is diffusion-limited, and if there is no barrier to attachment or incorporation, then one obtains so-called Witten-Sander or Diffusion-Limited Aggregation (DLA) clusters.[61,62] These have irregular fractal structure (Haussdorff-Besicovitch dimension $d_f \approx 1.71$ in 2D, and $d_f = 1.9$ in 3D) reflecting a Mullins-Sekerka type shape instability associated with preferential attachment at protrusions. On the other hand, if attachment or incorporation is strongly inhibited (so-called attachment- or interface- or reaction-limited growth), then the details of transport to the cluster are not so relevant, and in the simplest picture attachment occurs at essential random locations on the cluster periphery. The resulting so-called Eden clusters[63] are compact and nearly (but not exactly) rotationally symmetric in the large size regime, i.e., circular in 2D or spherical in 3D.[62] However, on a length scale smaller than the radius, the cluster periphery is kinetically roughened with detailed features such as local spatial correlations described by Kardar-Parisi-Zhang theory.[62,64]

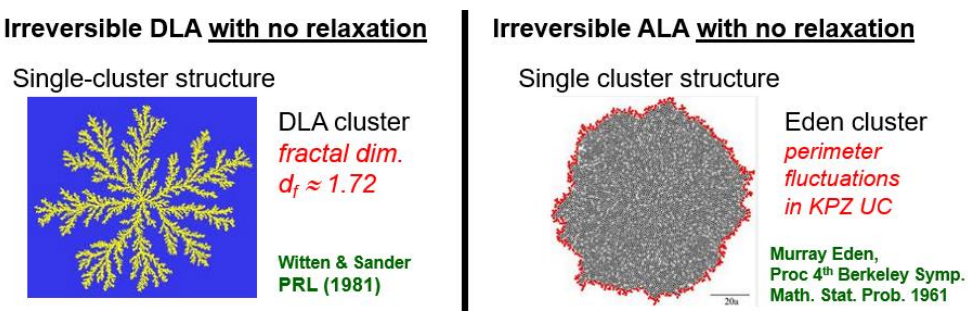

Figure 1. Schematics of the structure of 2D clusters formed by aggregation without relaxation.

It should be emphasized, however, that neither true DLA nor true Eden clusters are typically observed in experimental realizations of NC formation. There is invariably some degree of relaxation of aggregated species on the time scale of growth. For DLA-type processes, even with limited relaxation, the spindly “arms” of Witten-Sander clusters (the width of which is on the order of a few atoms) are thickened.[8,65-67] In addition, these clusters can adopt and overall dendritic structure or even compact structure reflecting a combination of relaxation kinetics and equilibrium structure[8,9]. Similarly, but perhaps less dramatically, relaxation would impact compact Eden type cluster growth. However, for attachment-limited growth, in general different surface orientations or facets will be associated with different attachment rates, thereby producing compact non-spherical and often kinetically faceted non-equilibrium growth shapes. Various possible regular and irregular growth shapes are shown for 2D epitaxial metal islands in Figure 2[8,23,57,68] and various kinetically faceted growth shapes for unsupported 3D crystalline NCs are shown in Figure 3. Of course, if relaxation is sufficiently facile, then at least close to equilibrium Wulff shapes or their analogues for supported NCs[5,69,70] would be achieved during growth for either diffusion-limited or attachment-limited growth.

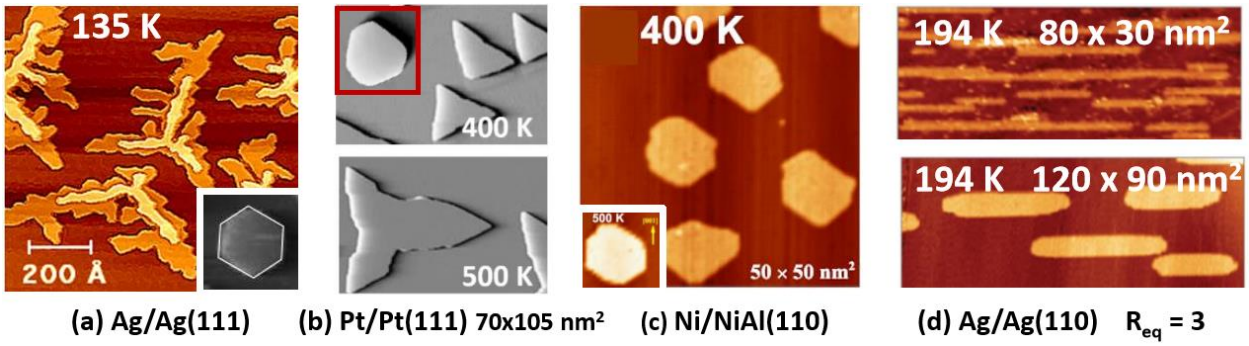

Figure 2. Illustrations of growth shapes of 2D epitaxial NCs. Insets in the left three frames show the equilibrium shapes. The equilibrium aspect ratio for Ag/Ag(110) is R_{eq} = 3. Reprinted with permission from Ref.s [(a)[68], (b)[8], (c)[23], (d)[57]]. Copyright 2005 (a) 2013 (d) American Physical Society; 2004 Springer Verlag; 2011 American Institute of Physics.

The above focuses on NC shape which is of primary interest for single-component NCs. Additional challenges and opportunities arise for multi-component NCs. One can synthesize core-shell structures, or more complex layered onion-like structures, by sequential or alternating deposition of different components for the case of supported NCs, or by sequential or alternating introduction of metal precursors for solution-phase synthesis. Perhaps surprisingly, there are relatively few examples available for 2D epitaxial core-ring structures (i.e., the analogue of core-shell structures in 3D) formed by deposition, although at least for some systems STM imaging can provide a detailed characterization of these features.[71-73] For 3D supported NCs formed by deposition, there have been several studies of sequential codeposition,[74-78] but there is a lack of high-resolution imaging characterizing of core-shell structure. For solution-phase synthesis of core-shell and onion-like structures, high-fidelity control of such processes has now been developed, and there is extensive TEM and EDX imaging

providing detailed characterization of the resulting structures.[79-82] Often the synthesized core-shell structure will not correspond to the equilibrium NC structure, which might instead be an intermixed alloy or intermetallic structure. Thus, post-synthesis evolution will involve intermixing on a time scale reflecting the relevant intermixing mechanism and kinetics. This opens the possibility for more exotic behavior such as a nanoscale version of Kirkendall voiding,[54,55] as will also be discussed in the following sections.

Structures	Shapes	Schematic drawings	Metals
single-crystal	perfect/truncated cube[a]		Pd, Ag, Au, Pt, Cu, Rh, Bi, Fe
	perfect/truncated octahedron[a]		Pd, Ag, Au, Pt
	perfect/truncated tetrahedron[a]		Ag, Au, Pt, Rh
	rectangular bar		Pd, Ag, Pt
	octagonal rod		Pd, Au, Fe, Co, Ni
	rectangular or octagonal wire	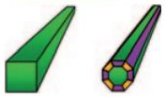	Pb, In, Sn, Sb, Fe, Co

Figure 3 Kinetically faceted growth shapes for 3D unsupported crystalline NC[3]. Facet color scheme: orange = {111}, green = {100}, purple = {110}. Reprinted with permission from Ref.3. Copyright 2009 Wiley-VCH.

We emphasize that the focus of this review is not on growth, but rather on post-assembly or post-synthesis evolution, which can also be characterized as an analysis of the stability (or lack of stability) of synthesized non-equilibrium NC ensembles. This presentation will include description equilibration processes both at the level of individual NCs (reshaping, compositional evolution), and at the ensemble-level (coarsening via OR or SR).

2.2. Self-assembly 2D and 3D supported NCs via surface deposition

A schematic for the formation of supported NC by deposition is shown in Figure 4 for the case of 2D epitaxial NCs on a fcc(100) or bcc(100) surface with square symmetry. Specifically, Figure 4 illustrates the case of sequential co-deposition resulting in a core-ring or core-shell NC. The basic features are: random deposition on the surface; facile diffusion of deposited species; nucleation of NCs when a sufficient number of diffusing species meet; and growth of nucleated NCs by incorporation of subsequently deposited species. The latter involves shape relaxation of NCs by periphery diffusion of aggregated atoms and possible detachment-reattachment. These are also the ingredients for the formation of 3D supported NCs.

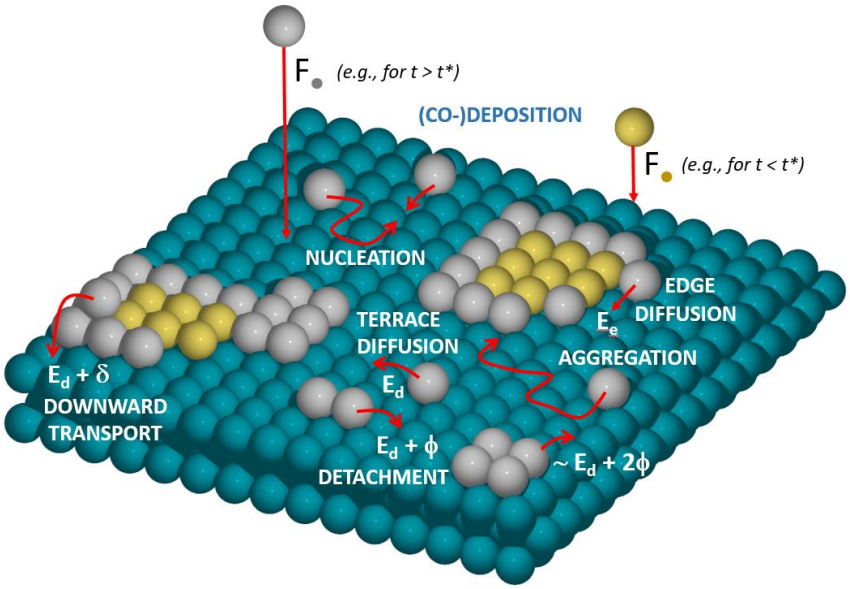

Figure 4. Schematic of NC nucleation and growth by (co-)deposition on a metal (100) surface.

2.2.1 Ensemble-level features. First, here we describe ensemble-level features of NC self-assembly during deposition. In the commonly adopted far-from-equilibrium picture, there exists a well-defined critical size, i, such that islands of greater than i atoms are regarded as being stable. Subcritical NCs of size i and below are regarded as being in a quasi-equilibrium with adatoms, and supercritical NCs with size above i effectively grow irreversibly.[9,83] As a consequence, in this picture, we effectively assume a separation of time scales between NC formation and post-synthesis evolution. We emphasize that for metallic systems at temperatures around room temperature or below, the critical size is often small including the case i = 1 corresponding to irreversible NC formation nucleated when a pair of adatoms meet and involving irreversible incorporation of subsequent adatoms. In some sense, for i = 1, the deviation from equilibrium is most extreme.

Mean-field rate equation treatments dating from late 1960's[83,84] which are based on this picture correctly predict the mean island density, P_{isl}, for surface deposition as a function of control parameters (deposition rate, F, and surface temperature, T, and coverage, θ) and system parameters including critical size, i. More sophisticated rate equation formulations determine "capture numbers" which control NC growth rates in a self-consistent fashion by solving the deposition-diffusion equation for aggregation with a single stable island in an appropriately described effective medium of other islands.[84,85] This analysis incorporates the feature that the adatom density vanishes approaching the periphery of the island which is a trap for deposited atoms. This in turn implies that islands are less likely to nucleate, and thus less likely to be found close to other islands, i.e., the island distribution is non-random. However, even these self-consistent MF treatments fail to describe more detailed features such as the NC size distribution.[9,86,87]

The failure of MF treatments to predict the NC size distribution reflects the feature that the local environment of islands is not independent of their size (as

assumed in the effective medium picture). Specifically, there is a correlation between NC size and separation, larger NCs being further separated from the neighboring islands.[9,88] This feature is best illustrated by the introducing the concept of capture zones (CZs) where these are constructed by tessellating the entire surface into cells or CZs, one per island.[83,88-90] The basic idea is that deposited atoms tend to aggregate with the island associated with the CZ into which they were deposited. See Figure 5. Except for a very short initial transient regime, the system is in a quasi-steady state in the sense that there is a rough balance between the gain in adatom density due to deposition and the loss due primarily to aggregation with islands. Thus, CZ areas multiplied by the deposition flux determine NC growth rates, and thus CZ areas are essentially equivalent to the capture numbers mentioned above. CZ's can be reasonably be described by modified Voronoi cells constructed based on distance to the edge rather than the center of the islands.[91,92] Exact construction involves solving a boundary value problems for the deposition-diffusion equation for the complete distribution of islands.[71,91,92] Specifically, CZ's correspond to collections of deposition points for which following the surface diffusion flux lines leads to the same island. However, the key point is that larger NCs tend to have larger CZs, so the environment of a NC is strongly dependent on its size, and this feature controls the NC size distribution.[88]

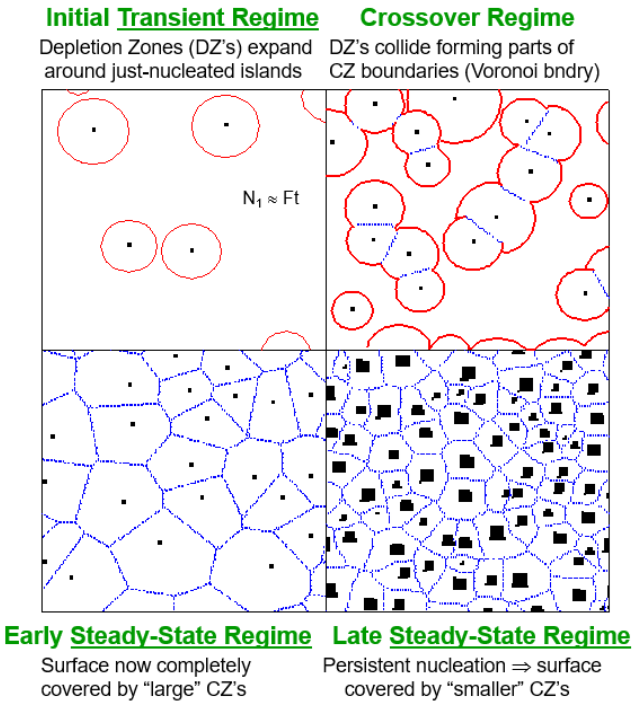

Figure 5. Stochastic geometry representation of the nucleation and growth process for 2D epitaxial NCs formed during deposition.

Two additional observations should be made regarding NC nucleation[9,93,94]. During a short transient regime at the onset of deposition, the adatom density grows uniformly until it reaches a sufficient magnitude where islands start nucleate at

essentially random positions. Depletion zones (in which the adatom density is reduced due to capture at NC peripheries) grow quickly about these NCs, colliding with each other and soon covering the surface. It is at this point, the steady-state regime emerges and one regards the entire surface as tessellated into CZs surrounding islands. It should also be emphasized that nucleation of new islands persists (and is generally dominant) in the steady-state regime, but now most nucleation occurs away from NCs along the CZ boundaries where the adatom density tends to be maximized. See again Figure 5.

An exact analysis at the ensemble-level of the NC formation process is not available. However, the most fundamental and comprehensive analyses should simultaneously consider both NC sizes and CZ area distributions.[95-98] Finally, we remark that subsequent post-deposition coarsening of the NC ensemble will reflect not just the island size distribution at the end of deposition, but also more detailed correlations between nearby island sizes and between size and separation.

2.2.2. Individual NC structure. As noted in Sec.2.1, facile relaxation on the time scale of growth lead to equilibrium shapes. For 2D epitaxial NCs, these shapes are determined by a 2D version of the Wulff construction where the input is the orientation-dependent (free) energy of steps bordering these NCs.[69] We note the existence of exact analysis of step energy at finite temperature for simple Ising-like models with NN lateral interactions.[99] There are no true facets for 2D shapes, no matter how large. However, step edges can be effectively faceted in the low temperature regime where the mean separation between thermally-generated kinks exceeds the characteristic linear size. For 3D supported NCs, the equilibrium shape is determined by a so-called Winterbottom modification to the traditional 3D Wulff construction.[5,70,100] This construction not only involves the orientation-dependent surface (free) energy, which tends to have local minima for low-index facets, but it also accounts for the adhesion energy of the cluster to the substrate. A supported NC has the same shape as the unsupported case, except that a portion of the NC adjacent to the supporting facet is removed, the extent of this removed portion increasing with the adhesion energy. See Figure 6. For the case of isotropic surface energy, this construction recovers the Young-Dupre equation prescribing the contact angle for the truncated spherical cluster.

With regard to deviations from equilibrium shape and structure, we first quantify the time scale for the growth of individual NCs. As noted above, after the short transient regime, the rate of growth of any NC is determined by the associated CZ area multiplied by deposition flux, F. Since the mean CZ area is given by $A_{CZ} = 1/P_{isl}$, it follows that the mean NC growth rate is given by $K_G = F/P_{isl}$. Correspondingly, the mean time between aggregation events is given by $\tau_G = 1/K_G = P_{isl}/F$. This characteristic growth time should be compared with the mean time scale for relaxation, τ_R, to determine the extent of equilibration during growth. Of course, τ_R depends on the mechanism of relaxation. For most of our studies, we will consider relaxation mediated by periphery diffusion (PD). If D_{PD} denotes the effective periphery diffusion rate, and L_c denotes the characteristic linear dimension of the NC, then the characteristic relaxation time should correspond to the typical time to diffusion around the NC. According to Einstein's relation, this implies that[9,66] $(L_c)^2 = D_{PD}\,\tau_R$. Thus, shape relaxation is facile (inhibited) for $\tau_R << \tau_G$ ($\tau_G << \tau_R$).

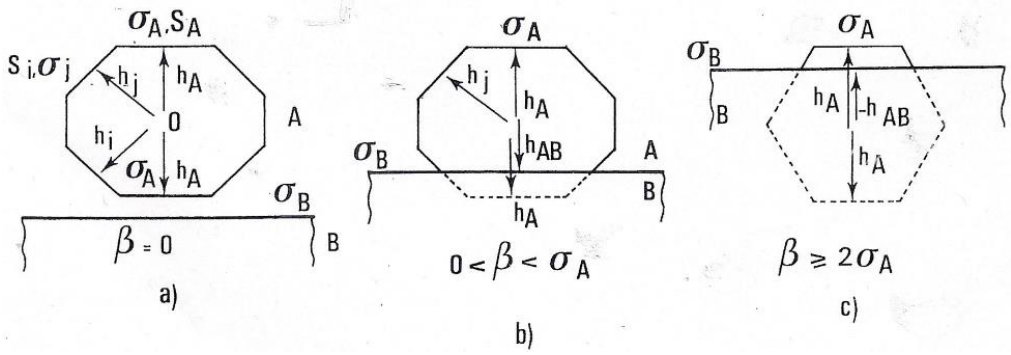

Figure 6. Equilibrium shapes of supported crystalline NCs. σ_A denotes the surface energy of the NC material A, and β denotes the adhesion energy between A and the substrate B. For isotropic surface energy, the Young-Dupre equation becomes $\sigma_A \cos\theta = \beta - \sigma_A$ where θ is the contact angle to the substrate $\theta = 0$ (π) for complete wetting (no adhesion). Often behavior is cast in terms of an A-B interface energy defined as $\sigma^* = \sigma_A + \sigma_B - \beta$. Reprinted with permission from Ref.[20]. Copyright 1979 North Holland.

In fact, shape relaxation mediated by PD can be significantly more complex than suggested by the above. For 2D epitaxial NC's, there are a variety of edge diffusion barriers depending on the local edge configuration. However, perhaps most important is to distinguish between diffusion along straight close-packed step edges, and diffusion around kinks or corners. The latter is potentially subject to an additional so-called kink Ehrlich-Schwoebel (ES) barrier, and the presence of such a barrier impacts the overall relaxation process. In general, limited edge diffusion will induce a DLA-type fractal growth instability. Even in the presence of substantial diffusion along straight step edges, presence of a substantial kink (1D) ES barriers will induce a shape instability where active edge diffusion will fatten the arms of the NC relative to DLA clusters, and dendritic rather than isotropic fractal shapes may develop.[66,101]

For 3D supported NC, concepts from multilayer epitaxial metal film growth[8,9] are relevant. One particularly significant additional kinetic parameter is the presence of a possible additional (2D) ES barrier for adatoms to cross single atom-high steps (either upward or downward). For downward transport of isolated atoms, this barrier is in addition to the terrace diffusion barrier. For upward transport, this 2D ES barrier is in addition to the terrace barrier plus an additional cost to extract from the step edge. The situation is more complex if multi-atom high facets develop on the sides of growing 3D NC's. Then atoms must cross between facets during growth in which case they may encounter a so-called 3D ES barrier[102-104] which is generally distinct from the standard (2D) ES barrier. One might anticipate that for the assembly of 3D NCs, where most aggregating atoms diffuse across the substrate and incorporate with the growing NC, that the presence of 2D and 3D ES barriers will inhibit upward transport and thus result in kinetically flattened NCs relative to their equilibrium shape. However, it might be noted that at least for the case of glancing angle-deposition[105] where shadowing effects are also important, the presence of a 3D ES barrier has been associated with the formation of nanorods protruding upward from the surface, i.e., structures which are more vertically elongated than equilibrium shapes.[106,107]

2.3. Post-assembly coarsening pathways for supported NCs

For ensembles of supported metal NCs formed by surface deposition, it should be emphasized that there generally exists a clear separation of time scales between NC formation (occurring on the time scale of deposition of tens of seconds or a few minutes) and the subsequent post-deposition coarsening (occurring on the time scale of tens of min, or of hours).[12-14,28,30] Thus, treatment and analysis of NC formation and of post-deposition coarsening, are naturally often performed separately. This time scale separation will not be so evident for solution-phase processes.

As indicated in Sec.1, the standard coarsening pathways are Ostwald ripening (OR) and Smoluchowski ripening (SR). These processes are illustrated in Figure 7 for 2D supported NCs. As discussed further in Sec.3, OR is usually described by Lifschitz-Slyosov-Wagner (LSW) theory.[12,14] LSW integrates an analysis of the growth or decay of individual NCs (which involves solving a boundary value problem for a simple steady-state diffusion equation) into a formulation to describe the size distribution for the evolution of the overall NC ensemble. As also discussed further in Sec.3, SR (NC diffusion and coalescence) is described in terms of Smoluchowski's equations for "coagulation",[108] where the key input is the size-dependent diffusivity of individual NCs.[14]

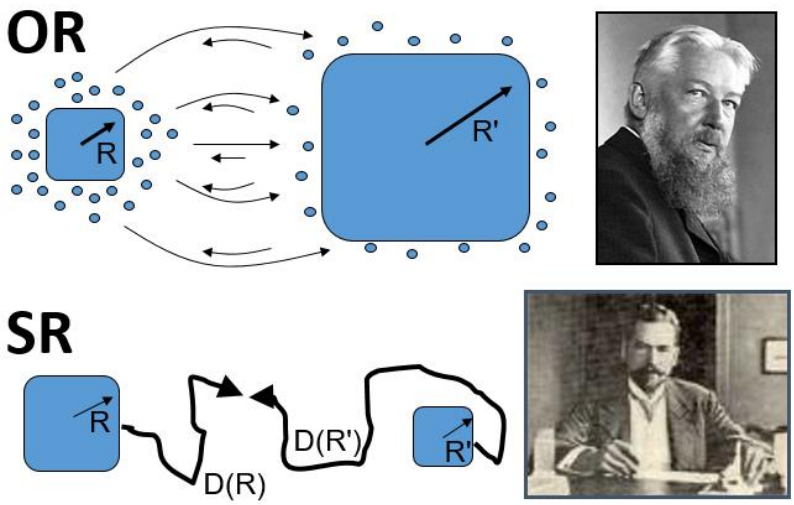

Figure 7. Schematic of coarsening pathways for supported 2D NCs: OR versus SR. Also shown are images of Ostwald (top right; http://www.wissen.de/lexikon/ostwald-wilhelm) and Smoluchowski (bottom right; https://jbc.bj.uj.edu.pl/dlibra).

For 2D epitaxial NCs which completely wet the substrate, perhaps the default expectation is that coarsening should occur via OR which involves diffusion of detaching adatoms across the surface[12] (but see below). For 3D supported NCs, it is less clear as to whether OR or SR dominates, and there has been extensive debate on this issue particularly for catalytic systems.[28,30,58] In the standard picture for OR, individual NC's are regarded as having equilibrated shape, and thus a well-defined chemical potential. Smaller islands have higher periphery curvature, and thus higher chemical potential according to the Gibbs-Thompson relation.[10,12-14] Thus, the adatom density associated

with attachment-detachment equilibrium at the island periphery is also higher. Consequently, adatom diffusion across the surface, which is downhill in chemical potential and adatom density, is from smaller to larger islands. See Figure 7. This results in the shrinkage and ultimate disappearance of smaller than average islands and growth of larger than average islands.

However, STM studies for 2D epitaxial NCs in the 1990's revealed that SR rather than OR can actually dominate in these systems.[14,109] Indeed, the great advantage of these UHV studies in well-controlled environments is that one can generate an STM movie in real time of the coarsening processes and directly assess whether OR, SR, or a combination of the two dominates evolution. Actually, the dominant pathway is system and condition specific. For fcc metals where NC's are 2D epitaxial adatom islands of the same material (i.e., homoepitaxial systems), it appears that OR does generally dominate coarsening for (111) surfaces, but that SR dominates for (100) surfaces. In these systems, NC diffusion is mediated by periphery diffusion (PD) of atoms around the edge of the NC.[13,14] The difference between behavior for (111) versus (100) systems ultimately derives from the feature that diffusion of atoms along close-packed straight steps on (100) surface is much more facile than terrace diffusion, but the opposite applies for (111) surfaces.

Determination of the dominant coarsening mechanism is complicated by a number of factors some of which we now list. **(i)** The selected mechanism naturally reflects the relative magnitude of the effective barriers $E_{eff,}$ for various pathways which will be described in Sec.3. **(ii)** However, behavior is complicated by the feature that rates for different pathways have different exponents describing the variation of coarsening rate with the typical linear size or "radii" of NCs[110] as also described in Sec.3. Thus, the dominant pathway potentially depends on the characteristic size of the NCs. For example, in systems where SR dominates for some regime of typical NC sizes, we will predict a crossover to OR for larger sizes (later in coarsening). **(iii)** The default mass carrier for OR is assumed to be adatoms diffusing across the surface, but it could instead be vacancies diffusing through the top surface layer.[14] This introduces additional possibilities for dominant coarsening mechanism and for switching between mechanisms. An even more novel possibility for mass carriers is described below. **(iv)** For SR, in principle the mechanism of cluster diffusion can change from PD-mediated to attachment-detachment mediated (and potentially this could involve not just detachment of atoms to the exterior of the NC, but detachment of vacancies to the interior). However, if detachment is facile, then this would also favor OR over SR.

There are additional possibilities for complex and unconventional behavior in OR. One relates to the default assumption that the individual NC's have equilibrated shapes and structure and thus well-defined chemical potentials. If there is a lack of complete equilibration of individual NCs, then there is the possibility of introducing partial chemical potentials, and developing a modified LSW type theory of OR based on these.[56,57,111,112] Another possibility relates to behavior in non-pristine systems where chemical additives even in trace amounts, where there is the potential of complex formation between the metal atoms and the additives.[58,59] These complexes could facilitate more facile mass transport during OR than is possible if transport is mediated by adatoms. Analysis of these significantly more complex systems involves solving an appropriate boundary value problem for a coupled non-linear set of reaction-diffusion

equations (describing complex formation, diffusion, and dissolution),[113] rather than the usual simple linear diffusion equation for transport of metal adatoms.

It is also appropriate to note that most theoretical studies of coarsening at the ensemble level, have focused on asymptotics, i.e., temporal scaling of the divergence of the mean NC size for long time, and particularly the non-trivial selection of an asymptotic shape of the NC size distribution.[12] However, in practice, experimental observations cover a substantial non-asymptotic regime, where behavior is impacted by the NC formation process and the details of the resulting NC distribution (as described in Sec.2.2). Thus, analysis of the associated transient behavior should also be of interest.

In addition to ensemble-level issues for coarsening described above, there is interest in and insight to be gained from analysis of behavior at the level of individual NC. In this review, we actually emphasize these features. We have already noted the feature that self-assembly can produce far-from-equilibrium structures for individual NCs. Thus, in general, there will be an initial post-assembly regime where these individual NC shapes are equilibrating. (However, in some unusual situations, non-equilibrium shapes persist throughout the coarsening process, as mentioned above.) For OR, it is common and instructive to analyze the decay of individual (smaller than average) NCs, as this provides insight into the details of the coarsening process[13,29]. For SR, as indicated above, the diffusivity, D_N, of individual NC's of size N atoms is of central importance,[14] and will be discussed in detail in Sec.8. Also since coarsening involves collision and coalescence of NC pairs, detailed analysis of this sintering processes is of particular interest.[27,114] and is described in Sec.5 and Sec.6.

Finally, with regard to 2D epitaxial NCs, we note that there exists the novel possibility to assess and compare with the "photographic negative" process of the coarsening of 2D single-atom deep vacancy nanopit NCs.[13,14,109] For systems described by pairwise lateral interactions, there is a particle-hole symmetry in the equilibrium properties. Also, in the regime of large sizes, adatom NCs and vacancy nanopits have the same equilibrium shape. However, any particle-hole symmetry is broken for kinetic processes such as coarsening. In fact, interestingly for fcc surfaces, there tends to be the opposite behavior for adatom NCs versus nanopits in terms of whether OR or SR dominates coarsening.

2.4. Solution-phase self-assembly and coarsening of 3D unsupported NCs

Formulations for solution-phase nucleation and growth of NCs tend to be based on classical nucleation theory (CNT)[115,116] combined with concepts from coarsening theory. We should also note that various refinements of the standard CNT picture have been developed in recent years which could be relevant to solution-phase NCs formation.[117,118] The latter include non-classical nucleation involving magic-sized subcritical clusters, and stepwise phase transitions involving amorphous to crystalline transitions for subcritical clusters.[118]

Traditional LaMer burst nucleation mechanism of sequential nucleation and growth considers the following three-stage picture: (i) a rapid increase in the concentration of free monomers in solution (e.g., obtained by reduction) to exceed a critical value; (ii) a "burst" of nucleation of NCs which rapidly reduces the free monomer

concentration below this value, thereby terminating nucleation; and (iii) sustained growth of NCs due to diffusion of monomers through the solution and aggregation with the NCs. See Figure 8. A more detailed characterization of the NC growth regime consistent with this mechanism showing different possible single-crystal growth shapes is presented in Figure 9. In this figure and more generally, it is common to distinguish somewhat ill-defined and poorly characterized "nuclei" (which presumably should be regarded as sub-critical clusters) from "seeds" (where the latter corresponding to super-critical stable clusters). Here "critical" refers to the critical size in class nucleation theory. The structure of the seeds (single-crystal, singly twinned, multiply twinned) naturally impacts the structure of the subsequent NCs. The single-crystal case is most relevant for the studies presented in this review. In the case of thermodynamic rather than kinetically controlled formation of critical cluster, classical nucleation theory implies that cluster shape should minimize the surface energy cost at the critical volume. Consequently, the Wulff construction also applies here to predict critical seed shape[3].

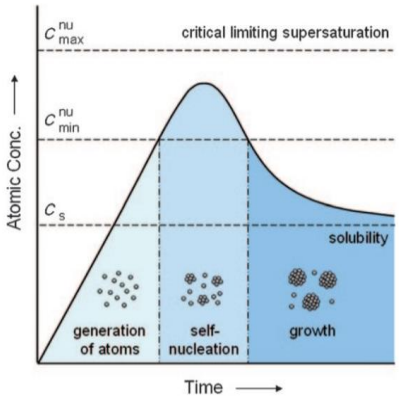

Figure 8. Schematic of LaMer burst nucleation process. Reprinted with permission from Ref.3. Copyright 2009 Wiley-VCH.

For solution-phase synthesis, the separation of the NC formation (nucleation and growth) stage and the coarsening stage is not as clear as for supported NCs formed by deposition. Indeed, coarsening is often intertwined with and identified as part of the growth stage for solution-phase synthesis (in contrast to growth during deposition of supported NCs with well-defined critical size which is quite distinct from coarsening). For solution-phase systems, Ostwald ripening (dissolution of smaller NCs and growth of larger ones) can be the dominant coarsening pathway. Traditional LSW theory is sometimes refined for solution-phase systems to incorporate the possibility of growth due to strong super-saturation of monomers in solution.[15] Associated simplified analysis of specific behavior (e.g., NC size distribution focusing or narrowing) is also extracted.[15] However, significant attention is being paid to the possibility of quite distinct Smoluchowski ripening type pathways, i.e., NC coalescence including the special case of oriented attachment.[40-44] The latter produces single-crystal aggregates versus multi-grain aggregate where the individual grains are separated by grain boundaries. See Figure 10 showing these possibilities. Again we note that the focus of this review will be on the evolution of single-crystal NCs, so the orientated attachment pathway is particularly relevant for such studies.

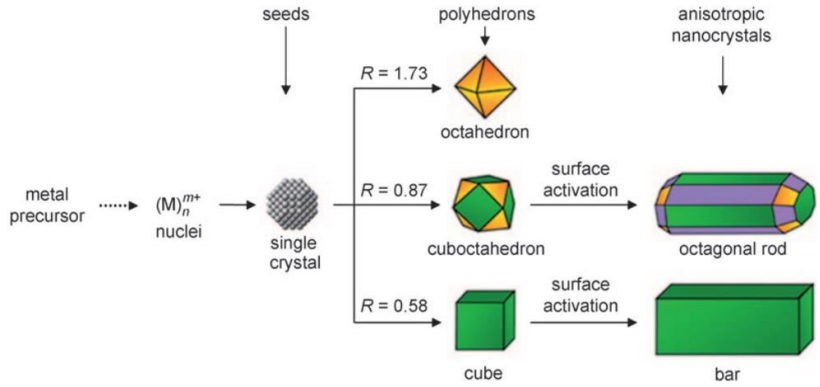

Figure 9. Schematic of the solution-phase nucleation and growth processes leading to various single-crustal NC structures. Color coded facets green, orange, purple = {100}, {111}, {110}. Reprinted with permission from Ref.3. Copyright 2009 Wiley-VCH.

A contrasting mechanism from LaMer burst nucleation is a Finke-Watzky two-step mechanism characterized by persistent nucleation in the first stage followed by so-called autocatalytic surface growth.[119] Generally, there is also regarded to be some overlap between these regimes. See Figure 10. By kinetic fitting using traditional mean-field rate equations, it has been suggested that this picture applies for many metallic systems including Ir, Pt, Ru, and Rh.[15]

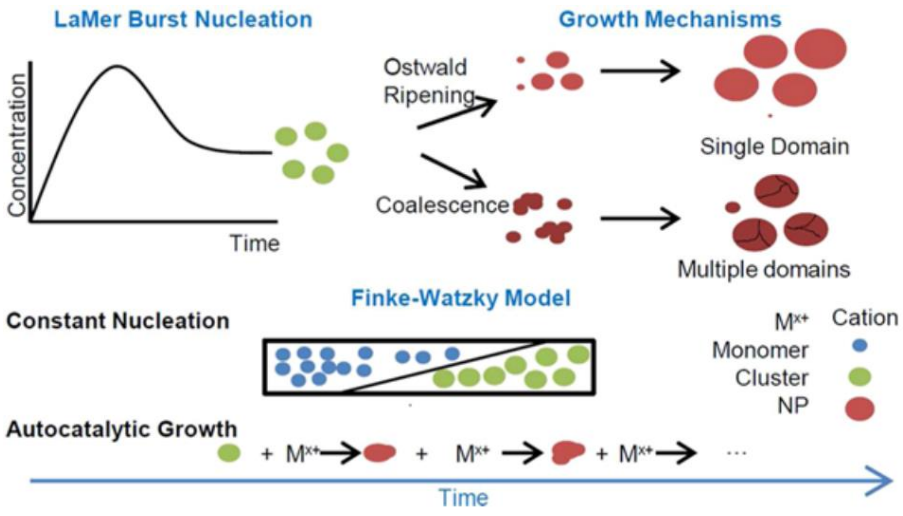

Figure 10. Overview of various NC formation and subsequent coarsening processes. Reprinted with permission from Ref.15. Copyright 2014 American Chemical Society.

3. OVERVIEW OF ATOMISTIC-LEVEL STOCHASTIC MODELING STRATEGIES

For atomistic-level modeling of the evolution of crystalline NCs, to assess the relevant time scale, it is particularly natural to implement stochastic lattice-gas models. In these models, atoms are located at a periodic array of crystalline lattice sites. The atoms move (e.g., hop) between these lattice sites with prescribed rates (e.g., mediating shape relaxation of NCs). The hop rates, h, will be assumed to have an Arrhenius form,

$$h = \nu \exp[-E_{act}/(k_B T)], \quad (1)$$

where ν is an attempt frequency. For simplicity, $\nu = 10^{12}$-10^{13} s^{-1} is chosen to be the same for all hops, but this is a reasonable assumption. The variation of these rates is thus determined by variation in activation barriers, E_{act}, which depend on the local environment of the hopping atom. Technically, it is assumed that there is an exponential waiting time between hops, where the mean waiting time is simply determined as the reciprocal of the corresponding hop rate. Within this framework, evolution corresponds to a Markov process in the state space of NC configurations, and is in principle described exactly by the corresponding master equations.[120] In practice, the state space is too large for effective analytic treatment of these equations, and thus instead model behavior is efficiently and precisely determined by Kinetic Monte Carlo (KMC) simulation which can track evolution over the appropriate time and length scales.[52]

In the context of supported 2D epitaxial NCs, the overall self-assembly process can be modeled within this framework by allowing form the addition of atoms to adsorption sites at a prescribed rate (corresponding to the deposition flux), and subsequent lateral surface diffusion of hopping between such sites which leads to both nucleation on NCs and subsequent growth.[8,9] The main challenge is accurate description of edge diffusion rates in the various local configurations at the periphery of the NC, and of rates for any intermixing processes for multi-component NCs.[24,25] As noted previously, NC structure is highly sensitive to the details of this prescription. For supported 3D epitaxial NCs (or more generally for multilayer epitaxial film growth), additional challenges include the treatment of interlayer transport where possible additional Ehrlich-Schwoebel type barriers can control behavior.[8,9,102,104,107]

In such modeling of self-assembly on supported NC ensembles, it is sometimes the case that various processes can be treated as effectively irreversible on the time-scale of the assembly process (at least at sufficiently low temperatures).[97] For example, prescription of critical size i = 1 means that atoms aggregate irreversibly. In a less extreme regime, one might anticipate that singly-coordinated atoms at the NC periphery are mobile around the periphery, but that more highly-coordinated edge atoms are effectively permanently trapped. However, for our focus on post-synthesis shape evolution and coarsening, it will be important to incorporate with non-zero rates all processes which could impact such evolution generally on longer time scales. Furthermore, it will be critical to ensure that the selected rates for such processes are consistent with detailed-balance[120] so that evolution will lead NCs to achieve their correct equilibrium shapes and structures.

For unsupported 3D crystalline NCs, stochastic lattice-gas modeling is naturally and efficiently used to describe structural evolution of the NC itself.[121-124] It should however be noted that there are a vast number of local environments even just at the surface of the NC in which atomic hopping must be reliably described. For self-assembly and growth, it is necessary to describe diffusion to and aggregation with the NC which might be achieved within an off-lattice or continuum formulation appropriately coupled to the lattice-based treatment on NC structure evolution. However, our focus will again be on post-synthesis shape and structure evolution including sintering. For nanoscale metallic NCs, there is a general expectation that these processes will be dominated by surface diffusion rather than attachment-detachment processes.[125,126] Consequently, relevant analysis can be performed completely within the framework of a lattice-gas model.

In addition to atomistic level stochastic-lattice gas modeling, it is valuable to explore coarse-grained continuum theory and modeling to assess NC self-assembly and stability, where the latter is our focus. Naturally for evolution of NC ensembles, atomistic-level treatment is generally computationally inefficient compared to continuum formulations (or possibly hybrid formulations).[10,12] Coarse-grained modeling might also be applied to analyze the evolution of individual NC's, as has been done for NC growth,[46] but more traditionally and more extensively for reshaping and sintering of NCs which is of central interest in this review. In fact, deterministic continuum modeling of reshaping mediated by surface diffusion goes back to classic work of Herring, Mullins, and others in the 1950's.[125,127,128] In addition to potential computational efficiency, a great advantage of such coarse-grained modeling is the additional insight into the evolution process which can derive from such formalisms. Finally, it might be noted that for nanoscale evolution, fluctuation effects can be significant. Then, the above deterministic treatments do not provide a complete picture, and thus it is natural to augment them with the appropriate addition of noise within a continuum Langevin type formulation[129].

3.1. Stochastic lattice-gas modeling of equilibrium NC structure

While our focus is on non-equilibrium evolution of NCs, it is necessary for the models to accurately describe equilibrium NC shape and structure. We thus provide some brief related comments here. For 2D epitaxial NCs, the equilibrium shape is determined by a 2D version of the Wulff construction for which the required input is the orientation-dependent step free energy. For fcc(100) or bcc(100) surfaces with a square array of adsorption sites, the simplest lattice-gas model with NN attractive pair interactions corresponds to the ferromagnetic Ising model on a square lattice. An exact analysis is available in this case for this system determining the T-dependence of equilibrium NC shapes.[99,130] Naturally, there have been various extensions of this work to treat hexagonal close-packed fcc(111) and hcp(0001) surfaces, and the effect of longer-range pair interactions.[131-133] For these 2D systems, we note that strictly step edges are never facetted for the fundamental reason that phase transitions do not occur in 1D systems. However, step edges can be effectively facetted on the length scale of the NC at lower T. It should be noted that for non-equilibrium NC shape evolution (and for equilibrium step fluctuations), a key parameter is the step stiffness which is determined

by the step free energy. Accordingly, some effort has been invested to produce conveniently usable expressions for this quantity.[134]

The presence of trio- and higher-order many-body lateral interactions as well as NN and longer-range pair interactions is well recognized for 2D epitaxial systems. Of particular relevance for this study is the feature that the equilibrium shape of 2D NCs on fcc(111) surface cannot in general be described by Ising type models with pairwise interactions, as these do not distinguish between distinct between {100} micro-facetted A-step edges and {111} micro-facetted B-step edges of NCs. Thus, it is necessary instead to apply so-called Awning models,[8] or to incorporate many-body interactions (the latter more realistic modeling being our strategy). Generally, a more complete set of pair and many-body interactions is determined systematically from ab-initio DFT calculations within a cluster expansion framework.[25,26,135-139] This larger set of interactions provides the input for Monte Carlo or KMC simulation. The cluster expansion approach was initially developed to describe the configuration-dependent energetics of multi-component bulk metallic alloys,[140] where a rigorous framework for convergence has been developed. However, it is recognized that there are practical complications when applied to epitaxial NCs since lateral relaxation of atoms near the step edges, i.e., near the NC periphery, can be quite distinct from that in the NC interior.[137,138] Finally, we mention that novel refinements of conventional cluster expansion approaches may be more effective in some 2D epitaxial systems.[141]

For 3D unsupported NCs, again fundamental insights into equilibrium shapes come from application of simple 3D Ising type models with pairwise interactions.[142] In 3D, true facets can exist below the roughening temperature, and the “phase boundaries” bordering these facets can be either first-order (slope discontinuity, shape edges) or second-order (no slope discontinuity, smooth edges). Higher-level treatments for both single- and multi-component NCs are again naturally based on ab-initio DFT energetics in combination with cluster expansions. However, analogous to concerns with the treatment of energetics near step edges for 2D epitaxial systems, there is an issue with conventional application of cluster expansion for bulk systems as relaxation of atoms near the surface of the NC will be distinct from that in the NC interior. This complication can be addressed using generalized cluster expansions where the strength of various pair, trio, etc., interactions depend on location relative to the NC surface.[143,144]

3.2. Generic and refined lattice-gas modeling of kinetics for individual NCs

A key requirement is the appropriate prescription of activation barriers for hopping of an atom from an initial site (i) to unoccupied final (f) neighboring lattice sites, where these barriers will depend on the occupancy of nearby sites. It will be convenient to introduce energies E_i and E_f equal to the total interaction energy for the atom at these sites at the initial and final sites, respectively, and we let E_{TS} denote the total interaction energy at a transition state (TS) for hopping between these sites. Then, a generic prescription for the activation barrier, $E_{act}(i \to f)$, is given by

$E_{act}(i \to f) = E_{TS} - E_i$, where E_{TS} is “symmetric” in i and f. (2)

By "symmetric" in i and f, we mean that E_{TS} is the same for forward (i→f) and reverse (f→i) transitions. This condition guarantees that detail-balance is satisfied,[120] which as noted above is key for reliable treatment of post-synthesis evolution (relaxation or equilibration).

Given the above symmetry constraint, there are several conventional formulations for the choice of E_{TS} which we now enumerate:

Metropolis (MET):[53] $E_{TS} = C + \max[E_f, E_i] = C + \max[0, E_f - E_i] + E_i$, (3)

so that $E_{act} = C + \max[0, E_f - E_i]$. Specifically, one has that $E_{act} = C + (E_f - E_i)$ for energetically uphill transitions with $E_f > E_i$, and one has the same $E_{act} = C$ for all downhill transitions with $E_f < E_i$.

General Brønsted-Evans-Polyani (BEP):[145,146] $E_{TS} = C + a(E_f + E_i)$. (4)

Butler-Volmer (BV) type BEP with $a = ½$:[147,148] $E_{TS} = C + ½(E_f + E_i)$, (5)

which has been used extensively for surface diffusion and where $E_{act} = C + ½(E_f - E_i)$.

IVA or bond-counting type BEP with $a = 0$:[9,52] $E_{TS} = C$. (6)

The latter Initial Value Approximation (IVA) choice is quite common, and corresponds to the case where $E_{act} = C - E_i$ is determined entirely by the initial state (i). The IVA is sometimes interpreted as corresponding to a scenario where the transition state is close to the final state (although there is no reason to expect that this is the case for surface hopping). For this reason, one might anticipate that the BV choice will in general be more appropriate.

A simple but particularly relevant example illustrating the limitations of the above choices is the case of 2D epitaxial NCs on fcc metal surfaces. Here, one naturally selects C to recover the terrace diffusion barrier, E_d, for isolated adatoms. These choices are very common in extensive modeling of both the formation of 2D epitaxial NCs during deposition, as well as post-deposition evolution. However, we shall see below in Sec.3.1.2 that these common choices fail completely to describe the most basic features of edge diffusion even in simple homoepitaxial systems.[9] To resolve this failure of conventional formulations of E_{act} to capture realistic kinetics, it is straightforward and effective to implement refined formulations for the choice of barriers. In these formulations described below, all possible hopping processes are divided into multiple classes labeled by α, say. Then, refinement allows each class to have its own $C = C_\alpha$ in the above prescriptions of rates. Detailed-balance will still be satisfied provided that forward and reverse processes are always included in the same class.

3.3. Application to 2D epitaxial nanoclusters.

As indicated above, metal homoepitaxial systems provide perhaps the simplest benchmark systems in which to test the effectiveness of the various prescriptions of kinetics described above. The most extensive experimental and theoretical studies are

available for Ag, Cu, and Pt. For these systems, we can write $E_{i(f)} = E_0 + \Phi_{i(f)}$ where $\Phi_{i(f)}$ denotes the total lateral interactions in the initial (final) state, and E_0 is the energy for an isolated terrace adatom at the most stable hollow adsorption site.

3.3.1 Conventional Formulations. Choosing the single *C* in the formulation of Sec.3.2 to recover the terrace diffusion barrier, E_d, yields

$$E_{act} = E_d + \max[0, \Phi_f - \Phi_i] \text{ (MET)}, \; E_{act} = E_d + (\Phi_f - \Phi_i)/2 \text{ (BV)}, \text{ or } E_{act} = E_d - \Phi_i \text{ (IVA)}. \quad (7)$$

The simplest but still reasonable model that one can adopt includes just NN attractive lateral interactions of strength $\phi > 0$, so one has that $\Phi = -m\phi < 0$ for lateral coordination number m. This prescription provides a reasonable description of the thermodynamics of metal homoepitaxial systems, as discussed further below. Initially, we also consider models where just hops to NN adsorption sites are incorporated, i.e., hops of distance 'a' (the surface lattice constant).

The two main cases of interest are: (a) fcc(100) and bcc(100) surfaces characterized by a square lattice of adsorption sites (coordination number 4), and which we will for brevity denote as {100} surfaces; (b) hexagonal close-packed fcc(111) and hcp(0001) surfaces characterized by a triangular lattice of adsorption sites (coordination number 6), and which we will denote as {111} surfaces. The above prescriptions for E_{act} for Metropolis and Butler-Volmer choices imply a barrier for edge diffusion along close-packed steps of $E_e = E_d$. This prescription fails severely since E_e is actually well below E_d for {100} surfaces at least for Ag and Cu, and far above E_d for {111} surfaces. The IVA prescription sets $E_e = E_d + \phi$ for {100} surfaces, and $E_e = E_d + 2\phi$ for {111} surfaces. Thus, IVA fails even more dramatically than Metropolis or BV for {100} surfaces, and it actually also overestimates E_e for {111} surfaces (although less severely).

Figure 11 provides a schematic of the edge diffusion along close-packed steps (as described above) and diffusion around kinks. Table 1 lists reasonable choices of the key energetic parameters for a few fcc metals, from which the above assessment of the failure of conventional Metropolis, BV, and IVA prescriptions can be quantified.

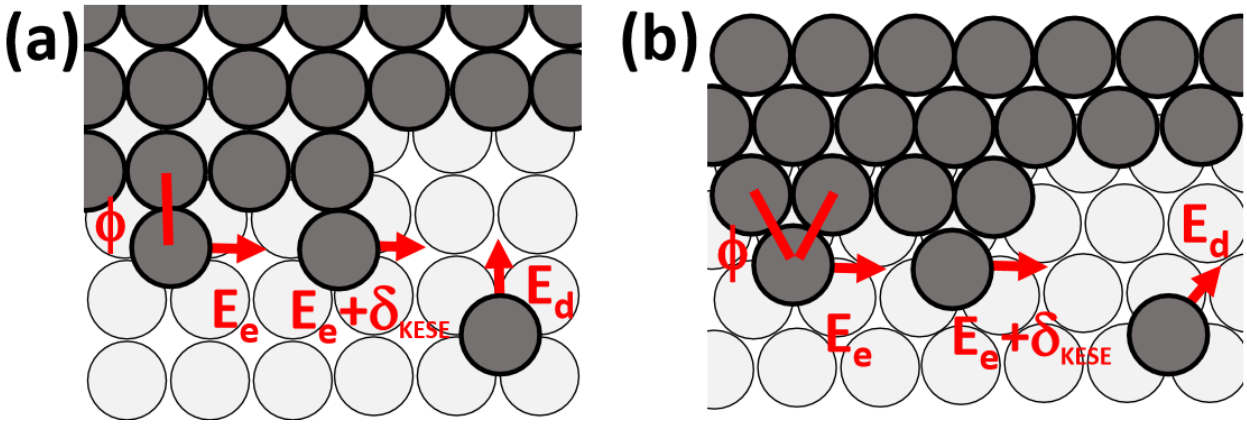

Figure 11. Schematics of key energetics for (a) {100} and (b) {111} surfaces.

Table 1. Approximate effective values of key barriers for hopping for fcc surfaces of Ag, Cu, and Pt (rounded to 0.05 eV). See Ref. 8, 9, 27, 149, 150. Note that for {111} surfaces, edge diffusion barriers actually differ somewhat for A- and B-steps. Results for Pt(100) are for an unreconstructed surface (where exchange has $E_d \approx 0.50$ eV).

	E_d (eV)	E_e (eV)	δ_{KESE} (eV)	ϕ (eV)
Ag(100)	0.45	0.25	0.15	0.25
Ag(111)	0.10	0.30	0.05	0.20
Cu(100)	0.50	0.30	0.20	0.30
Cu(111)	0.05	0.35 ?	0.05 ?	0.25 ?
Pt(100)	1.05?	0.60?	0.40?	0.55 ?
Pt(111)	0.25	0.85	0.50	0.50
Pd(100)	0.75	0.45	0.37	0.35
Pd(111)	0.35	?	?	0.30

3.3.2 Refined Formulations. The resolution to the above shortcomings of conventional formulations is simply achieved in a refined formulation by grouping hopping processes into two classes, $\alpha = T$ (terrace diffusion, attachment, detachment) and $\alpha = E$ (periphery diffusion), and assigning different values of $C = C_\alpha$ to different classes. One can choose a Metropolis or Butler-Volmer type prescription where

$$E_{act} = C_\alpha + \max[0, \Phi_f - \Phi_i] \text{ (MET)} \quad \text{or} \quad E_{act} = C_\alpha + (\Phi_f - \Phi_i)/2 \text{ (BV)}, \tag{8}$$

$$\text{with } C_T = E_d \text{ and } C_E = E_e \text{ (MET or BV)}, \tag{9}$$

and where E_d and E_e values are selected appropriately for the system of interest. See Table I. This refined Metropolis choice has been applied to assess NC diffusion on {100} surfaces.[151] It provides an effective description of attachment-detachment processes (from kinks to step edges, and from NC step edges to the terrace). Refined BV choice provides a somewhat less reliable description. A third reasonable alternative is a refined IVA type choice where

$$E_{act} = C_\alpha - E_i = k_\alpha - \Phi_i \text{ with } k_T = C_T - E_0 = E_d \text{ and } k_E = C_E - E_0 = E_e - \phi \text{ (IVA)}, \tag{10}$$

for which description of attachment-detachment mimics the refined Metropolis prescription.

For fcc metal surfaces, there is in general an additional “kink Ehrlich-Schwoebel barrier” (KESE) for an atom to round a kink or corner at the edge of an island relative to the barrier for diffusion along a close-packed kink-free step edge. See again Figure 11. The refined Metropolis choice sets $\delta_{KESE} = \phi$ which somewhat overestimates the barrier on {100} surfaces, and greatly overestimates it on {111} surfaces. The refined IVA type choice sets $\delta_{KESE} = 0$ neglecting a finite barrier. The refined BV choice yields $\delta_{KESE} = \phi/2$ somewhat underestimating the value for {100} surface, and somewhat overestimating it for {111} surfaces. In summary, overall any of the refined Metropolis, IVA and BV choices are reasonable, each one having advantages and disadvantages.

As an aside, we note that treatment of vacancy diffusion through the NC (where atoms hop to adjacent isolated vacancies and are this coordinated before and after hopping) corresponds to the $\alpha = E$ (periphery diffusion) class within the above refined formulations. Thus, for {100} surfaces, IVA predicts $E_v = E_e + 3\phi$, whereas Metropolis and BV choices predict $E_v = E_e$. In fact, E_v tends to be just slightly below E_d, at least for Ag and Cu.[152] So IVA corresponds to a large over estimate, and Metropolis and BV correspond to a significant underestimate.

Formulations incorporating more diverse dynamics than just hopping to NN sites, e.g., also including 2NN hops, provide additional options for simple prescriptions of E_{act} which capture more precisely the actual kinetics in experimental systems. Labeling different types (or lengths) of hops by β, we are free to choose different values of $C = C_\beta$ of each type of hop, and still preserve detailed-balance in the above prescriptions of E_{act}. More generally, one can identify different classes, α, and lengths, β, of hops and select different $C = C_{\alpha,\beta}$ for each. For example, consider the addition of 2NN hops to diagonally adjacent sites with separation $\sqrt{2}a$ on {100} surfaces. Then, considering class $\alpha = E$ of hops associated with periphery diffusion, for Metropolis and BV choices, we select

$C_{E,NN} = E_e$ for β = NN hops, and $C_{E,2NN} = E_e + \delta_{KESE}$ for β = 2NN hops (MET,BV). (11)

For the IVA choice, where $E_{act} = k_{\alpha,\beta} - \Phi_i$ with $k_{\alpha,\beta} = C_{\alpha,\beta} - E_0$, we select

$k_{E,NN} = E_e - \phi$ for β = NN hops, and $k_{E,2NN} = E_e - \phi + \delta_{KESE}$ for β = 2NN hops (IVA). (12)

These simple MET and IVA prescriptions do an excellent job of capturing not just edge diffusion, but also kink or corner rounding rates. The IVA choice has been used to effectively and elucidate fundamental NC diffusion, reshaping, and sintering processes on (100) surfaces.[153-156] See Figure 12 and also Sec.5.2, 5.4 and 8.1.

For the class α = T of hops, one could reasonably select $C_{T,NN} = C_{T,2NN} = E_d$ for MET and BV, and $k_{T,NN} = k_{T,2NN} = E_d$ for IVA. However, our main focus with these models is in analysis of PD-mediated processes where these $\alpha = T$ choices do not have a significant impact. Furthermore, it is often convenient in these studies to impose a connectivity constraint which actually blocks detachment (and so attachment also does not occur), in which case $\alpha = T$ hops are not active or relevant.

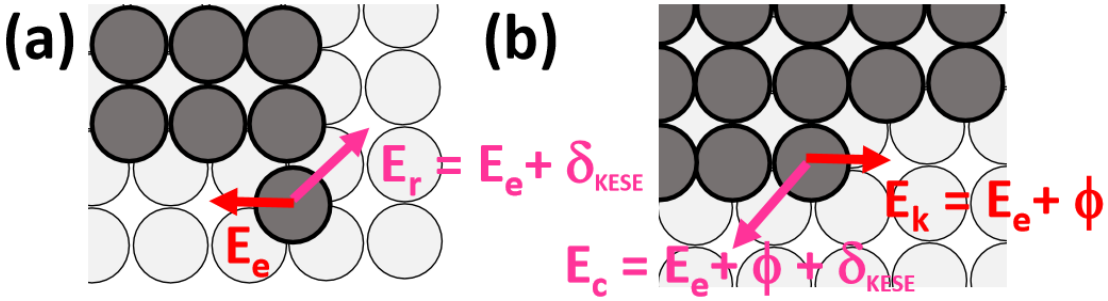

Figure 12. Schematic of dominant periphery diffusion processes and barriers in tailored model with NN and 2NN edge diffusion hops.

3.4. Application to 3D unsupported (and epitaxial supported) nanoclusters.

A modeling framework is presented here first to describe surface diffusion processes for unsupported 3D fcc metal NCs. For predictive modeling of NC reshaping, it is important not just to reliably describe terrace diffusion across the most prominent {100} and {111} facets, but also to describe diffusion along step edges and around kinks and corners on both of these facets, and diffusion across step edges and between facets. This constitutes a vast number of possible local configurations. Characterization of these numerous configurations, as well as description of system thermodynamics, in the model formulated below is motivated by work of Abild-Pedersen and coworkers.[157] With regard to the prescription of thermodynamics, similar to the above discussion for 2D epitaxial NCs, we will assume that energetics is dominated by NN attractive interactions of strength $\phi > 0$ noting that each atom has 12 neighbors for the fcc lattice. This simplified description has been shown reasonable at for various metals.[158] In this model, the Wulff shape is a truncated cuboctahedron bounded by {111} and {100} facets. The length edges joining {111} facets to {100} facets (a_{100}), and to other {111} facets (a_{111}), are equal in the macroscopic regime.[70] On the nanoscale, these shapes are most closely achieved for certain magic numbers of atoms.[159] Choices with $a_{111} = a_{100}$ and with $a_{111} = a_{100} + 1$ (in surface lattice constants) should correspond to local energy minima.[70] The number of atoms, $N_W(a_{100}, a_{111})$, in the NC satisfies $N_W(3,3) = 201$, $N_W(3,4) = 314$, $N_W(4,4) = 586$, etc.

In the most basic model, atoms are just allowed to hop to vacant NN fcc sites. Thus, the initial site has 11 neighbors (other than the final vacant NN site) which could have various occupancies. Likewise, the final site has 11 neighbors (other than the initial site). Also, 4 of the 11 neighbors of the initial and final sites are shared. Thus, there are a total of 11+11 - 4 = 18 sites whose occupancy potentially impacts the activation barrier, E_{act}, for hopping. The number of distinct possible configurations is large, but less than $2^{18} = 26{,}112$ accounting for symmetry equivalence. See Figure 13 where the NN of the initial (final) site that are not shared are labeled mi (mf) with m = 1-7. The shared sites are labeled 1, 2, 3, and 4.

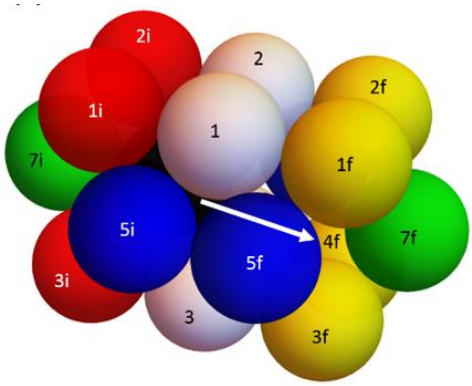

Figure 13. Illustration of 18 sites impacting barriers for the black hopping atom. 4 sites NN to both initial (i) and final (f) sites labeled 1-4. 7 additional sites NN to i (1i-7i) and 7 additional sites NN to f (1f-7f). Some sites are not visible (4i,6i,6f).

The key challenge is the realistic description of activation barriers, E_{act}, or equivalently of transition state energies, E_{TS}, for all possible local configurations around the hopping atom. By way of illustration, here we will present a refined Volmer-Butler type scheme to describe the activation barriers, E_{act}, for these 3D fcc NC systems[160] which as noted above has the form

$$E_{act} = E_{TS} - E_i \text{ with } E_{TS} = C_\alpha + (E_f + E_i)/2, \quad (13)$$

with $E_i = -n_i \phi$, and $E_f = -n_f \phi$ where n_i (n_f) is the number of occupied sites which are NN to site i (f). The constants C_α are assigned for multiple judiciously selected classes α of diffusion processes, as described in the following paragraph. Our strategy is to choose the C_α to capture experimentally validated values of surface diffusion energetics on multiple facets, across terraces, along steps across step edges and between facets. This validation process has exploited a substantial set of integrated Scanning Tunneling Microscopy and stochastic modeling studies for homoepitaxial thin film growth on extended fcc(100) and fcc(111) surfaces. Such studies are most extensive for Ag[68,161-164] and Pt.[8] From such studies, one might reasonably select ϕ = 0.225 eV for Ag[160] and ϕ = 0.347 eV for Pt.[15].

Specifically, it is appropriate to consider four basic classes of hopping processes, each of which will be divided into two subclasses.[160] These four basic classes are: **(i)** terrace diffusion on a {100} terrace or facet (α = 100TD); **(ii)** terrace diffusion on a {111} terrace or facet (α = 111TD); **(iii)** edge diffusion along a {100}-microfaceted A-step on a {111} terrace or facet (α = 111A); and **(iv)** edge diffusion along a {111}-microfaceted B-step on a {111} terrace or facet (α = 111B). It is particularly appropriate to note that edge diffusion along an A-step on a {111}-facet is locally equivalent to edge diffusion along a close-packed step on a {100} terrace or facet. Thus, our modeling framework will constrain these processes to have the same barrier. In fact, diffusion barriers for these two processes are close, at least for Ag, as determined by direct energetic analysis of these cases. Thus, the constraint in this modeling framework that they are set equal is not unreasonable. In addition, we note that in-channel terrace diffusion on a {110} facet is locally equivalent to diffusion along a B-step on a {111}-facet, so barriers are set equal in this modeling framework, which is also realistic. These key relationships between barriers for diffusion processes on different facets have not been emphasized previously.

The first subclass of these process corresponds to intralayer diffusion where both the initial and the final state are fully supported at a hollow site created by atoms in the lower supporting layer. In this case, C_α adopt "base values" denoted by c_α, i.e.,

$$C_\alpha(intra) = c_\alpha \ (= c_{TD100}, c_{TD111}, c_{111A}, \text{ or } c_{111B}), \quad (14)$$

where values for Ag and Pt are given in Table 2. There is one possible point of ambiguity for α = 111A which we now clarify: in order for the final state to satisfy the criterion for intralayer diffusion, one needs either 3 supporting sites on a {11} facet, or 4 supporting sites on a {100} facet to be populated (but not both). See Figure 14 for a characterization of these intralayer diffusion classes. For the {100} facet, the supporting

layer could include atoms at sites 3i,4i,3,4,3f,4f (or instead 1i,2i,1,2,1f,2f). For the {111} facet, the supporting layer could include atoms at sites 4i,4,4f,6i,6f (or 3i,3,3f,5i,5f).

Table 2. Values for c_α (in eV) for intralayer diffusion for Ag and Pt.

	C_{TD100}	C_{TD111}	C_{111A}	C_{111B}
Ag	0.425	0.100	0.275	0.300
Pt	0.47	0.26	0.84	0.90

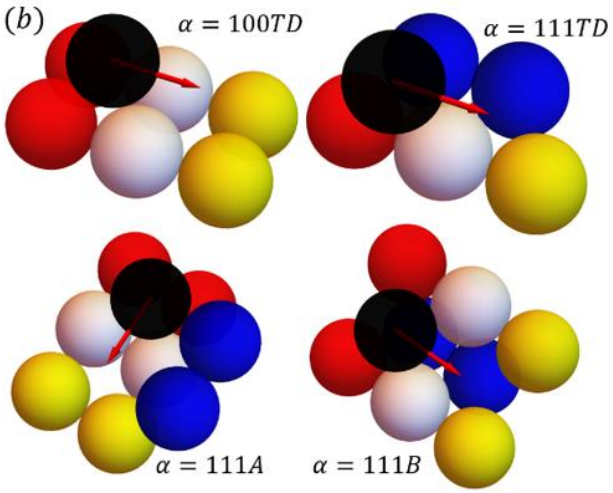

Figure 14. Four classes of intralayer terrace and edge diffusion

The second subclass of these processes corresponds to interlayer diffusion. More precisely, this subclass corresponds to the first stage of interlayer diffusion, where the atom hops out over the edge of a step. A reliable analysis of interlayer diffusion, not just across monatomic steps, but between facets, is clearly important for reliable modeling of the reshaping of 3D NCs. Thus, modeling must account for the possible presence of an Ehrlich-Schwoebel (ES) barriers, δ_{ES}, i.e., an additional barrier beyond that for terrace diffusion. To treat this behavior, when an atom hops from a site with a complete facet to incomplete facet, one sets

$C_\alpha(inter) = c_\alpha - m\phi/2$ (+ δ_{ES}), where m is the number of missing supporting atoms. (15)

The term $-m\phi/2$ compensates for the contribution of $+m\phi/2$ which comes from the term $(E_f - E_i)/2$ in $E_{act} = C_\alpha + (E_f - E_i)/2$. As noted above, the same C_α must be assigned to the corresponding reverse process in order to preserve detail-balance, and describe in the following when the δ_{ES} term is included. Whether or not the ES barrier is included depends upon the details of the step edge configuration as described below.

To elucidate this prescription regarding inclusion of the ES barrier, we first consider the case of interlayer diffusion from an "incomplete" {100} facet for α = 100TD. Figure 15 shows a case of an incomplete {100} facet where relative to the above example for intralayer diffusion, either two atoms are missing to create a close-packed

step (m=2) or just one atom is missing to create a kink. For example, if all of 3i,4i,3,4,3f,4f are populated in the complete {100} facet, then removing atoms at both of 3f and 4f correspond to m = 2, and at just 3f corresponds to m = 1. In this case, $c_\alpha = c_{100TD}$, which corresponds to the terrace diffusion barrier on {100} facets, and since $(E_f - E_i)/2 = +m\phi/2 = +\phi$, it follows that $E_{act} = c_{100TD}$ (+ δ_{ES}). The ES barrier, δ_{ES}, is included for m = 2 corresponding to descending a close-packed step edge, but not for m = 1 corresponding to descending at a kink site. The rationale is that there does generally exist a finite ES barrier for hopping down a close-packed step (m=2), where the barrier for descent by exchange is even higher so hopping dominates downward transport. We choose δ_{ES} = 0.10 eV for Ag which is close to the best experimental estimate of around 70 meV.[161,163] (As an aside, DFT estimates[149,165] do not seem consistent with experimental observations.) However, for m=1, downward exchange is more facile than hopping and has a negligible ES barrier. The modeling framework just incorporating hopping captures this feature by not including the ES barrier term for m = 1. Related to this simplification, we note that a previously utilized successful strategy to model epitaxial thin film growth with a hopping model has been to choose barriers to mimic the dominant process be it either hopping or exchange.[9]

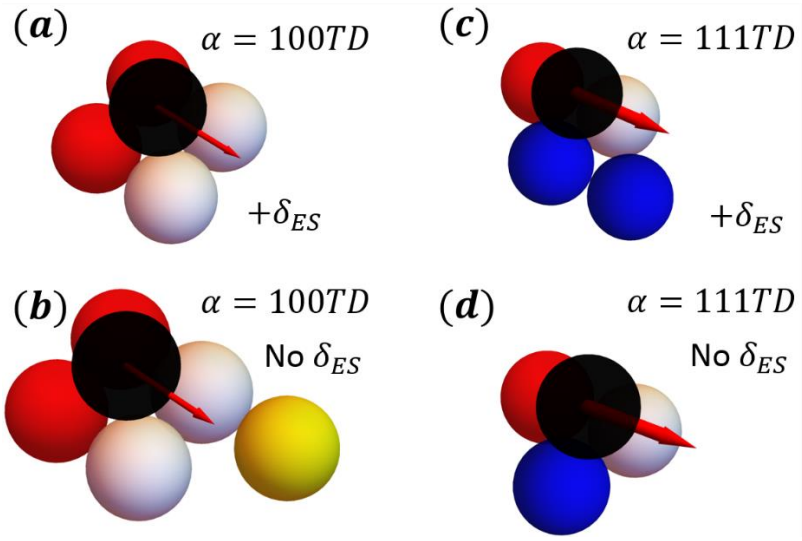

Figure 15. Examples of {100} interlayer diffusion with (top) and without (bottom) an ES barrier. (a) {100} facet is formed by 3, 4, 3i, 4i; while 3f and 4f are missing, leaving the {100} facet incomplete, $C = c - 2\phi/2 + \delta_{ES}$. Thus $E_{act} = c_{TD100} + \delta_{ES}$. (b) {100} facet is formed by 3, 4, 3i, 4i, 3f; while 4f is missing, corresponding to a kink site in this {100} layer, $C = c - \phi/2$. Thus $E_{act} = c_{TD100}$.

For interlayer transport from a {111} facet, a simple general prescription which is appropriate for Ag (but not Pt), is that the ES barrier is included if m = 1 (one atom missing), but not for m = 2 (two atoms missing). The rationale is as follows. One example of m = 1 is descent at a straight A-type step corresponds to a scenario where, e.g., 3, 3i, 5i, and 5f are occupied, but 3f is missing. For Ag(111) system, it is believed that the A-step has the largest ES barrier and that downward transport is mediated by hopping. One example of m = 2 is descent at a straight B-type step corresponds to a scenario where, e.g., 3, 3i, 5i are occupied, but 3f and 5f are missing. Here, it is

believed that the ES barrier is lower, and that exchange dominates hopping as the pathway for downward transport. We set δ_{ES} = 0.10 eV for Ag.[164] Our prescription reasonably treats other more complicated cases. For example, descent at a kink on an A-step where the pathway is believed to be exchange with a low barrier for Ag and corresponds to m = 2 where we do not include δ_{ES}. Descent at a kink on a B-step where the pathway is believed to be hopping with a higher barrier for Ag corresponds to m = 1 where we do include δ_{ES}. See Figure 15.

For Pt(111) surfaces, the details of interlayer transport are believed to contrast those for Ag(111).[8] Downward transport is more facile at straight A-step (ES barrier: 0.02 eV exchange, 0.24 eV hop) than at a straight B-step (ES barrier: 0.35 eV exchange, 0.51 eV hopping). This is the opposite of Ag. Thus, the prescription used for Ag must be reversed to include an ES barrier for {111} terraces for Pt for m = 2, but not m = 1.

Finally, we offer some comments on modifications required to the above formalism to treat supported epitaxial NCs. In a simple but reasonable scenario, the NC is adhered to a {100} (or {111}) surface of a supporting lattice-matched substrate by a single low-index {100} (or {111}) facet. Then, atoms just in the lowest layer of the NC are directly interacting with the substrate in a NN interaction model. Thus, an additional NN interaction, ϕ_s, describing the strength of the attractive interaction between NC and substrate atoms must be specified. The strength of adhesion to the substrate is determined by ϕ_s, and the equilibrium NC shape prescribed via a Winterbottom construction[5,100] (in the large size regime) is determined by the ratio ϕ_c/ϕ. Atoms both in the lowest layer of the supported NC can be regarded as located at a periodic lattice of adsorption sites provided by the crystalline substrate. Any atoms detaching to or attaching from the surface are regarded as located at and hopping between adjacent sites on this same lattice of substrate adsorption sites. Except for the lowest layer of atoms in the NC, and for atoms in the second layer hopping to the lowest layer, the prescription of hopping kinetics discussed above for unsupported NC's can be used to describe surface diffusion around the NC. These rules need to be appropriately modified for the lowest layer where the atoms are interacting with those of the substrate (and possibly also for those hopping to the lowest layer). These modifications will reflect the strength, ϕ_c, of adhesion of metal NC atoms to the substrate.

3.5. Stochastic lattice-gas modeling with ab-initio based kinetics

For single-component systems, the refined formulations described in Sec.3.3 and 3.4 can reasonably, but not precisely, describe diverse diffusion behavior. Thus, there is some motivation to develop more precise treatments not only for single-component systems, but also for multi-component systems where it is less viable to develop effective "simple" refined formulations. The precise treatments, potentially incorporating ab-initio DFT energetics, will be based on the exact result, $E_{act}(i \to f) = E_{TS} - E_i$, where E_{TS} is "symmetric" in i and f. The E_i are determined from the specification of system thermodynamics, i.e., the specification of energetics for all allowed crystalline configurations of the system. In lattice-gas modeling of equilibrium single-and multi-component systems, typically precise DFT analysis of system energetics is used to systematically extract a complete set of pair, trio, quartet, etc. interactions via cluster

expansion techniques[140] thereby allowing efficient determination of all E_i. However, E_{TS} involves a configuration with at least one atom at a non-crystalline site, and thus cannot be precisely determined by the thermodynamic interactions (despite the attempt in BEP and other formulations to do so). Thus, it is required to directly and systematically probe interactions in the TS. In other words, one needs not only an ab-initio treatment of system thermodynamics, but also of kinetics. The latter is relatively uncommon. Below we describe ab-initio kinetics formulations for 2D epitaxial and 3D NCs.

3.5.1. 2D epitaxial NCs. We will refer to the formulation described below as a multi-site lattice-gas (msLG) formulation since we consider not just conventional lateral adatom interactions between atoms at a single type of adsorption site (and possibly between atoms at multiple stable adsorption sites), but also unconventional lateral interactions between collections of adatoms where one is as a transition site for hopping (rather than at a stable adsorption site).

For simplicity, we first describe an ab-initio based formulation of such an analysis for 2D epitaxial NC's on {100} surfaces with four-fold hollow (4fh) adsorption sites forming a square grid, and transition states (TS) located close to bridge sites midway between these hollow sites. However, we will describe methods applicable to multi-component as well as single-component NCs. We will focus on a formulation to precisely describe periphery diffusion (see Figure 16) which is key for describing both growth shapes during self-assembly and post-synthesis reshaping, e.g., sintering of pairs of NCs. In Sec.7.1.3, we will describe refinements required to accurately describe vacancy diffusion through the interior of NCs which is a primary mechanism for intermixing in multicomponent NCs. In the basic formula $E_{act}(i \to f) = E_{TS} - E_i$, in is instructive to write $E_i = E_{ads} + \Phi_i$, where E_{ads} is the adsorption energy of an isolated adatom at the 4fh site, and Φ_i is the total lateral interaction of the atom with other nearby atoms in the initial state. Similarly, we write $E_{TS} = E_d + E_{ads} + \Phi_{TS}$, where E_d is the terrace diffusion barrier for an isolated adatom (i.e., the difference in adsorption energy at 4fh and bridge sites), and Φ_{TS} is the total lateral interaction energy in the TS.

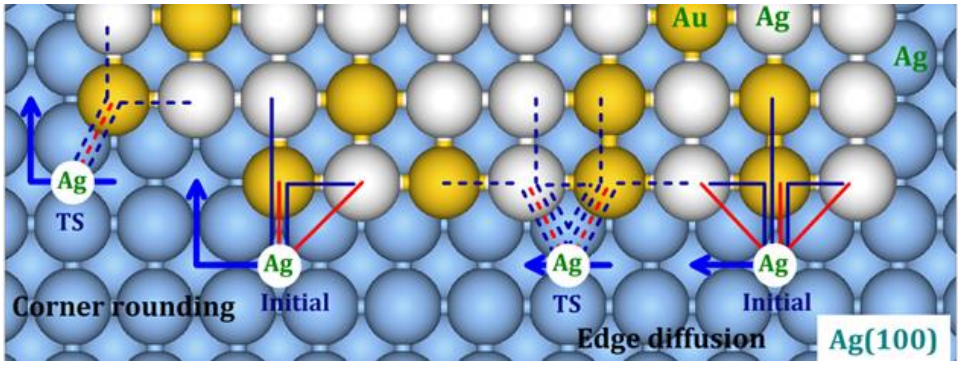

Figure 16. Key periphery diffusion processes for an Au + Ag bimetallic 2D epitaxial NC on Ag(100). Reprinted with permission from Ref. 25. Copyright 2014 American Chemical Society.

Determination of Φ_i can be achieved with conventional thermodynamic cluster expansion methods which have been applied extensively to epitaxial metal

adlayers.[25,26,135-139] The basic idea is that the lateral interaction energies, Φ_i, can be obtained from a many-body cluster expansion as a sum of pair, trio, quartet, etc. contributions. For {100} surfaces, the expected dominant pair and trio interactions are shown in Figure 17 (left frame), although in some systems other interactions can be significant.[26,139] One direct large unit-cell strategy to determine the constituent pair, trio, etc. interactions using large unit cell DFT analysis is sequential determination of: (i) adsorption energies for isolated adatoms; then (ii) the energy of isolated pairs of atoms for various separations (from which the pair interaction energy is obtained after subtracting adsorption energy contributions); then (iii) the energy for isolated trios of atoms with various configurations (from which the true trio interaction can be obtained after extracting pair and single-atom adsorption energy contributions); etc. A possible concern is the computational cost of these large unit cell calculations. Most often an alternative cluster expansion procedure is applied where a priori it is decided to retain M pair, trio, etc. interactions. Here, one directly calculates the total energy of M distinct periodic overlayer configurations, thus providing M independent relations (for a suitable selection of adlayer configurations) for M unknowns. Various refinements of this basic approach have been developed to assess the robustness of such estimates.[138,166] A general issue is that lateral relaxation of isolated pairs, trios, etc. of atoms or of atoms in periodic overlayer configurations might be quite different from that of atoms in NCs particularly near NC edges.[137,138]

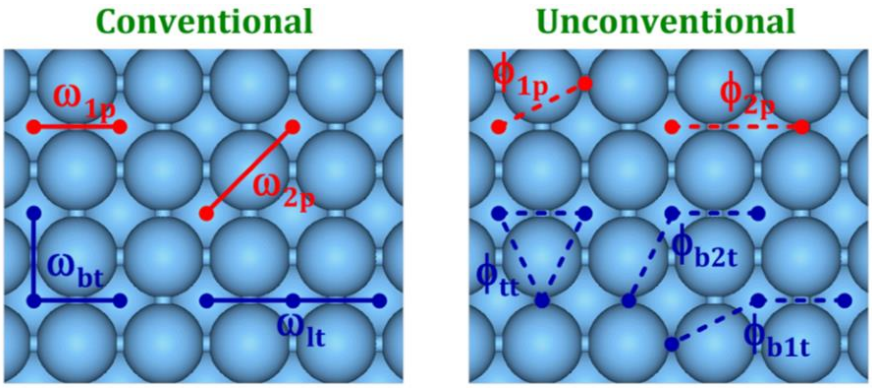

Figure 17. Anticipated dominant pair and trio interactions on {100} surfaces. Reprinted with permission from Ref. 25. Copyright 2014 American Chemical Society.

One could however argue that a less generic and more application-targeted approach would be more appropriate and effective, particularly given the anticipated limitations of conventional cluster expansion analysis for epitaxial NCs due to distinct relaxation of atoms at the periphery and in the interior.[137,138] For example, for analysis of sintering of pairs of NCs, it is the accurate description of the step edge thermodynamics (rather than the thermodynamics of periodic adlayer structures) that is most relevant for accurate description of NC shape evolution. Such step edge specific thermodynamics includes: (orientation-dependent) step energy, γ; step stiffness, $\tilde{\gamma}$; kink creation energy, ε_k (which is related to step stiffness via $\tilde{\gamma} \sim \exp[2\varepsilon_k/(k_BT)]$ for large $\varepsilon_k/(k_BT)$); edge atom formation energy (associated with moving kink atoms to step

edges); and other “extraction” energies, e.g., for moving atoms from straight steps of various orientations to become isolated edge atoms[27,69] Thus, optimal determination of pair, trio, etc, interactions should be based on recovery of these key step edge energies.[27]

Determination of Φ_{TS} is not a conventional problem, and has received less attention.[23-27] Again, cluster expansion based approach is natural, but now the constituent pair, trio, etc., interactions are “unconventional” in the sense that no longer are all atoms located at adsorption sites. Rather one atom is located at a bridge-site TS in the systems considered here, and one must determine interactions between this atom and nearby atoms. For {100} surfaces, the expected dominant unconventional pair and trio interactions are shown in Figure 17 (right frame). Again, a straightforward direct large-unit cell strategy to determine these constituent interactions is to sequentially analyze energies for isolated configurations of atoms, pairs, trios, etc., although now one atom must be fixed (laterally) at the TS location.[23,24] However, again it may be more effective to adopt an alternative application-targeted procedure. Considering again sintering of pairs of NCs mediated by periphery diffusion, key parameters are the barriers for edge diffusion along close-packed steps, and additional KESE barriers to round kinks or corners. One could also consider barriers for other rearrangements of atoms on step edges which would impact step fluctuation dynamics. Then, the unconventional pair, trio, etc., interactions are ideally determined within a cluster expansion framework to recover these various edge diffusion barriers.[25,27]

Analysis of 2D epitaxial NCs on {100} surfaces is perhaps the simplest possible system in which to develop an ab-initio based description of kinetics in part due to the assumed well-defined unique bridge-site transition state. In fact, even this picture is an approximation since the TS location will depend somewhat on the local NC configuration for edge diffusion, but such deviations are relatively small. An example of typical values for both conventional and unconventional interactions for the Ag+Au on Ag(100) system is provided in Table 3, where we note that it is necessary not just to specify interactions between Ag, and between Au, but also Ag-Au lateral interactions. Additional complications arise in the determination of unconventional interactions if interactions are fairly long ranged, and if a cluster expansion based approach is used exploiting energies of configurations for relatively small sized unit cells.[139]

However, analysis can be substantially more complicated for other 2D epitaxial systems. One such example where there has been previous ab-initio based multi-site lattice-gas (msLG) modeling involves the self-assembly and post-assembly equilibration of Ni + Al NCs on the binary alloy NiAl(110). This system provides a setting for ab-initio studies of alloy self-growth for deposition of stoichiometric 1:1 ratio of Ni:Al, but it also has the advantage that the equilibrium structure of NCs is clear as this structure must propagate the perfect binary alloy ordering of the substrate. Here, there are two distinct types of adsorption sites which might be described as Ni-bridge and Al-bridge for both species. For terrace diffusion of Al in the two orthogonal directions aligned with the principle substrate axes, there are two distinct transition states. A separate diffusion pathway with diagonal hops has a separate TS. Ni has a single diffusion pathway with diagonal hops and a single TS. See Figure 18. The modeling of this system has just incorporated pair interactions See Figure 19 and Table 4.

Table 3. Ag (S) + Au (G) on Ag(100) interactions. We set $\phi_{b2t} = (3\phi_{b1t} + \phi_{tt})/4$.

conventional	conventional	conventional	unconvent.	unconvent.	unconvent.
ω_{1p}(SS) -0.283	ω_{lt}(SSS) -0.016	ω_{bt}(SSS) +0.032	ϕ_{1p}(SS) -0.212	ϕ_{b1t}(SSS) -0.020	ϕ_{tt}(SSS) +0.049
ω_{1p}(GG) -0.201	ω_{lt}(GGG) -0.065	ω_{bt}(GGG) +0.016	ϕ_{1p}(GG) -0.141	ϕ_{b1t}(GGG) -0.031	ϕ_{tt}(GGG) +0.044
ω_{1p}(SG=GS) -0.285	ω_{lt}(SGG=GGS) -0.046	ω_{bt}(SGG=GGS) +0.026	ϕ_{1p}(SG) -0.188	ϕ_{b1t}(SGG) -0.049	ϕ_{tt}(SGG) +0.059
ω_{2p}(SS) -0.027	ω_{lt}(GSS=SSG) -0.021	ω_{bt}(GSS=SSG) +0.036	ϕ_{1p}(GS) -0.225	ϕ_{b1t}(GSS) -0.027	ϕ_{tt}(GSS) +0.054
ω_{2p}(GG) +0.030	ω_{lt}(SGS) -0.022	ω_{bt}(SGS) +0.028		ϕ_{b1t}(SGS/SSG) -0.038/-0.001	ϕ_{tt}(SGS/SSG) +0.033
ω_{2p}(SG=GS) -0.010	ω_{lt}(GSG) -0.034	ω_{bt}(GSG) +0.030		ϕ_{b1t}(GSG/GGS) -0.011/-0.045	ϕ_{tt}(GSG/GGS) +0.043

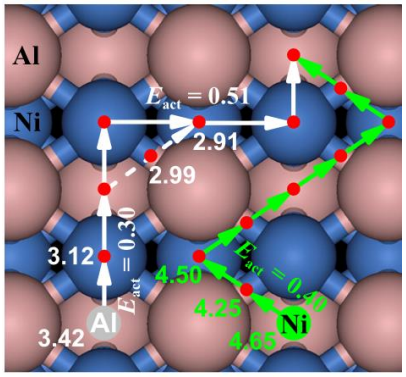

Figure 18. Terrace diffusion for Ni and Al on NiAl(110). Adsorption energies in eV are shown. Reprinted with permission from Ref. 24. Copyright 2012 American Physical Society.

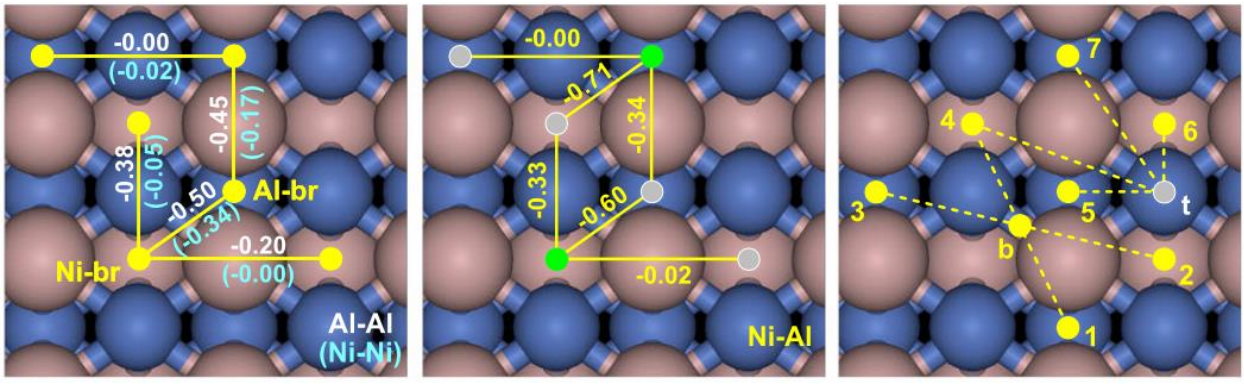

Figure 19. Pairwise interactions incorporated in Ni+Al on NiAl(110) model: conventional Al-Al and Ni-Ni interactions (left); Al-Ni interactions (middle); unconventional interactions (right). Reprinted with permission from Ref. 24. Copyright 2012 American Physical Society.

Table 4. Unconventional pair interactions in eV with one atom at Al-br or at Ni-br and one at a t or b transition state.

Ni(b)-Ni(1) -0.30	Al(b)-Al(1) -0.45	Al(t)-Al(4) -0.02
Ni(b)-Ni(2) -0.14	Al(b)-Al(2) -0.40	Al(t)-Al(5) +1.00
Ni(b)-Ni(3) -0.18	Al(b)-Al(3) -0.20	Al(t)-Al(6) +12.00
Ni(b)-Ni(4) -0.25	Al(b)-Al(4) -0.29	Al(t)-Al(7) -0.12
Ni(b)-Al(1) -0.85	Al(b)-Ni(1) -0.73	Al(t)-Ni(4) -0.01
Ni(b)-Al(2) -0.28	Al(b)-Ni(2) -0.24	Al(t)-Ni(5) -0.44
Ni(b)-Al(3) -0.14	Al(b)-Ni(3) -0.18	Al(t)-Ni(6) +6.55
Ni(b)-Al(4) -0.71	Al(b)-Ni(4) -0.62	Al(t)-Ni(7) -0.06

Although the formation of epitaxial NCs on hexagonal close-packed fcc(111) surfaces is in some sense simpler than for the above binary alloy surface, there are some substantial complications not seen above. In the default picture for terrace diffusion, the pathway is natural and well-defined: an atom starting in the preferred fcc adsorption site hops through a bridge site TS to a neighboring hcp adsorption site (which is locally stable but slightly less favorable than the fcc site); then the atom returns to an fcc site after hopping through a bridge site TS. Thus, it is reasonable for the modeling to include both fcc and hcp adsorption sites (which also enables the description of the formation and evolution of stacking-fault islands).[167,168] However, the complication arises for edge diffusion where the diffusion path is significantly distorted from that of an isolated adatom in the center of a terrace. Our analysis for Ag/Ag(111) using semi-empirical (2NN MEAM) potentials indicates that for edge diffusion along a {100}-micro-faceted A-step, the pseudo-hcp adsorption site on the diffusion path is displaced inward by 0.36 A towards the A step edge. See Figure 20 (left). For edge diffusion along a {111}-micro-faceted B-step, one could anticipate “inner” and “outer” paths for edge diffusion. See Figure 20 (right). We find that the inner path is preferred for Ag/Ag(111), but that the pseudo-hcp adsorption site on the diffusion path is displaced outward by 0.99 A from the B step edge. Thus, ab-initio level analysis of the kinetics in these systems is more complex, however a multisite lattice-gas (mslg) framework could still be implemented including geometric and multiple shifted fcc and hcp adsorption sites, and also geometric and multiple shifted br site TS.

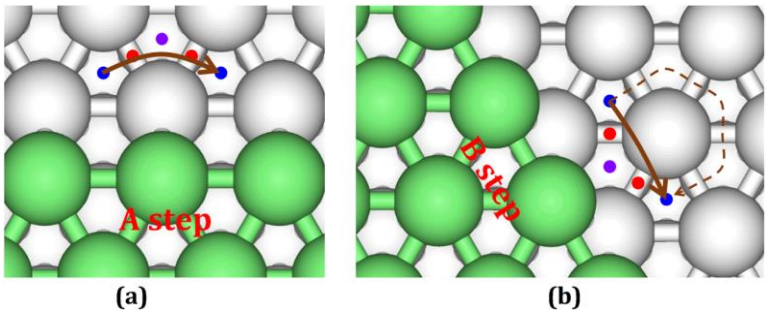

Figure 20. Edge diffusion in fcc(111) homoepitaxial systems. Outer B-path is not preferred.

3.5.2. 3D fcc NCs. The simplest case is naturally unsupported NCs, but the basic strategy developed for those systems extends to epitaxial supported NCs (at least after some approximations or assumptions). Just as for the tailored models described in Sec.3.3 and 3.4, analysis is based upon the fundamental relation for the activation energy for hopping, i.e., $E_{act}(i \to f) = E_{TS} - E_i$, where E_{TS} is "symmetric" in i and f. Here, we describe the implementation of Abild-Pedersen and coworkers.[157] For the determination of initial state energy, E_i, the same approximate formulation as described for out tailored model was implemented, i.e., $E_i = -n_i \phi$ varies linearly with the coordination number n_i of the atom in the initial site, and where the effective NN interaction strength ϕ was determined from DFT analysis for atoms in various configurations. This approximation could be improved by accounting for coordination to nearby atoms in the second shell, but at significant additional computational cost in KMC simulations. Thus, the simpler treatment was implemented in Ref. 157.

The bigger challenge is reliable determination of E_{TS} without resorting to crude IVA and Metropolis, or imperfect BEP treatments, or even refined versions of these. The strategy involving direct NEB-based determination implemented in Ref. 157 was to develop a database of precise values for hopping barriers obtained from nudge-elastic-based (NEB) analysis based on DFT energetics for diffusion processes on {111}, {100}, and {211} surface facets with various local environments of the hopping atom. This analysis noted the presence of atoms along the diffusion pathway can lower the barrier (rather than increase it due, e.g., to steric hindrance), a feature which is most dramatic for {100} surfaces as described above in Sec.3.3. Then, for atom hopping in the 3D fcc NC simulations, the local configuration is mapped onto an entry in this data-base accounting particularly for the occupancy of the 4 NN sites which are shared by both the initial and final site (see Figure 12).

Incorporation of both 2D and 3D ES barriers is clearly important for reshaping of unsupported 3D NCs. Traditionally, these barriers have been discussed primarily in the context of multilayer film growth,[8,9] and for the case of 3D ES barriers also for growth and relaxation of supported 3D NC's, including 3D nanorods protruding from the substrate.[104] Here, the most reliable strategy for incorporation of these barriers into modeling would be to perform direct NEB-aided DFT analysis to determine the barriers for key step edge and facet boundary geometries.[104] Then, the barriers would be utilized in KMC simulation which however would need to identify interlayer or inter-facet hops for these specific geometries. Such modeling has not been implemented to date.

Next, we consider the treatment of supported 3D epitaxial NCs. Abild-Pedersen and coworkers[157] used an implicit treatment of the substrate in that substrate atoms were not explicitly included, but an adhesion energy was assigned to atoms in the lowest layer of the cluster which depended on their coordination to other metal NC atoms. Heuristic account of strain due to possible lattice mismatch was also included. See Sec.8.3. A simple alternative for perfect epitaxy (with negligible mismatch) as indicated above is to regard atoms in the lowest layer of the NC (generally assumed to correspond to a {100} or {111} facet of the NC) as residing at a periodic array of adsorption sites on the substrate) with the same lattice constant as the NC. Adaption of the above algorithms naturally refines the analysis of initial state energies for atoms in the lowest layer as these are directly coordinated to atoms in the substrate. As also noted above, one introduces a different NN binding energy of NC atoms to substrate

atoms of strength ϕ_s, say. In principle, a separate additional assessment of TS energies is needed for atom hops between the lowest layer to the next highest layer, as these energies will generally be affected by interaction with the substrate, and thus differ from those for hops in geometrically equivalent local configurations in higher layers. An ab-initio level incorporation of such refined barriers has not yet been implemented (but rather approximate estimation has been used). It should also be noted that one could include attachment-detachment of atoms from the lowest layer to the substrate adsorption sites between which they could hop, as would be appropriate, e.g., for modeling of growth of 3D supported NCs during deposition.

Finally, we mention that one might consider an msLG type cluster expansion alternative[25,27] for the ab-initio level analysis of TS energies as discussed extensively for 2D epitaxial NCs. With the assumption that the transition states (TS) for hopping are located mid-way between the initial and final fcc lattice sites, then one can use a cluster expansion based approach using directly calculated energies for M configurations with the hopping atom fixed at this TS to determine a set of M unconventional interactions. This approach has not been implemented to date. We caution, however, that the above assumption of a geometrically simple TS location has its limitations. Even for diffusion on {100} facets for the TS is close to the bridge site, it is not exactly between the initial and final hollow sites as its height relative to the {100} plane is greater (a feature incorporated into our modeling for 2D epitaxial NCs). For diffusion on {111} facets, we have indicated above more severe complications.

3.5.3. Concerted many-atom processes. From studies of homoepitaxial thin film growth, it is well recognized that concerted processes (typically two-atom processes) can dominate single-atom hopping as the dominant mass transport pathway.[150] For terrace diffusion on unreconstructed Pt(100) facets, exchange of an adatom with the substrate atom dominates hopping.[169,170] The surface atom displaces one of the four supporting atoms which is pushed up to a second NN hollow site. For terrace diffusion on {110} facets, often cross-channel exchange dominates hopping[150]. For interlayer transport, often exchange dominates (e.g., at kinked steps on {100} facets, or at straight B-steps or at kinks on A-steps on {111} facets for Ag) as discussed in Sec.3.4.[9] Thus, rather than single atom hopping to NN fcc sites as discussed above, ideally one should also implement at least two-atom exchange processes. In fact, this was also done in the analysis of Ref. 157 for Pt NCs.

It is appropriate to also comment on possible strategies for reliable determination of TS energies for these two-atom exchange processes (where initial and final state energies are determined within the framework described above). Naturally, direct NEB-based determination is the most precise approach. However, it is necessary to tabulate such TS energies for all possible local environments, so generally some approximation must be adopted to obtain energies for general configurations from a limited subset. One might also consider an msLG type cluster expansion alternative for ab-initio level analysis. However, for the case of two-atom exchange, this will involve determination of a separate class of unconventional interactions where not just one atom is at a non-fcc lattice TS, but both atoms in the exchanging pair are displaced from fcc sites and are interacting with other nearby atoms at fcc sites. One complication is the need to determine these TS atom locations. This could be done for one choice of local

environment must be determined for each t as determined by NEB analysis, and then the same choice of locations used for analysis of TS energies for other environments.

3.6. Off-lattice atomistic-level stochastic modeling for supported NCs

For supported NC's, in general lattice mismatch between the NC and the crystalline substrate will induce strain in the NC, and in more extreme situations defects such as dislocations and stacking faults. In these cases, conventional lattice-based stochastic models and KMC simulation have clear limitations. For a precise treatment, it is necessary to resort to off-lattice formalisms[171-173] where atom positions are free to adjust to accommodate strain (but where in the simpler case, the NC is still crystalline, and is in coherent or epitaxial contact with the substrate). Stochastic kinetic modeling must appropriately evolve the NC between locally stable configurations (in the simplest case, distorted or strained fcc structures) with the appropriate rates. Again a standard Arrhenius form is adopted with barriers, $E_{act}(i \to f) = E_{TS} - E_i$, where E_{TS} is "symmetric" in i and f. Now, in principle E_i must be determined after each Monte Carlo step by relaxing the entire NC which is computationally significantly more expensive than for lattice-based models (and as a result sometimes just partial or local relaxation of atoms close to the hopping event is implemented). However, even more demanding is the off-lattice search for the possible TS at each step. There appears to be currently limited application of these methods on analysis of strained supported metal NCs.

4. OVERVIEW OF COARSE-GRAINED CONTINUUM MODELING AND COARSENING THEORIES

4.1. Coarse-grained continuum modeling of shape evolution for individual NCs

4.1.1. Shape evolution of 2D epitaxial NCs. We focus on so-called Lagrangian front-tracking approaches for periphery-diffusion (PD)-mediated shape evolution in 2D epitaxial systems which treat the peripheral step edge of the NC as a "sharp" continuous curve. Here, we focus on shape evolution mediated by periphery diffusion. Then, neglecting fluctuations (cf. Sec.4.2), a deterministic macroscopic continuum formulation gives the normal propagation velocity, V_n, of the step edge in terms of the flux, J_{PD}, of atoms diffusing around the NC periphery where J_{PD} is a function of its local geometric properties (orientation, curvature) and of system parameters (orientation-dependent step edge stiffness and step edge mobility). This two-dimensional theoretical formulation is analogous to the classic treatments of the relaxation of film morphology due to surface diffusion in three dimensions.[125,127,128]

Let μ denote the chemical potential of the step edge, σ_{PD} the mobility of step edge atoms, $\tilde{\gamma}$ the step edge stiffness, and κ the step edge curvature which is defined to be negative for a circular NC. We note that σ_{PD} might be better described as the step edge conductivity by analogy with electrical conductivity and within the general framework of transport theory where conductivity is the product of a carrier density and an intrinsic carrier mobility.[153,174,175] Then, neglecting fluctuations in step edge evolution, one has that[153,176,177]

$$V_n = -\nabla_s J_{PD}, \text{ where } J_{PD} = -(k_B T)^{-1}\sigma_{PD}\nabla_s \mu \text{ with } \mu = -\tilde{\gamma}\kappa, \qquad (16)$$

where $\nabla_s = \partial/\partial s$ denotes the derivative with respect to arc length, s, along the step. Both $\sigma_{PD} = \sigma_{PD}(\phi)$ and $\tilde{\gamma} = \tilde{\gamma}(\phi)$ depend in general on step orientation ϕ, and where $\tilde{\gamma}(\phi) = \gamma(\phi) + \gamma''(\phi)$ is determined by an orientation-dependent step energy $\gamma = \gamma(\phi)$.[14,69] These system parameters describing step edge thermodynamics and kinetics can be determined by non-trivial statistical mechanical analysis of atomistic models. For {100} facets accounting for just NN attractive interactions between adatoms, we can exploit the exact result of Rottman and Wortis for the T-dependent step energy.[99] For {111} facets, analogous results are also available, as well as guidance on practical numerical implementation.[131,134] Usually the anisotropy in σ_{PD} is ignored assuming that the anisotropy of $\tilde{\gamma}$ will dominate shape evolution. Indeed, σ_{PD} is isotropic in simple solid-on-solid model without a kink ES barrier.[175] However, introduction of a kink ES barrier does introduce anisotropy in σ_{PD}[153], and a simple form for this dependence has been proposed.[178]

With regard to numerical analysis of (16), the default approach is to suitably distribute discrete points around the perimeter of the NC. One tracks the coupled evolution of these points which is determined by a version of (16) replacing continuous derivatives by discrete differences based on the location of nearby points to that of interest. Particularly for strongly anisotropic step energies and for complicated

morphological evolution, it may be necessary to occasionally redistribute these points to sufficiently accurately treat regions with high curvature, etc. We note that there are refined high-precision algorithmic approaches which suitably move the points both along the NC perimeter as well as orthogonal to the perimeter.[179,180]

Next, we present some additional general comments giving an additional perspective on the origin of the evolution equation (16) and also on the nature of its solutions. Equation (16) can be obtained adopting so-called model B conserved dynamics associated with an appropriate free energy functional $F = \int ds\, \gamma(\phi(s))$ where $\gamma(\phi(s))$ depends on the step orientation $\phi(s)$ at s. To illustrate this approach, it is more convenient to consider a benchmark analysis for an extended step oriented in the x-direction with small displacement $y(x)$ in the orthogonal direction. The x-direction is assigned here as having an orientation $\phi = 0$, typically corresponding to a local minimum in step energy which is typically a local maximum in stiffness. Then, one has

$$F = \int dx\, [1 + (dy/dx)^2]^{1/2}\, \gamma(\phi(x)) = F_0 + \tfrac{1}{2} \int dx\, \tilde{\gamma}(0)\, (dy/dx)^2, \qquad (17)$$

where F_0 is the free energy for the perfectly straight step, and where a Taylor expansion has been employed for $\gamma(y')$ about zero slope $y' = dy/dx = 0$ to obtain the latter expression. Then, evolution of the step edge accounting for mass conservation has the form

$$\partial/\partial t\, y(x, t) = -\partial/\partial x\, J(x, t), \text{ where } J(x,t) = -(k_B T)^{-1} \sigma_{PD}\, \partial/\partial x\, [\delta F/\delta y], \qquad (18)$$

and where evaluation of the functional derivative yields $\delta F/\delta y = -\tilde{\gamma}\, \partial^2/\partial x^2\, y$.

Continuing this benchmark analysis for small perturbations of the extended straight step, (18) becomes

$$\partial y/\partial t \approx L_x\, y \text{ with } L_x = -(k_B T)^{-1} \sigma_{PD}(0)\, \tilde{\gamma}(0)\, \partial^4/\partial x^4. \qquad (19)$$

The differential evolution operator, L_x, has eigenfunctions $y_q(x) = e^{iqx}$ with a continuous spectrum of negative eigenvalues, λ_q, and corresponding decay times $\tau_q = 1/|\lambda_q|$ of the form

$$\lambda_q = -(k_B T)^{-1}\, \sigma_{PD}(0)\, \tilde{\gamma}(0)\, q^4 \text{ and } \tau_q = (k_B T)/[\, \sigma_{PD}(0)\, \tilde{\gamma}(0)\, q^4]. \qquad (20)$$

The λ_q extend to the origin (i.e., there is no spectral gap), and the τ_q diverge for small wavenumbers $q \to 0$. Solutions of (19) have the form

$$y(x,t) = \int dq\, y_q(t)\, e^{iqx} \text{ where } y_q(t) = \exp(-t/\tau_q)\, y_q(0) \text{ for } q \neq 0, \qquad (21)$$

and mass conservation implies that $y_{q=0} \equiv 0$. One can show that $y(x,t) \sim t^{-1/4}$ exhibits slow algebraic decay in time. We shall contrast this algebraic decay with exponential decay for NC shape relaxation below.

Now, we return to more general analysis relevant to NC shape relaxation. First, we assess size scaling based on the general form of (16). Since κ is given by the second derivative of step position, there are a total of four derivatives along the step edge in the expression for V_n. Consequently, increasing the length scale by a factor of b will slow the time evolution by a factor of b^4. Consequently, the characteristic time for relaxation, τ_{eq}, scales with linear feature size, L, like $\tau_{eq} \sim L^{\alpha^*}$, with $\alpha^* = 4$.

Next, we provide a more detail analysis of time evolution for reshaping of finite NCs. To analyze this problem, it is convenient to introduce polar coordinates, where $r(\theta, t)$ gives the distance of the step edge from the origin for polar angle θ, where $0 \le \theta \le 2\pi$. For the problems of interest, the natural choice of origin is clear as the "center of mass" of the cluster. In this coordinate system, one has that[181]

$$V_n = [1 + (r^{-1}\, \partial r/\partial\theta)^2]^{-1/2}\, \partial r/\partial t \quad \text{and} \quad \kappa = [1 + (r^{-1}\, \partial r/\partial\theta)^2]^{-3/2}\, [r^{-1} + \partial^2/\partial\theta^2 (r^{-1})]. \qquad (22)$$

Then the evolution equation (16) becomes

$$\partial/\partial t\, r(\theta, t) = -\, [1 + (r^{-1}\, \partial r/\partial\theta)^2]^{1/2}\, (k_B T)^{-1}\, \partial/\partial s\, [\sigma_{PD}\, \partial/\partial s\, (\tilde{\gamma}\, \kappa)], \qquad (23)$$

with κ from (22) and where $\partial s \approx r\, \partial\theta$. We also introduce the equilibrium radius, $r_{eq}(\theta)$, where $r(\theta, t) \to r_{eq}(\theta)$, as $t \to \infty$. This $r_{eq}(\theta)$ is determined from a 2D Wulff construction given $\gamma = \gamma(\phi)$, which implies that the corresponding curvature $\kappa_{eq}(\phi)$ satisfies $\tilde{\gamma}(\phi)\, \kappa_{eq}(\phi) = -\mu_{eq}$ which is constant (i.e., independent of θ or ϕ). Considering asymptotic decay of an NC to its equilibrium shape, it is also natural to introduce a measure $g(\theta, t)$ of the deviation of $r(\theta, t)$ from $r_{eq}(\theta)$ via

$$r(\theta, t) = r_{eq}(\theta) + \langle r_{eq} \rangle g(\theta, t) \text{ where } \langle r_{eq} \rangle \text{ is an average of } r_{eq}, \qquad (24)$$

and $g(\theta, t) \to 0$, as $t \to \infty$. See Figure 21. For small g, the right-hand-side (RHS) of (23) becomes a fourth-order differential evolution operator (in θ) with periodic boundary conditions on $0 \le \theta \le 2\pi$ which must have discrete eigenvalues, λ_n. Apart from growth (n=0) and translational (n=1) eigenmodes, one should specifically have $\lambda_n < 0$, corresponding to decay times of $\tau_n = 1/|\lambda_n|$. Asymptotic decay is exponential on a time scale $\tau_{eq} = \max(\tau_{n>1})$, i.e., $g(\theta, t) \sim \exp(-t/\tau_{eq})$.

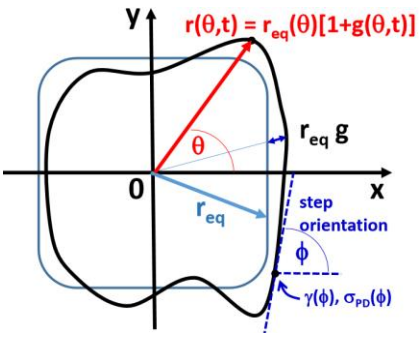

Figure 21. Schematic of NC geometry and polar coordinates (with r_{eq} reflecting a {100} facet).

Given the variable coefficients in the general evolution operator described above for anisotropic surface energy, the analysis of corresponding eigenmodes and eigenvalues, λ_n, is non-trivial. For this reason, it is instructive to consider the simple special isotropic case, behavior for which should illustrate the basic features of the more general case. Here, $\tilde{\gamma} = \gamma$ and σ_{PD} are independent of orientation, and $r_{eq} = \langle r_{eq} \rangle$ is constant, i.e., the equilibrium shape is circular. For $g << 1$, one has that $[1 + (r^{-1}\, \partial r/\partial\theta)^2]^{m/2} = 1 + O(g^2)$, so these terms are replaced by unity, and

$$\kappa \approx -(r_{eq})^{-1} (g + \partial^2/\partial\theta^2\, g) \text{ and } \partial^2/\partial s^2\, \kappa \approx -(r_{eq})^{-3} (\partial^2/\partial\theta^2 + \partial^4/\partial\theta^4)\, g. \quad (25)$$

Consequently, (23) reduces to

$$\partial/\partial t\, g(\theta, t) \approx -(k_B T)^{-1} \sigma_{PD}\, \gamma\, (r_{eq})^{-4} (\partial^2/\partial\theta^2 + \partial^4/\partial\theta^4)\, g(\theta, t). \quad (26)$$

(cf. Ref. 174 which is missing the $\partial^2/\partial\theta^2$ term). Now, the eigenfunctions of the evolution operator on the RHS of (26) have the simple form $\phi_n(\theta) = e^{in\theta}$. As a result, the eigenvalues, λ_n, and decay times, $\tau_n = 1/|\lambda_n|$, satisfy[181]

$$\lambda_n = -(k_B T)^{-1} \sigma_{PD}\, \gamma\, (r_{eq})^{-4}\, n^2(n^2 - 1), \text{ so that } \tau_n = (k_B T)(r_{eq})^4/[\sigma_{PD}\, \gamma\, n^2(n^2-1)]. \quad (27)$$

Note that n = 0 corresponds to a pure growth/decay mode, and n = ±1 correspond to translational modes to lowest-order which do not evolve under mass-conserving periphery diffusion, and thus have $\tau_0 = \tau_1 = 0$. Solutions of (26) have the form

$$g(\theta, t) = \sum_n g_n(t)\, e^{in\theta} \text{ where } g_n(t) = \exp(-t/\tau_n)\, g_n(0). \quad (28)$$

With regard to asymptotic shape evolution, the equilibration time is given by

$$\tau_{eq} = \max(\tau_{n>1}) = \tau_2 = (k_B T)(r_{eq})^4/(12\, \sigma_{PD}\, \gamma). \quad (29)$$

This result for τ_{eq} will be directly compared with experimental observations in Sec.5.1.

From the above discussion, it should be clear that PD-mediated shape evolution, which is described by a fourth-order differential evolution operator, is quite distinct from curvature-driven evolution where $V_n \propto \kappa$, which is described by a second-order differential evolution operator. This is particularly clear regarding consideration of pinch-off phenomena. For curvature-driven evolution in 2D, Grayson's theorem[182] states that any shape no matter how irregular can never pinch-off into sub-clusters, but rather shrinks achieving an increasingly circular shape. It has been argued[177] that the lack of pinch-off also applies for a modified model $V_n \propto (\kappa - \kappa_0)$, which corresponds to shape evolution via an evaporation-condensation pathway (see below). Numerical implementation the above 2D continuum formulation of PD-mediated shape evolution has enabled effective description of the evolution of large irregular shaped vacancy nanoclusters where pinch-off is observed experimentally.[177] See Sec. 5.5.1. This phenomenon can be described qualitatively even with an isotropic formulation.

Quantitative description is achieved by including anisotropy in the step energy. There also exist generic modeling studies revealing pinch-off in these 2D systems.[183]

However, we should emphasize that while the above continuum formulation must provide a precise description of evolution for sufficiently large sized clusters, it can fail on the nanoscale. A dramatic example is provided by consideration of the evolution of convex elongated NCs back to their equilibrium Wulff shapes.[176] A breakdown of continuum theory applies if the linear size, L, of the NCs is less than the characteristic separation between kinks on close-packed step edges, $L_k \approx \frac{1}{2} \exp[+\varepsilon_k/(k_B T)]$ (in units of surface lattice constants), where ε_k denotes the kink creation energy, so the step edges are effectively faceted. In this case, reshaping is limited by nucleation of new edge layers on these facetted step edges in order to widen the elongated NC, and size scaling of the relaxation time, $\tau_{eq} \sim L^n$, is described by $n < 4$. Even in cases where reshaping is not mediated by nucleation of new edge layers, continuum theory can fail in the presence of large kink Ehrlich-Schwoebel barriers, δ_k, specifically in the case where the corresponding kink ES length, $L_\delta = \exp[\delta_k/(k_B T)] - 1$, exceeds L.[153] Furthermore, the presence of large kink ES barriers produces even greater deviations from the predictions of continuum theory in cases where reshaping is nucleation mediated.[153] Examples of such deviations will be presented in Sec.5.

Above, we have focused exclusively on PD-mediated NC reshaping. We note that a general universal continuum formulation exists accounting for shape evolution via all of: periphery-diffusion (PD); detachment and correlated reattachment (also known as terrace diffusion or TD) noting that in the absence of an attachment barrier, reattachment will generally occur close to the detachment point; and uncorrelated detachment-reattachment (also known as evaporation-condensation or EC) applying for a significant step attachment barrier.[129,174] Different size-scaling applies to TD and EC versus PD. However, since PD-mediated reshaping applies for system of interest here, we do not discuss further the more general formulation.

4.1.2. Shape evolution of 3D NCs. Next, we consider analogous Lagrangian front-tracking approaches for surface-diffusion-mediated shape evolution of 3D NCs. As indicated above, such studies have a long history. Traditional continuum modeling for PD mediated-shape evolution has been based on classic work of Herring, Mullins, Nichols, et al.[125,127,128], motivated by early experiments.[184] There exists more recent sophisticated simulation analysis by Eggers.[126] The basic formalism is entirely analogous to that presented above after accounting for diffusion across the 2D surface of 3D NCs versus the 1D periphery of 2D NCs. Following the treatment and notation of the classic Mullins papers which considered isotropic surface tension, γ, (which is thus equivalent to the isotropic surface stiffness) and isotropic surface diffusivity, the velocity, V_n, normal to the surface satisfies

$$V_n = -\Omega \nabla_{\mathbf{s}} \cdot \mathbf{J}_{SD}, \text{ where } \mathbf{J}_{SD} = -(k_B T)^{-1} D_S \nu \nabla_{\mathbf{s}} \mu \text{ with } \mu = +\gamma \kappa_S \Omega. \quad (30)$$

Here $\mathbf{J}_{SD}$ is the (vector) surface diffusion flux, $\nabla_{\mathbf{s}}$ is the surface divergence, D_S is a surface diffusion coefficient, and ν is the density of diffusing surface atoms (i.e., of mass carriers). The form of the chemical potential is analogous to 2D except that now the surface curvature, κ_S, is obtained from $\kappa_S = 1/R_1 + 1/R_2$ where R_1 and R_2 are the

principle radii of curvature. Ω is the atomic volume. Since the expression for V_n includes four spatial derivatives as in the 2D case, it still follows that the characteristic time for relaxation, τ_{eq}, scales with linear NC size, L, like $\tau_{eq} \sim L^{b^*}$, with $b^* = 4$.

As for the 2D case, it is also appropriate to assess the nature of the time evolution. Again, one naturally considers the asymptotic behavior for the approach to 3D equilibrium Wulff shapes of convex 3D NCs. However, complete analytic treatment is only viable assuming isotropic surface energy and surface diffusivity, so that the Wulff shape is a sphere of radius r_{eq}. Let $r(\theta, \phi, t)$ gives the distance of the surface from the center of mass origin for polar angle θ, where $0 \leq \theta \leq \pi$ and asimuthal angle ϕ, and set $r(\theta, \phi, t) = r_{eq} [1+ g(\theta, \phi, t)]$, so that $g(\theta, \phi, t) \rightarrow 0$, as $t \rightarrow \infty$. Then, for small deviations from spherical shape $g << 1$, one has that

$$\kappa_S \approx -2/r + r^{-2} \Delta_{\theta,\phi}\, r, \text{ and } (\nabla_s)^2\, \kappa_S \approx -(r_{eq})^{-3} [2\Delta_{\theta,\phi} + (\Delta_{\theta,\phi})^2]\, g, \quad (31)$$

where $\Delta_{\theta,\phi} = (\sin\theta)^{-1}\, \partial/\partial\theta\, (\sin\theta\, \partial/\partial\theta) + (\sin\theta)^{-2}\, \partial^2/\partial\phi^2$ is the angular part of the Laplacian. Consequently, one has that

$$\partial/\partial t\, g(\theta, \phi, t) \approx -(k_B T)^{-1}\, D_S\, \nu\, \gamma (r_{eq})^{-4} [2\Delta_{\theta,\phi} + (\Delta_{\theta,\phi})^2]\, g(\theta, \phi, t), \quad (32)$$

The eigenfunctions of the differential operator on the RHS of (32) are spherical harmonics, $Y_l^m(\theta,\phi)$, with eigenvalues are $\lambda_l = -(l-1)l(l+1)(l+2)\, (k_B T)^{-1}\, D_S\, \nu\, \gamma (r_{eq})^{-4}$. Analogous to the discussion of shape evolution in 2D, the corresponding to decay times are $\tau_l = 1/|\lambda_l|$. Note that $l = 0$ corresponds to a growth/decay mode, and $l = 1$ corresponds to translational modes to lowest order which do not evolve under mass-conserving periphery diffusion, and thus have $\tau_0 = \tau_1 = 0$. With regard to shape evolution, the asymptotic equilibration time is given by $\tau_{eq} = \max(\tau_{n>1})$. Consequently, the above results imply that

$$\tau_{eq} = \tau_2 = 1/|\lambda_2| = (k_B T)(r_{eq})^4/(24\, D_S\, \nu\, \gamma). \quad (33)$$

Rather than focus on asymptotic decay to equilibrium, classic studies have considered initial neck growth behavior for sintering problems. Benchmark geometries correspond to sintering of two spheres of radius R (i.e., sintering of unsupported spherical 3D NCs),[126,128] and sintering of a single sphere of radius "a" with a plane (i.e., wetting or merging of a 3D supported spherical NC with a support of the same material).[128,184] Specifically, interest is in initial growth of the radius of the neck, $\varkappa$, for these geometries. Early analysis utilized simplified models for the geometry in the neck region (cf. Figure 22a taken from the Kuczynski paper[184] for sintering of a sphere with the plane). The result was that[128]

$$\varkappa^7/R^3 = C\, (k_B T)^{-1}\, D_S\, \nu\, \gamma\, t, \quad (34)$$

where the numerical constant C differs for the two cases, but for both $\varkappa \sim t^n$ with $n = 1/7$. Early numerical analysis indicated at least transient behavior closer to $n = 1/6$. [28]

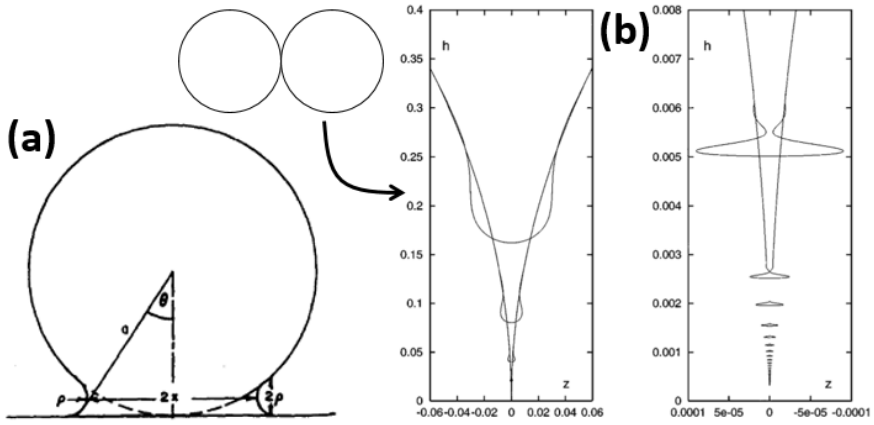

Figure 22. (a) Sintering of a sphere with a plane. Reprinted with permission from Ref. 184. Copyright 1949 American Institute of Physics. (b) Sintering of 2 spheres revealing void formation in the neck region. Reprinted with permission from Ref. 126. Copyright 1998 American Physical Society.

Later more sophisticated numerical analysis of evolution of sintering for two equal sized spheres[126] found extraordinarily rich and topologically distinct behavior from the traditional picture involving the formation of enclosed voids behind the advancing neck. See Figure 22b. This study confirmed the classic exponent n = 1/7, but also rationalized the occurrence of a transient regime with n = 1/6. Finally, we note that early analysis has also considered the effect of anisotropy in surface energy.[185]

Just as for the 2D cases, pinch-off phenomena are evident when considering evolution of more complex NC shapes. In fact, one might anticipate that these phenomena will be more prevalent in 3D as there is no Grayson's theorem to block pinch-off even for curvature driven evolution. The classic example which has received considerable recent attention is the surface-diffusion analogue of the Rayleigh-Plateau instability for fluid jets.[186,187] For an effectively infinite cylindrical NC (nanorod) of radius r_0 and diameter $d_0 = 2r_0$, linear stability analysis of evolution under surface diffusion predicts a most unstable wavelength of $\lambda_0 = 8.89\ r_0 = 4.44\ d_0$ leading to pinch-off into a sequence of NC droplets.[124,188] Numerical integration (beyond the linear stability regime) yielded a consistent estimate of $\lambda_0 = 4.5\ d_0$.[189] Analogous instability naturally does not occur for an infinite nanorod in 2D since opposite sides do not communicate with each other. However, we will discuss in Sec.5.5.2 analogous pinch-off in 2D for finite nanorods where fluctuations can play an important role.

Analogous to the 2D case, there has also been recognition of shortcomings the above classic continuum treatment for shape evolution of convex facetted 3D NCs at temperatures below the roughening transition.[121,190] Similar to our discussion of reshaping of small convex effectively facetted 2D NCs, evolution of 3D NCs is limited by nucleation of new layers. However, there are also fundamental differences between the 2D and 3D cases. Size scaling of the relaxation time, $\tau_{eq} \sim L^n$, is described by $n > n_c = 4$ (rather than $n < n_c = 4$ as in 2D), where classic continuum behavior with $n = n_c$ is obtained only at sufficiently high temperature.[121] The basic picture is that there exists a nucleation barrier which increases with NC size, so that τ_{eq} actually increases

exponentially with size, and reshaping is effectively blocked for NC sizes above the nanometer regime.[121,190]

Finally, one might consider continuum modeling of partially-wetting 3D supported NCs. In this case, the Winterbottom construction (or the Young-Dupre equation for isotropic surface energy) demonstrates that there is a well-defined "contact line" between the NC and the substrate for the equilibrium NC shape. Starting with a non-equilibrium shape for the supported NC, this contact line must evolve (as well as the entire NC shape) to achieve its correct equilibrium form. There have been extensive studies of such dynamics for liquid droplets,[191,192] but not for supported crystalline NCs. One could anticipate a stochastic version of such models enabling description of, e.g., the diffusion of supported 3D NCs.

4.2. Incorporating fluctuations into coarse-grained modeling for individual NCs

The deterministic continuum treatments of Sec.4.1 completely neglect the effect of thermal fluctuations, which in general will become more significant for smaller length scales. In Sec.5.5.2, we shall see that they have a major effect on pinch-off in 2D systems. Perhaps more significantly, inclusion of fluctuations is essential for the description within a continuum formulation of the diffusion of supported NCs. Such a treatment has been developed in detail for diffusion of 2D epitaxial NCs, and more generally for fluctuations at step edges on extended surfaces.[129,174,193]

Here, we focus on the development of a formulation to treat PD-mediated diffusion of 2D epitaxial NCs as developed by Khare *et al.*[174,193] It is necessary to supplement (23) with a suitable zero-mean conserved noise term, η, which is delta-function correlated in time and positional variable, and with an amplitude determined by the fluctuation-dissipation relation. Thus, we analyze the Langevin equation $V_n = -\nabla_s J_{PD} + \eta$. As in Sec.4.1, we use polar coordinates, where $r(\theta, t)$ gives the distance of the step edge of the NC from the origin for polar angle θ, where $0 \le \theta \le 2\pi$, and introduce the equilibrium radius, $r_{eq}(\theta)$. For simplicity, we ignore anisotropy in step edge mobility and stiffness so that $r_{eq}(\theta) = r_{eq}$ is constant, and we set $r(\theta, t) = r_{eq}[1+ g(\theta, t)]$. Now, NC evolution is described by (26) after including fluctuations, i.e.,

$$\partial/\partial t\, g(\theta, t) = - (k_B T)^{-1} \sigma_{PD} \gamma (r_{eq})^{-4} (\partial^2/\partial\theta^2 + \partial^4/\partial\theta^4)\, g(\theta, t) + \eta(\theta, t)/r_{eq}. \quad (35)$$

It is instructive to introduce a Fourier decomposition for both $g(\theta, t) = \sum_n g_n e^{in\theta}$, where $g_n = g_{-n}^*$, and $\eta(\theta, t) = \sum_n \eta_n e^{in\theta}$, where $\eta_n = \eta_{-n}^*$. The n = 0 mode is absent by mass conservation for g, and due to a zero overall noise for η. Further specification of the noise term is provided below. Fourier analysis of (35) yields

$$\partial/\partial t\, g_n(t) = -g_n(t)/\tau_n + \eta_n(t)/r_{eq}, \text{ where } \tau_n = (k_B T)(r_{eq})^4/[\sigma_{PD} \tilde{\gamma}\, n^2(n^2-1)], \quad (36)$$

and $\langle \eta_n(t)\eta_{-m}(t')\rangle = f_n \delta_{n,m}\, \delta(t-t')$. Integration of (36) with $g_n(t) = 0$ reveals that

$$\langle |g_1|^2\rangle = f_1\, t/(r_{eq})^2 \text{ for n = 1, and } \langle |g_n|^2\rangle \to \tfrac{1}{2} f_n \tau_n/(r_{eq})^2 \text{ for n > 1 as } t\to\infty. \quad (37)$$

More complete analysis for this system utilizes the fluctuation-dissipation relation to determine the amplitudes, f_n, of the Fourier amplitude of the noise in terms of key system parameters. This in turn requires further consideration thermodynamic framework underling the continuum evolution equations. For isotropic step energy, one can rewrite the free energy, F, introduced in (17), in a form appropriate for NCs as

$$F = \gamma P \text{ for perimeter length } P = \int d\theta\, [r^2 + (dr/d\theta)^2]^{1/2}. \quad (38)$$

Again setting $r(\theta, t) = r_{eq}[1+ g(\theta, t)]$ with $g << 1$, one obtains

$$F = \int ds\, \gamma = F_0 + \Delta F, \text{ where } \Delta F \approx r_{eq}\, \gamma \int d\theta\, [g + \tfrac{1}{2} (dg/d\theta)^2], \quad (39)$$

where $F_0 = 2\pi\, r_{eq}\, \gamma$ is the free energy for a perfect circular cluster, and we have used that $\int d\theta\, g = 0$ as a result of mass conservation. Decomposition of ΔF into contributions from specific Fourier modes shows that[181]

$$\Delta F = \pi\, \gamma\, r_{eq}\, (2g_0 + \sum_n n^2\, |g_n|^2). \quad (40)$$

For small $g << 1$, conservation of the total mass, $M = \tfrac{1}{2} \int d\theta\, r(\theta, t)^2$, implies that

$$2g_0 + \sum_{n>0} |g_n|^2 = 0 \quad (41)$$

neglecting the $|g_0|^2$ term relative to g_0. Thus, (40) can be rewritten as

$$\Delta F = \sum_n \Delta F_n \text{ where } \Delta F_n = \pi\gamma\, (n^2 -1) r_{eq}\, |g_n|^2. \quad (42)$$

The fluctuation-dissipation relation requires that the free energy content of the n^{th} Fourier mode, ΔF_n, must equal $\tfrac{1}{2}\, k_B T$ for $n > 1$ in equilibrium as $t \to \infty$, so that

$$\langle |g_n|^2 \rangle \to k_B T/[2\pi\gamma(n^2 -1) r_{eq}] \text{ for } n > 1 \text{ as } t \to \infty. \quad (43)$$

Comparing (43) and (37) implies that the noise fluctuation amplitude, f_n, is given by

$$f_n = \sigma_{PD}\, n^2/[\pi (r_{eq})^3]. \quad (44)$$

Although the above analysis of f_n strictly applies only for $n>1$, we will also use (44) for $n = 1$. This produces results for cluster diffusivity which are consistent with independent derivations.

As an aside, using (44) together with the above specification of $\langle \eta_n(t) \eta_{-m}(t') \rangle$, one can assess further properties of the noise $\eta(\theta,t)$. In particular, one finds that $\langle \eta(\theta,t)\, \eta(\theta',t') \rangle \propto \delta''(\theta-\theta')\, \delta(t-t')$, where δ'' denotes the second derivative of the periodic version of the Dirac delta function (the derivatives arising since noise is conservative).

Finally, we utilize the above results to determine the <u>NC diffusion coefficient</u>, D_{NC}, obtained from $D_{NC} = \lim_{t\to\infty} \langle (\delta r_{CM})^2 \rangle /(4t)$, where $\delta \mathbf{r}_{CM}$ is the displacement in the NC center of mass over a time period t, $(\delta r_{CM})^2 = \delta \mathbf{r}_{CM} \cdot \delta \mathbf{r}_{CM}$, and <-> denotes an ensemble

average. In fact, for atomistic models of NC diffusion, back-correlations in the walk of the NC lead to enhanced values of $<(\delta r_{CM})^2>/(4t)$ for short times[155], but we find that the ratio is constant in the continuum Langevin formulation. To evaluate D_{NC}, it is necessary to first rewrite $<(\delta r_{CM})^2>$ in terms of suitable ensemble averages over g or related quantities. With regard to center of mass displacement, it is clear that only the n = ±1 modes will contribute, and an explicit calculation assuming that $g << 1$ yields

$$\delta \mathbf{r}_{CM} = r_{eq}(g_{-1} + g_1)\mathbf{e}_x - i\, r_{eq}(g_{-1} - g_1)\mathbf{e}_y, \text{ so that } (\delta r_{CM})^2 = 4\, r_{eq}\, |g_1|^2. \quad (45)$$

As a consequence, since $<|g_1|^2> \approx f_1\, t/(r_{eq})^2$ for all t from (4.12), it follows that

$$D_{NC} = <(\delta r_{CM})^2>/(4t) = r_{eq} <|g_1(t)|^2>/t = f_1 = \sigma_{PD}/[\pi (r_{eq})^3]. \quad (46)$$

As indicated above, this result can be derived independently from a more heuristic approach $D_{NC} = k_B T V/\mathcal{F}$ where V is the drift velocity of the NC subject to an external force $\mathcal{F}$, the challenging being to determine V in terms of $\mathcal{F}$ for PD-mediated diffusion. Thus, PD-mediated diffusion of an NC of size N atoms (so that $N \sim R^2$ where R is the "radius"), one has that $D_{NC} \sim N^{-\beta}$, with $\beta = 3/2$. The above analysis has been extended to consider TD- (AD-) mediated cluster diffusion showing that $\beta = 1$ ($\beta = ½$).

Again, while the continuum formulation provides a precise description of evolution for sufficiently large sized clusters, it can fail on the nanoscale. Just as it fails for the nucleation-mediated evolution of convex elongated NCs back to their equilibrium shapes, it also fails for the prediction of cluster diffusion for smaller NC sizes and lower temperatures where lower effective exponents, $\beta_{eff} < 3/2$ are observed. See Sec.8.1.

Finally, we briefly comment on the incorporation of fluctuations into evolution of 3D NCs. For unsupported NCs where surface energy and diffusivity are isotropic, one can follow the above approach be decomposing the evolution into distinct spherical harmonic models and prescribing the properties of the noise for each such mode.

4.3 Other continuum formulations for NC shape evolution

4.3.1. Continuum multi-field formulations. In our discussion of conventional continuum formulations above in Sec.4.1 and Sec.4.2, we have noted the shortcomings of the conventional continuum theory for evolution of NCs for smaller sizes and lower temperatures. This motivated an attempt by Pierre-Louis[194] to refine the conventional treatment to account for distinct behavior at lower temperatures within a continuum multi-field formulation for 2D epitaxial NCs. Here, for simplicity we first consider an extended step aligned with the x-axis with mean position $y = 0$. This approach includes an extra field, the density $c(x, t)$ of diffusing atoms along the step edge, as well as considering the location of the step edge, $y(x, t)$. See Figure 23. Then, the conventional overall step free energy, $F = \int ds\, \gamma = \int dx\, \gamma\, [1 + (\partial y/\partial x)^2]$, is replaced by

$$F = \int dx\, \{\gamma\, [1 + (\partial y/\partial x)^2]^{1/2} + ½\, \alpha(\delta c)^2\} \approx F_0 + \int dx\, \{ ½\, \tilde{\gamma}(\partial y/\partial x)^2 + ½\, \alpha(\delta c)^2\}, \quad (47)$$

where $\delta c = c - c^0_{eq}$ and c^0_{eq} denotes the equilibrium concentration of diffusing step edge atoms along a straight step,[194] and a small slope expansion is performed of the first term. Next, a Fourier decomposition is introduced for $y(x, t) = (2\pi)^{-1/2} \int dq\, y_q(t)\, e^{iqx}$, and similarly for δc. Then, treating $\tilde{\gamma}$ as a constant, and performing a corresponding decomposition of the free energy yields

$$F = \int dq\, F_q \text{ where } F_q = \tfrac{1}{2} \tilde{\gamma}\, q^2 |y_q|^2 + \tfrac{1}{2}\, \alpha\, |\delta c_q|^2. \quad (48)$$

In the presence of thermal noise, equipartition of energy in thermodynamic equilibrium implies that[194]

$$\tfrac{1}{2} \tilde{\gamma}\, q^2 \langle |y_q|^2 \rangle = \tfrac{1}{2}\, \alpha \langle |\delta c_q|^2 \rangle = \tfrac{1}{2}\, k_B T. \quad (49)$$

Also assuming that edge atoms are non-interacting and can be treated at a mean-field level implies that $\langle |\delta c_q|^2 \rangle = c^0_{eq}$, so that $\alpha = k_B T / c^0_{eq}$ determining this key parameter[194].

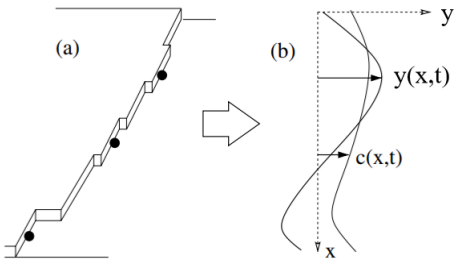

Figure 23. Schematic of multi-field treatment of step edges where *y(x, t)* denotes step displacement and *c(x, t)* denotes the edge atom concentration. Reprinted with permission from Ref. 194. Copyright 2001 American Physical Society.

Evolution equations are obtained by appropriate functional differentiation of the free energy, an approach which we have also described for the conventional continuum theory. One adopts Model A type non-conserved dynamics for y, and Model B type dynamics for the conserved total mass reflected by the combination $\psi = y/\Omega + \delta c$ where Ω is the unit cell area. This yields[194]

$$\Omega^{-1}\, \partial/\partial t\, y = -A\, \delta F/\delta y \text{ and } \partial/\partial t\, \psi = \partial/\partial x\, [B\, \partial/\partial x\, (\delta F/\delta \psi)], \quad (50)$$

where *A* and *B* are kinetic coefficients, and appropriate noise terms can be added to these equations for analysis of fluctuation effects and NC diffusion. Evaluation of the functional derivatives and recasting the equation for ψ in terms of *c* yields[194]

$$\Omega^{-1}\, \partial/\partial t\, y = \nu(c - c_{eq}) \text{ and } \partial/\partial t\, c = \partial/\partial x\, [\eta\, \partial/\partial x\, c] - \nu(c - c_{eq}), \quad (51)$$

$$\text{where } c_{eq} = [1 + \kappa\, \Omega\, \tilde{\gamma}/(k_B T)] c^0_{eq}, \quad (52)$$

and $\kappa = -\partial^2 y/\partial x^2$ is the local curvature. Also, one has that $\nu = \Omega^{-1}\alpha A$ and $\eta = \alpha B$. Note that the dependence of c_{eq} on y through κ fully couples these equations. We emphasize that the quantity c_{eq} in (52) naturally emerges as the local equilibrium adatom concentration at the curved step edge consistent with the Gibbs-Thomson equation. This result uses the above expression for $\alpha = k_B T/c^0_{eq}$. Again, appropriate noise terms can be added to these evolution equations. Additional heuristic arguments indicate that η is proportional to the step edge diffusivity (which reflects the diffusion rate along close packed step edges with some correction reflecting kink rounding barriers and the kink density).[194] It is also argued that the macroscopic attachment coefficient, ν, corresponds to the inverse of the characteristic time for an edge atom to reach a kink. Thus, according to Einstein's relation, $\nu \sim \eta/(L_k)^2$, where L_k denotes the mean kink separation.[194]

As an initial application of the refined dynamics (51), we determine the modification to the standard continuum prediction (20) for the decay rates and decay modes for eigenmodes of an extended step edge where we ignore anisotropy in step edge energies and mobilities. We implement an eigenfunction expansion $y(x, t) = (2\pi)^{-1/2} \int dx\, y_q\, e^{iqx}$ and $\delta c(x, t) = (2\pi)^{-1/2} \int dx\, \delta c_q\, e^{iqx}$. Recalling that c_{eq} involves $\partial^2 y/\partial x^2$, one obtains a coupled linear pair of equations for y_q and δc_q for each q of the form

$$\Omega^{-1}\, d/dt\, y_q = \nu\, \delta c_q - K_q\, y_q \text{ and } d/dt\, \delta c_q = -\eta\, q^2\, \delta c_q - \nu\, \delta c_q + K_q\, y_q, \qquad (53)$$

where $K_q = \nu\, \Omega\, \tilde{\gamma}/(k_B T)]c^0_{eq}\, q^2$. The decay rate, λ_q, for mode q comes from analysis of the eigenvalue of the 2x2 matrix version of these equations. However, it is convenient to implement a simpler "quasi-static" analysis regarding decay in the edge atom density, δc_q, to be much faster than that of the step edge displacement, y_q. Setting $d/dt\, \delta c_q = 0$ yields a characteristic decay time, $\tau_q = 1/|\lambda_q|$, from the y_q-equation of

$$\tau_q = [q^2 + (\nu/\eta)](k_B T)/[\nu\, \Omega^2\, \tilde{\gamma}\, c^0_{eq}\, q^4]. \qquad (54)$$

Since $\nu/\eta \approx (L_k)^2$, there is a crossover from the behavior for traditional continuum theories $\tau_q \sim q^{-4}$ for $qL_k << 1$ (long wavelength regime) to $\tau_q \sim q^{-2}$ for $qL_k >> 1$ (short wavelength regime).

For analysis of <u>shape evolution for finite NCs</u> with isotopic step energy and mobility, we adopt polar coordinates as in Sec.4.1.1 and Sec.4.2. The above analysis is adapted polar coordinates making the replacements $dx \to r_{eq}\, d\theta$, $y(x, t) \to r_{eq}[1+ g(\theta, t)]$, considering small deviations from circular shapes so $g << 1$ where $\kappa = -(r_{eq})^{-1}\, (g + d^2 g/d\theta^2)$. We implement an eigenfunction expansion $g(\theta, t) = \sum_n g_n\, e^{in\theta}$ and $\delta c(\theta, t) = \sum_n \delta c_n\, e^{in\theta}$. Then, substitution into (51) yields

$$\Omega^{-1}\, r_{eq}\, d/dt\, g_n = \nu\, \delta c_n - K_n\, g_n \text{ and } d/dt\, \delta c_n = -\eta\, n^2/(r_{eq})^2\, \delta c_n - \nu\, \delta c_n + K_n\, g_n, \qquad (55)$$

where $K_n = \nu\, \Omega\, \tilde{\gamma}/(k_B T)]c^0_{eq}\, (n^2-1)/r_{eq}$. A "quasi-static" analysis assuming rapid decay in the edge atom density, δc_n, yields a characteristic decay time, $\tau_n = 1/|\lambda_n|$, from the g_n-equation of[194]

$$\tau_n = [n^2 + (\nu/\eta)(r_{eq})^2]\,[\{(k_BT)(r_{eq})^2\}/\{\nu\,\Omega^2\,\tilde{\gamma}\,c^0_{eq}\,n^2(n^2\text{-}1)\}]. \quad (56)$$

As with the traditional continuum analysis, the equilibration time for asymptotic shape relaxation is determined that of the slowest decay mode, $\tau_{eq} = \tau_2$ [cf. (29)], noting that n = 0 is a forbidden growth/decay mode, and n = 1 is a translation mode. It is clear that (56) predicts cross-over behavior as the parameter $(\nu/\eta)(r_{eq})^2 \sim (r_{eq}/L_k)^2$ passes through unity, where again L_k denotes the mean kink separation. One has that

$$\tau_{eq} \approx (k_BT)(r_{eq})^4/(12\,\Omega^2\,\eta\,c^0_{eq}\,\tilde{\gamma}) \text{ for } r_{eq} >> L_k,$$

$$\text{and } \tau_{eq} = (k_BT)(r_{eq})^2/(12\nu\,\Omega^2\,c^0_{eq}\,\tilde{\gamma}) \text{ for } r_{eq} << L_k. \quad (57)$$

The former case recovers the result of traditional continuum analysis recognizing that the product of step edge mobility and equilibrium adatom concentration gives the step edge conductivity. The latter case indicates distinct scaling of relaxation time with characteristic size, r_{eq}, in the case where NCs are smaller or temperature is lower and step edges are effectively facetted. This behavior will be confirmed in Sec.5.1 and 5.2. Finally, this result for τ_1 can also be used in the analysis of NC diffusion following the formulation in Sec.4.2 to indicate a crossover from the traditional continuum prediction, $D_{NC} \sim \sigma_{PD}(r_{eq})^{-3}$ for $r_{eq} >> L_k$, to $D_{NC} \sim \sigma_{PD}(L_k)^{-2}(r_{eq})^{-1}$ for $r_{eq} << L_k$.

4.3.2. Evolution of faceted NCs. Lagrangian interface tracking approaches have also been tailored to consider the evolution of faceted NCs. Here, the need to appropriately determine a discrete set of normal propagation speeds for each facet accounting for, e.g., diffusion between facets of 3D supported or unsupported NCs.[45,46,195] Although 2D epitaxial NCs are not strictly facetted, as noted previously they can become effectively facetted at sufficiently low temperature. Thus, rather than implement the "smooth" continuum type models described in Sec.4.1, one might anticipate that it is more efficient and reasonably effective to track evolution in models where 2D NCs are treated as faceted. However, in such models with facetted 2D NCs, it is necessary to appropriately specify the normal propagation velocity, V_i, of each step edge facet i in a way which is consistent with the underlying mechanism of mass transport, e.g., PD-mediated shape evolution. The appropriate non-trivial procedure is described in Ref. 196. For a Wulff shape with M distinct facets i = 1,2,…,M, we denote their lengths by Λ_i for some specified area. Then, for a general polygonal NC of the same area where a facet of type i has a length L_i, one defines a weighed curvature for that facet via $\kappa_i = \sigma_i\,\Lambda_i/L_i$, where the convexity factor is +1, 0, or -1, as shown in Figure 24. These κ_i determine the average chemical potential $(L_i)^{-1}\int_{0<s<Li}\mu_i(s)$ on the facet. As usual $V_i \propto -d/ds\,J_i$ and $J_i \propto -d/ds\,\mu_i(s)$. Since V_i is constant for each facet, this implies that the chemical potential varies quadratically along each facet. Imposing continuity of μ around the NC perimeter ultimately gives a set of equations which can be solved to determine the V_i. It is possible that during evolution, some facets will shrink to

zero lengthy and be eliminated, or that new facets need to be created for reasons of stability. We refer the reader to Ref. 196 for a detailed description.

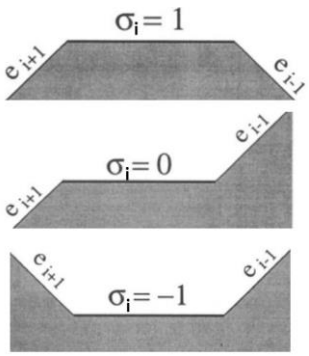

Figure 24. Weighted curvature for evolution of 2D facetted NCs. Reprinted with permission from Ref. 196. Copyright 1995 Elsevier Science Ltd.

One limitation of this modeling strategy is that evolution of non-equilibrium NC shapes, even starting from a collection of facets with preferred orientations, can involve evolution through shapes with significant portions of step edges of unfavorable orientations. This feature is not captured within the above modeling framework. However, we shall see in Sec.5.5.2 that this approach is quite successful in capturing overall behavior, e.g., for reshaping on nanorods as determined by more realistic modeling. A novel limiting case of this modeling strategy comes from allowing multiple facet orientations, $2\pi n/M$ for integer n with large M thereby mimicking isotropic step energy. We shall also see in Sec.5.2.2 that results are quite close to that obtained from analysis of a traditional continuum isotropic model. Finally, we remark that there is motivation to extend this approach to 3D where NCs can be truly facetted.

4.3.3. Multilayer step dynamics. The above Lagrangian formalisms have focused on 2D epitaxial NCs representing the NC periphery as an evolving sharp curve. This approach is also naturally referred to as step dynamics modeling. The approach can be naturally extended to multilayer step-dynamics modeling of supported 3D epitaxial NCs, provided that these NCs have no overhangs, where this semi-continuum approach treats lateral step positions between layers in a continuous step dynamics formulation, but retains a discrete description of vertical layer structure.[197,198] See Figure 25. The requirement for no overhangs should naturally apply in the equilibrium structure which from Figure 5b implies that the adhesion energy for the NC to the substrate should exceed the surface energy for the NC material. One could imagine deposition creating an artificially tall 3D NC which then would relax in height and spread. If the substrate and NC material are the same (so the adhesion energy is double the surface energy), then the NC will decay into a single layer on the substrate. This type of evolution has been considered in detail using this step dynamics approach, where often the goal is to systematically coarse-grain the semi-discrete formulation to obtain a fully continuum partial differential equation (PDE) description. Sometimes, however, atomistic-level information is required as input to the PDE, e.g., the decay times of disappearing top-level 2D layers on the 3D NC.[198] It should also be noted that this multi-

layer step dynamics approach has been implemented to describe the growth of 3D epitaxial mounds.[199,200]

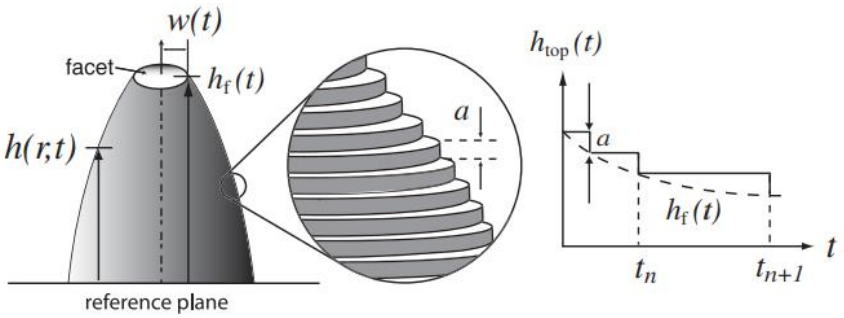

Figure 25. Schematic of coarse-graining from continuum to multilayer step-dynamics formulation. Reprinted with permission from Ref. 198. Copyright 2006 American Physical Society.

4.3.4. Eulerian versus Lagrangian dynamics. Rather than Lagrangian sharp-interface tracking approaches of Sec.4.1 and 4.2, an alternative is of Eulerian approaches for NC shape evolution, typically based on the phase-field method.[201] Here, the atomically sharp NC periphery is smeared out and described by a continuous order-parameter whose evolution satisfies a continuum partial differential equation encoding the relevant physics. This approach has been applied extensively to analyze sintering, where we note that the formulation is flexible and can account for different mass transport mechanisms and also grain orientation, and thus the presence and evolution of grain boundaries between sintered NCs.[202-204] This formulation can also naturally treat topological changes, i.e., pinch-off of NCs into separate smaller NCs, although such work seems to have focused on liquid systems. A refinement of the standard phase-field method to incorporate greater atomistic detailed, particularly local crystal structure, is the phase-field crystal approach.[205] However, this strategy does not seem to have been applied yet to NC shape evolution.

4.4. Post-assembly coarsening for ensembles of supported NCs

Here, we present the basic formulation of coarsening theory first for Ostwald Ripening (OR) and then for Smoluchowski Ripening (SR). In both cases, the theory is built around an analysis of the evolution of a single NC (NC growth or shrinkage for OR, and NC diffusion for SR). This information provides input for an ensemble-level description of evolution of the entire NC distribution.

4.4.1. Ostwald Ripening (OR). OR considers the coarsening of ensembles of immobile supported NCs below. For simplicity, we also assume weak anisotropy in step or surface energies so that NCs are roughly circular for 2D NCs and are treated as hemispheres for 3D NCs, characterized by a radius R. It is straightforward to generalized the treatment to more general spherical caps for 3D NCs. Description of OR kinetics is based on analysis of the density, ρ (per surface unit cell), of the species transporting mass across the surface between NCs. The default expectation is that this species is adatoms, but it could be vacancies in the top surface layer.[14] This analysis

exploits the Gibbs-Thomson relation[10-14] which gives an expression for the equilibrium density, $\rho^{eq} = \rho^{eq}(R)$, of this species at the edge of a NC of radius R in terms of its value for a very large NC ($R = \infty$) as

$$\rho^{eq}(R) \approx \rho^{eq}(\infty) \exp[+(d-1)\tilde{\gamma}\Omega/(k_B T R)], \text{ with } \rho^{eq}(\infty) \approx \exp[-E_{form}/(k_B T)]. \quad (58)$$

Here, $\tilde{\gamma}$ is the step stiffness per unit length for 2D NCs, or the surface stiffness per unit area for 3D NCs, and Ω is the unit cell size (so $\Omega \sim a^2$ is unit cell area for 2D NCs, and $\Omega \sim a^3$ is the unit cell volume for 3D NCs, and where 'a' is the lattice constant). This result reflects the feature that a finite size NC has an excess chemical potential, $\Delta\mu = +(d-1)\tilde{\gamma}\Omega/R$ relative to a large NC.

E_{form} is the formation energy for creating a terrace adspecies by extraction from a very large NC. This corresponds to the difference in energy of an atom in the bulk of the NC and an isolated terrace atom. For 2D NCs, E_{form} can also be regarded as the energy cost to extract an adatom from a kink site on the linear step bordering a large NC, which roughly corresponds to the cost of breaking lateral bonds at the kink site (noting that the atom is interacting with the substrate both before and after detachment). For a 3D NC, E_{form} corresponds to the energy of extracting an atom from a kink site on an extended stepped surface of the NC material (i.e., the bulk cohesive energy for that material) less the energy gain from adsorbing the atom on the substrate (i.e., the magnitude of the adsorption energy).

Below, the terrace diffusion coefficient is denoted as $D = D_0 \exp[-E_d/(k_B T)]$, where E_d is the terrace diffusion barrier. Any additional barrier for a species to attach to NC edges is denoted by δ, and the effective activation barrier for OR-mediated coarsening is denoted as E_{eff}. The standard picture is that atoms can potentially attach anywhere along the periphery for 2D NCs, but just along the contact line between the NC and the substrate for 3D NCs.

During OR, the adatom density is regarded as relaxing quickly to that in equilibrium with the instantaneous cluster distribution. Thus, it suffices to solve the boundary value problem (BVP) for the steady-state diffusion equation with appropriate boundary conditions (BCs)[13,14]

$$0 \approx \partial\rho/\partial t = D\,\nabla^2\rho \text{ in 2D, with } D\,\partial\rho/\partial r|_{\perp} = K\,[\rho - \rho^{eq}(R)] \text{ at NC edges,} \quad (59)$$

where $\partial\rho/\partial r|_{\perp}$ denotes the normal gradient of ρ at cluster edges $r = R$, and K is a kinetic coefficient describing the ease of attachment to step edges. The traditional Chernov formulation of kinetic coefficients sets $K = K_\delta = D/L_\delta$, where $L_\delta = a[\exp[\delta/(k_B T)] - 1]$ denotes the attachment length in the case of an additional energy barrier, δ, for attachment. Commonly there is no additional attachment barrier ($\delta = 0$) for metallic NCs, so $L_\delta = 0$ and $K_\delta = \infty$, in which case one would traditionally adopt a Dirichlet BC, $\rho = \rho^{eq}$. In general, one might anticipate that the relative magnitude of L_δ and the mean NC separation, L_c, will be a key factor, noting that the boundary conditions are imposed at island edges separated by a distance of order L_c.

We should note that the traditional Chernov theory applies to meso- or macroscale geometries where characteristic lengths far exceed those describing atomistic-level features of step edges such as the mean kink separation. Recent treatments for 2D epitaxial systems systematically coarse-graining semi-discrete treatments[206] or atomistic treatments[207,208] reveal corrections to Chernov theory. K should actually also depend on (and increase with) kink density since atoms are incorporated into the growing crystal at kink sites, and thus $K < \infty$ even if $\delta = 0$. [207,208] This feature is important for coarsening in some systems. See Sec.8.2. In addition to a more precise treatment of K for 2D epitaxial systems, one might also account for step permeability or transparency which leads to further modification of the above BC.[206,209]. However, such effects are not generally included in development of OR theory.

The most direct analysis of OR would attempt to solve (e.g., with numerical methods) the above BVP for a prescribed distribution of clusters. See Sec.8.2. However, for purposes of developing general theory in the spirit of Lifschitz-Slyosov-Wagner (LSW), one considers a BVP involving a single NC embedded in an effective medium representing other NCs which is described by a suitable "outer" BC.[3,73] If L_c denotes the mean NC separation, then this outer BC requires that ρ approaches a value $\rho^{eq}(R_c)$ at a distance from the NC center corresponding to roughly ½ L_c (i.e., mid-way between the NC and its neighbors). Here, the critical radius, R_c, provides a measure of the average cluster size, R_{av} (i.e., $R_c \sim R_{av}$). Consequently, the total coverage of material, φ, on the surface incorporated in the NCs which is constant in time satisfies $\varphi \sim (R_c)^d/(L_c)^2$ in d = 2D or 3D. Solving this BVP gives the rate of growth (or shrinkage) of an NC of radius R, determined from the total net flux of adatoms attaching to that cluster, J (in atoms per unit time). Setting $K = D/L_\delta$ yields the form[10,14,210]

$$J \approx 2\pi\, D\, \Omega^{-2/d}\, \rho^{eq}(\infty)\, \{\exp[+(d-1)\tilde{\gamma}\Omega/(k_BTR_c)] - \exp[+(d-1)\tilde{\gamma}\Omega/(k_BTR)]\}\ \ [L_\delta/R + \ln(L_c/R)]^{-1}$$

$$\approx 2\pi\,(d-1)\, D\, \Omega^{-2/d}\, \rho^{eq}(\infty)\, \tilde{\gamma}\, \Omega/(k_BT)\, [L_\delta + R\, \ln(\varphi^{-1/d}\, (L_c)^{(d-2)/d})]^{-1}\, [R/R_c - 1]. \qquad (60)$$

The appearance of the ln-term is expected for analysis of the Laplace equation in 2D, and mandates imposition of the outer BC at a finite distance. The second simplified expression also replaces R by R_c in the ln-term, or equivalently neglects a $\ln(R_c/R)$ term. Commonly reported simplified expressions for J performs a Taylor expansion on the exponentials which is often reasonable for small (but not too small) R relative to R_c. However, care must be taken in application to analysis of experimental NC decay behavior.[13] Let N denote the number of atoms in the NC, so that $J = dN/dt$.

Finally, we utilize the result (60) for J to obtain a growth law, i.e., an expression for dR/dt, for an NC of radius R. Using that the area, $A = \pi R^2$ of the circular NC in 2D satisfies $A = \Omega N$, and that the volume $V = 2/3\ \pi R^3$ of the hemispherical NC in 3D satisfies $V = \Omega N$, one has $dR/dt = (2\pi R^{d-1})^{-1}\, \Omega J$. In presenting simplified forms for the growth law, we note that there are two distinct extreme regimes for kinetics: (a) terrace diffusion (TD)-limited mass transport where $\delta \approx 0$, so that $L_\delta \approx 0$, $\rho \approx \rho^{eq}$ at step edges, and $E_{eff} = E_d + E_{form}$; (b) attachment-detachment (AD)-limited mass transport with large δ, so that $L_\delta >> L_c$, $\rho \approx \rho^{eq}(R_c)$ tends to be spatially uniform across terraces, and $E_{eff} = E_d + E_{form} + \delta$. Thus, for d = 2 or 3 D NCs, (60) becomes

$dR/dt \sim R^{-\lambda}\,[R/R_c - 1]$, where λ = d-1 (d) for AD (TD), (61)

so that $R \sim (t_0 - t)^{1/(\lambda+1)}$ when $R \to 0$ at $t = t_0$, (62)

for shrinking and disappearing NCs with small R. Thus, for 2D epitaxial NCs, the area of decaying NC satisfies $A \propto R^2 \sim (t_0 - t)$ for AD (linear decay), and $A \sim (t_0 - t)^{2/3}$ for TD (non-linear decay).[10,12,14,210] For 3D supported NCs, the volume of the decaying NC satisfies $V \propto R^3 \sim (t_0 - t)$ for AD (linear decay), and $V \sim (t_0 - t)^{3/4}$ for TD (non-linear decay). We emphasize that actual behavior of individual decaying NCs in the TD regime is complicated being strongly impacted by the local environment of islands. See Sec.8.2. For the TD regime, the adatom density on the surface is more uniform being controlled by the mean island size versus NCs sizes in the vicinity of the decaying NC. This corresponds to a simpler mean-field type scenario. See Figure 26.

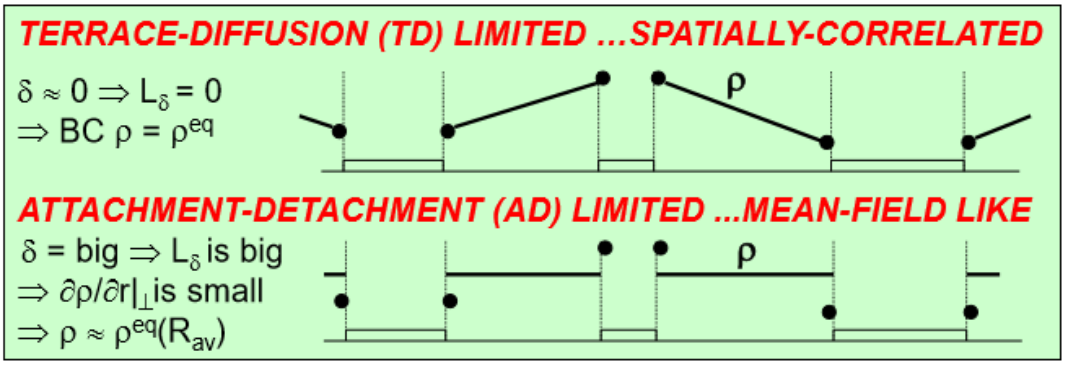

Figure 26. Behavior of the adatom density, ρ, for TD versus AD for an array of supported 2D NCs. Black dots denote equilibrium values at NC edges (higher for small NCs). Atoms detach from the smaller central NC and attach to the larger NCs.

LSW theory incorporates the NC growth law into a formulation for analysis of the NC size distribution, $F(R, t)$ (the density or population of NCs of a certain size), traditionally formulated as a function of NC radius, R. This distribution is normalized so that $\int dR\, F(R, t) = P_{av}(t)$, where P_{av} is the mean NC density (which decreases in time). Also, one has that $\int dR\, R\, F(R, t) = R_c(t)\, P_{av}(t)$ where $R_c(t)$ increases with time and $P_{av}\,(R_c)^d \sim \varphi$ (fixed) for d = 2 or 3 D NCs. Evolution of $F(R, t)$ is described by the continuity equation

$\partial/\partial t\, F(R, t) + \partial/\partial R\, J(R, t) = 0$ with $J = dR/dt\, F(R, t)$. (63)

The strategy is to look for a long-time scaling solution $F(R, t) \approx (P_{av}/R_c)\, f(R/R_c)$, where the scaling function $f(x)$ describes the asymptotically selected shape of the distribution with $\int dx\, f(x) = \int dx\, x\, f(x) = 1$. Self-consistency for the scaling solutions determined the temporal scaling $R_c \sim t^{1/2}$ ($t^{1/3}$) for AD (TD) for 2D epitaxial NCs, and $R_c \sim t^{1/3}$ ($t^{1/4}$) for AD (TD) for 3D supported NCs.[12]

Various extensions or refinements of this OR theory are straightforward. For 2D systems, it is natural to consider the coarsening of ensembles of single-atom deep monolayer vacancy pits (as well as single-atom high adatom island NCs). In addition, it is possible that mass transport can be mediated by diffusion on monomer vacancies through the top surface layer versus atoms on top of the surfaces.

4.4.2. Smoluchowski Ripening (SR). In SR, clusters diffuse and irreversibly aggregate or coalesce or coagulate upon meeting to form larger clusters. For supported NCs, it is generally the case that coagulation is diffusion-limited. The dependence of the cluster diffusion coefficient, D_{NC}, on cluster size is the key factor controlling evolution. Typically, treatments assume that $D_{NC} \sim N^{-\beta}$ for size N atoms.[14,211,212] For our analysis, rather than the linear size or "radius" R of the NC used in the analysis of OR, it will be more convenient to use the size, N, of the NC as the independent variable. Rather than the size in atoms, one could use the area $A = \Omega N$ for 2D NCs or the volume $V = \Omega N$ for 3D NCs where Ω is the unit cell size (area in 2D and volume in 3D). It is traditional to regard the size variable as continuous, which is natural for A or V, and we will do the same for N. Thus, sums over discrete size N are replaced by integrals below. Thus, we write the cluster diffusion coefficient as

$$D_{NC}(N) \approx D^0_{NC} \exp[-E_{diff}/(k_B T)] \, N^{-\beta}, \qquad (64)$$

where E_{diff} is the effective barrier for diffusion of large NCs. Our focus is on analysis of the NC size distribution, $\widetilde{F}(N, t)$ (again the population or density of NCs of a certain size) which is here more naturally formulated as a function of NC size in atoms, N. This distribution satisfies the normalization relations $\int_{N>0} dN \, \widetilde{F}(N, t) = P_{av}$, the mean NC density, and $\int_{N>0} dN \, N \, \widetilde{F}(N, t) = P_{av} \, N_{av} = \varphi$, where N_{av} denotes the mean cluster size. N_{av} increases in time compensating the decrease of P_{av} in time. Then, Smoluchowski's coagulation equations for the evolution of this distribution has the form[14,108,213,214]

$$d/dt \, \widetilde{F}(N, t) = \tfrac{1}{2} \int_{0<N'<N} dN' K(N-N', N') \widetilde{F}(N-N', t) \widetilde{F}(N', t)$$

$$- \int_{0<N'<\infty} dN' K(N', N) \widetilde{F}(N', t) \widetilde{F}(N, t). \qquad (65)$$

where the "kernel" satisfies $K(M, N) = \sigma[D_C(M) + D_C(N)]$. The first term represents creation of a cluster of size N from smaller clusters of size N' and $N-N'$. The second represents removal of a cluster of size N by coalescence with another of size N'.

From this equation, it is also clear that the effective barrier for SR-mediated coarsening is given by $E_{eff}(SR) = E_{diff}$ corresponding to the effective barrier for diffusion of large NCs. For 2D epitaxial NCs, one has that $E_{diff} = E_e + E_{eform} + \delta_{KESE}$ where E_e is the barrier for diffusion along close-packed step edges, E_{eform} is the formation energy to create an edge atom by extraction from a kink site, and δ_{KESE} is any extra barrier for edge atoms to round kinks and corners (which is typically not zero).

Analogous to the LSW treatment of OR, one seeks a long-time scaling solution of the form $\tilde{F}(A, t) \approx (P_{av}/N_{av})\, \tilde{f}(y=N/N_{av})$, where $N_{av} = N_{av}(t)$ increases appropriately with time.[215] The scaling function $\tilde{f}(y)$ describes the asymptotically selected shape of the distribution where $\int_{y>0} dy\, \tilde{f}(y) = \int_{y>0} dy\, y\, \tilde{f}(y) = 1$. Finally, substituting the scaling solution into (65) and using the relation $P_{av} = \varphi/N_{av}$ immediately shows that[14,215] $N_{av} \sim t^{1/(\beta+1)}$ and $R_{av} \propto (N_{av})^{1/d} \sim t^{1/(\beta d+d)}$. For 2D epitaxial NC systems β exceeds ½ and is usually between 1 and 3/2 (the asymptotic large size value).

4.4.3. General issues for OR and SR including crossover. There has been extensive rigorous analysis on the subtle selection of the shape of the asymptotic size distribution in coarsening for both OR[216,217] and SR.[215,217,218] However, for practical analysis of experimental data, it is also important to characterize the transient initial behavior reflecting the "initial conditions" controlled by the NC nucleation and growth during deposition.[219] In fact, it seems that there has been little consideration of the appropriate "complete" specification of initial conditions (not just the initial NC size distribution, but information on the spatial distribution, and correlations between NC size and the local environment).[9,88]

To provide a unified description of coarsening which will allow assessment of the dominant pathway and possible crossover behavior, we adopt a more complete (but approximate[220]) description of temporal evolution than the above simple scaling laws. For either OR or SR, the time evolution of the mean NC "radius", $R_{av}(t)$, is written as

$$R_{av}(t) \approx R_{av}(0)[1+ t/\tau]^{n}, \text{ where } \tau = \tau_0 \exp[+E_{eff}/(k_B T)], \quad (66)$$

where n denotes the relevant temporal scaling exponent, τ denotes the characteristic time and E_{eff} the effective activation barrier for coarsening. Thus, for example, for 2D epitaxial NCs, one has that

$$n = n_{OR} = 1/3\ (1/2) \text{ for TD (AD) OR, and } n = n_{SR} = 1/(2\beta + 2) \text{ for SR.} \quad (67)$$

For the macroscopic value for PD-mediated NC diffusion of $\beta = 3/2$, one has that $n_{SR} = 1/5$. However, values of β down to $\beta \approx 1$, and thus n up to $n_{SR} = ¼$, are observed for typical N. This implies that invariably $n_{OR} > n_{SR}$.

In terms of the mean NC density, P_{av}, the fixed total amount of deposited material satisfies $\varphi \sim P_{av}\, (R_{av})^{d}$. Then, we define a scaled coarsening or ripening rate for a specific φ as[14]

$$K_R \sim -(P_{av})^{-1}\, d/dt\, P_{av} \sim (R_{av})^{-1}\, d/dt\, R_{av}, \text{ so that} \quad (68)$$

$$K_R \sim \exp[-E_{eff}/(k_B T)]\, (R_{av})^{-m}, \text{ where } m = n^{-1} - 1. \quad (69)$$

Thus, for our above example of 2D epitaxial NCs, one has that $m_{OR} < m_{SR}$. The conclusion from (69) that the dominant coarsening pathway does not just depend on relative values of the effective barriers E_{eff}. Rather, since different pathways have

different scaling exponents n (and thus m), the dominant pathway also depends on the characteristic size of the NCs. This can lead to crossover behavior. For example, SR often dominates for typical NC sizes on metal(100) surfaces since $E_{eff}(SR) < E_{eff}(OR)$. However, one expects a crossover to OR for larger sizes (later in coarsening) since $m_{OR} < m_{SR}$ meaning that K_R exhibits a slower decay with increasing NC size for OR than SR.

Finally, we mention that while the above treatment of both OR and SR is at the continuum level, in principle atomistic-level or hybrid treatments are also possible. Treatment of the overall coarsening processes via KMC simulation of stochastic models is expected to be computationally inefficient. This has motivated consideration of hybrid treatments.[221] Such a treatment has been implemented for coarsening of adatom NCs in metal(100) homoepitaxial systems where NCs are reasonably described as square. Conventional simulations determine both the size-dependence of the NC diffusion rate, $D_{NC}(N)$, and the rate for detachment of atoms from island. In the simulations the square undergo a random walk with motion consistent with $D_{NC}(N)$, and atoms are detached from NCs at the appropriate size-dependent rate, Such detached atoms undergo a diffusive random walk across the surface until reaching and attaching to the same or a different NC.

4.5. Solution-phase self-assembly and coarsening of 3D unsupported NCs

Our focus here is on evolution of the NC size distribution after the initial nucleation of NCs. First, we present a traditional formulation for coarsening via Ostwald Ripening within a traditional LSW formulation. The treatment is similar to that in Sec.4.4.1 for OR of supported NCs, but differs in some basic respects: **(i)** the diffusion problem is now solved in 3D rather than 2D, and attachment-detachment occurs anywhere on the 3D NC surface (rather than at a 2D perimeter or contact line); **(ii)** the "background" concentration is no longer constrained by the average NC size, but can be greater corresponding to a super-saturation of precursor atoms in the solution; **(iii)** the details of the solutions differ from Sec.4.4.1 due to the 3D nature of diffusion and attachment-detachment. Analogous to Sec.4.4.1, we will neglect anisotropy in surface energies, so shape-equilibrated clusters are spherical with radii denoted by R.

The relevant Gibbs-Thomson relation for the equilibrium density, $\rho^{eq} = \rho^{eq}(R)$, of the precursor at the edge of a NC of radius R has the form[222]

$$\rho^{eq}(R) \approx \rho_0 \exp[+2\tilde{\gamma}\Omega/(k_B T R)], \qquad (70)$$

where ρ_0 is the limiting value for a large NC (related to the solubility of the NC material) which has units of inverse volume. Also, $\tilde{\gamma}$ is the surface stiffness per unit area, and $\Omega \sim a^3$ is the unit cell volume for 3D NCs, and where 'a' is the lattice constant. Note that a finite size NC has an excess chemical potential, $\Delta\mu = +2\tilde{\gamma}\Omega/R$ relative to a large NC. Analogous to the treatment for supported NCs, we solve the steady-state diffusion equation, $0 \approx \partial\rho/\partial t = D\,\nabla^2\rho$, but now in 3D, and adopt a BC of the form (59) at NC surfaces, i.e., $D\,\partial\rho/\partial r|_{\perp} = K\,[\rho - \rho^{eq}(R)]$, where again K is a kinetic coefficient describing the ease of attachment. Here, D is the solution-phase diffusion coefficient, and it is convenient to write $K = k\,D$, so k has units of inverse length.

To assess the growth or decay of a specific NC with radius R, we solve a BVP for the steady-state diffusion equation with the BC (59) at the cluster surface, and specify that ρ approaches ρ_b corresponding to the bulk precursor concentration far from the NC (noting that logarithmic behavior seen in 2D is absent here in 3D). For the bulk concentration, it will be convenient to write $\rho_b \approx \rho_0 \exp[+2\tilde{\gamma}\Omega/(k_B T R^*]$, where R^* corresponds to the radius of an NC which would be in equilibrium with this bulk concentration. Straightforward solution of this BVP for the net flux, J (in atoms per unit time) of precursor species attaching to the NC yields

$$J = 4\pi D \rho_b \{\exp[+2\tilde{\gamma}\Omega/(k_B T R^*)] - \exp[+2\tilde{\gamma}\Omega/(k_B T R)]\} kR^2 [1+kR]^{-1}, \quad (71)$$

Since $J = dN/dt$, and using that the volume of the spherical NC of N atoms satisfies $V = \Omega N = 4/3\ \pi R^3$, one obtains the growth law, $dR/dt = (2\pi R^2)^{-1}\ \Omega J$. To obtain conventional simplified expressions, one performs a Taylor expansion on the exponential terms. In presenting these simplified forms for the growth law, we note that again there are two distinct extreme regimes for kinetics: (a) diffusion-limited (DL) mass transport where large $k >> 1/R$, so that at step edges; (b) attachment- or reaction-limited (RL) mass transport with small $k << 1/R$, where ρ tends to be spatially uniform. Then, (71) becomes[15,222]

$$dR/dt \approx A_{RL(DL)} R^{-\lambda} [R/R^* - 1], \text{ where } \lambda = 1\ (2) \text{ for RL (DL) regime.} \quad (72)$$

For solution-phase systems, it is common to perform a simple analysis exploiting the growth law (72) to determine at least some basic features of the evolution of the NC size distribution. This analysis considers narrow distributions of width ΔR and mean island size of $\langle R \rangle$. First, for the DL regime, one determines the difference between the rate of growth for radii, $R_\pm = \langle R \rangle \pm \frac{1}{2} \Delta R$ using (72). This analysis reveals that

$$d/dt\ \Delta R = d/dt\ (R_+ - R_-) = A_{DL}\ \Delta R\ \langle R \rangle^{-3}\ (2 - \langle R \rangle / R^*). \quad (73)$$

Thus, one has that $d/dt\ \Delta R < 0$ for high super-saturation where $R^* < \frac{1}{2} \Delta R$ which corresponds to narrowing of the NC size distribution. In contrast, $d/dt\ \Delta R > 0$ for lower super-saturation where $R^* > \frac{1}{2} \Delta R$ which corresponds to broadening of the NC size distribution. A similar analysis for the RL regime reveals that

$$d/dt\ \Delta R = A_{RL}\ \Delta R\ \langle R \rangle^{-2} > 0, \quad (74)$$

so that the NC size distribution always broadens.

As for supported NCs, the growth law (72) can be incorporated into a continuity equation, $\partial/\partial t\ F(R, t) + \partial/\partial R\ J(R,t) = 0$ with $J = dR/dt\ F(R, t)$, for evolution the NC size distribution, thereby obtaining a more complete picture of scaling of the mean NC size and of the entire distribution.[223] Comprehensive analysis incorporates the feature that the solutions depend on the "initial" form of the flux which is determined from analysis of the nucleation process. On an intermediate time-scale after an abrupt drop in super-saturation following a nucleation pulse, the NC size distribution adopts a novel scaling

form differing from standard Gauss or log-normal forms. This behavior also from the true asymptotic form for OR which is achieved on a much longer time scale.[223] Additional studies have considered the influence of fluctuation effects on the NC size distribution.[224,225]

Rather than the above formulations for continuous NC size, one can consider analogous formulations with discrete NC sizes. Within this class, the classic Becker-Doering equations (which incorporate both attachment and detachment from clusters with the appropriate rates) are traditionally used to analyze the nucleation process.[226] When mass conservation is incorporated into these equations, eventually the nucleation stage is exhausted, and ultimately replaced by a ripening regime. There is a large difference in time-scale for these two regime, making analysis of the crossover difficult. Nonetheless, recent theoretical analysis has probed this crossover and further showed the special "double-exponential front" of the NC size distribution emerging from the nucleation regime plays a key role in selection of the asymptotic LSW type distribution following prolonged coarsening.[220] Again, there is still extensive interest in this selection problem and in the sensitivity to the "initial conditions" from the nucleation stage.[216,217]

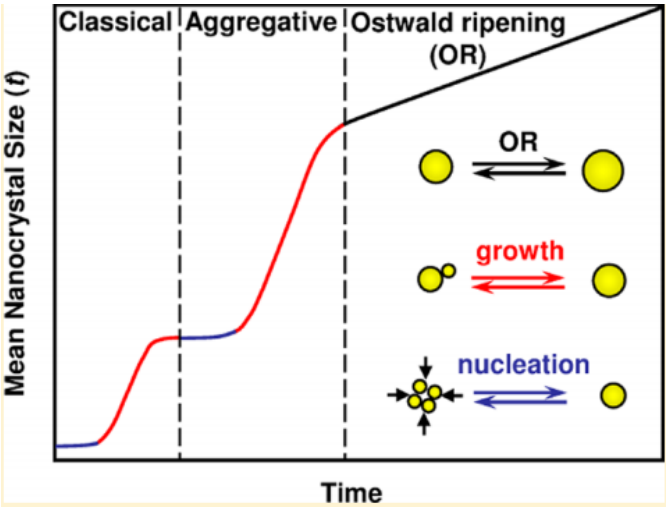

Figure 27. Schematic of the evolution of the mean NC size during various nucleation and growth, and well as coarsening regimes. Reprinted with permission from Ref. 44. Copyright 2014 American Chemical Society.

Analogous to our discussion for supported NCs, coarsening for unsupported NCs can occur via Smoluchowski ripening or aggregative growth in the terminology of this field, rather than (or in addition to) Ostwald ripening.[44] In fact, a general scenario includes the possibility of one or both of these mechanisms. The scenario in Figure 27 shows aggregative growth preceding OR which mimics our discussion in Sec. 4.4.3 of crossover for supported NCs. Aggregative growth can correspond to either diffusion-limited colloid aggregation (DLCA) or reaction-limited colloid aggregation (RLCA).[44] In fact, systems can be tuned to crossover between DLCA and RLCA (as is the case for Au colloids by adding different amounts of pyridine to tune the aggregation rates).[227] For DLCA, simulation simplified to neglect relaxation upon aggregation has explored the fractal nature of the aggregates,[228,229] and this analysis was later extended to include

relaxation via bond-breaking.[230] Analysis for RLCA has also explored fractal structure.[231] These processes are naturally analyzed by application of the Smoluchowski coagulation equation (analogous to the treatment of SR for supported NCs in Sec.4.4.2) which can be applied to either DLCA or RLCA although the kernel in the equations will have quite different form.[232] There has been extensive interest in analysis of the scaling form of the solution to these equations, and its dependence on the form of the kerne.l[233,234]

5. SHAPE EVOLUTION OF SINGLE-COMPONENT 2D EPITAXIAL NCs

Shape evolution of 2D epitaxial NCs is described where there exists extensive experimental STM data and also detailed modeling.[14] Specifically, we consider evolution of non-equilibrium shapes mediated by periphery (edge) diffusion which is believed to be the dominant mas transport pathway for the systems considered here. First, we consider initially convex NC's evolving to their equilibrium Wulff shapes. In this case, nanoscale evolution can be mediated by the nucleation of new outer layers, and behavior can deviate dramatically from predictions of macroscale theories.[176] Another scenario is particularly relevant for SR, i.e., cluster diffusion and coalescence, where often clusters formed by coalescence events initially have non-equilibrium dumbbell-type shapes with concave portions of step edges. Here, evolution at least in the initial stages is not nucleation-mediated, and thus is quite distinct from the above case.[114,153] Finally, we consider the evolution of more exotic NC shapes, e.g., "worms" and elongated nanorods.[177]

5.1. Reshaping for convex 2D epitaxial NCs: fcc(111) homoepitaxial systems

For initially convex NCs, we describe relevant experimental data as well as detailed system-specific modeling exploring reshaping. Examples include reshaping of elongated and "elliptical" NCs and triangular NCs to hexagons or distorted hexagons in fcc(111) metal homoepitaxial systems. In Sec.5.2 we consider analogous reshaping of rectangular nanoclusters to squares in fcc(100) metal homoepitaxial systems. We will consider behavior for both adatom island NCs and vacancy pit NCs.

We discuss several examples where there exist experimental data and theoretical analysis considering both size-scaling of relaxation and temporal evolution. We start by highlighting a key early theoretical study by Jensen et al.[176] for a generic lattice-gas (LG) model revealing that behavior on the nanoscale deviates from size-scaling behavior of classic continuum formulations. Figure 28 shows results of KMC simulations for the evolution of an elongated nanorod of N atoms back towards a hexagonal equilibrium shape with rounded corners. The LG model includes NN attractions of strength ϕ = 0.1 eV on a triangular lattice, and atom hopping rates described by a standard IVA or bond-counting prescription (with activation barrier just determined by the initial coordination). The relaxation time, t_{eq}, is taken as the first time that the aspect ratio of y- to x-dimensions fluctuates below unity. However, presumably similar scaling would be obtained by exponential fitting asymptotic decay of the aspect ratio to unity. The key result is that the size-scaling exponent, α, in the relation $t_{eq} \sim N^{\alpha}$ agrees with traditional continuum theory prediction of $\alpha = 2$ only at high T, but appears to adopt a lower value, $\alpha \approx 1$, at low T. It is also common to describe scaling in terms of the linear size, L, of the NC, where $N \sim L^2$ where $t_{eq} \sim L^{\alpha^*}$ where $\alpha^* = 2\alpha$. Then $\alpha^* = 4$ corresponds to continuum theory, but $\alpha^* = 2$ is observed above for low T.

This deviation is associated with feature that the NC step edges are effectively facetted at low T, i.e., their length is below the typical separation of kinks on an equilibrated straight close-packed step edge. Consequently, reshaping to equilibrium requires the nucleation of new outer layers on step edges.[176] This study suggested that the rate of decay of a deviation of linear size δL from equilibrium scales for an NC with

linear size L like the product of the associated kink (or corner) density imbalance on different steps, $\sim \delta L/L^2$, times the rate to nucleate new step edges, $D_e(n_{eq})^2$. Here, D_e is the edge diffusion coefficient, and n_{eq} is the equilibrium edge atom density. This formulation immediately yields $\alpha = 1$ or $\alpha^* = 2$, and also determines the effective activation barrier for reshaping as $E_{eff} = E_e + 2E_{eform}$, where E_e is the edge diffusion barrier for close-packed step edges, and E_{eform} is the formation energy for edge atoms (extracted from kinks).[176]

Analyses presented below of metal(100) systems provide an alternative derivation of the above scaling result based on atomistic-level model incorporating appropriate results from random walk theory.[153,235] The above result is also generalized to account for the presence of an additional kink ES barrier for corner rounding. Furthermore, we will provide a detailed comparison of the predictions of atomistic and continuum modeling.

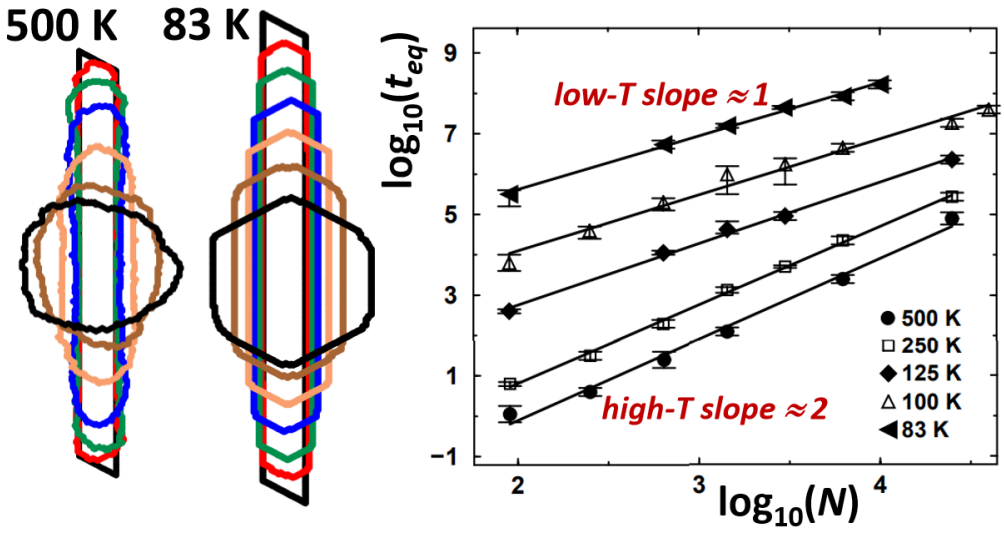

Figure 28. Simulation of NC shape evolution on a triangular lattice for a model with NN attractions of strength ϕ = 0.1 eV [so $\phi/(k_BT) = 2.3$ *at* 500 K *and* $\phi/(k_BT) = 14$ *at* 83 K] and IVA hop rates. *Left:* Simulated configurations for N = 6250 atoms. Right: Size scaling of relaxation times where curves for low T should bend to achieve a slope of 2 for large enough N. Reprinted with permission from Ref. 176. Copyright 1999 American Physical Society.

There is limited experimental STM data available tracking evolution of convex adatom NCs on fcc(111) surfaces. However, one example shown in Figure 29 tracks the reshaping of an “elliptical” Ag adatom NC or island on Ag(111), a surface for which there has been extensive analysis of NC formation and post-formation evolution.[13] These images actually correspond to the late stages of corner-to-corner coalescence (considered in Sec.5.3). A second example is shown in Figure 30 for Au(111) surfaces which we should emphasize are of central interest for various applications including self-assembled monolayers, functional 3D NCs for various applications, and catalysis.[236-238] Surprisingly, there appears to be a lack of previous studies of the evolution of homoepitaxial Au(111) NCs. The STM analysis shows the slow evolution of an elongated NC back towards a more hexagonal shape. For the Au system, we caution

that the finer details of the equilibrium shape, and no doubt of shape evolution, are complicated being impacted by the presence of a herringbone reconstruction of the Au(111) surface.[239] However, this does not appear to impact the basic features of evolution shown in Figure 30. For either of these systems, there has not been quantitative analysis of evolution. At least for the Au system, there is not sufficient data to assess asymptotic approach to equilibrium.

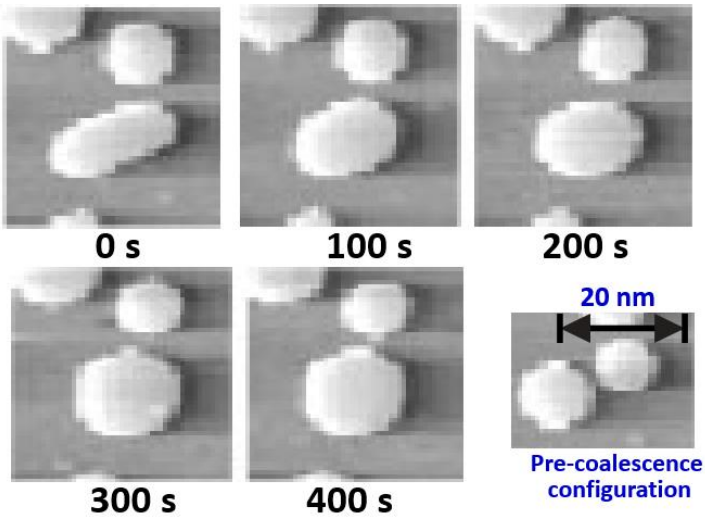

Figure 29. Reshaping of an “elliptical” Ag NC on Ag(111) at room temperature. Reprinted with permission from Ref. 13. Copyright 2005 Wiley-VCH.

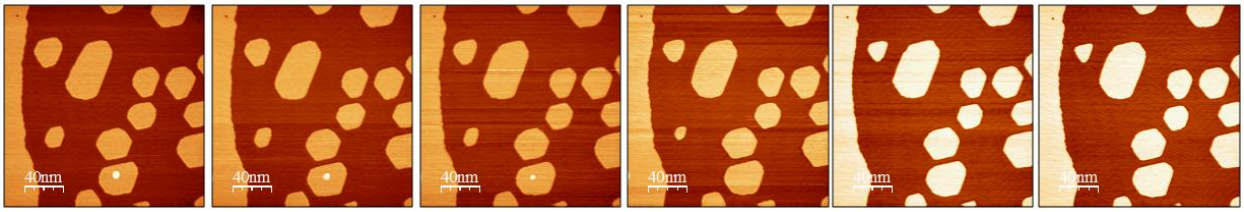

Figure 30. Reshaping of an elongated Au NC on Au(111) at 300K with 200 min between images.

It is however instructive to compare evolution in the above experimental examples with the predictions of reshaping for similar NC geometries of continuum modeling including an anisotropic step energy compatible with a hexagonal equilibrium shape. To this end, we select equal energies for A- and B-type steps, which is reasonable at least for Ag. The step edge mobility is selected to be isotropic. The prescription of anisotropic step energies is taken from Ref. 134. We show behavior for a simple stretched hexagonal geometric shape with close-packed step edges in Figure 31. Reshaping evolved through quasi-elliptical shapes, reminiscent of Figure 29, before reaching the equilibrium hexagonal shape. Note that topologically distinct behavior is observed for extreme elongations. See Sec.5.5.2.

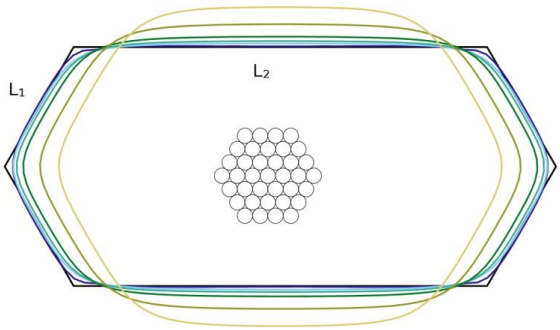

Figure 31. Continuum modeling of shape evolution for an elongated island on an fcc(111) surface where A- and B-type steps have the same energy. Parameters: $L_2/L_1 = 3$; $\varepsilon_k/(k_BT) = 4.7$.

It is natural to consider the evolution of NCs with other simple geometric far-from-equilibrium shapes back to equilibrium. Motivation comes from the observation that solution-phase synthesis can produce various simple non-equilibrium geometric shapes for 3D fcc metal NCs (cubes, tetrahedra, etc.)[3,4] for which it is also natural to explore post-synthesis shape equilibration. In this spirit, we note that NC growth kinetics during deposition on fcc(111) surfaces offers the possibility to create near-triangular NCs. See Figure 32 for the Ag/Ag(111)[164] and Pt/Pt(111)[8] systems, although there does not exist experimental data tracking the evolution from triangular to hexagonal (or distorted hexagonal) equilibrium shapes. Despite this fact, it is instructive to examine both atomistic-level and continuum modeling to elucidate this evolution.

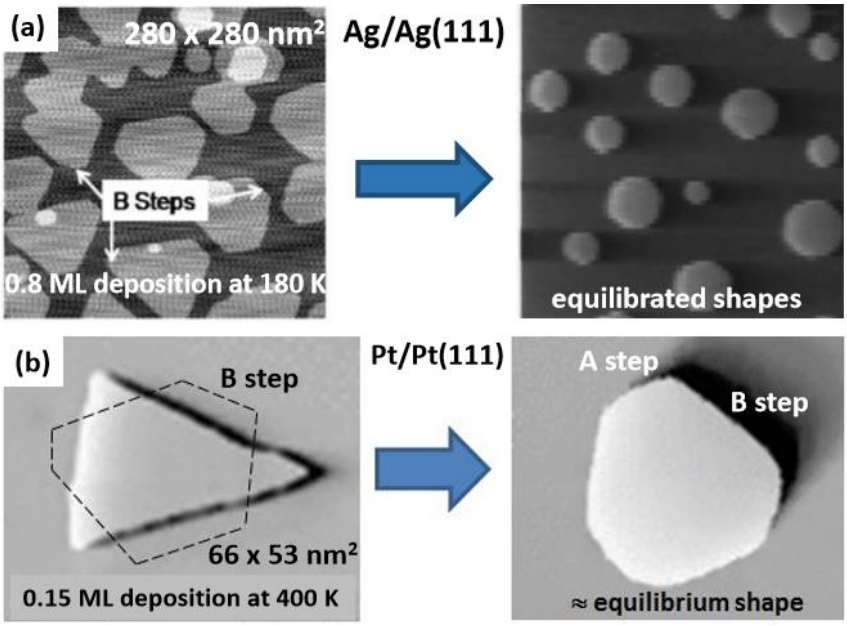

Figure 32. (a) Evolution from triangular to hexagonal Ag NCs on Ag(111). Reprinted with permission from Ref. 164. Copyright 2008 American Physical Society. (b) Evolution from triangular to distorted hexagonal Pt NCs on Pt(111). Reprinted with permission from Ref. 8. Copyright 2004 Springer Verlag.

For systems with roughly equal A- and B-step energies, subtle purely kinetic effects control growth shape deviation from hexagonal. A difference in edge diffusion barriers alone would lead to faster growth and disappearance of the steps with higher edge diffusivity.[8] However, other factors such as "corner-rounding anisotropy"[67,240] and non-uniform interlayer transport[164] often dominate the selection of growth shapes. For Ag/Ag(111) where equilibrium shapes are near-hexagonal, it is possible to achieve near-triangular shapes by appropriate tuning of deposition conditions, where the triangular shape derives from non-uniform downward transport of atoms deposited on top of the islands.[164] A lower ES barrier for B steps means that these are fed atoms at a greater rate than A-steps, and thus mostly grow out. However, to achieve these triangular Ag NC shapes, it is necessary to choose not only the appropriate temperature window, but also to deposit higher submonolayer coverages to increase the proportion of deposition on top of islands. See Figure 32(a).

Next, we consider atomistic simulations mimicking Ag NC evolution on Ag(111) where equilibrium shapes are effectively hexagonal with rounded corners. Again, the LG model includes just NN attractions with strength ϕ = 0.2 eV on a triangular lattice, but in this case atom hopping is determined by the generalized BEP type prescription in Sec.3.4 for surface diffusion on 3D NCs. This yields a kink ES barrier of δ = 0.1 eV, somewhat above the values obtained from EAM energetics. Time evolution is reported as a function of $h_e t$, where $h_e = \nu \exp[-E_e/(k_B T)]$ is the hop rate along close-packed step edges. Actual times can be determined using reasonable choice of $\nu = 10^{12.5}$/s and E_e = 0.3 eV for Ag(111). Simulated evolution at 300 K starting with a perfect triangle is shown in Figure 33. As shown in Figure 34, we quantify the decay kinetics by considering the "pedal radii" r_A and r_B measuring the distance from the center of the NC to alternating step edges, tracking evolution of the ratio to unity. As expected from Sec.4.1, kinetics of the asymptotic decay of $r_B/r_A - 1$ is described by a single exponential (but not kinetics of the entire decay process). Corresponding decay times, τ, are extracted for a range of NC sizes from N = 528 to N = 5050 atoms, and the associated size scaling $\tau \sim N^{\alpha} \sim L^{\alpha^*}$ thereby determined. This analysis indicates that α = 1.41 (α^* = 2.82), a value between the classic continuum value of α = 2 (α^* = 4) and the pure nucleation-mediated value of α = 1 (α^* = 2). In this system, the kink separation of $L_k \sim$ 24a at 300 K is comparable to the initial triangle edge lengths of 32a-100a, and to the shorter edge lengths of the developing hexagon. Thus, such intermediate values of α or α^* are expected.

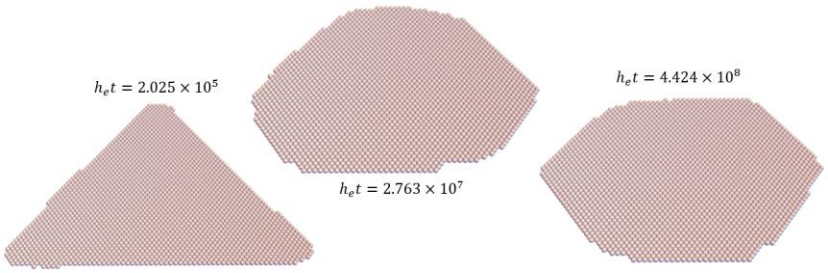

Figure 33. Simulation of reshaping of a triangular NC for fcc(111) homoepitaxy for a model with NN attractions ϕ = 0.2 eV and hexagonal equilibrium NC shape at 300 K for size N = 2485 (side length > L = 70 a = 20.2 nm).

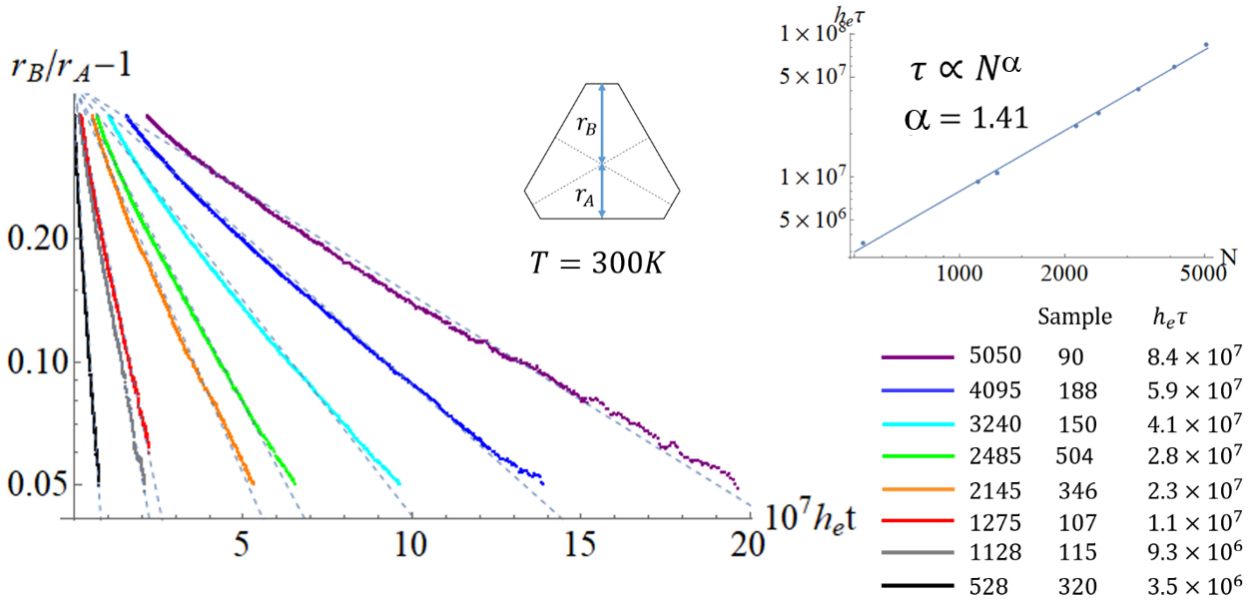

Figure 34. Relaxation to an equilibrium hexagonal shape for the model in Figure 33.

The scenario where NC growth most readily generates extreme (perfect) triangular shapes corresponds to systems with unequal A- and B-step energies like Pt/Pt(111).[8] Here, non-equilibrium shape selection directly reflects system thermodynamics as well as kinetics. Considering the Potential Energy Surface (PES) for an atom traversing the NC perimeter, the key point is that the PES is higher for the preferred steps (the B-steps for Pt) with lower step energy (atoms are bound more weakly to those steps). Thus, in equilibrium, the edge adatom density on the preferred steps is lower. However, there is a balance between the atom flux from B to A steps and from A to B steps, since the effective barriers for corner rounding compensate exactly for the edge atom density imbalance (as ensured by detailed balance). However, under growth conditions, the edge atom densities are supersaturated and become more equal (i.e., their ratio is closer to unity) which induces a strong net flux to the less preferred steps (the A-steps for Pt) which thus quickly grow out. See Figure 35. Thus, near-perfect triangular Pt NCs on Pt(111) can be formed by deposition in a suitable deposition window (around 400 K).[8] See Figure 32(b).

Next, atomistic modeling is presented appropriate to the Pt/Pt(111) system where equilibrium shapes are distorted hexagons due to unequal step energies of A- and B-steps for Pt. The standard LG model on a triangular lattice with just NN interactions of course does not incorporate this feature, so modification of the modeling strategy is required. One possibility is to use a so-called Awning approximation, which prescribes the energy of NC configurations as a sum of step edge contributions each of which depends on the orientation of segments of its step edges.[8] However, we prefer a more conventional LG modeling approach where one introduces many body-interactions in addition to NN pair interactions. For fcc(111) adlayers, one can prescribe two distinct types of triangular trio interactions, ϕ_Δ and ϕ_∇, for up-pointing versus down-pointing trios of atoms. DFT analysis confirms that such interactions have significant strength, and also differ from each other. For Pt(111), we choose the value of the NN interaction

strength of ϕ = 0.48 eV. The values of the trio interactions are selected to recover the A-step energy, $\beta_A = \phi + (\phi_\Delta + 2\phi_\nabla)/3$, and B-step energy, $\beta_A = \phi + (\phi_\nabla + 2\phi_\Delta)/3$ (where these formulae follow from assessing broken bonds at step edges), and thus their ratio which determines the equilibrium shape. This requires repulsive trios (consistent with DFT analysis) which have negative values in the notation used here, and we set ϕ_Δ = -0.15 eV and ϕ_∇ = 0. Time evolution is again reported as a function of h_e t where actual times can be obtained by selecting a standard attempt frequency and edge diffusion barrier of $E_e \approx 0.9$ eV for Pt(111). Simulated evolution from an initial perfect triangle with *N* = 1830 atoms and side length 60 atoms is shown on Figure 36. The distorted hexagonal equilibrium shape is reflected in the long-time image.

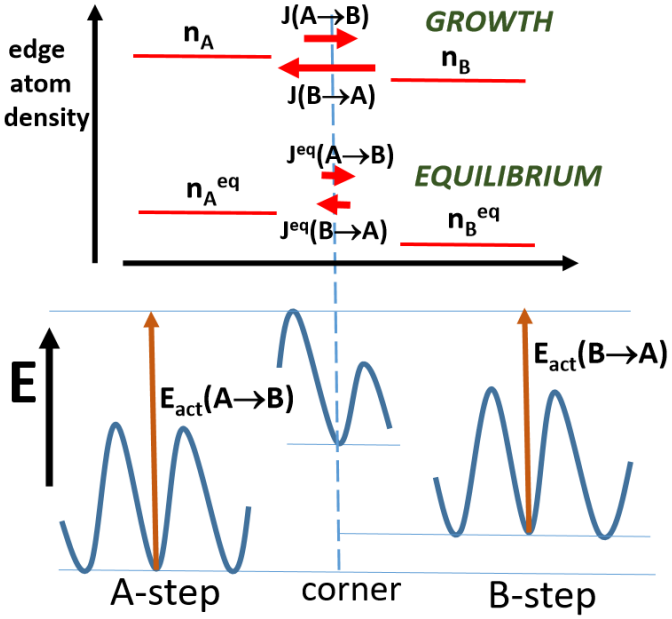

Figure 35. Top: adatom densities on steps and fluxes between steps for equilibrium and growth scenarios. Bottom: Schematic of PES for edge atoms for Pt/Pt(111).

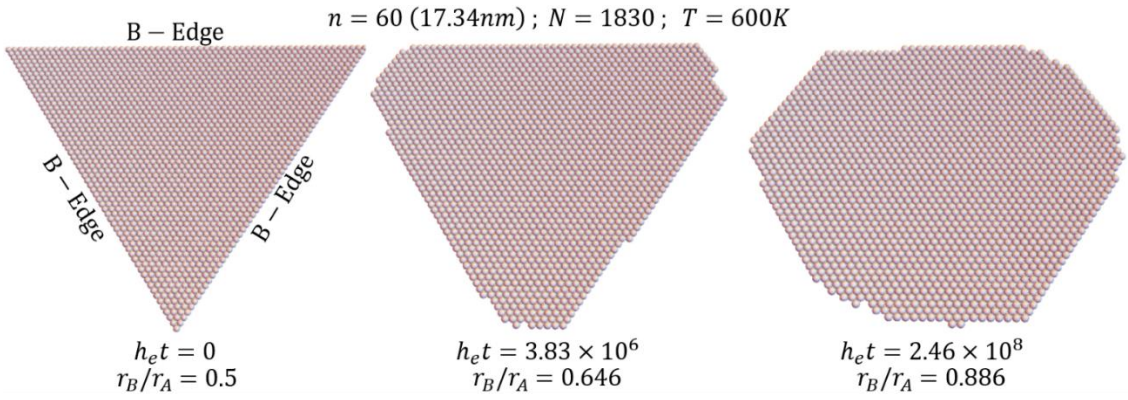

Figure 36. Simulations of relaxation of Pt triangles on Pt(111) with trio interactions to break 6-fold symmetry of the equilibrium NC shape. $\phi = 0.48\ eV;\ E_\Delta = -0.15\ eV;\ E_\nabla = 0.00\ eV;$ T = 600 K.

Next, for completeness, we compare shape evolution in the above atomistic modeling with the predictions of continuum modeling including an anisotropic step energy appropriate for an fcc(111) surface but producing a distorted hexagonal equilibrium shape (cf. Sec.4.1). Specifically, the formulation for the anisotropic step energy is taken from Ref. 134 with the ratio of step energies on the A- and B-type step edges is chosen as 2. An isotropic step edge mobility is incorporated. Evolution stating with a perfect triangular shape with close-packed step edges is shown in Figure 37.

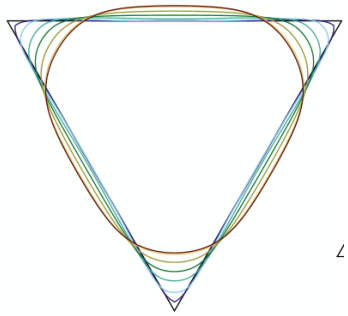

Figure 37. Continuum modeling for evolution of a triangular NC on an fcc(111) surface to a distorted hexagonal equilibrium shape. Parameters are: $\varepsilon_k(A)/(k_BT) = 3$; $\varepsilon_k(B)/(k_BT) = 6$.

We mentioned above that experimental data is not available tracking shape evolution of non-equilibrium NC triangles (or strongly distorted hexagons) back to equilibrium shapes for Ag/Ag(111) or Pt/Pt(111). However, STM data is available for Au/Au(111) at 300 K for at least the first stage of evolution of a strongly distorted hexagonal growth shape back towards the equilibrium shape (which seems to be close to a hexagon). This is shown in Figure 38 where we note that the total time spanned by this sequence of images is 20 hr. Given the complexities associated with the herringbone reconstruction on the Au(111) surface (which however does not seem to impact the basic features of evolution), we do not attempt detailed modeling for this system.

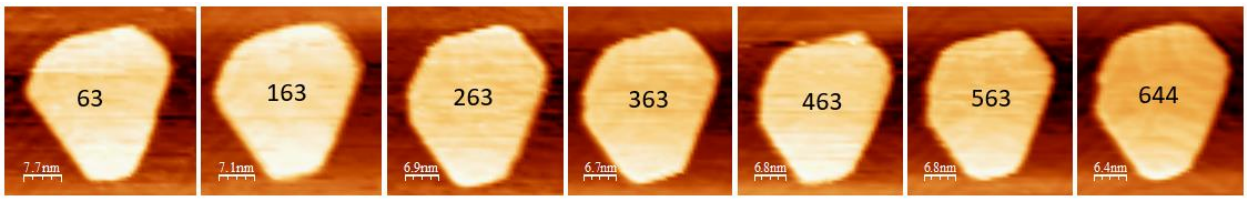

Figure 38. Evolution of an Au NC on Au(111) at 300 K with 200 min between images. Average lengths of the short (L_{short}) and long (L_{long}) step edges were determined: initial L_{long} = 19.5 nm, L_{short} =10.7 nm; final L_{long} = 15.8 nm, L_{short} = 12.0 nm.

In contrast to adatom nanoclusters, systematic STM data is available for the shape relaxation of single-layer deep convex vacancy NCs or nanopits on Ag(111).[241,242] This in part reflects the feature that coarsening of nanopit arrays on Ag(111) is mediated by Smoluchowski ripening, so nanopit sizes tend to be preserved

for long times. In contrast, coarsening of adatom NCs is mediated by Ostwald Ripening, so sizes tend to change providing a less ideal situation for analysis of shape evolution.

In Figure 39, the evolution of initially "elliptical" nanopits on Ag(111) at 300 K back to their equilibrium near hexagonal shapes (where we note that islands and pits have the same equilibrium shape, at least for systems with NN interactions).[13,241] It is clear comparing part (a) and (b) that there is a strong dependence of the relaxation time on NC size. To quantify this behavior, evolution of the orthogonal major and minor axes of the "ellipse" were tracked for the nanopit shown in Figure 39(a) yielding the results shown in Figure 40. [241] These were fit appropriately based upon exponential decay to their limiting values. The decay times for the two cases were similar, and the average, τ_c, was taken as the decay time for that particular nanopit size. The results of comprehensive analysis for size dependence (including many sizes beyond those shown in Figure 39) of the decay time are shown in Figure 41 where the linear size, d_{cl}, corresponds to the (equal) long-time values of the major and minor axes described above. The lines on the plot correspond to the dependence $\tau_{cl} \sim (d_{cl})^{\alpha^*}$ with $\alpha^* = 3$ and $\alpha^* = 4$ (the continuum value). Plausibly, behavior is better described by $\alpha^* = 3$, and a least-squared fit to data points actually gives $\alpha^* = 3.2$. Since for this system, the kink separation should be roughly $L_k \sim 24a \sim 7$ nm at 300 K which is well below the linear size of the nanopits, so one might have anticipated an exponent closer to $\alpha^* = 4$. Perhaps the shape relaxation kinetics of nanopits (which is distinct from that of atom NCs) is more susceptible to deviations from macroscopic behavior? As an aside, Ref. 241 proposed relation between the reshaping exponent α and the exponent describing the size-dependence of the NC diffusion, β, of the form $\beta = \alpha - 1$, where the latter issues will be discussed in Sec.8.1.

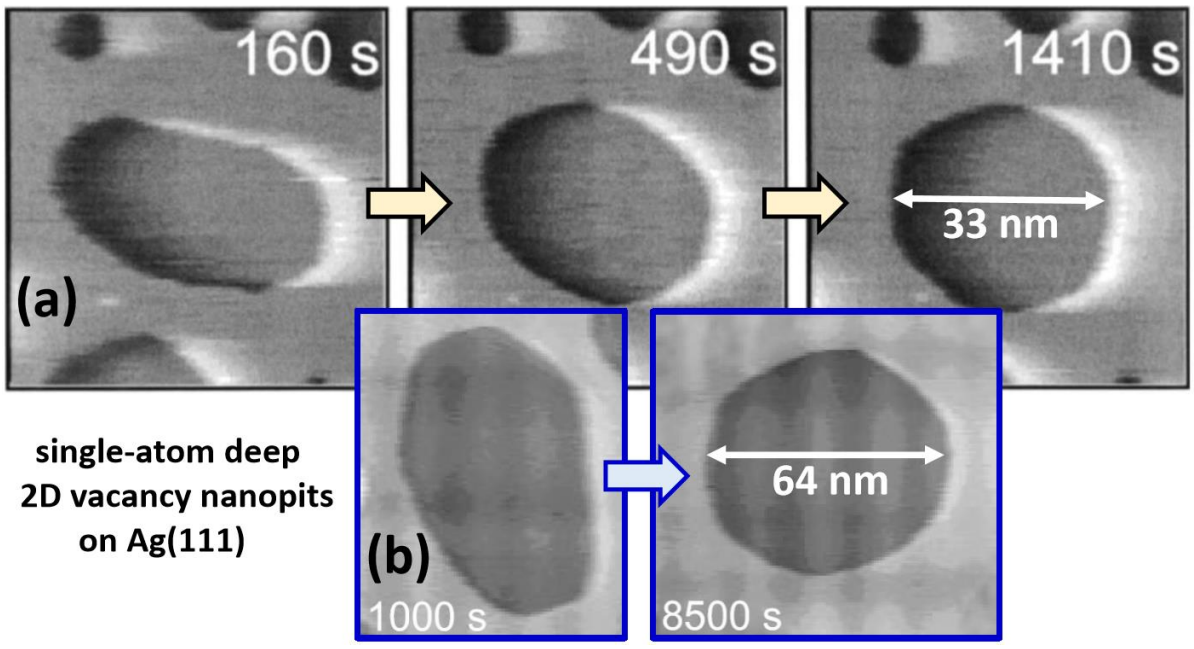

Figure 39. Reshaping of elliptical nanopits on Ag(111) at 300 K: (a) Smaller pit. Reprinted with permission from Ref. 241. Copyright 1998 Elsevier. (b) Larger pit. Reprinted with permission from Ref. 242. Copyright 1998 Materials Research Society.

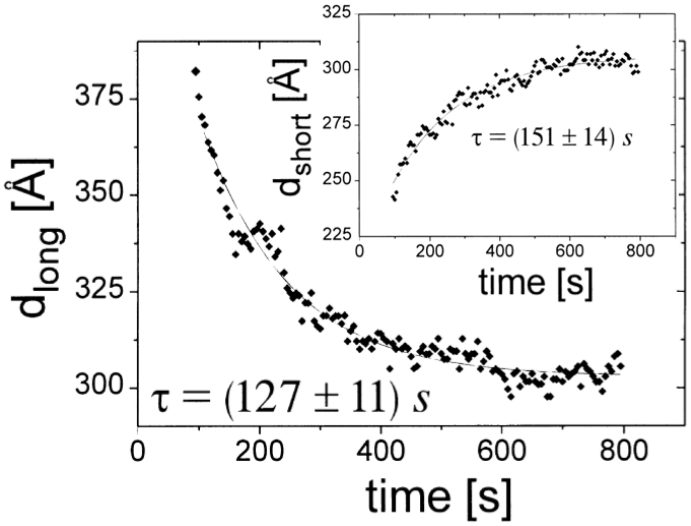

Fig.40: Exponential shape relaxation to equilibrium for the long and short dimensions of the elliptical nanopit on Ag(111) in Figure 39(a) at 300 K. Reprinted with permission from Ref. 241. Copyright 1998 Elsevier.

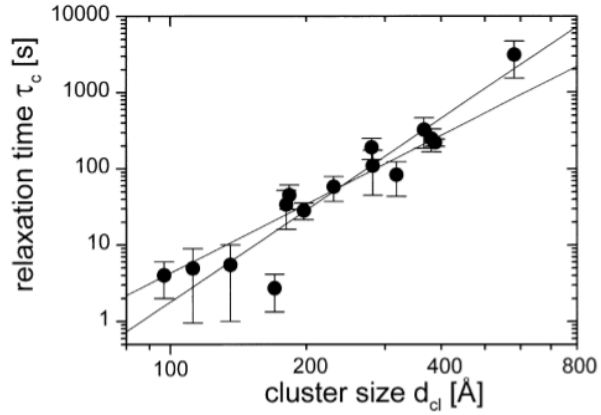

Figure 41: Size-scaling of the relaxation time for nanopits on Ag(111) at 300 K. The lines correspond to exponent $\alpha^* = 3$ and 4. A least-squares fit gives $\alpha^* = 3.2$. Reprinted with permission from Ref. 241. Copyright 1998 Elsevier.

Rather than just consider the size scaling of relaxation, it is appropriate to discuss theoretical estimation of the actual value of τ_c. One simple strategy is to exploit the result (29), $\tau_c = \tau_{eq} = \tau_1 = (k_B T)(r_{eq})^4/(12\sigma_{PD}\,\gamma)$, from continuum theory corresponding to the characteristic time for slowest decay mode. At 300 K, we choose r_{eq} = 17 nm = 60 a, γ = 0.2 eV, and $\sigma_{PD} = \nu \exp[-E_e/(k_B T)]\, n_e$ with E_e = 0.3 eV and where $n_e = \exp[-\phi/(k_B T)]$ with ϕ = 0.24 eV denotes the equilibrium density of edge atoms. Then, one obtains $\tau_c = \tau_{eq} \approx 50$ sec, of the same order as experimental estimates in Figure 40. It is also plausible that the simplified linearized analysis leading to (29) where n = 1 deviation from a circular shape is treated as a purely translational mode has some limitations.

5.2. Reshaping for convex 2D epitaxial NCs: fcc(100) homoepitaxial systems

Some experimental data exists for the evolution of convex NCs on fcc(100) homoepitaxial systems.[114] Occasional side-by-side coalescence of pairs of mobile near-square adatom NCs results in rectangular clusters for equal-sized NC pairs, or structures which "quickly" evolve to rectangular NCs for unequal-sized NC pairs as shown in Figure 42(a) for Ag/Ag(100). Deposition of near-monolayer coverages on flat surfaces produces isolated nanopits which sometimes quickly reshape to near-rectangular nanopit structures as illustrated in Figure 42(b) for Ag(100).[114] In either case, the rectangular NCs naturally evolve back to their near-square shapes, as also indicated in Figure 42. Comparison of behavior in these two cases suggests that perhaps nanopit reshaping is somewhat faster than that for atom NCs. To explore this hypothesis, the modeling framework incorporating ab-initio kinetics for Ag/Ag(100) described in Sec.3.5.1 can be utilized to perform a benchmark analysis for rectangular nanopits and nanoislands of the same size.[27] However, the default version of such modeling where energetic parameters are selected to recover ab-initio edge diffusion kinetics around convex nanoislands predicts much faster decay for nanopits compared to nanoislands. We track this failure to an artificially low barrier in the model for an atom to slide out of the corner of a rectangular pit along the step edge. This shortcoming is corrected[27] by adding additional unconventional interactions into the model determination of E_{act}, as discussed in detail in Sec.7.1.3. Results from modeling after incorporating this correction are shown in Figure 43.

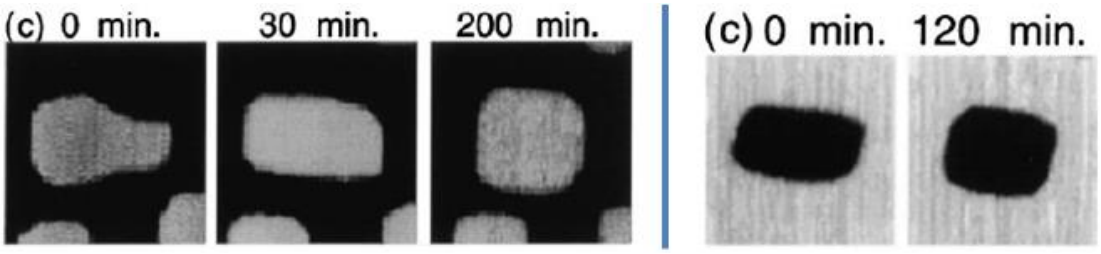

Figure 42. Left: Ag NC on Ag(100) (35 x 35 nm^2 images). Right: nanopit on Ag(100) (45 x 45 nm^2 images). Evolution at 295 K. Reprinted with permission from Ref. 114. Copyright 1998 American Physical Society.

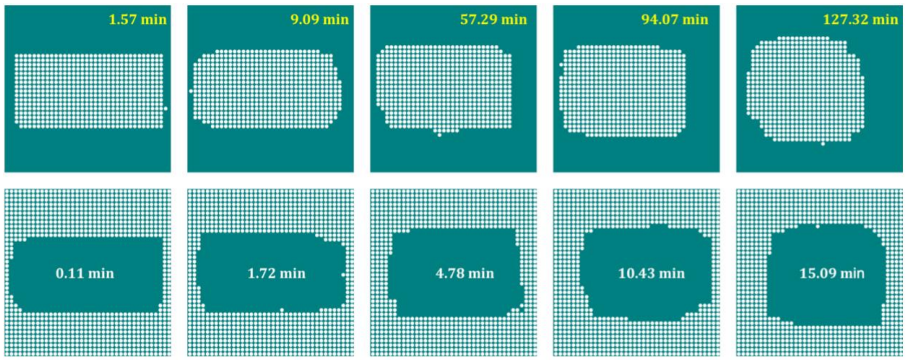

Figure 43. Reshaping of 34x17 atom/vacancy NCs: ab-initio modeling for Ag(100). Reprinted with permission from Ref. 27. Copyright 2016 American Chemical Society.

In Figure 44(a), we show experimental STM data for the reshaping of a smaller rectangular Ag nanocluster on Ag(100) formed by side-to-side coalescence of similar-sized square adatom NCs. In this case, the shorter relaxation time for smaller NC sizes facilitates KMC simulation with ab-initio kinetics (as discussed in Sec.3.5.1) to compare with experimental observations. The results considering just evolution of the central rectangular NC, shown in Figure 44(b), are reasonably consistent with experimental observations. The lower right frame shows significant variations between different simulation trials particularly in the later stages of evolution.

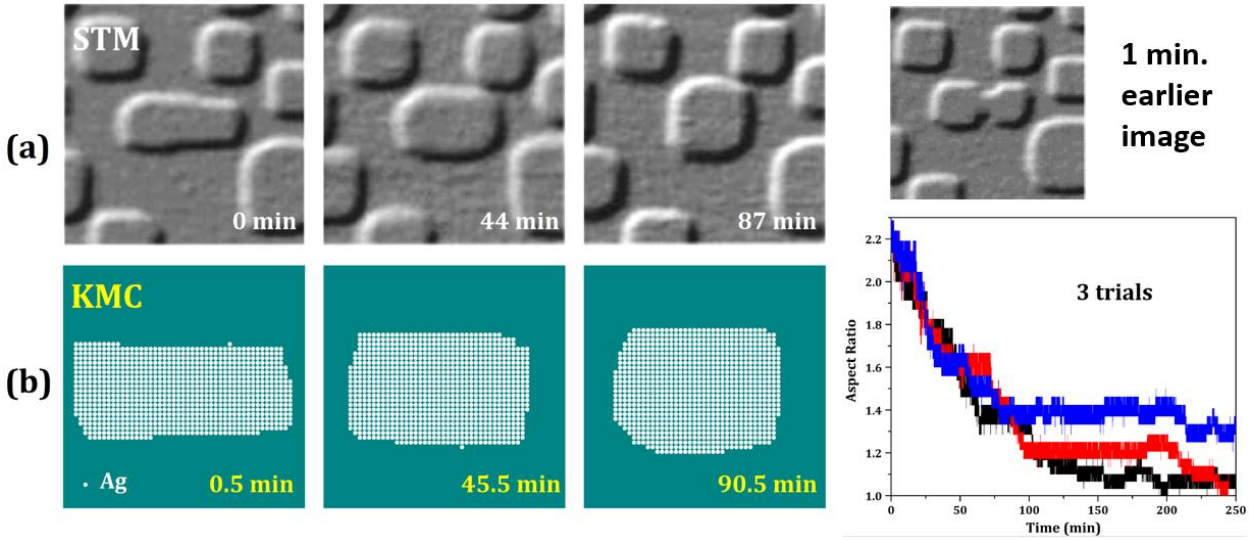

Figure 44. Reshaping of a rectangular Ag NC on Ag(100). (a) Experiment (28 x 28 nm^2 images)[14] . Initial size: 14 nm x 5.4 nm; final size: 8.7 nm x 8.7 nm. (b) Simulation with ab-initio kinetics[27] for initial NC matching experiment.

For a more fundamental understanding and analysis of reshaping of convex NCs, it is instructive to utilize the simpler tailored model[153] of Sec.3.3.2 where atoms of a square lattice of adsorption site interact with NN interactions ϕ.[153] Periphery diffusion includes NN hops with barrier E_e and rate h_e for isolated edge atoms on close-packed step edges, and 2NN hops to describe corner or kink rounding of isolated edge atoms with generally higher barrier of $E_e + \delta$. Barriers for other processes such as escape from kinks to step edges are controlled by detailed-balance as described in Sec.3.3.2. In Figure 45 (left), we compare results of atomistic simulations with continuum theory for the evolution of a rectangular NC in this model with $\delta = 0$. [153] Clearly, there is a large discrepancy between predictions for evolution as expected from the discussion of nucleation-mediated step evolution above for metal(111) surfaces. Figure 45 (right) shows size scaling with $\alpha^* = 2.7$ deviating from continuum model predictions with $\alpha^* = 4$ for the case $\delta = 0$. This behavior is reasonably consistent with the analysis in Sec.5.1 for metal(111) systems. Presumably, simulations with smaller NCs or lower T should produce behavior closer to $\alpha^* = 2$. In fact, introduction of a significant extra corner rounding barrier $\delta > 0$ into the model results in further modification to this size scaling

with an even lower α^* relative to our results for $\delta = 0$ (and again simulations for smaller NCs or lower T are expected to produce even lower α^* likely below 2).

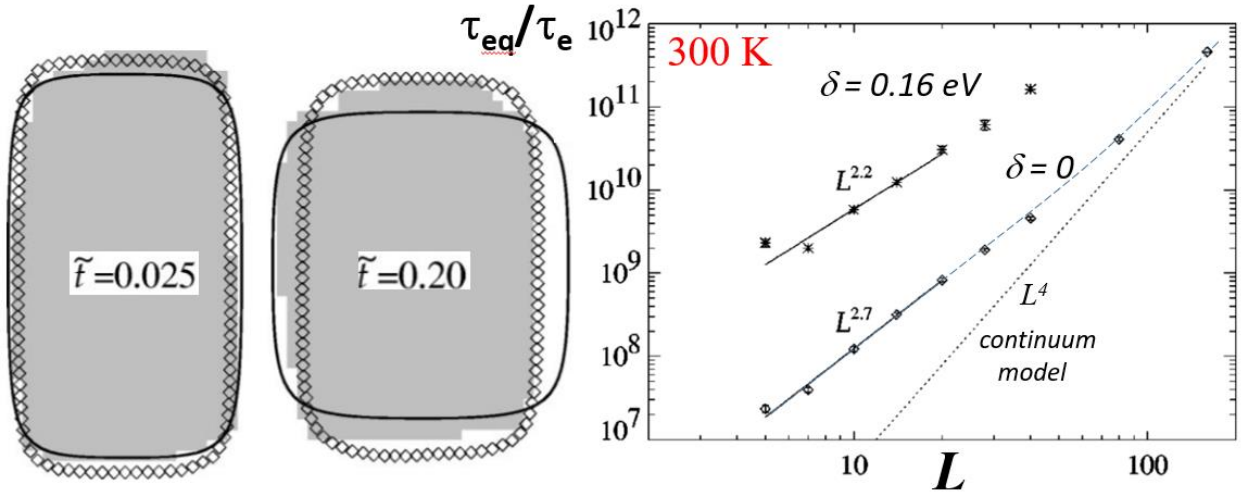

Figure 45. Left: comparison of atomistic and continuum modeling with ϕ = 0.235 eV, δ = 0, 300 K. Right: anomalous scaling in atomistic model for δ = 0 and δ = 0.16 eV. Reprinted with permission from Ref. 153. Copyright 2002 American Physical Society.

To elucidate this anomalous size-scaling, further assessment of behavior in the atomistic model exploiting random walk concepts, is instructive.[153,235] Consider evolution from a perfect rectangular NC which is effectively facetted since $L << L_c$. Initially, a pair of atoms must be transferred from the short edge to the long edge nucleating a new layer on the longer step edge. However, there is no energetic advantage to transferring a third, fourth, etc. atom from the now incomplete short edge to continue growth of the new layer on the long edge. From this perspective, the thermodynamic driving force for reshaping to a near-square shape is not immediately apparent. However, the resolution to this dilemma is that when the last atom on the incomplete short edge is transferred to grow the new layer on the long edge, the energy of the system is in fact lowered.[235] In the more detailed analysis presented below, it is instructive to first determine the characteristic time, τ_{layer}, to remove a complete layer from the short edge. Then, the characteristic time for the overall shape equilibration process will scale like $\tau_{eq} \sim L\ \tau_{layer}$.

It is instructive to start by considering the case of large additional corner rounding barrier $\delta > 0$, corresponding to the regime with the associated characteristic corner rounding length, $L_\delta = \exp[\delta/(k_BT)] - 1 \approx a \exp[\delta/(k_BT)] >> L$ (the characteristic linear NC size), and where lengths are in units of lattice constant. Then, we will write

$\tau_{layer} \sim \tau_{nuc}/ P_{trans\_all}$ for "nucleation time" τ_{nuc} and "transfer probability" P_{trans_all}. (75)

Specifically, τ_{nuc} is the characteristic time to nucleate a dimer on the long edge. P_{trans_all} is the probability that once that dimer is nucleated, the entire rest of the atoms on the incomplete short edge are transferred to the long edge, rather than all atoms returning

to the short edge to recomplete it. Next, we write $\tau_{nuc} \sim n_{eq}(tot)\, h_c$ where $h_c = \exp[-\delta/(k_B T)]\, h_k \approx h_k/L_\delta$ is the rate for the corner atom on the short edge to round the corner and reach the long edge. Also, $n_{eq}(tot) \sim L \exp[-\phi/(k_B T)]$ is the total equilibrium population of isolated atoms on the long edge. The rationale here is to consider that the first corner atoms has reached the long edge (corresponding to the $n_{eq}(tot)$ factor), and that when the second atom reaches that edge as characterized by rate h_c, it will almost certainly meet the first atom and nucleate a dimer since there is a larger extra barrier for either atom to return to a short edge. The last non-trivial issue is to determine the transfer probability, P_{trans_all}. Once the dimer is formed on a long edge, the system undergoes a random walk in configuration space labeled by the number n of atoms transferred to the long edge, transferring atoms backwards and forth between the short and long edges. Imagine staring in state n = 2 where completely transferring all atoms to the long edge (n ~ L) or back to the short edge (n = 0) can be regarded as adsorbing or trapping states in this 1D random walk problem. Then standard analysis shows that $P_{trans\_all} \sim 1/L$. Combining the above results yields[153]

$$\tau_{layer} \sim L_\delta \exp[-\phi/(k_B T)]\, h_k \text{ and } \tau_{eq} \sim \exp[-\phi/(k_B T)]\, h_k\, L_\delta\, L, \text{ for } L_\delta << L << L_c, \qquad (76)$$

corresponding to an anomalously low size scaling exponent $\alpha^* = 1$.

Next we consider the case of small (or zero) kink rounding barriers where $L << L_\delta$ and L_c. A somewhat simplistic analysis would argue that there must be a continuous crossover from the behavior in this regime to that describe above as L increases through L_δ and behavior becomes edge-diffusion limited rather than corner-rounding-limited. From this perspective, one expects that[153,176,235]

$$\tau_{layer} \sim L \exp[-\phi/(k_B T)]\, h_k \text{ and } \tau_{eq} \sim \exp[-\phi/(k_B T)]\, h_k\, L^2 \text{ for } L << L_\delta \text{ and } L_c. \qquad (77)$$

Consequently, in this regime $\alpha^* = 2$ consistent with results from the analysis for metal(111) surfaces. A more detailed and rigorous analysis of behavior in both regimes follows from a more comprehensive analysis of evolution in configuration space based on the appropriate master equations. Finally, we remark that for the case where $L >> L_c$, continuum theory applies to give $\alpha^* = 4$.[153]

5.3. Coalescence of pairs of 2D epitaxial NCs: fcc(111) homoepitaxial systems

For coalescence or sintering of side-by-side pairs of hexagonal NC in these fcc(111) systems, the first stage is not limited of nucleation of new outer layers, only the last stage once the coalesced pair has evolved to a convex shape as described in Sec.5.1.1. Experimental data and analysis is somewhat limited (in contrast to the fcc(100) homoepitaxial systems described in Sec.5.4) and the best examples consider sintering of nanopits (rather than adatom islands) noting again that SR rather than OR dominates coarsening in these systems, at least for Ag and Cu.[13,1]. In Figure 46, we show STM images for the sintering of nanopits on an Ag(111) surface at 300 K. [241] For this system, analysis of experimental data for the initial stage of neck growth, as illustrated in Figure 47, is available.[242] Most data is for unequal pit sizes and a characteristic time, τ_{eq} for the initial neck growth is defined to correspond to the time

when the neck width equals the "diameter", d_1, of the smaller of the two nanopits. Analysis of the scaling of $\tau_{eq} \sim (d_1)^{\alpha^*}$ indicates an exponent of $\alpha^* = 2.6$ [241] significantly below the continuum theory prediction of $\alpha^* = 4$. This exponent is somewhat above the exponent $\alpha^* = 2.84$ reported in Sec.5.1.1 from simulations of nucleation-mediated reshaping of Ag nanoislands on Ag(111). In Sec.5.2.2, we shall develop a detailed formulation of anomalous exponents for sintering of nanoparticles.

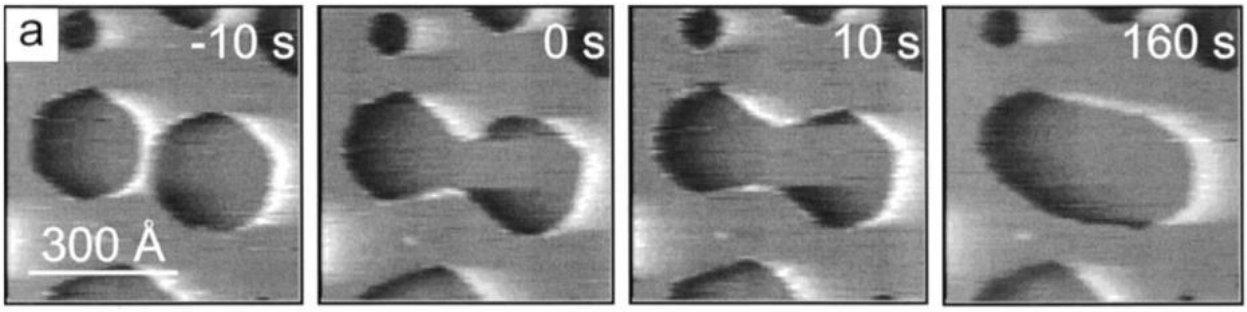

Figure 46. Sintering of nanopits on Ag(100) at 300 K. Reprinted with permission from Ref. 241. Copyright 1998 Elsevier.

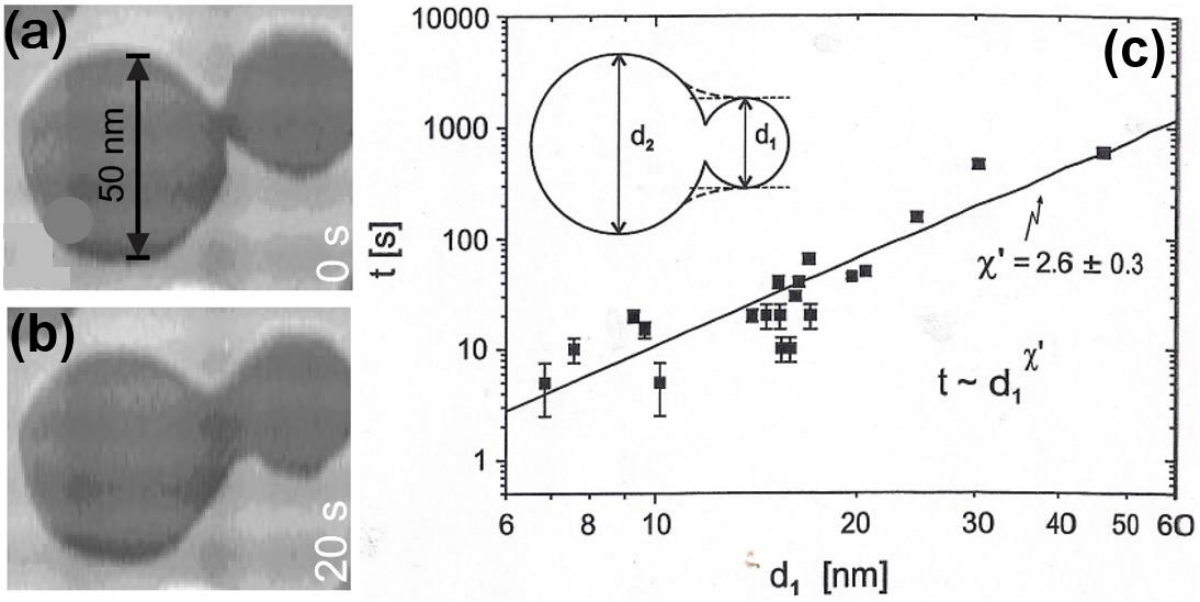

Figure 47. Analysis of the characteristic time for neck formation for sintering of nanopits on Ag(111). Reprinted with permission from Ref. 13. Copyright 2005 Wiley-VCH.

Next, we remark that analogous behavior has been observed for sintering of nanopits on Cu(111) surfaces.[243] See Figure 48. In this case, the diameter of the smaller of the nanopits is roughly $d_1 \approx 8$ nm, and the characteristic neck growth time defined as above is roughly τ_{eq} ~12-14 s. This is somewhat below the corresponding value for nanopits on Ag(111) from Figure 47(c) even though the temperature in the Cu experiments is somewhat higher. This is reasonable based upon the higher interaction and edge diffusion barriers expected for Cu relative to Ag.

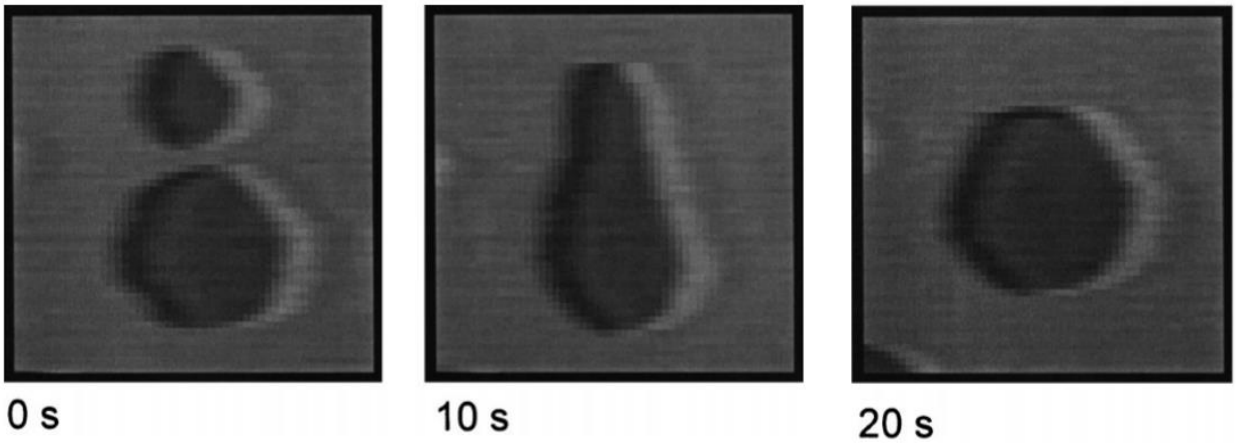

Figure 48. Sintering of nanopits on Cu(111) at 328 K. Image size: 30x30 nm^2. Reprinted with permission from Ref. 243. Copyright 2000 Elsevier.

With regard to experimental studies, we note that there does not appear to be published data for sintering of Ag or Cu adatom islands in these fcc(111) homoepitaxial systems (partly since OR rather than SR dominates coarsening for these systems). However, data is available as shown in Figure 49 illustrating at least the latter part of the sintering process for Au islands on Au(111) where again we note the significance of the Au(111) surface for various applications.

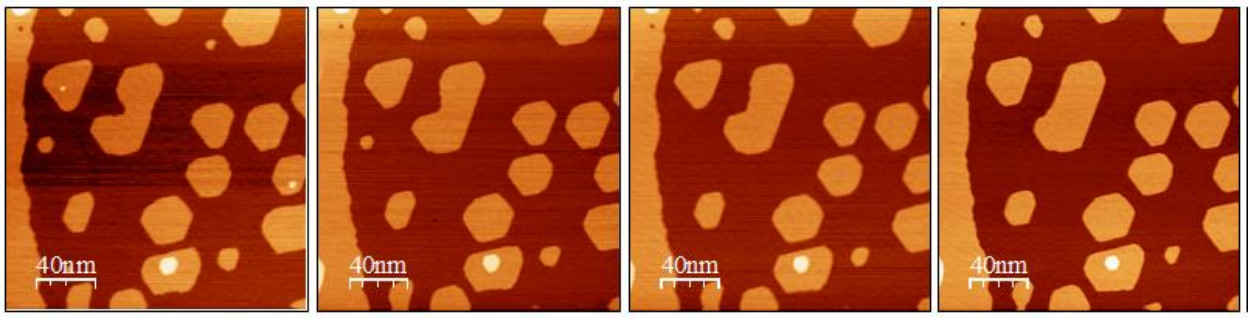

Figure 49. Partial coalescence of Au NCs on Au(111) at 300 K. 200 min between images.

Finally, it is instructive to show the predictions of continuum theory for sintering of equal sized hexagonal NCs for a model based on Ag(111) surface where NCs have hexagonal equilibrated shapes. The theory applies equally for adatom islands or NCs and nanopits. The two natural scenarios are side-to-side and corner-to-corner “collision” as shown in Figure 50 where a sequence of sintering shapes for subsequent times is illustrated. The former case applies to the nanopit examples shown above for both Ag(111) and Cu(111).

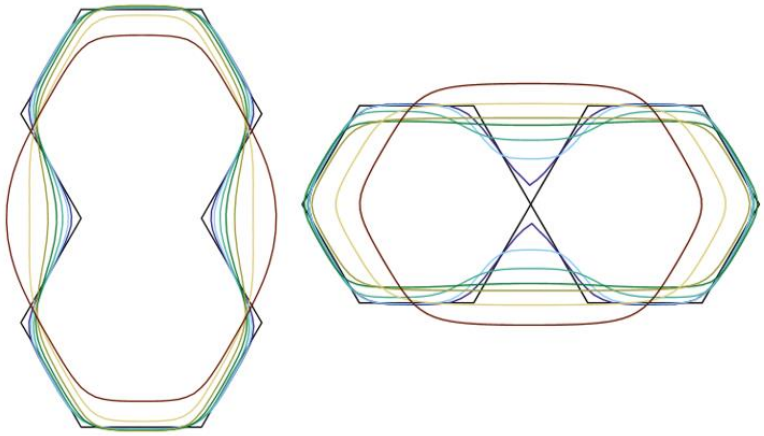

Figure 50. Continuum modeling of sintering on an fcc(111) surface with equal step energies for A- and B-type steps for $\varepsilon_k/(k_BT) = 4.7$: edge-to-edge and corner-to-corner cases.

5.4. Coalescence of pairs of 2D epitaxial NCs: fcc(100) homoepitaxial systems

In this case, most examples of sintering apply for adatom islands which "collide" corner-to-corner resulting in an initial "dumbbell" type shape. Most comprehensive analysis is available for Ag/Ag(100) which is the only system where there exists systematic data for a range of NC sizes.[27] Figure 51 shows two examples of STM data where the individual NCs in the pair have roughly equal sizes, ~5x5 nm^2 in one case and ~12x12 nm^2 in the other. The dramatically slower time-scale for sintering for larger NC sizes is evident. In addition, Figure 51 shows the result of our modeling with ab-initio kinetics for periphery diffusion as described in Sec.3.5.1 where we select the initial NC sizes and configuration to match experiment. It is clear that the model recovers not just the time scale for a single NC size, but also the size scaling. Assigning L as the side-length of the individual NCs before sintering, and considering scaling of the relaxation time $\tau_{eq} \sim L^{\alpha^*}$, one roughly estimates $\alpha^* \sim 2.6$ just for the two different sizes shown in Figure 51. Analyzing a more extensive data set for Ag/Ag(100) for a range of NC sizes suggests that $\alpha^* \approx 3$. [114,178] Below, we develop a theoretical formulation for anomalous size scaling in this sintering process, where this is most conveniently presented for a simplified tailored model.

Next, we present an example of analogous corner-to-corner sintering of nanoislands for Cu/Cu(100) at 300 K.[244] See Figure 52. Accounting for the size of the islands, one finds that the sintering time of 15 min is substantially faster than the time for the same sized Ag/Ag(100) islands. Given that interaction energies and edge diffusion barriers are higher on the (100) surface of Cu relative to Ag,[27] this trend would not be predicted by atomistic modeling (wherein Cu/Cu(100) sintering is substantially slower). The reason for this discrepancy is not entirely clear. It is possible that sintering for Cu/Cu(100) is accelerated by the presence of trace impurities, e.g., S from the bulk. However, preliminary DFT analysis has failed to date to find a pathway whereby the presence of S at step edges enhanced edge diffusion or corner rounding.

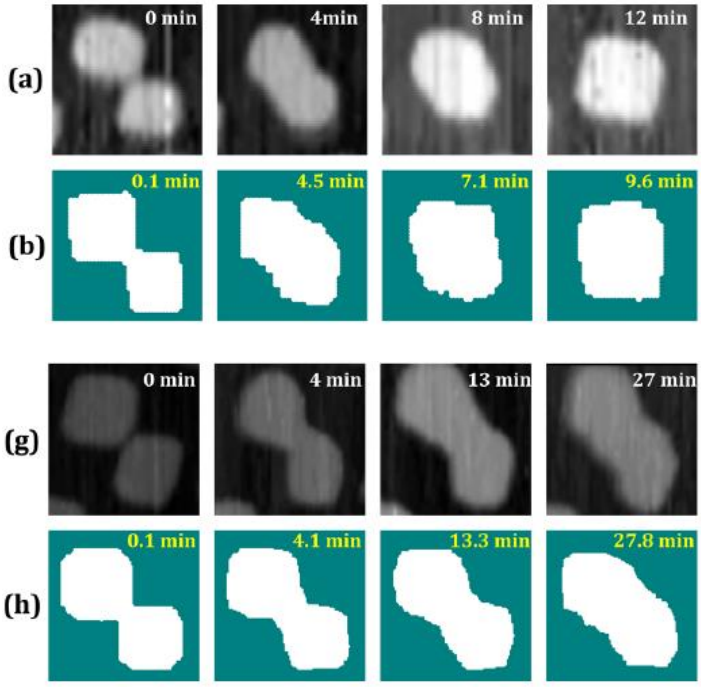

Figure 51. Corner-to-corner sintering of Ag NCs on Ag(100) at 295 K. Top: 5.2x5.2 + 4.5x4.5 nm^2 NCs. Bottom: 13.0x13.0 + 11.5x11.5 nm^2 NCs. Reprinted with permission from Ref. 27. Copyright 2016 American Chemical Society.

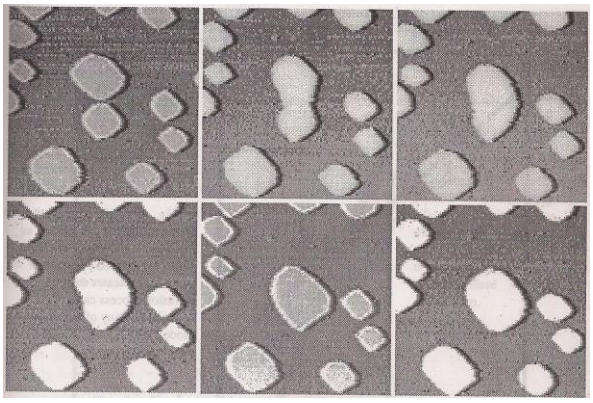

Figure 52. Corner-to-corner sintering of 14.3 x 11.7+ 9.1 x 9.1 nm^2 Cu NCs on Cu(100) at 295 K with 3.5 min. between successive images. Image size: 50 x 50 nm^2 with NCs. Sintering is complete in ~15 min. [244] The caption in Ref. 244 incorrectly states the combined NC size is 400 atoms. Reprinted with permission from Ref. 244. Copyright 1998 World Scientific.

As for fcc(111) surfaces, it is of interest to consider sintering of nanopits as well as nanoislands. However, for fcc(100) surface, examples for nanopits are limited, in part since coarsening of nanopits is dominated by OR in contrast to SR for nanoislands. One example for corner-to-corner sintering of nanopits on Ag(100) is shown in Figure 53.[114] This very limited data suggests that sintering of nanopits is no slower than nanoislands of the same size, and is possibly faster. To further assess this comparison, benchmark simulations can be performed utilized an atomistic model with ab-initio kinetics staring

with the same sized nanopits and nanoislands in a corner-to-corner configuration.[27] Results shown in Figure 54 are consistent with somewhat faster nanopit sintering. We emphasize that these results follow from a refinement of the ab-initio modeling to include additional unconventional interactions which ensure that periphery diffusion processes on concave step edges are described accurately.[27] See Sec.7.1.3.

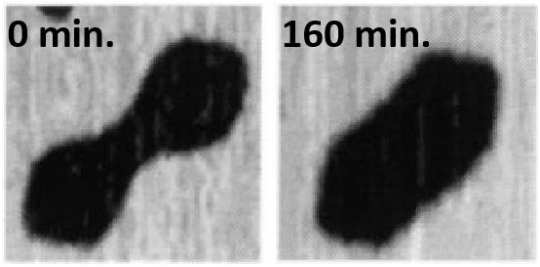

Figure 53. Corner-to-corner sintering of nanopits on Ag(100) at 295 K. Image size: 54x54 nm^2. Reprinted with permission from Ref. 114. Copyright 1998 American Physical Society.

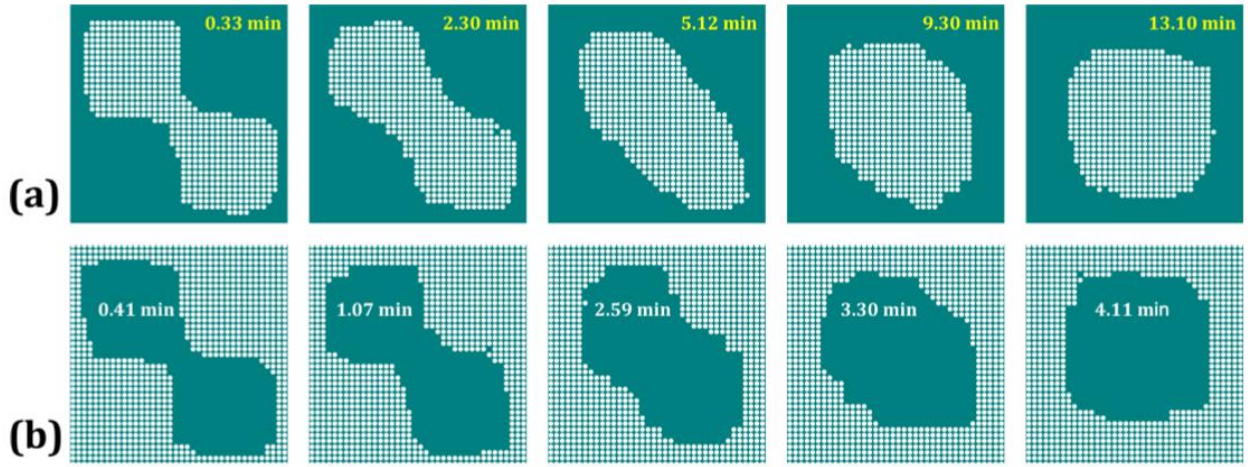

Figure 54. Benchmark comparison of corner-to-corner sintering for islands and pits for the same (smaller) size on Ag(100) at 295 K. Reprinted with permission from Ref. 27. Copyright 2016 American Chemical Society.

Finally, we present a fundamental analysis for corner-to-corner sintering on fcc(100) surfaces utilizing a tailored atomistic model developed in Sec.3.5.1 and applied in Sec.5.1.2 for reshaping of convex NCs. In addition, we compare predictions of atomistic modeling and continuum theory. First, it should be noted that there are two stages for the sintering process.[153] In the first initial stage of neck growth, atoms are moved from the outer corners of the NC pair and moved to the neck region, but outer edges of the NC pair are not completely removed. See Figure 55. For the configurations shown, it is clear that the number of broken bonds ate the NC periphery equals the total perimeter length on the NC pair which in turn equals the perimeter length of the smallest inscribing rectangle. Thus, during this first stage since outer edges are not completely removes, the total energy of the NC pair is constant. Thus, evolution is entropy (not

energy) driven.[153] Simulation results indicate that the size scaling of neck growth in this initial entropic regime is consistent with continuum theory, i.e., $\alpha^* = 4$. [153]

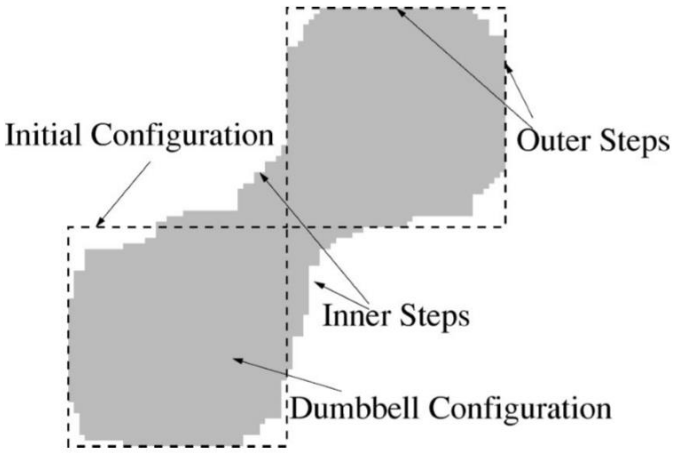

Figure 55. Initial "entropic" stage of sintering and neck growth. Reprinted with permission from Ref. 153. Copyright 2002 American Physical Society.

However, more relevant for comparison with experiment is analysis of the subsequent energy-driven regime where outer edges are completely removed and the energy of the systems decreases.[153] Analogous to our analysis in Sec.5.1.2 for reshaping of rectangular NCs, we will introduce characteristic time, τ_{layer}, to remove a complete layer from the outer edge, and then determine the characteristic time for the overall shape equilibration process from $\tau_{eq} \sim L\ \tau_{layer}$. Removal of outer step edges involves transfer of atoms from a kink site along a straight outer step edge around a corner and along another straight step edge to a kink closer to the neck region. We let τ_0 denote the characteristic time for transfer of a single such atom, which is a key component controlling τ_{layer}. Since the transfer of atoms between the two kinks corresponds to a random walk in the configuration space of the number of transferred atoms, the characteristic time to transfer ~ L atoms completely removing an outer edge must scale like $\tau_{layer} \sim L^2\ \tau_0$ which follows from Einstein's relation for random walks.

If $h_0 = 1/\tau_0$ denotes the characteristic rate to transfer a single atom, then we write $h_0 = P_{trans\_one}\, h_k$, where h_k gives the rate of the initial escape from the kink to the step edge, and P_{trans_one} gives the probability that once the atom escapes the kink site it is successfully transferred around the corner to the other kink closer to the neck region (rather than returning to the original kink). This process corresponds to a 1D random walk between traps separated by ~L sites where the rate for one of the hops between the traps is reduced by a factor of $\exp[-\delta/(k_B T)] \sim 1/L_\delta$ relative to the other hops. This step with the reduced hop rate corresponds to rounding the corner between the kinks. Analysis of this random walk problem reveals that $P_{trans\_one} \sim 1/(L+L_\delta)$. Consequently, one has that $\tau_0 \sim (L + L_\delta)\tau_k$ where $\tau_k = 1/h_k$ is the typical time to escape a kink. Thus to summarize, one has[153,178]

$\tau_{eq} \sim L\ \tau_{layer}$ where $\tau_{layer} \sim L^2\ \tau_0$ and $\tau_0 \sim (L + L_\delta)\tau_k$, so $\tau_{eq} \sim L^3(L+L_\delta)\tau_k$. (78)

This result explains the crossover from size scaling with the continuum $\alpha^* = 4$ for small kink rounding barrier, to $\alpha^* = 3$ with large barrier.

As a final complementary analysis, we compare the predictions of our tailored atomistic modeling with continuum theory predictions incorporating appropriate anisotropic step energies. For the case with $\delta = 0$, there is essentially perfect agreement even on the nanoscale. See Figure 56.This is consistent with the above analysis revealing classic scaling with $\alpha^* = 2$ in this case. However, introducing finite $\delta > 0$, such analysis reveals strong deviations between atomistic and continuum models, as also expected from the above analysis.

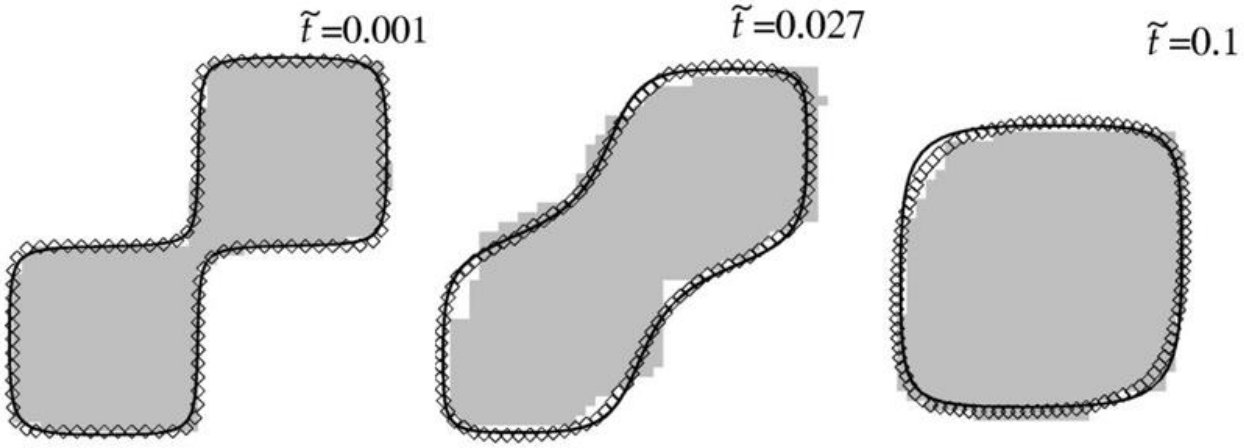

Figure 56: Comparison of atomistic and continuum modeling of corner-to-corner sintering of Ag NCs on Ag(100) at 295 K for $\delta = 0$. Reprinted with permission from Ref. 153. Copyright 2002 American Physical Society.

5.5. Analysis of evolution for "extreme shapes" of 2D epitaxial NCs

5.5.1 Irregular NCs. Behavior observed for the evolution of irregular shaped NCs provides a clear signature that evolution is PD-mediated (and thus governed by an evolution equation which is fourth-order in space) rather than curvature driven (where Grayson's theorem applies to preclude pinch-off in 2D).[177] First, we consider the evolution of large "worm-like" vacancy nanoclusters on Cu(100), where we note that analogous behavior has been observed for Ag(100).[177] These morphologies are created by deposition of near-monolayer coverages of Cu on Cu(100), or Ag on Ag(100). Figure 57 shows STM data for the evolution of a vacancy nanoworm on Cu(100) which is compared against the predictions of isotropic continuum theory. The most dramatic feature is pinch-off in experiment after 2800 s, which is qualitatively described by the isotropic model exhibiting pinch-off at 3500 s. Likely, this discrepancy is partly due to fluctuation effects not included in continuum modeling (see below). Naturally, nanoworm shape in the continuum model is not accurately described, particularly near the ends of the worm where the shape is more rounded than in experiment. However, these deficiencies are corrected in modeling which incorporates anisotropy in step energy.[177] See Figure 58.

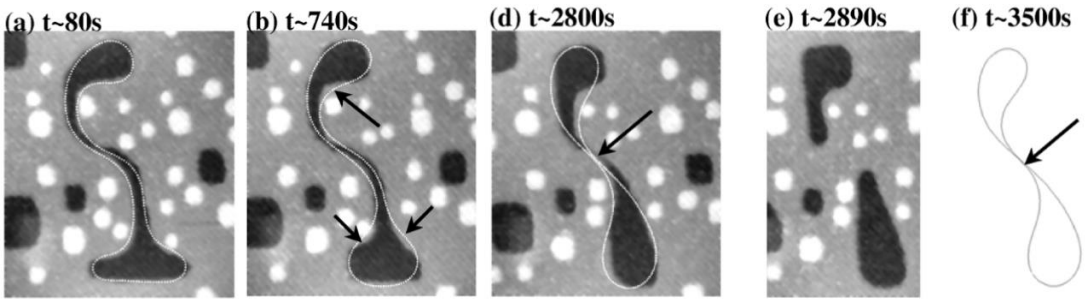

Figure 57. Pinch-off of a large worm-like nanopit on Cu(100) at 295K. Comparison between experiment and isotropic continuum theory. Image height: 75 nm. Reprinted with permission from Ref. 177. Copyright 2001 American Physical Society.

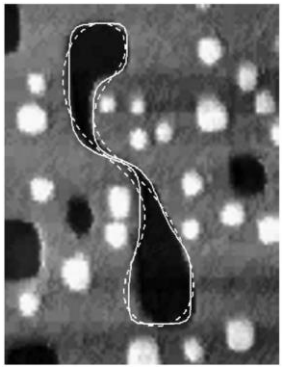

Figure 58. Pinch-off of a large worm-like nanopit on Cu(100) at 295K. Comparison of anisotropic with isotropic continuum theory. Reprinted with permission from Ref. 177. Copyright 2001 American Physical Society.

A more extreme realization of pinch-off occurs during the post-synthesis evolution of dendritic or fractal islands. Figure 59 provides an example of such evolution for Ag/Ag(111) NCs formed by low-temperature deposition. In the image on the right, the small roughly circular NC droplets are formed by pinch-off of the arms of the dendrites.[14] One generic modeling study utilizing continuum theory with isotropic step energy considered the evolution of fractal clusters via edge diffusion revealing multiple pinch-off events.[183] In Sec.6.5, it is shown that analogous behavior occurs for supported fractal NCs where the arms formed as aggregates of individual small compact 3D NCs.

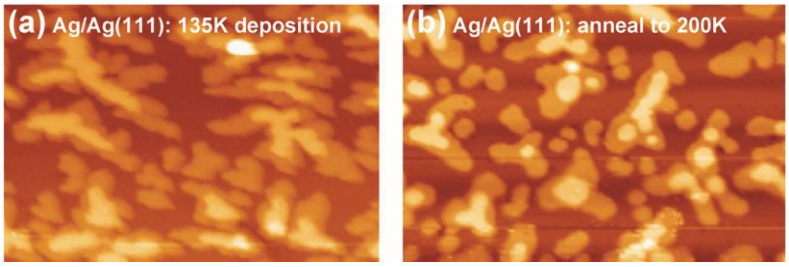

Figure 59. Annealing of Ag/Ag(111) dendritic islands leading to pinch-off. Reprinted with permission from Ref. 14. Copyright 2009 American Chemical Society.

5.5.2. Elongated nanorods. Lastly, pinch-off is analyzed in more controlled but still "extreme" NC geometries, specifically highly elongated 2D nanorods. The motivation for this analysis is partly for comparison with analogous 3D behavior noting that pinch-off has been recently observed and modeled for 3D elongated nanorods. See Sec.6.5. We caution, however, that there are fundamental differences between the 2D and 3D cases.

For analysis of the evolution of elongated 2D "nanorod" NCs based on deterministic continuum theory, the basic phenomenon is that these relax back to equilibrium shapes if their aspect ratio, A, is not too large, but pinch-off above a critical aspect ratio, A_c. Thus, a central issue is the determination of A_c. Naturally, the answer will depend on anisotropy in the step edge stiffness (and thus on orientation of the nanorod), and potentially on the prescription of step edge kinetics. Benchmark studies including isotropic step energy and stiffness and isotropic mobility are illustrated in Figure 60. The top frame shows that pinch-off does not occur even for large aspect ratio of $A \approx 20$. In fact, one finds that $A_c \approx 65$ is significantly larger (see bottom frame). These results are independent of temperature as evolution is purely geometric. For the extreme case of evolution of an effectively semi-infinite nanorod, see Ref. 183.

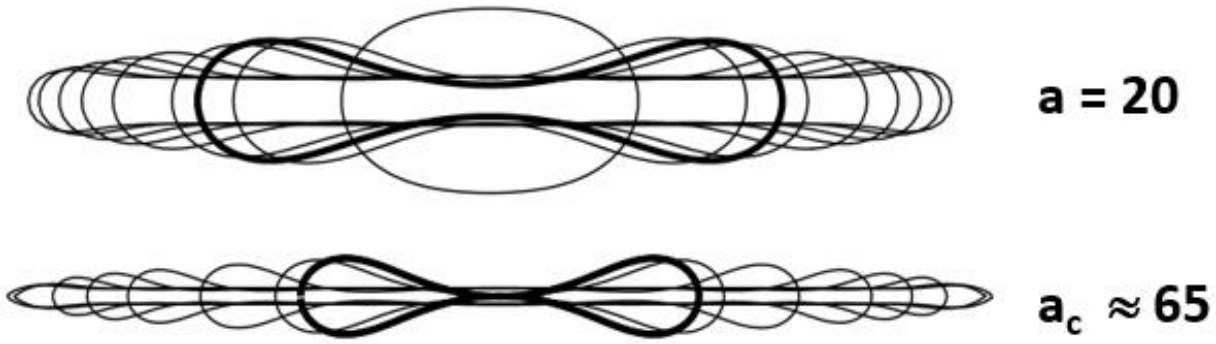

Figure 60. Reshaping of rectangles in isotropic model: Top: no pinch-off for $A = 20$. Bottom: Pinch-off at the critical $A_c \approx 65$. The thick line is at pinch off for $A_c \approx 65$.

Next incorporating step edge anisotropy corresponding to an Ising type model with NN interactions on a square lattice describing a fcc(100) surfaces, we consider behavior for rectangular NC oriented with sides corresponding to both close-packed step edges and open kinked step edges (45° rotated from first case). Pinch-off propensity depends strongly on step edge orientation being much easier for kinked step edges ($A_c = 35$) than close-packed step edges ($A_c = 203$) at 300 K. A comparison of behavior for $A = 35$ is shown in Figure 61. More comprehensive analysis of dependence of A_c on $\phi/(k_BT)$ also considering models for both fcc(100) and fcc(111) surfaces with NN interactions. See Table 5. For open kinked step orientations, where pinch-off is easier, A_c increases monotonically with decreasing $\phi/(k_BT)$ to reach ~65 for $\phi/(k_BT) = 0$ corresponding to the isotropic case. For close-packed step orientations, where pinch-off is difficult, A_c decreases monotonically with decreasing $\phi/(k_BT)$ to reach ~65 for $\phi/(k_BT) = 0$.

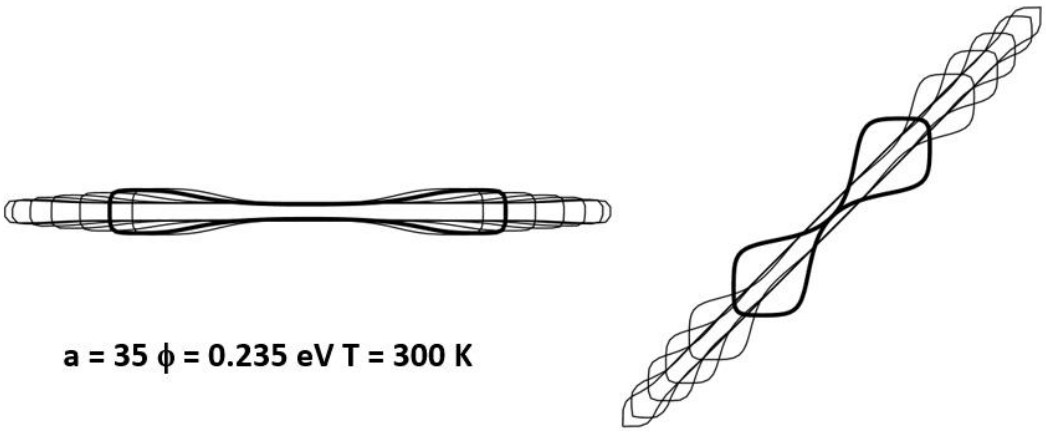

Figure 61. Anisotropic continuum model nanorod evolution for a fcc(100) surface symmetry. $\phi/kT = 9.09$ [so $\varepsilon_k/kT = 4.545$]

Table 5. Critical pinch-off aspect ratio from continuum modeling for nanorods.

$\varepsilon_k/(k_BT)$	{100} facet close-packed	{100} facet kinked step	{111} facet close-packed	{111} facet kinked step
0 (isotropic)	65	65	65	65
2.56	97	48	86	56
2.88	108	45	95	51
4.70	203	35	168	45

For these deterministic continuum models, it is also useful to extract additional results on evolution which will important for analysis of stochastic models below. Specifically, we consider continuum modeling for fcc(100) surfaces in the case of diagonally oriented nanorods are oriented (i.e., nanorods oriented at 45° from close packed direction) with maximally kinked open step edges. Again, for this orientation, pinch-off is most facile. Our focus here is on behavior for $A < A_c$ where pinch-off does not occur, but where the middle of the nanorod initially becomes narrower before finally broadening during evolution to the equilibrium shape. For $\phi/(k_BT) = 5.12$ [so $\varepsilon_k/(k_BT) = 2.56$] (e.g., for $\phi = 0.20$ eV and T = 450 K), we determine the ratio of the initial width, w_{init}, to the minimum width, w_{min}, for $A < A_c$. We find that $w_{min}/w_{init} = 0.942, 0.810, 0.449, 0.141, 0.050, 0$ for $A = 5, 10, 25, 40, 45, 48$, respectively. The significance of these results is that in the context of stochastic modeling, the state corresponding to the minimum width is where the NC is most vulnerable to fluctuation-induced pinch-off.

Finally, before describing stochastic modeling, it is instructive to compare results reported above from conventional continuum modeling of shape evolution for nanorods with that from the “simplified” modeling described in Sec.4.3.2 where the step edge of NCs is treated as faceted with a discrete number of allowed orientations.[196] Figure 62(a) shows evolution allowing a large number (16) of facet orientations which mimics closely evolution with isotropic surface energy shown in Figure 60. Figure 62(b) shows evolution allowing four facet orientations which mimics evolution of nanorods on a fcc(100) surface aligned with close-packed step directions as shown in Figure 61 (left).

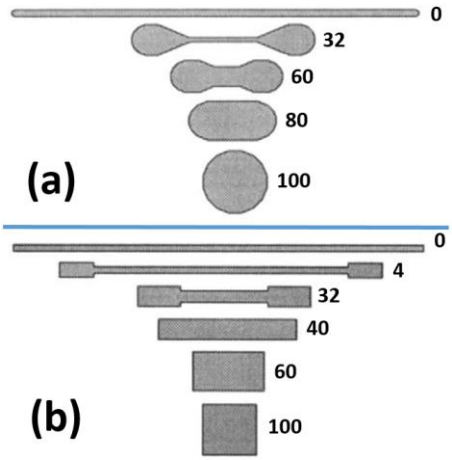

Figure 62. Periphery-diffusion mediated evolution in a model for purely facetted 2D NCs. (a) 16 facet orientations; (b) 4 facet orientations. Reprinted with permission from Ref. 196. Copyright 1995 Elsevier.

Next, we consider stochastic atomistic modeling for pinch-off of elongated nanorods. We consider rectangular NCs on an fcc(100) surface with a diagonal orientation and maximally kinked step edges. Figure 63 shows a sequence of configurations revealing pinch-off for A = 21 (with ϕ= 0.20 eV and T = 450 K where continuum theory predicts that A_c = 48). From more extensive KMC simulation analysis, it is natural extract the probability of pinch-off, $P(A)$, as a function of aspect ratio, A (where we keep the width of the rectangular NC fixed). Repeating simulations for different choices of initial width, w_{init}, generates a family of curves shown below in Figure 64. As $w_{int} \to \infty$, behavior in the stochastic model should approach that of the deterministic continuum treatment where $P(A) = H(A - A_c)$, where $H()$ is the Heaviside step function and again A_c = 48 for our parameter choice. The simulation results are not inconsistent with this limiting behavior (where we emphasize that statistics are quite limited for larger nanorod widths). With more extensive statistics, one expects that the $P(A)$ versus A curves would be smooth and progressively steepen as they approach the step function for $w_{int} \to \infty$.

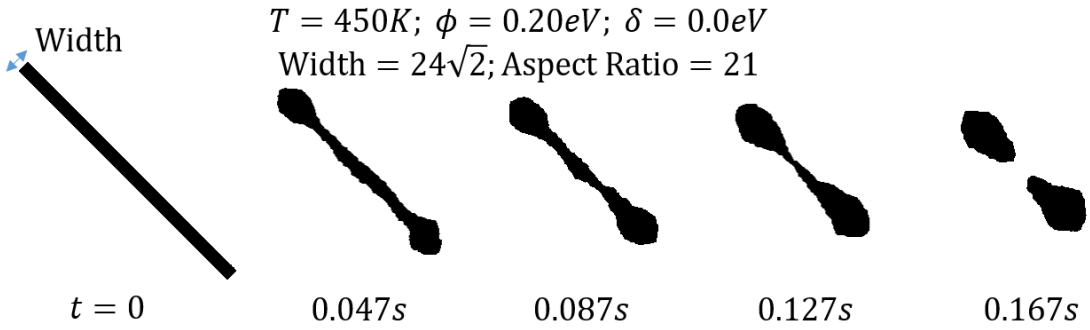

Figure 63. Stochastic modeling of fluctuation mediated pinch-off of an elongated 2D epitaxial NCs on a {100} surface with kinked step edges (i.e., a diagonal orientation).

Further elucidation of the above observations follows from development of a heuristic theory for stochastic pinch-off. One might naturally apply the criterion that

pinch-off occurs in the stochastic model (with probability ~1/2) when w_{min} has decreased to $2w_{fluct}$, where w_{fluct} is the amplitude of fluctuations at a single step edge. The underlying picture is that the presence of fluctuations means that steps on the opposite sides of the nanorod are likely to touch when $w_{min} \approx 2w_{fluct}$, and that such touching will lead effectively irreversibly to pinch-off. Using this criterion to interpret the above simulations results yields w_{fluct} = 4.25, 5.3, 6.25,… for $w_{init} = 8\sqrt{2}, 10\sqrt{2}, 13\sqrt{2},\ldots$ (in units of lattice constant), respectively. Extrapolating these results $w_{init} = 17\sqrt{2}$, $19\sqrt{2}$, and $24\sqrt{2}$, indicates that w_{fluct} = 7.25, 7.7, and 8.75, so that w_{min} = 14.5, 15.4, and 17.5, and thus w_{min}/w_{init} = 0.60, 0.57, and 0.52, respectively. Then, based on results reported above from continuum modeling, one would predict that $P(A) = ½$ for A = 19, 20, and 22.5, for $w_{init} = 17\sqrt{2}$, $19\sqrt{2}$, and $24\sqrt{2}$, respectively. These values are somewhat above those obtained from the simulation results reported in Figure 64, although the general trend is captured.

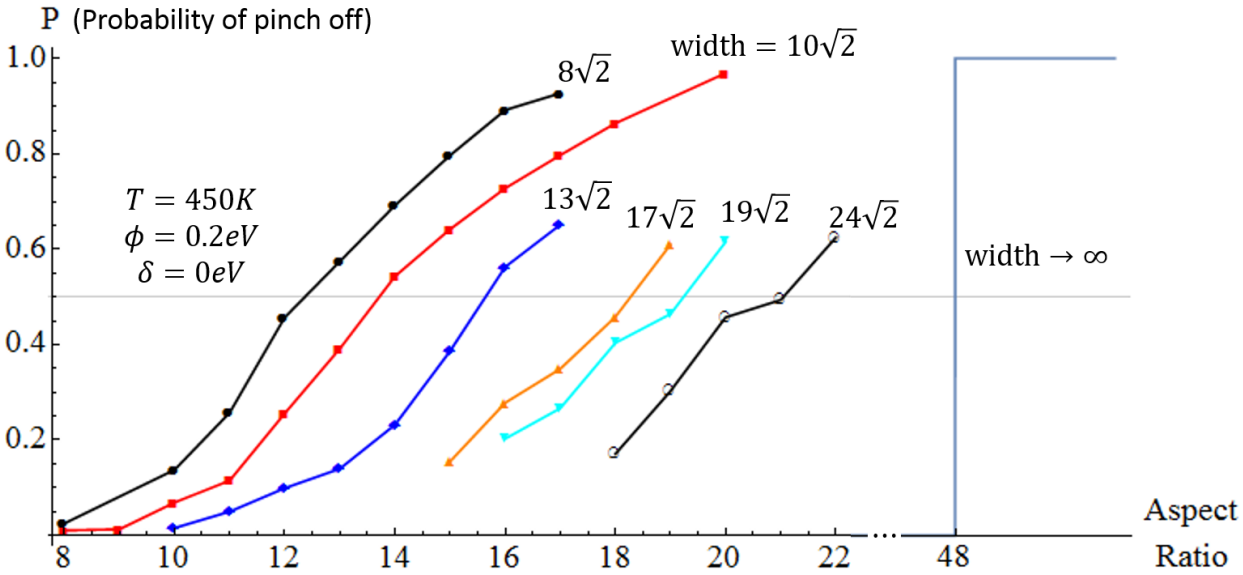

Figure 64. Pinch-off probability, *P(A),* as a function of aspect ratio for elongated 2D epitaxial NCs on a {100} facet. Limiting deterministic behavior follows from the appropriate anisotropic continuum model.

Finally, we emphasize again that there are fundamental differences between pinch-off phenomenon for 2D elongated NCs and the “analogous” pinch-off of nanorod in 3D (discussed in Sec.6.3). The key point is that for an infinitely long nanorod, the evolution of opposite sides is independent in 2D (unless wandering induced by fluctuations lead to collision of opposite sides). However, opposite sides are connected in 3D by surface diffusion.

6. SHAPE EVOLUTION OF SINGLE-COMPONENT 3D fcc NCs

6.1. Atomistic modeling for initial convex shapes of unsupported 3D NCs

Just as for shape relaxation of 2D NCs, one might anticipate that predictions of continuum theory for surface-diffusion mediated reshaping of 3D NCs break down on the nanoscale, particularly for size scaling. This seems particularly likely as 3D crystals are truly facetted below the roughening temperature, which is the regime of interest. Indeed, strong deviations from continuum predictions are observed although detailed behavior is quite different than in the 2D case. As with our analysis of 2D reshaping, we start by highlighting a key early theoretical study by Combe, Jensen, and Pimpinelli[121] for a generic lattice-gas (LG) model for fcc NCs including NN attractions of strength ϕ = 0.1 eV and surface atom hopping rates described by a standard IVA or bond-counting prescription (with activation barrier just determined by the initial coordination). Figure 65 shows results of KMC simulations for the evolution of an elongated nanorod of N atoms back towards the equilibrium octahedral Wulff shape. The scaling exponent, α, for the size-dependence of the relaxation time, $t_{eq} \sim N^{\alpha}$, agrees with continuum theory predictions α = 4/3 only at high T. The exponent adopts increasingly higher values as T is lowered.[121] This contrasts the 2D case where α decreases for lower T, and also adopts a well-defined limiting value for low T.

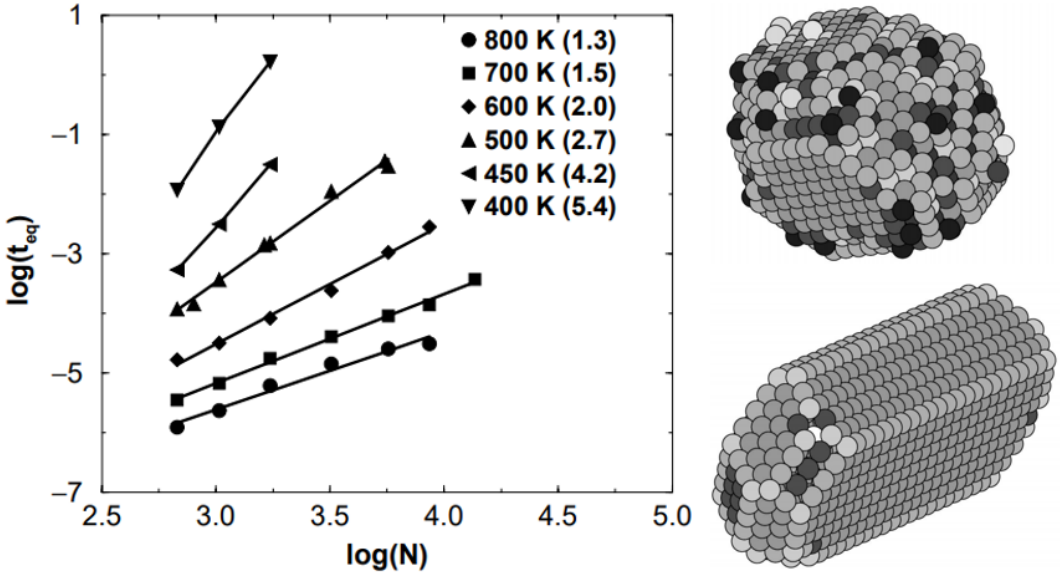

Figure 65. Reshaping of a 3D NC. Left: scaling of the relaxation time, t_{eq}, with NC size N atoms for various T. Right: typical NC configurations for N = 1728 at 700 K (top) and 300 K (bottom). Reprinted with permission from Ref. 121. Copyright 2000 American Physical Society.

However, as for the 2D case, deviations from continuum predictions are associated with the difficulty in nucleating new layers on outer surface facets noting that this is a necessary component of shape relaxation to equilibrium.[121,190] Indeed, consistent with this picture, Figure 65 shows a clear difference between the typical

facetted NC morphology at low T (where continuum theory fails) and the rounded rough morphology at high T (where continuum theory applies). In fact, it is suggested that the progressive increase in exponent shown in Figure 65 reflects the possibility of an actual exponential dependence of t_{eq} on NC size and on T.[121,190] In this picture, the relaxation time, t_{eq}, corresponds to the characteristic time, $t_{nuc} \sim \exp[\Delta G^*/(k_B T)]$, to form a critical nucleus leading to formation of a new layer. Here, ΔG^* denotes the corresponding free energy barrier. Simulations were performed using an umbrella sampling technique to assess the excess free energy, $\Delta G(q)$, as a function of the number of atoms, q, transferred to a 2D cluster of atoms or "germ" formed on the initially bare facet. Based on classical nucleation theory, one expects the form $\Delta G(q) \approx 2\gamma(\pi q)^{1/2} - q\Delta\mu$, where γ denotes the step energy and $\Delta\mu$ is the chemical potential difference for an atom going from a "tip" of the cluster to the facet. The simulation estimates for $\Delta G(q)$ versus q shown in Figure 66 are consistent with this form and clearly show an increase in ΔG^* with increasing NC size.[121] The latter is consistent with an exponential dependence of t_{eq} on NC size.

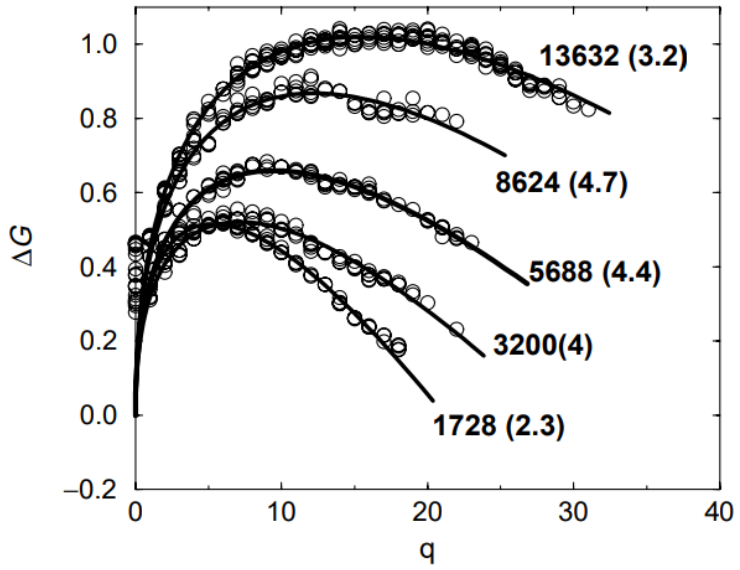

Figure 66. Excess free energy, ΔG, at 400 K for q atoms transferred to a bare facet during NC reshaping as a function of NC size N from 1728 to 13632 atoms. The initial aspect ratio is indicated in parenthesis. Reprinted with permission from Ref. 121. Copyright 2000 American Physical Society.

As noted in Sec.2.1, solution phase nanosynthesis can create NCs for fcc metals including Ag, Au, Pt, etc., with almost perfect simple geometric shapes including cubes, tetrahedra, etc.[3,4] These shapes optimize desired properties for catalysis, etc., so it is important to assess the stability of these special NC shapes against evolution towards their equilibrium Wulff shapes. See Figure 67. Any model which incorporates a reasonable description of NC thermodynamics, and which selects surface diffusion rates consistent with detailed-balance will evolve to the appropriate equilibrium shape. However, the detailed form of this non-equilibrium shape evolution will reflect the prescription of kinetics. Thus, we describe simulations of Ag NC reshaping applying a

stochastic lattice-gas modeling with realistic kinetics as well as thermodynamics developed in Sec.3.4.[160] First, we describe in some detail the canonical problem of evolution from Ag nanocubes, and then describe more briefly evolution from Ag tetrahedra (again noting that Ag NCs can be synthesized with both these shapes).

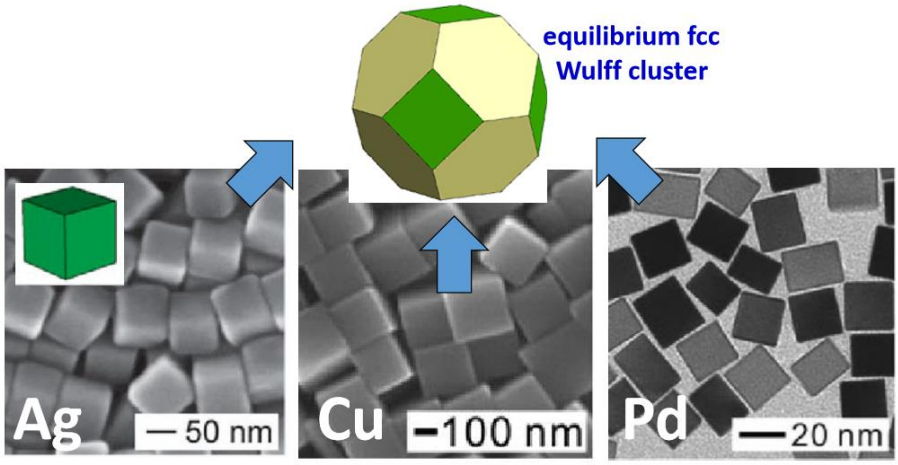

Figure 67. Evolution of nanocubes to Wulff clusters. Reprinted with permission from Ref. 4. Copyright 2013 Materials Research Society.

Complete nanocubes of fcc metals with {100} facets have unstable low-coordinated corner and edge atoms. Thus, for an initial configuration in the simulations which better mimics synthesized structures, it is appropriate to remove all atoms that have less than six NN. Results of KMC simulations[160] for evolution at 1100 K starting with such a truncated Ag nanocube with N = 1584 atoms are shown in Figure 68 (top). To illustrate the utility of "atom tracking" KMC simulations in Figure 68 (bottom), we show the same simulated configurations, but now with atoms which were initially at the corners and edges of the nanocube are colored red. Consequently, one can track the change in their locations in the NC during subsequent evolution.

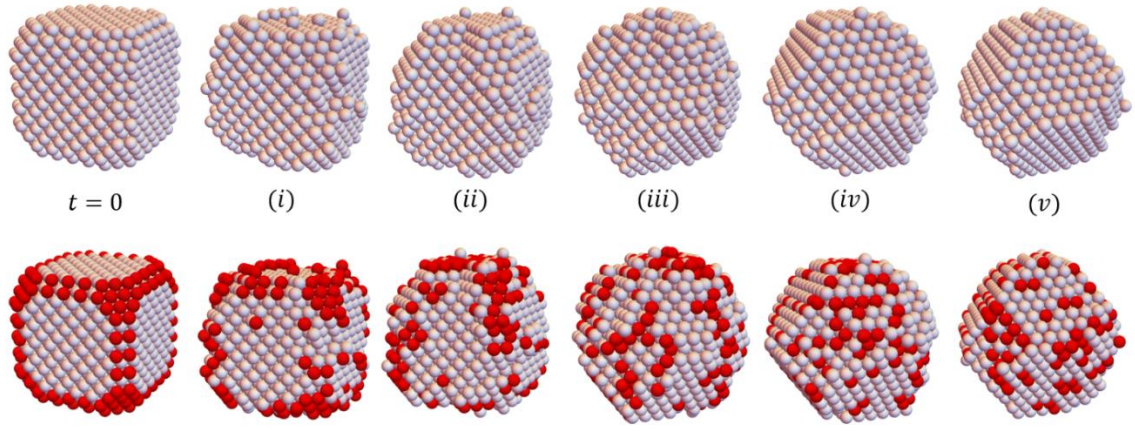

Figure 68. Simulated reshaping of an Ag nanocube with N = 1584, T = 1100 K (top) [160]. Atom-tracking of the location of corner and edge atoms (bottom). Reprinted with permission from Ref. 160. Copyright 2018 American Physical Society.

To quantify the T-dependence and size (*N*)-dependence of relaxation, we monitor evolution of the "width" h_{100} (h_{111}) between the outermost {100} facets ({111} facets) on opposite sides (corners) rescaled by the interlayer spacing to monitor the number of {100} and {111} layers [160]. See Figure 69. This definition identifies every plane with at least one atom as a layer. Results for larger *N* = 1584 show distinct stages in the formation of new {100} facets and dissociation of {111} facets. In addition to the final equilibrium plateau, there is a weak plateau for h_{100} increasing by two layers (due to the nucleation of one new layer on each {100} facet), and h_{111} decreasing by two layers (due to complete dissociation and removal of a {111} facet from each corner). These features are less clear for NCs of smaller size.

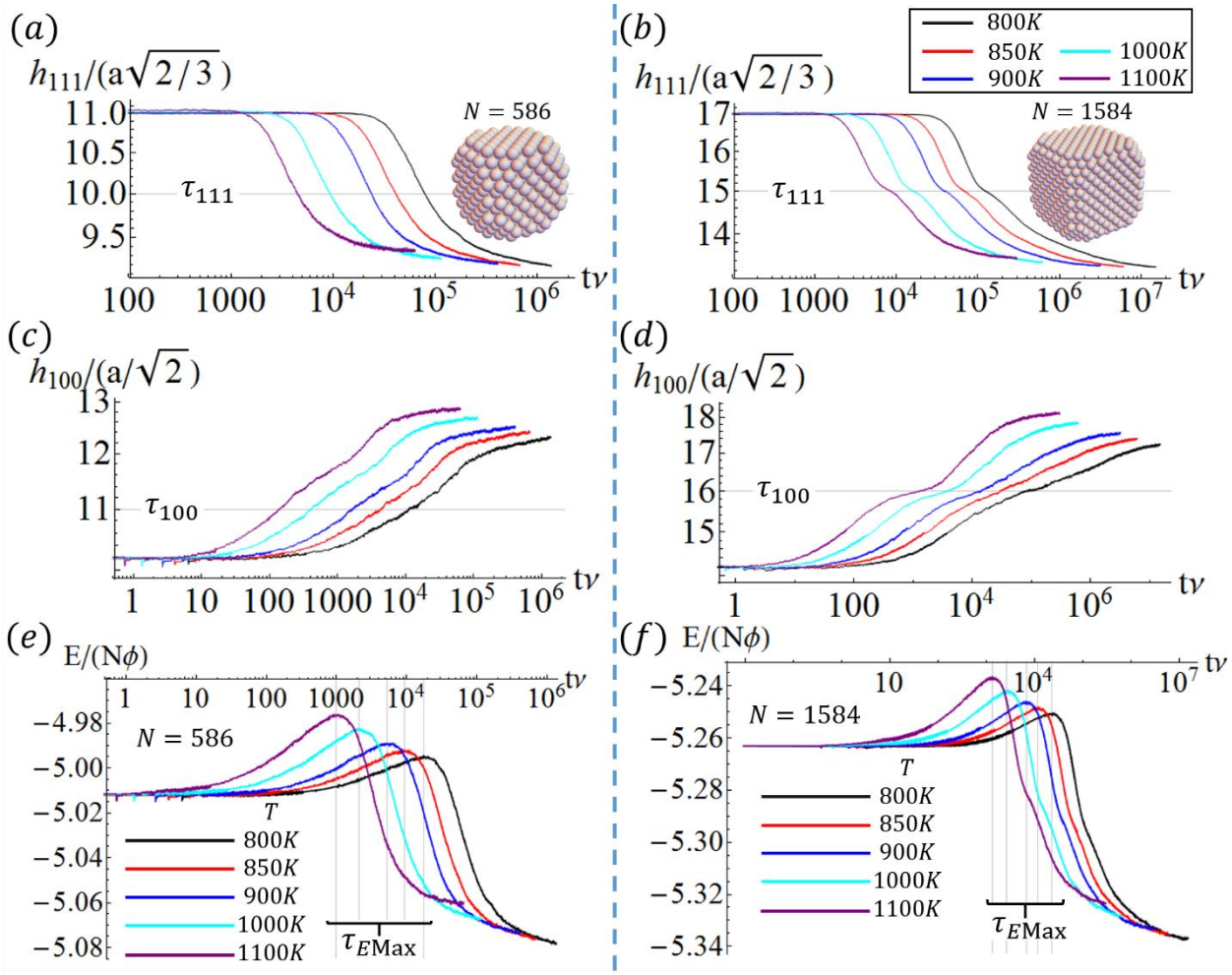

Figure 69. Analysis of the temperature dependence of reshaping of Ag nanocubes for *N* = 586 (left) and *N* = 1584 (right). Linear dimensions, h_{111} (top), h_{100} (middle), and total NC energy, *E* (bottom). Reprinted with permission from Ref. 160. Copyright 2018 American Physical Society.

It is instructive to introduce characteristic times, $\tau_{\mathrm{relax}} = \tau_{100}$ (τ_{111}) reflecting significant changes in h_{100} (h_{111}), and from these assess effective Arrhenius energies, E_{eff}. Clearly $\tau_{\mathrm{relax}} = \tau_{111}$ characterizes dissociation of a {111} corner facet and transfer of

its atoms to a {100} facet, and associated Arrhenius analysis yields $E_{eff} \approx 0.7$ eV. See Figure 70. To provide an atomistic-level interpretation of this barrier, we consider the multi-step process of transferring an atom from the corner atom on the {111} facet to the {100} facet. One can show that the highest barrier is for the last step to reach the final adsorption site on the {100} facet which is $\Delta E = +2\phi$ above the initial site energy. Since the atom must surmount a barrier of energy c_{TD100} above the final state energy, one concludes that $E_{eff} = c_{100TD} + \Delta E = 0.875$ eV.[160] This result is somewhat above the simulation result presumably because our simplified analysis neglects entropic factors which are significant for higher T, e.g., the NC is likely thermally excited from the truncated nanocube so analysis based on an ideal ground state geometry is oversimplified.

Complementary insight into evolution comes from consideration of $\tau_{relax} = \tau_{100}$ which characterizes the nucleation of new {100} layers by atoms which are freed from {111} corner facets and which diffuse onto {100} facets. Arrhenius analysis yields $E_{eff} \approx 1.1$ eV. See Figure 70. One might associate this barrier with that for the formation of a relatively stable square tetramer of atoms on a {100} facet. This process can be divided into two stages. In the first stage, 3 of the 12 atoms on the initial complete {111} corner facet are transferred to a single {100} facet to form a trimer. This involves breaking a total of 8 lateral bonds on the {111} facet, but forming 2 lateral bonds in the trimer. Also accounting for the increased coordination of 4 to supporting atoms on the {100} facet relative to the coordination of 3 to supporting atoms in a {111} facet, the total energy change for this process is $\Delta E_{123} = +3\phi$. The second stage involves transfer of a fourth atom from the {111} facet to the {100} facet to stabilize the trimer to which we assign a barrier of E_4. This process is controlled by last step to reach a {100} adsorption site yielding a barrier $E_4 = 0.75$ eV, giving an effective nucleation barrier of $E_{eff} = E_4 + \Delta E_{123} = 1.42$ eV. However, if the trimer is at the {100} facet edge so that the atom from the {111} facet can hop directly into a site with two lateral bonds forming the square tetramer, then E_4 is reduced to 0.525 eV, and $E_{eff} = 1.20$ eV close to simulation results.[160]

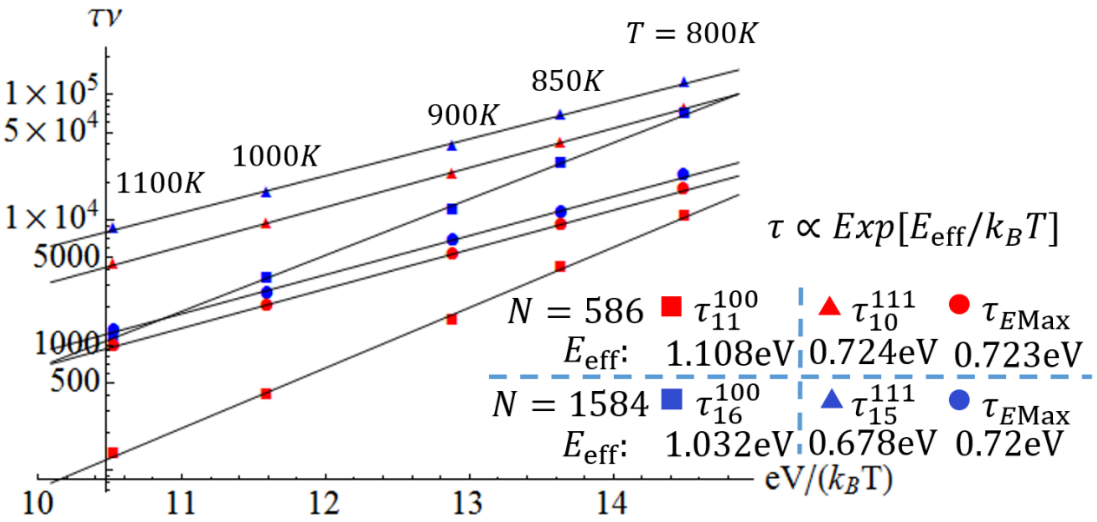

Figure 70. Arrhenius behavior for characteristic times for Ag nanocube reshaping 160.

An alternative measure of evolution comes from tracking the total NC energy *E*. See Figure 69 which shows that *E* first increases through a peak value, E_{max}, before decreasing to its equilibrium value. Thus, it is natural to define a reshaping time $\tau_{relax} = \tau_{E\mathrm{Max}}$ corresponding to the peak energy. Note that both peak *E* and equilibrium E are larger for higher T due to entropic effects. Arrhenius analysis for $\tau_{E\mathrm{Max}}$ yields $E_{eff} \approx 0.72$ eV effectively coinciding that for τ_{111} [160]. Thus, E_{max} corresponds to the early-stage disruption of {111} facets, *E* being lowered only after nucleation and growth of new {100} layers.

Knowledge of Arrhenius behavior allows prediction of relaxation time scales for lower T. The nucleation process with the higher $E_{eff} \approx 1.1$ eV will be rate controlling so that, e.g., $\tau_{relax} \approx \tau_{100} \approx 10^{-3.6}$, $10^{-0.8}$, and $10^{3.8}$ sec. at 500K, 400K, and 300K, respectively, choosing $\nu = 10^{12.5}$ s^{-1}. We caution that these estimates are lower bounds as E_{eff} should increase somewhat for lower T where entropic effects are less significant and our estimates of E_{eff} based on analysis of atomistic processes are more reliable.

We can also roughly assess size scaling of τ_{relax} based on just two NC sizes *N* = 586, 1584. Analysis of $\tau_{relax} \sim N^{\alpha}$ corresponding to the late stages of the process (where h_{111} has evolved 90% from its initial to final value) yields α decreasing from $\alpha \approx 1.7$ at 800 K to $\alpha \approx 1.3$ at 1000 K where the latter is close to the classic continuum value of α = 4/3. [160] Thus, behavior is analogous to that described in Figure 65 above consistent with the presence of a nucleation-mediated process with finite effective barrier.

Next, we consider the evolution of truncated Ag nano-tetrahedra, where analogous to the case of nanocubes, low coordinated atoms at the corners and along the edge are removed in the initial configuration. Results of KMC simulations for evolution at 1000 K starting with *N* = 1028 atoms are shown in Figure 71 (top). In Figure 71 (bottom) we show the same simulated configurations, but now with atoms which were initially at the corners of the tetrahedron are colored red. Tracking their locations during subsequent evolution reveals that most of these atoms participate in the nucleation and growth of a new {111} layer on one side of the tetrahedron.

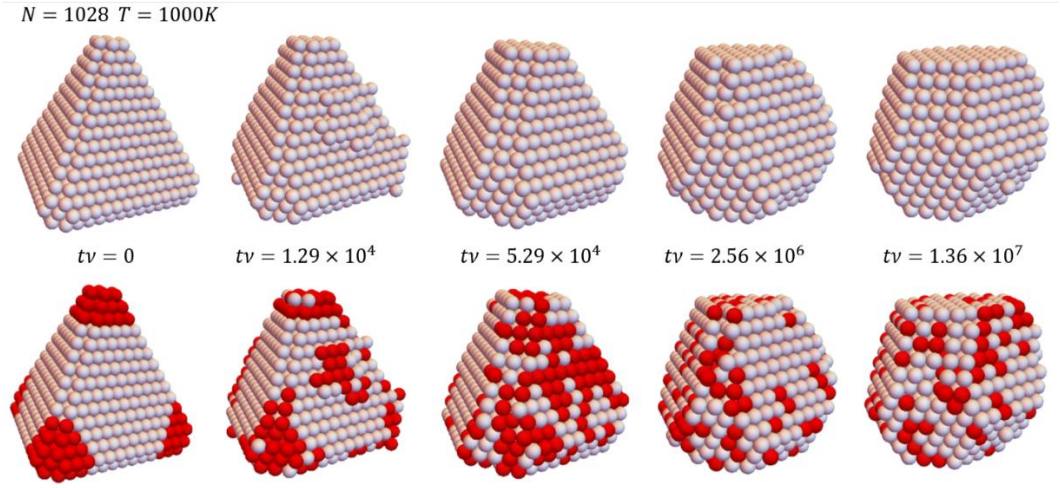

Figure 71. Simulated reshaping of an Ag tetrahedron with *N* = 1028, T = 1000 K (top). Atom-tracking of the location of corner atoms (bottom).

As for nanocube evolution, more detailed analysis follows from tracking evolution of characteristic dimensions of the NC and/or tracking the total NC energy, *E*. See Figure 72. After an initial plateau, a rapid drop is evident in *E* which corresponds to an increase of number of bonds in the cluster associated with building up a large 2D cluster on one of the large {111} facet by transfer of atoms from the small {111} facets at the truncated corners of the tetrahedron. Extracting the timescale t_{drop} associated with the rapid drop in *E* (from the time midway between the initial and lower plateaus), one can perform an Arrhenius analysis to extract an effective energy barrier $E_{eff} \approx 0.8$ eV. One can also track, e.g., the average number of {111} layers, n_{build}, above center of mass parallel to the initial four large {111} facets. This number of layers naturally increases with time as new layers are nucleated. Furthermore, we can see that the timescale of rapid drop in *E* corresponds to the plateau in n_{build}, which is a signature of nucleation on these large {111} facets.

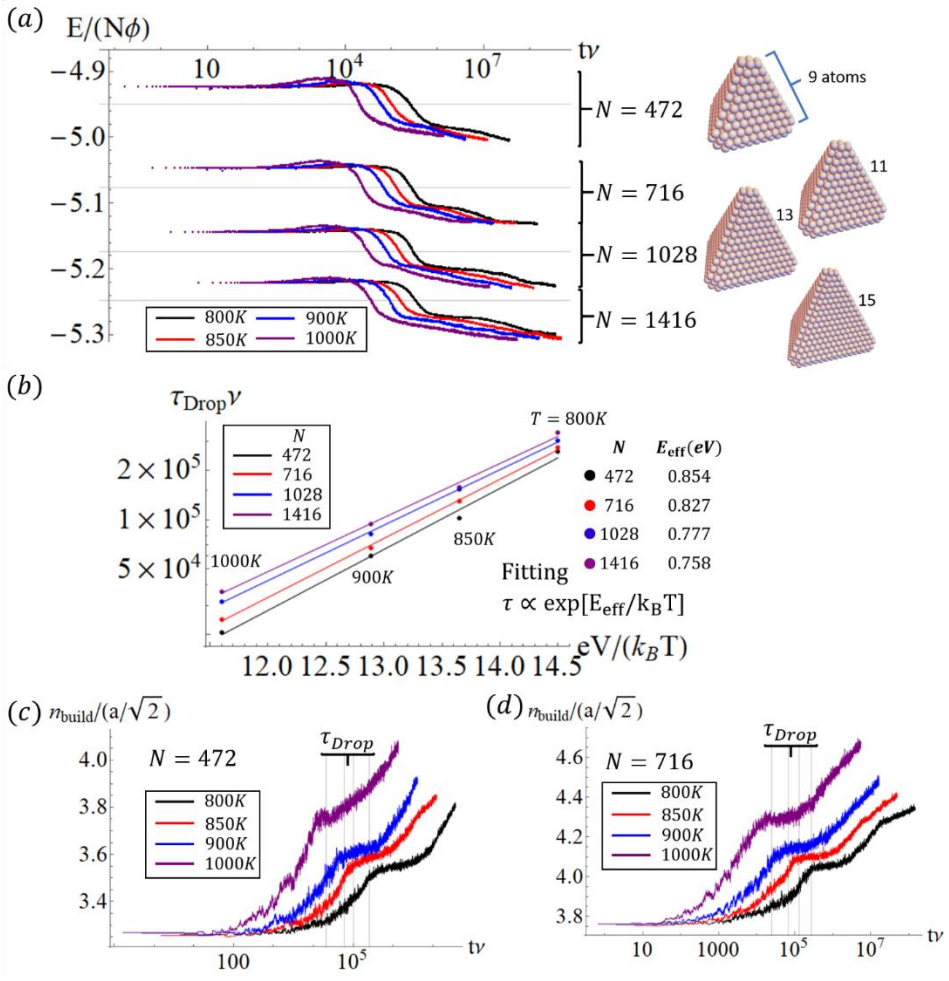

Figure 72. (a) Total energy evolution for reshaping of an Ag tetrahedron with various *N* and T. (b) Arrhenius behavior of the relaxation time. (c) Evolution of linear dimension, n_{build}.

6.2. Experiment and modeling of coalescence of pairs of unsupported 3D NCs

In-situ liquid cell TEM imaging is providing detailed insights into solution-phase growth and coarsening of metallic NCs.[31,33] Rather than Pt NC growth exclusively by monomer-addition, coalescence processes have also been shown important and characterized in some detail, where often these involve oriented-attachment or other processes leading to the preservation of a single-crystal structure of the NCs. Also novel features such as a pause in NC growth immediately after coalescence were observed in the early studies. Resolution in the initial TEM studies was limited in part due to the thick silicon nitride or oxide cell windows. One strategy to resolve this limitation involved the development of graphene liquid cell TEM where a droplet of the growth solution is contained between two graphene sheets.[33] This system has the advantage that the interaction of the NP is weaker than with the glass window, and thus perturbs less growth and coalescence processes. For the modeling presented in this review, a key issue is the formation of single-crystal NC structures after coalescence. Even if NCs coalescence with some low-index plane aligned in the sense that their normal vectors are parallel, they can still be azimuthally misaligned. However, high-resolution TEM confirm the existence of oriented-attachment mechanisms which result in perfect alignment and resulting post-coalescence perfect single-crystal structures.[33] This is shown in Figure 73 for Pt NPs where contact occurs at {111} planes in part due to minimal ligand obstruction. Note however that the same study does reveal other coalescence events producing twinned NCs. Figure 74 shows a more detailed analysis quantifying key dimensions during shape evolution for a Pt NC coalescence event.[33]

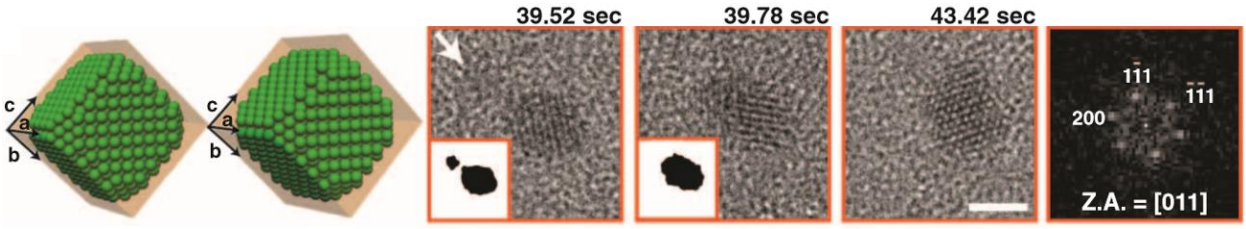

Figure 73. HRTEM showing oriented-attachment of a pair of Pt NCs[33] Reprinted with permission from Ref. 33. Copyright 2012 American Association for the Advancement of Science.

Next, we describe a detailed study of neck growth during coalescence of decahedral Au NCs incorporating both in-situ TEM analysis in combination with stochastic lattice-gas modeling and KMC simulation.[32] The individual NC size is around 12 nm and the pair of NCs intersect at {100} lattice planes. TEM images of sintering shown in Figure 75 allow tracking of the growth of the neck width, x, which for moderate times satisfies $x \sim t^{0.32\text{-}0.37}$, and which for shorter times is subject to strong variations between different examples of sintering. This behavior is far from the classic continuum prediction[128] of $x \sim t^{1/7}$, but this is perhaps not surprising since the continuum result reflects the singular initial geometry of two touching spheres, and the experiment is far from this situation. Atomistic simulation results supplementing the above TEM analysis utilized a generic lattice-gas model for an fcc lattice with NN interactions of strength ϕ = 0.1 eV, and a bond-counting or IVA prescription of surface hop rates.[32] Results also

shown in Figure 75 are reasonably consistent with experiment (after arbitrarily adjusting *T* to match the experimental time scale).

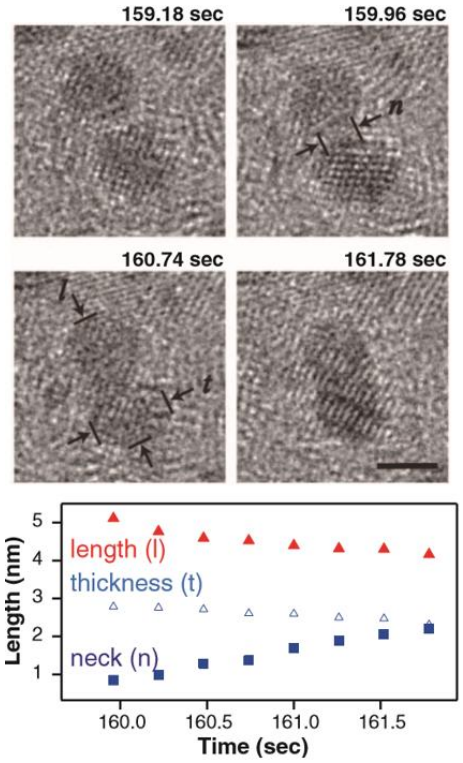

Figure 74. HRTEM quantification of the variation of key dimensions during oriented-attachment of a pair of Pt NCs. Scale bar = 2 nm. Reprinted with permission from Ref. 33. Copyright 2012 American Association for the Advancement of Science.

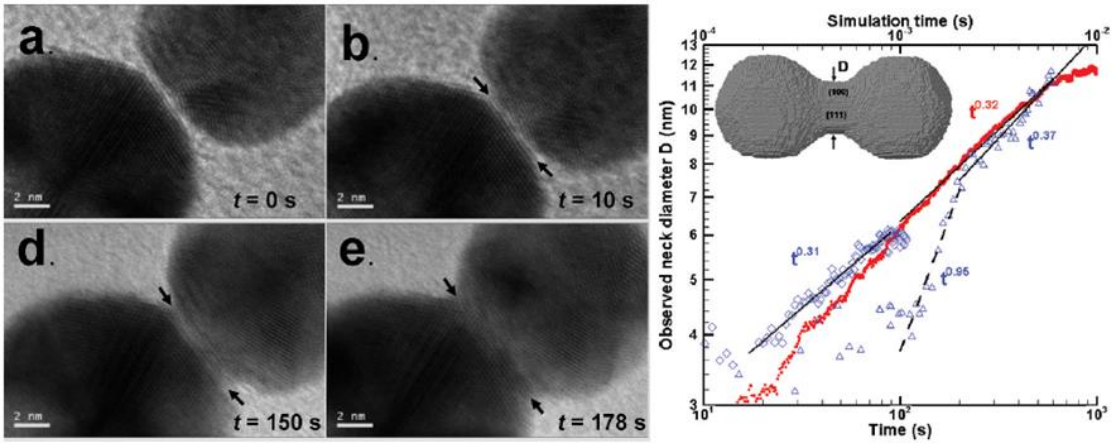

Figure 75. Sintering of orientationally aligned Au NCs intersecting at a {100} plane (left) and experimental and simulation results for evolution of the neck width (right). Reprinted with permission from Ref. 32. Copyright 2012 American Chemical Society.

The generic lattice-gas model used in the above study was also applied in a more extensive exploration of sintering behavior where individual (large) NCs ranged in

size from 28000 to 68000 atoms, and where planes of intersection were either {001} or {111}.[122] Figure 76 shows simulated evolution for coalescence of a pair of NCs at 400 K, each with radius R = 14 (in units of the fcc lattice constant) intersection at a {100} plane. Initially atoms are readily incorporated at high coordination sites in the neck region, but attachment at the neck is more difficult by stage c). By stage d), {110} facets form in the neck region and it is proposed that slow diffusion on these facets facilitates nucleation of new layers capturing material from the outermost {100} and {111} facets. In stage e), the dumbbell has been replaced by a facetted rod with alternating {100} and {110} side facets. The final stage further eliminates the outermost facets and nucleates new layers in the central region. The growth of the neck radius and reduction in overall energy (i.e., the increase in the total number of NN bonds) during this process are shown in Figure 77. Note that the total energy is almost constant during stage d) where new layers are nucleating on the central {110} facets, but these new layers do not have highly coordinated atoms relative to the {100} and {111} facets.

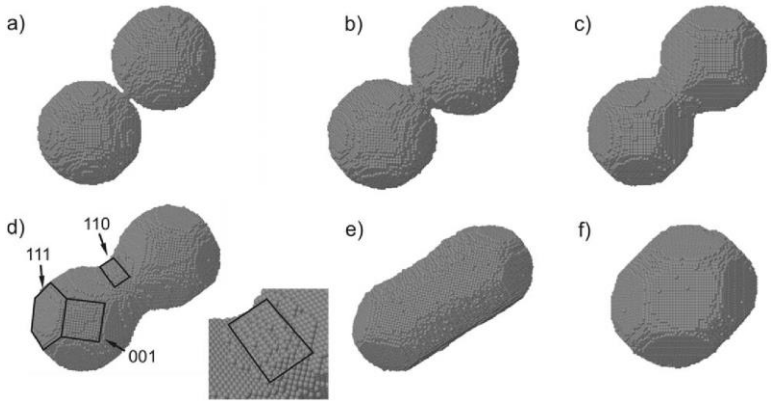

Figure 76. Simulated evolution of coalescence at 400 K of a pair on NCs with radii 14 lattice constants intersecting at the {100} plane. Reprinted with permission from Ref. 122. Copyright 2009 American Physical Society.

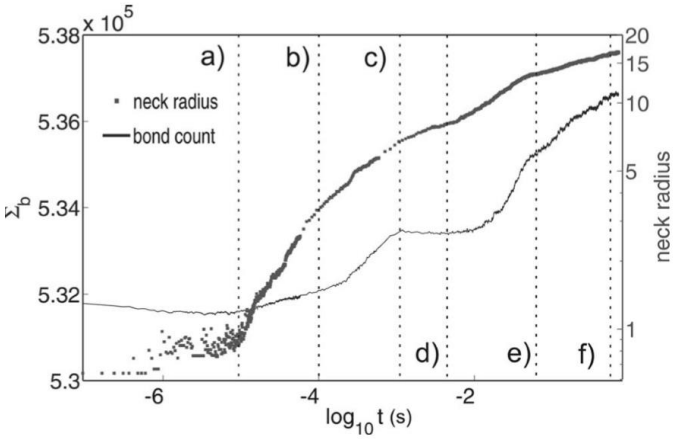

Figure 77. Total energy and neck radius during the evolution of Figure 76. Reprinted with permission from Ref. 122. Copyright 2009 American Physical Society.

For contrast, Figure 78, shows simulated morphologies for coalescence of two NCs again with R = 14 at 400K, but now intersecting at a {111} plane. Note the structure in the neck region is quite distinct from above with three {100} and three {111} facets developing in the neck region, and with atoms diffusion from the outer regions initially being captured at the intersection of these facets. As coalescence proceeds, new layers spread across the {111} facets capturing outer atoms at step edges.

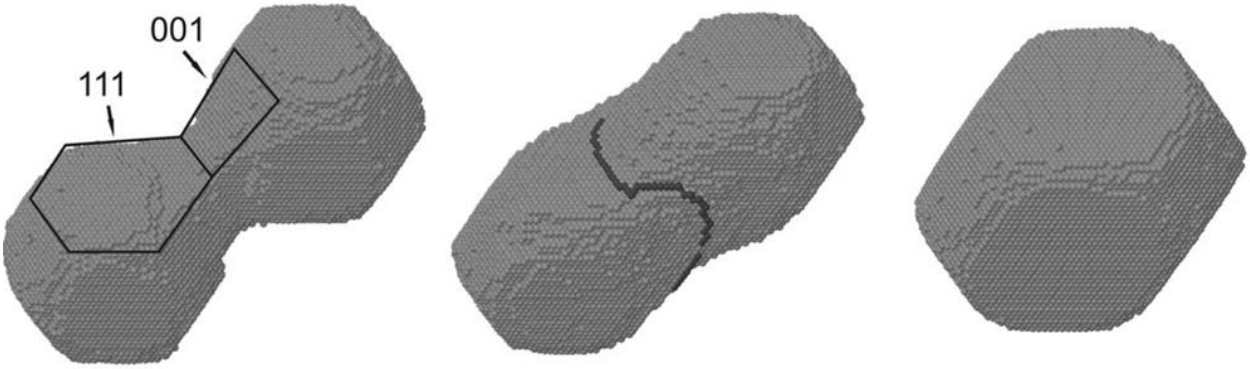

Figure 78. Simulated evolution of coalescence at 400 K of a pair on NCs with radii 14 lattice constants intersecting at the {111} plane[122].

Quantitative analysis of the above simulation data for the size dependence and Arrhenius behavior of relaxation yields the following observations.[122] Here, the equilibration time, t_{eq}, was defined as the time to reduce ratio of length to neck width for the coalesced pair of NCs to a value of 1.2. For NC intersection at a {100} plane, one finds that the size scaling exponent α in $t_{eq} \sim N^{\alpha}$ increases smoothly from α = 1.33 (the classic continuum value) to α = 1.55 at 450 K to α = 2.3 at 400 K. This is consistent with a picture where shape evolution is limited by nucleation on the {110} layers in the neck region. For NC intersection at a {111} plane, α depends weakly on size consistent with a picture where this reshaping process in not nucleation-limited.

Regarding the T-dependence of t_{eq}, Arrhenius analysis for {111} intersection (where reshaping is not nucleation-mediated) reveals a constant effective energy of E_{eff} = 0.6 eV for the entire temperature range considered. This value corresponds to the barrier for an atom to hop out of a kink site at a step edge on either the {100} or {111} facet (for the simple IVA specification of rates which does not realistically capture diffusion on metal surfaces). Behavior for {100} intersection is more complicated. For higher T, one again obtains E_{eff} = 0.6 eV. However, higher values of E_{eff} are realized for lower T where reshaping is nucleation-mediated.[122]

For larger NCs and for reshaping behavior which is largely controlled by system thermodynamics, the use of generic IVA type prescriptions of surface diffusion rates is sufficient. However, in general a more realistic description of these rates is required. Thus, it is instructive to consider in detail the sintering of two Ag Wulff nanoclusters utilizing the more realistic prescription of surface diffusion kinetics described in Sec.3.4. Specifically, we consider the case where the two nanoclusters are initially joined by oriented attachment with aligned {100} facets.[160] Figure 79 shows the evolution at T = 600 K for clusters with edge lengths $a_{100} = a_{111} = 4$ and $N_W(4,4) = 586$, so $N = 2N_W$ =

1172 (cf. Sec.3.4) Initial evolution involves rapid transfer of atoms from the ends of the NC pair to the concave neck region where they are readily captured. See Figure 79(i). Once the neck is filled in, a convex elongated structure is obtained, the sides of which ideally correspond to alternating {100} and {110} facets. See Figure 79(ii). Late-stage equilibration transferring atoms from the ends of this elongated convex shape, nucleating new {100} layers, and eliminating {110} side facets. Figure 79 also shows atom tracking KMC indicating the evolution of atoms initially at the outer ends of the NC pair.

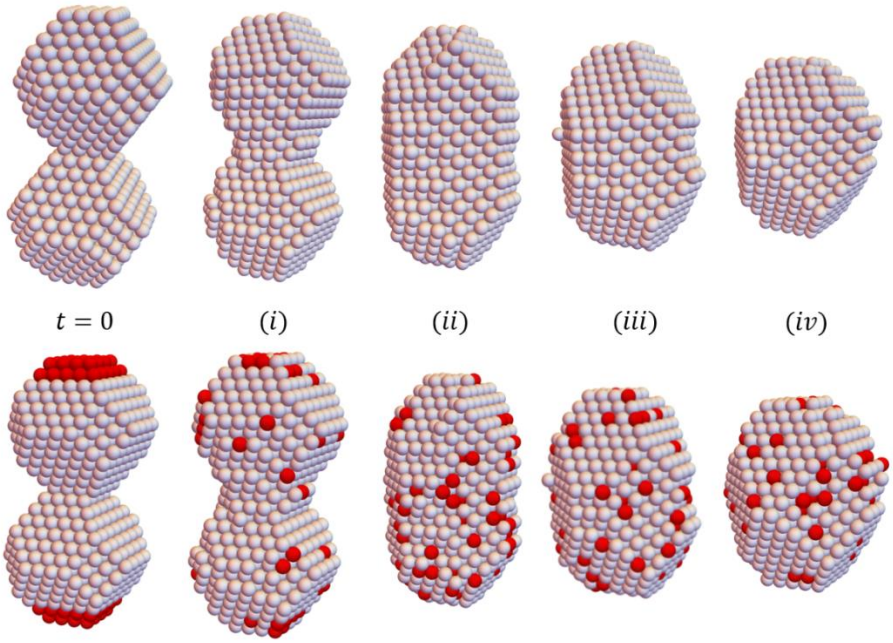

Figure 79. Coalescence of Ag Wulff clusters with total N = 1172, T = 600 K (top). Atom-tracking of the location of end atoms (bottom). Reprinted with permission from Ref. 160. Copyright 2018 American Physical Society.

We analyze neck growth as quantified by tracking the average number of atoms A in each of the two {100} planes at the center of the NC pair orthogonal to their long axis. Thus, A measures the neck area, and $A^{1/2}$ reflects the neck radius, $\varkappa$. We estimate the limiting value, A_∞, of A as $t \to \infty$, from the Wulff-like equilibrium cluster. Figure 80 shows the evolution of A/A_∞ for N = 1172 and various T [160]. The first stage leading to formation of a convex-shaped NC is facile, and ends when A/A_∞ reaches around 0.6. A distinct sharp transition from this first stage to the late stage of nucleation-mediated evolution after convex shapes are achieved is not evident for higher T or smaller sizes, but is apparent at 650 K and below corresponding to the elbow in the curves of Figure 80.

As expected, in the initial neck filling regime, there is no indication of classic continuum scaling $A^{1/2} \sim t^{\alpha}$ with α = 1/7 for short t. However, one can extract an effective exponent, α_{fill}, for neck filling from the slope of the log-log plot in Figure 80 at the inflection point (which is just below the elbow for lower T). For N = 1172, we obtain values from $\alpha_{fill} \approx 0.43$ at 600 K to $\alpha_{fill} \approx 0.24$ at 900 K. An effective exponent, $\alpha_{nuc} \approx$

0.06, for the later nucleation-mediated evolution regime is extracted at 600 K, although we discount the significance of this value. From the trajectory of a single simulation at 600 K (green data), it is evident that the increase in A involves distinct steps corresponding to nucleation of new layers.

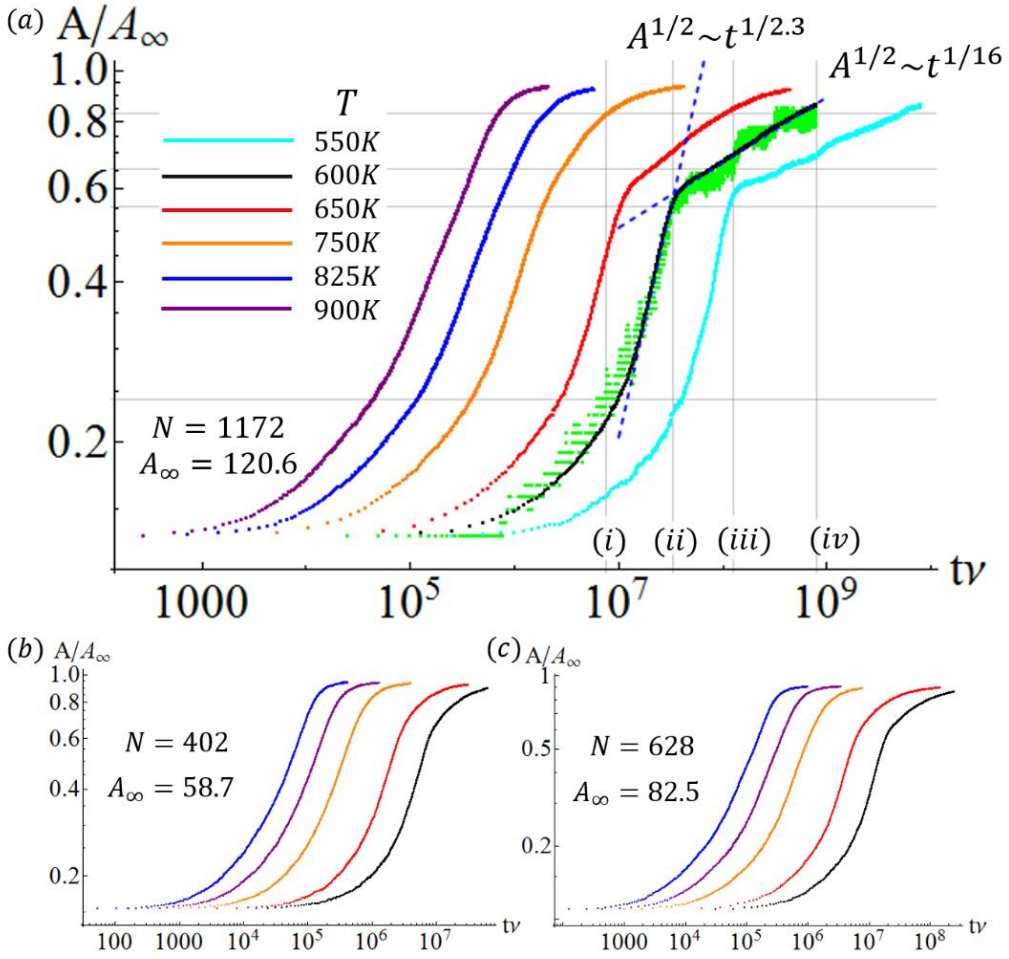

Figure 80. Neck area evolution during coalescence of Ag Wulff clusters. Reprinted with permission from Ref. 160. Copyright 2018 American Physical Society.

To further quantify the *T*-dependence of the evolution, we introduce characteristic times, τ_{fill} determined when $A/A_\infty = 0.45$ (reflecting the neck-filling stage), and τ_{nuc} determined when $A/A_\infty = 0.85$ (reflecting the final nucleation stage). Arrhenius analysis for τ_{fill} yields $E_{eff} \approx 0.75$ eV. In a simplistic analysis, a corner atom of the {100} facet transfers to the {111} facet. The barrier for the first step is relatively low. However, to reach the final adsorption site on the {111} facet, the atom must surmount a barrier of energy $c_{TD111} + \delta_{ES}$ above the final state energy which itself is $\Delta E = +3\phi$ above the initial site energy. Thus, the effective barrier for atom transfer is $E_{eff} = c_{111TD} + \delta_{ES} + \Delta E = 0.875$ eV which is comparable to the simulation result noting our neglect of entropic effects.[160] Arrhenius analysis for τ_{nuc} yields E_{eff} ranging from 0.85 eV for $N = 402$ to 1.10 eV for $N = 1172$ (with slightly higher values at lower *T*). The value for $N = 1172$ is similar to the

barrier nucleation of {100} facets for nanocube equilibration, and the analysis and discussion presented in that case also applies here. In addition, we have analyzed size scaling $\tau_{fill} \sim N^{\alpha}$ for the neck filling regime and find that α increases above the classic continuum value of $\alpha = 4/3$ for lower T, similar to behavior observed for nanocube reshaping.[160] See Figure 81.

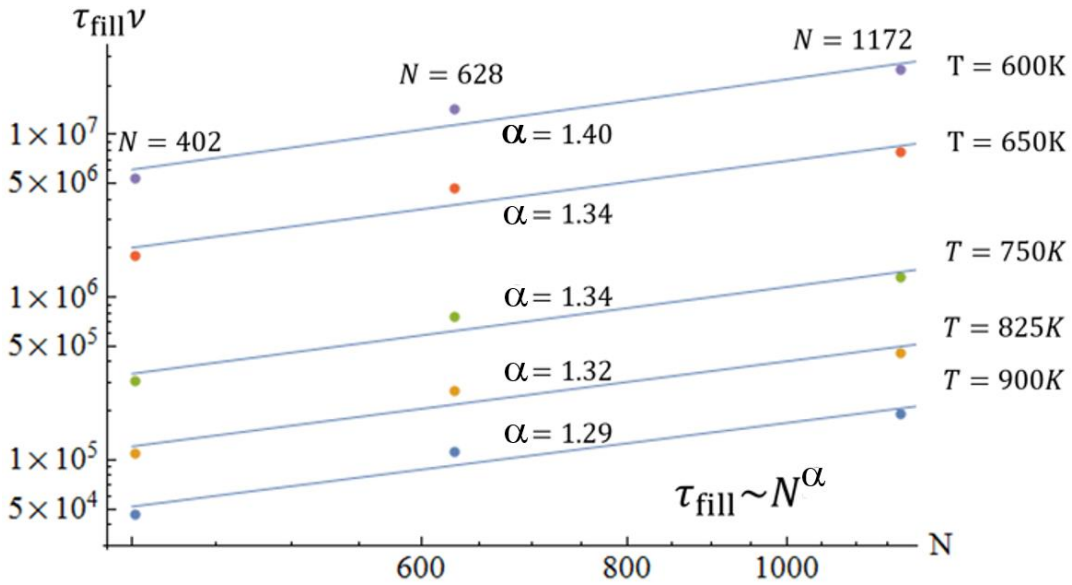

Figure 81. Arrhenius behavior of the characteristic time for neck filling during coalescence of Ag Wulff clusters[160].

There are other atomistic lattice-gas model studies of sintering phenomena for more complex arrangements of NCs, e.g., involving bi-model sizes of NCs where small NCs between larger ones can facilitate neck formation.[123] See Figure 82. However, the model used in this analysis did not satisfy detailed-balance and also allowed detachment as well as surface diffusion. There is an effective balance in attachment-detachment processes as the simulation was performed in a finite container with an equilibrated concentration of “gas phase” detached atoms, and this maintains a roughly constant total NC size. As this model is different in nature from other described in the review (which focus on surface diffusion mediated evolution consistent with detailed-balance), we do not provide further detailed discussion.

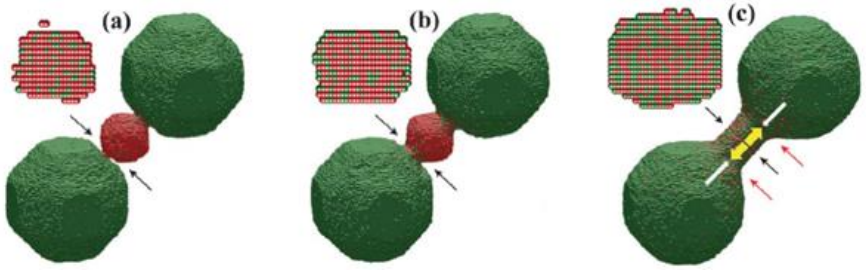

Figure 82. Simulated evolution of sintering aided by a small NC in the neck region. Reprinted with permission from Ref. 123. Copyright 2013 Royal Society of Chemistry.

6.3. Evolution of unsupported 3D nanrods

As described in Sec.2.4, solution-phase synthesis can produce nanorods (either rectangular bars or rods with octagonal cross-sections of alternating {100} and {110} facets) of various fcc metals.[3] By analogy with Rayleigh-Plateau instabilities in liquid jets (and nanojets), one might anticipate instabilities could develop in the nanorods for shape evolution mediated by surface diffusion. Indeed, this was confirmed in classic continuum modeling for infinitely long cylindrical rods for which linear stability analysis for weak perturbations in the radius, $r(x) = r_0 + \varepsilon \sin(2\pi x/\lambda)$, along the axis x of the rod revealed an intrinsic instability of wavelength $\lambda_0 \approx 8.89\ r_0$.[128] This analysis applies for isotropic surface energy and surface mobility. It is appropriate to emphasize that such an instability does not occur in 2D where opposite sides of an infinite rod are dynamically disconnected. In contrast, they are coupled in the 3D case by azimuthal diffusion. Figure 83 shows the results of numerical simulations of a somewhat more complex scenario where a nanorod is grown in the first 76 time units by adding spherical clusters periodically to its ends, but the abovementioned instability has led to pinch-off before growth has terminated and subsequent pinch-off occurs into smaller clusters subsequently.[189] Despite the more complex scenario, the distribution of distances, λ, between neighboring cylindrical fragments after pinch-off satisfies, $\lambda = 9.0\ r_0$, consistent with classic cylinder pinch-off.

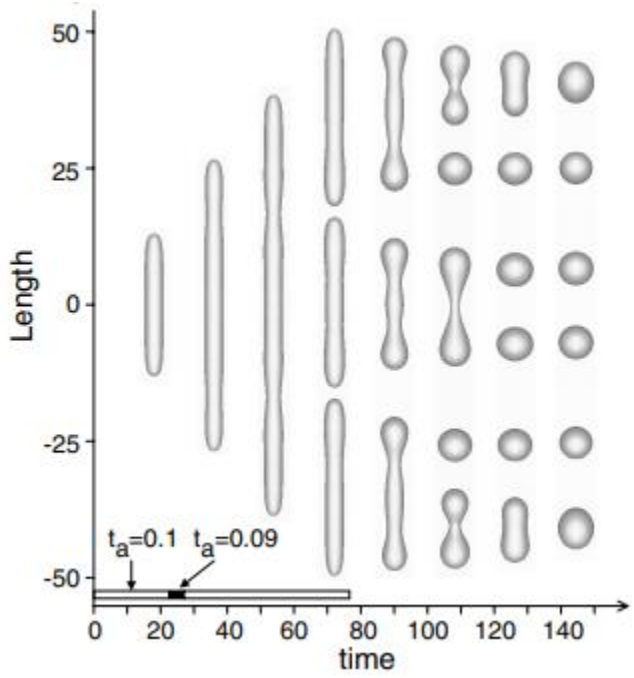

Figure 83. Isotropic continuum analysis of pinch-off of an initially growing roughly cylindrical nanorod where growth ceases at time 76. Reprinted with permission from Ref. 189. Copyright 2002 American Physical Society.

With regard to atomistic-level modeling of nanorod evolution, one extensive study utilized the same atomistic lattice-gas model as discussed at the end of Sec.6.2 (in the context of sintering of different sized NCs).[124] Again, this model did not satisfy detailed-balance and also allowed detachment as well as surface diffusion, but there is an attachment-detachment equilibrium which maintains constant nanorod size. In Figure 84, we just show one illustrative example of morphological evolution for a nanorod with its axis along the {100}-type orientation which captures multiple pinch-off events.[124] Various insights followed from this and other simulations. Initial neck formation proceeds via two mechanisms. Necks can form in the middle of a sufficiently long nanowire driven by the instability mechanisms described above for the continuum model, but they can also form as a result of the special nature of evolution at the ends of the nanowire. The latter corresponds to rounding and fattening at the ends which induces formation of a narrower region near the ends, which in turn can lead to subsequent pinch-off near the ends. It was also noted that pinch-off can lead to multi-bulb structures, particularly dumbbells, some of which are quite long-lived.

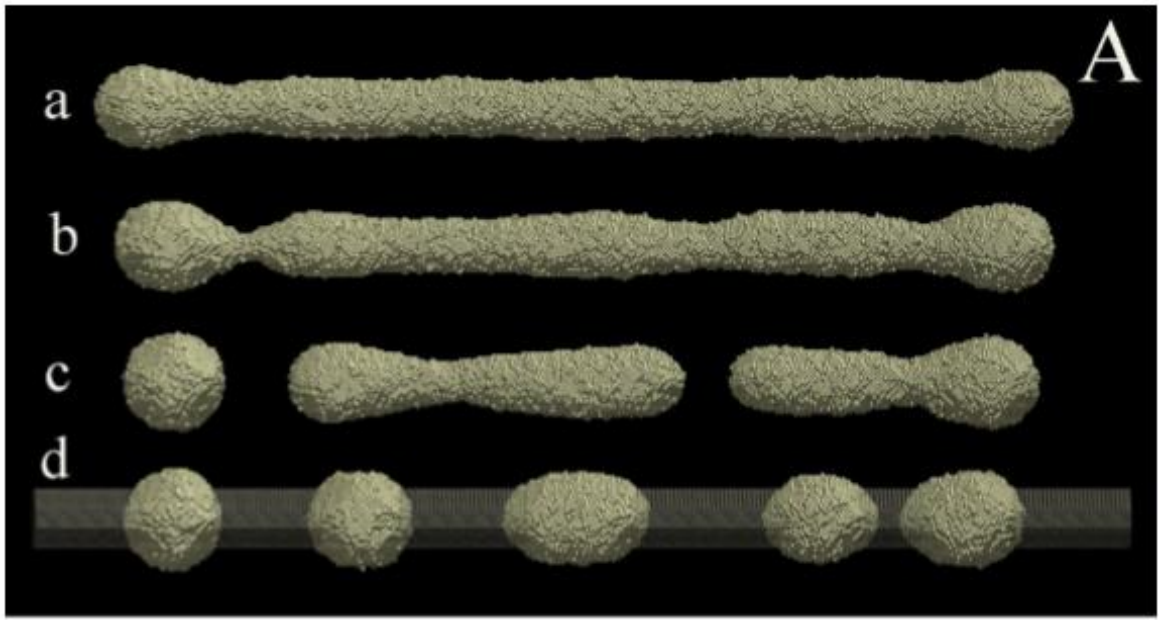

Figure 84 Simulated pinch-off of a 3D nanorod with its axis along a {100}-type orientation. Reprinted with permission from Ref. 124. Copyright 2017 American Institute of Physics.

Simulations for nanorods with a {111} orientation shows more regular periodic bulging in the center of the nanowire.[124] See Figure 85. Breakup into round “isomeric” and dumbbell fragments where the dumbbells are long-lived and eventually round-up. A portion of the nanorod which eventually breaks up into an isomeric fragment is shown in the inset and has a typical length of $\Lambda \approx 7.1\, r_0$. The significant role of fluctuations in the pinch-off process is confirmed by running additional simulations with the same initial configuration as in Figure 85 (but a different random number seed) where a different arrangement of fragments results. Additional simulations for nanorods with a {110} orientation showed a strong resistance to pinch-off.

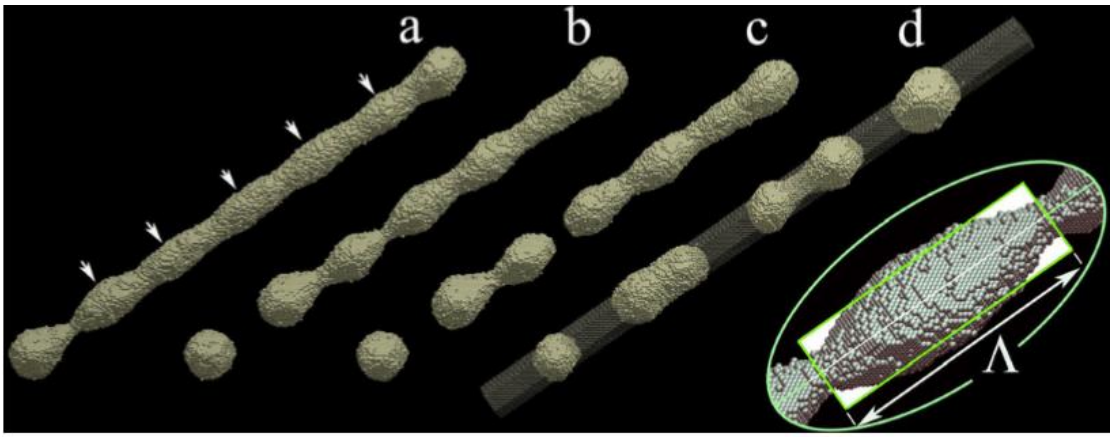

Figure 85. Simulated pinch-off of a 3D nanorod with its axis along a {111}-type orientation. Reprinted with permission from Ref. 124. Copyright 2017 American Institute of Physics.

Finally, this simulation model has been used to provide a more detailed characterization of end-effects in the pinch-off process. As noted above, evolution of the nanowire ends can drive breakup by progressively generating sequences of nanoparticles which are more likely to have a rounded isomeric form than those fragments originating from the interior region. Images of evolution allow characterization of the morphology just before pinch-off as shown in Figure 86 (for which the nanorod has the same {100} orientation as in Figure 84). This image also indicates the significant shrinkage in length from the initial geometry which corresponds to an octagonal nanorod with alternating {100} and {110} side facets (shown a semi-transparent background). Analysis of sequence of such images allows assessment of mass flow during the initial stages of neck formation at the end of the nanorod.

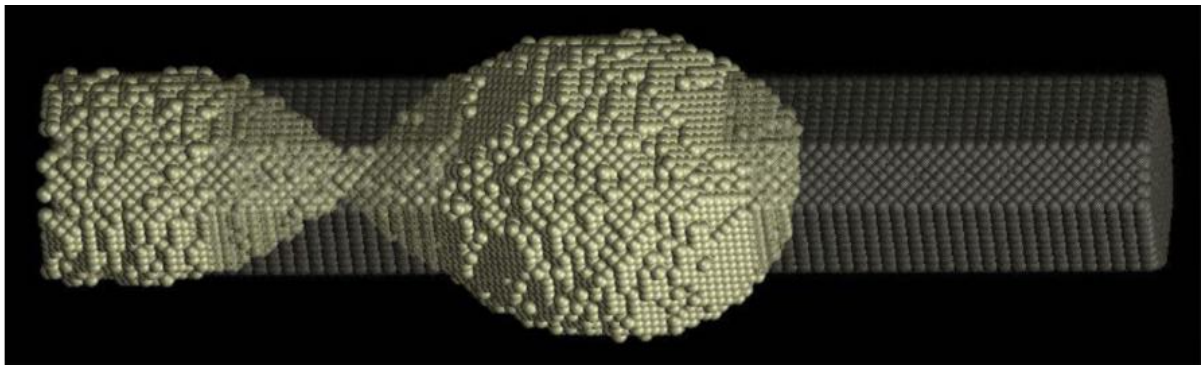

Figure 86. Evolution near the end of a 3D nanorod with its axis along a {100}-type orientation. Reprinted with permission from Ref. 124. Copyright 2017 American Institute of Physics.

As noted in Sec.2.1, Ag nanorods can be synthesized with either an octagonal cross-section having alternating {100} and {110} side facets, and {100} end facets, or as nanobars with square cross-section and {100} side facets[3]. The continuum theory described above for isotropic surface energy and mobility indicates an instability with wavelength $\lambda \approx 4.45 \times$ rod diameter, so $\mathcal{R}_c \approx 4.5$ gives rough estimate of the critical

value of rod length to rod “diameter” for pinch-off. Thus, there is motivation to employ a model described in Sec.3.4 with realistic surface diffusion kinetics satisfying detailed-balance to explore pinch-off phenomena for these Ag nanorod systems. Simulations illustrated Figure 87 suggest that $\mathcal{R}_c \approx$ 7-8 for the selected width of 9 layers for nanorods with octagonal cross-section.[160] The difference in $\mathcal{R}_c$ from the continuum value reflects nanoscale effects including finite nanorod length and also faceting associated with non-isotropic step energy. Furthermore, fluctuation effects are significant on the nanoscale as quantified in Figure 88 which gives the pinch-off probability, *P*, as a function of nanorod aspect ratio. However, we note that fluctuation effects are much weaker than for a 2D nanorod of the same width (i.e., *P* versus aspect ratio is much closer to a step function for the 3D case versus the 2D case). Finally, for comparison, Figure 89 shows simulation results for the pinch-off for a nanobar with square cross-section.

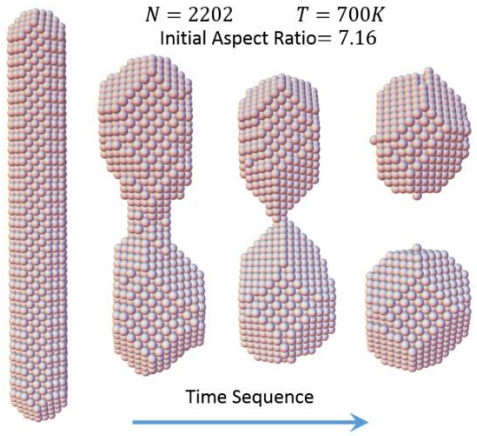

Figure 87. Simulated pinch-off of an Ag nanorod with octagonal cross-section at 700 K[160]. Reprinted with permission from Ref. 160. Copyright 2018 American Physical Society.

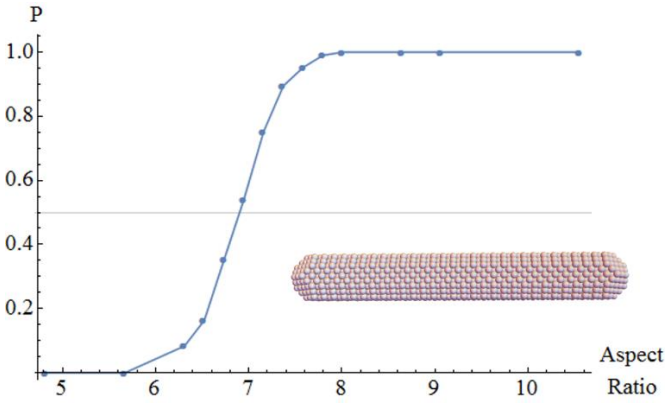

Figure 88. Simulated pinch-off probability of Ag nanorods at 700 K as a function of initial aspect ratio.

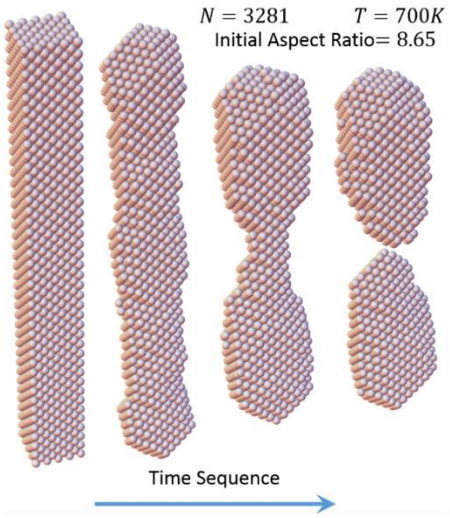

Figure 89. Simulated pinch-off of an Ag nanobar at 700 K.

6.4. Shape evolution of supported 3D NCs: Wetting and de-wetting

First, we describe a detailed atomistic modeling study[245] of surface-diffusion-mediated shape evolution of strain-free supported 3D NCs for different strengths of adhesion to the substrate. The model incorporates an fcc crystal structure where the support is a {111} facet of an extended substrate. The NC atoms interact with a NN attraction of strength ϕ_0 = 0.1 eV, and NC atoms interact with substrate atoms with a NN attraction of strength ϕ_1 (where the latter also describes the strength of adhesion of the NC to the substrate). It is assumed that the NC material is epitaxially matched to the substrate, so there is no strain energy contribution to the overall system energy. Hopping of surface atoms is described within a bond-counting or IVA prescription. It is instructive to show how the equilibrium shape of NCs in this model depends on both the strength of adhesion and on T. Results are shown in Figure 90 for high *T* (top) and low *T* (bottom).[245] Also, the difference between shapes for low adhesion (left) and high adhesion (right) is consistent with the Winterbottom construction.

The first application of the above model is to what might be described as partial dewetting of supported NCs. We have noted in Sec.2.2.2 that the presence of 2D and 3D ES barriers can limit upward transport of adatoms diffusing across the substrate and aggregating with growing 3D NCs. Thus, as-synthesized NCs could be flatter than their equilibrium shapes. In this case, post-deposition evolution will result in an increase in height and decrease in width of the NC to approach the equilibrium shape.[246] Simulation reshaping configurations are shown in Figure 91 for 500 K for weaker adhesion with ϕ_1/ϕ_0 = 0.5. [245] More detailed analysis of the *T*-dependence of reshaping also shown in Figure 91 indicate a process mediated by nucleation of new top layers at lower *T* = 300 K (as evidenced by a step-wise decrease in the total system energy), but not at higher *T*. Consistent with this picture of nucleation-mediated evolution, a more comprehensive analysis of size scaling of the equilibration time for different temperatures (and also considering different adhesion strengths indicates that the size scaling exponent increases with decreasing temperature (analogous to behavior described in Sec.6.1 for

unsupported NCs). Actually a single exponent does not describe well size-scaling for the lowest *T* consistent with an exponential dependence on size. See Figure 92.

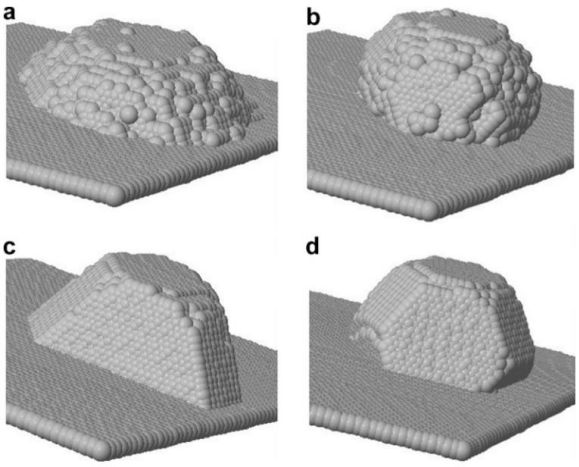

Figure 90. Equilibrium configurations of supported NCs: ϕ_1/ϕ_0 = 0.8 (left), 0.5 (right). Top 700 K. Bottom: 300 K. Size *N* = 8232 atoms. Reprinted with permission from Ref. 245. Copyright 2007 Elsevier.

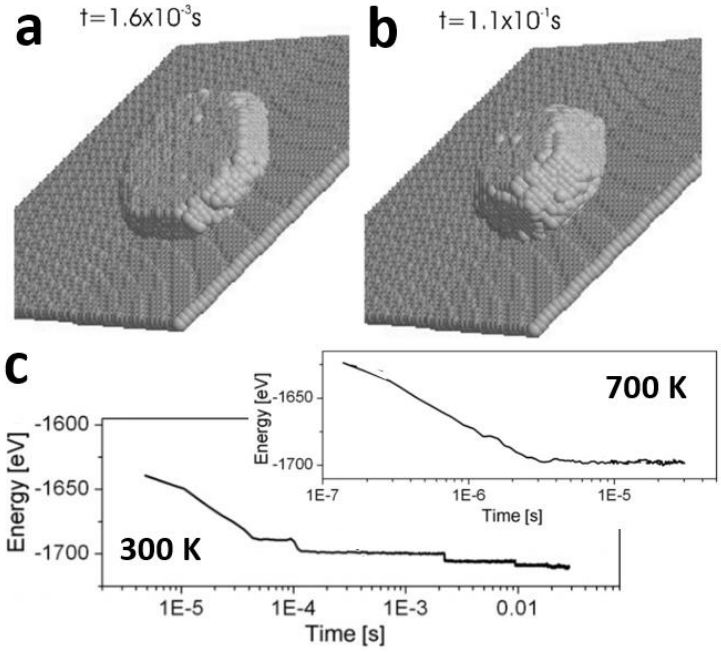

Figure 91. Simulation of partial de-wetting. ϕ_0=0.1 (NN bonding), ϕ_1 = 0.05 eV (adhesion). T = 500 K and *N* = 3888. (a,b) configuration evolution; (c) total energy evolution. Reprinted with permission from Ref. 245. Copyright 2007 Elsevier.

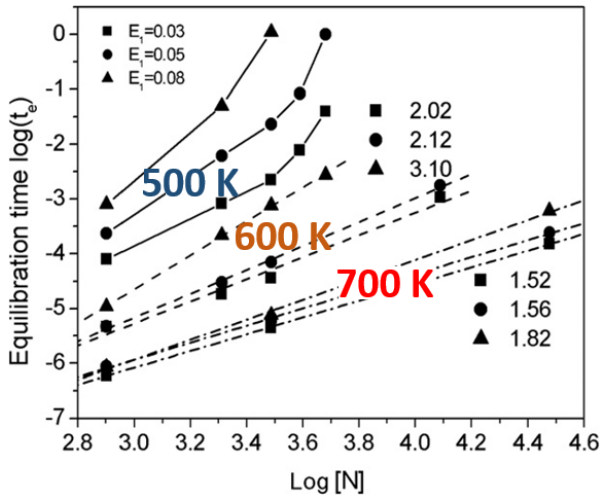

Figure 92. Scaling of the equilibration time for partial de-wetting. Reprinted with permission from Ref. 245. Copyright 2007 Elsevier.

Next, we consider partial wetting of supported NCs with moderate adhesion, $\phi_1/\phi_0 \geq 0.5$, say, or complete wetting which applies, e.g., when $\phi_1/\phi_0 = 1$ (corresponding to 3D clusters formed on a homoepitaxial support). We have also noted in Sec.2.2.2 that glancing angle-deposition[105] in the presence of a 3D ES barrier can produce nanorods protruding upward from the surface. As these are generally more vertically elongated than equilibrium shapes, they should shrink in height. Partial wetting of such nanorods simulated with the model of La Magna is shown in Figure 93. For low temperature, evolution is mediated by nucleation of new layers on the vertical side facets of this protruding nanorod. The signature of this behavior is again a step-like decrease in the total system energy as also shown in Figure 93. Additional analysis of size-scaling of the equilibration time shows the expected increase in exponent from $\alpha = 1.55$ (1.60) for 700K, to 1.65 (1.80) for 500 K to 2.75 (2.90) for 300 K for $\phi_1/\phi_0 = 0.5$ (0.8).

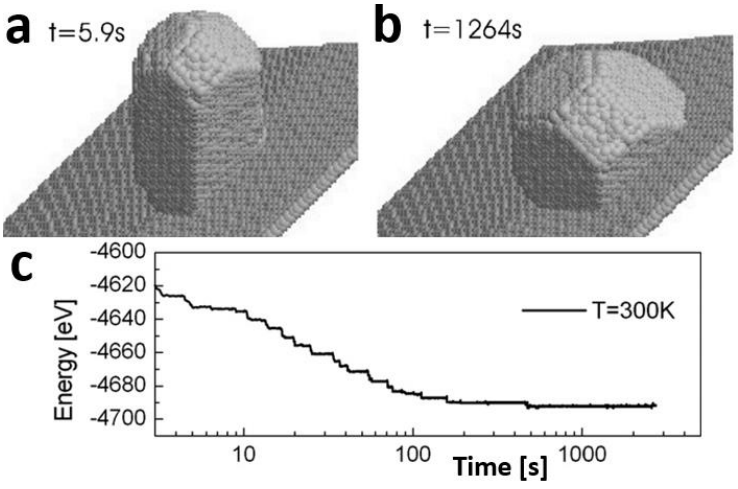

Figure 93. Simulation of partial wetting. ϕ_0=0.1 (NN bonding), ϕ_1 = 0.05 eV (adhesion). T = 300 K and *N* = 8232. (a,b) configuration evolution; (c) total energy evolution. Reprinted with permission from Ref. 245. Copyright 2007 Elsevier.

There are other scenarios where partial or complete wetting is manifested. Growth of multilayer thin films in the presence of an ES barrier produces “mounds” whereas the equilibrium film structure is flat. Consequently, these mounds will decay in height.[8,9] Li et al.[247] analyze this behavior for Cu on Cu(100) homoepitaxy, where they emphasize that behavior depends on the details of interlayer diffusion kinetics which are not captured by IVA type modeling. Another scenario leading to wetting is deposition of 3D clusters on a substrate, e.g., of the same material, where we assume that the initial configuration of the supported cluster has an unsupported 3D Wulff shape epitaxially adhered to the substrate through a single facet of the Wulff cluster. As an aside we note that such deposited clusters will not in general be epitaxially aligned with the substrate. For Cu_{220} NCs deposited on Cu(100), in general a grain boundary is initially formed at the interface between the NC and the substrate. However, this grain boundary was proposed to sweep upwards through the NC resulting in an NC epitaxially aligned with the substrate.[248]

Motivated in part be the last example, we analyze the associated complete wetting of such a supported Ag NC on Ag(100) using realistic surface diffusion kinetics as described in Sec.3.4. This is important to reliably describe transport between layers and facets. Figure 94 shows simulated evolution at 700 K of the Ag NC expitaxially adhered to the substrate through a {100} facet for size N = 2406 atoms. Evolution is quite distinct from the classic Kuczynski continuum picture[184] where a simple neck develops at the NC-substrate interface. Instead a pyramidal base forms and grows upward from the substrate. Ultimately, the portion of the 3D NC remaining on top of this pyramidal base is incorporated into the base which finally decays and spreads to form a single layer on the substrate (consistent with the thermodynamic equilibrium state).

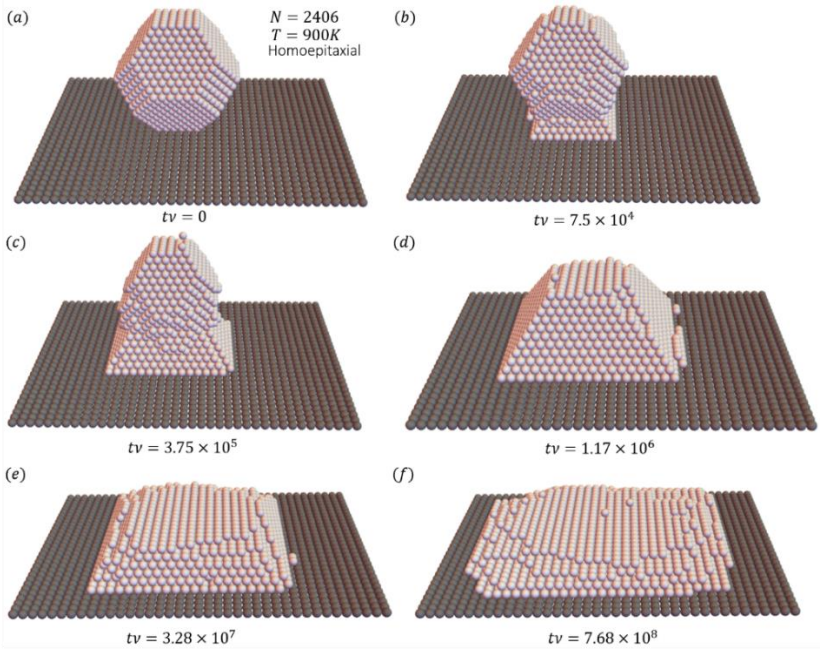

Fig. 94. Simulation for an Ag/Ag(100) homoepitaxial system of complete wetting of supported Wulff shape cluster.

Above, we mentioned that the detailed features of nanoscale partial or complete wetting of supported 3D NCs cannot be captured by the classic Kuczynski macroscale continuum treatment of a sphere merging with a planar substrate.[184] It is however appropriate to note that multi-layer step dynamics formulations provide an alternative treatment which is intermediate between fully atomistic modeling and continuum treatments[197,198]. Here, as described in Sec.4.3.3, this formalism can be used to track the positions of step edges (described as continuous curves) separating layers in a single 3D mound where layers with decreasing height are progressively larger, so there is no overhang as with the last example of a supported 3D Wulff cluster. Indeed, such step dynamics modeling has been extensively applied to analyze the decay of 3D mounds, i.e., wetting, often focusing on evolution near the top of an initially conical mound. The effect of the substrate is not significant for such evolution. Key observations include the growth of a large flat top facet (which generally supported a single shrinking 2D island), and the self-selection of the form of slope versus radius near this top facet.[197] Coarse-graining the step dynamics model to obtain a continuum partial differential equation, the boundary conditions for this equation depend on nanoscale details of evolution on the top facet.[198]

6.5. Sintering and breakup of supported 3D NCs

There is extensive discussion in the classic thin film literature through the 1970's of the possible mobility and coalescence of supported metallic 3D NCs on alkali halide and oxide supports.[20] One prominent example is Au/KCl(100).[20] Immense interest in this topic derives from its relationship to catalyst degradation. A subsequent review by Jensen[249] focused on cluster deposition where often clusters of $O(10^2)$ metal atoms are deposited on graphite (HOPG). The mobility of deposited clusters is self-evident as it leads to the formation of fractal aggregates of the deposited NCs. Mobility of Au_{250} on graphite was particularly high but not on NaCl (compatible with 1970's studies). Partial coalescence of Au NC was deduced on graphite as the arms in the fractal aggregates exceeded the size of the individual NCs. The review also discussed cluster-cluster coalescence, but referred to classic continuum studies and also MD studies[249] which are not so relevant for our considerations.

Here we focus on HRTEM studies providing insight into the details of NC sintering on carbon supports. One early study in 1991 tracked the coalescence of Au NCs on silica.[250] For 2-3 nm NCs well-bonded to the substrate, coalescence occurred on the order of seconds. Lattice fringes of both particles were seen to align before they made contact. It was also suggested that formation of an Au monolayer on the substrate in the small gap between the NCs was a precursor to sintering. A more recent study explored the sintering of a pair of 15 nm Ag NCs on particulate carbon support (Ketjen, Tokyo).[251] See Figure 95. The sintered product typically contain twins, although particle rotation of a few degrees was also observed during sintering. Diffusion and sintering processes for smaller 6 nm and 2 nm Ag NC's was also observed.

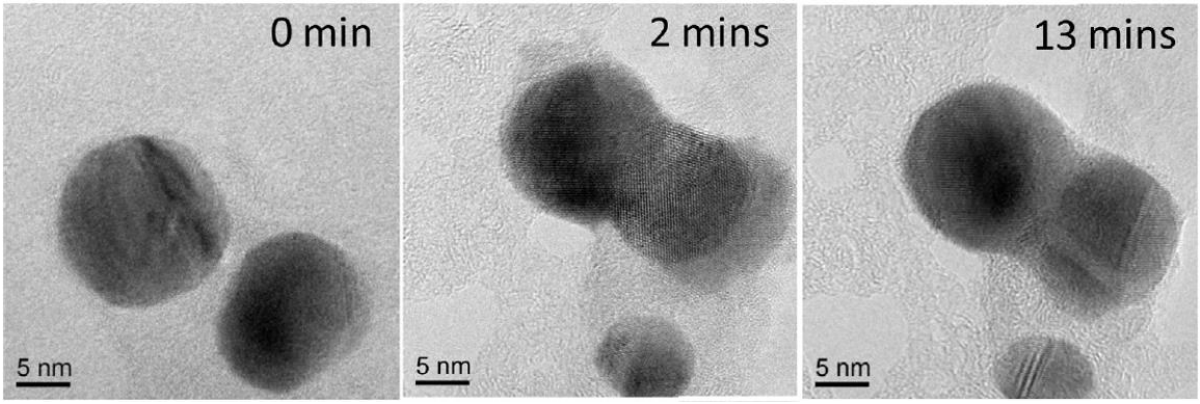

Figure 95. HRTEM of sintering of 15 nm Ag NCs at 200 °C on a particulate carbon support. Reprinted with permission from Ref. 251. Copyright 2014 Elsevier.

The modeling highlighted in this review focuses on reshaping and sintering of single-crystal NCs. However, in general pairs of supported NCs will not be crystallographically aligned upon coalescence resulting in twinning and grain boundaries. However, the above suggested that reorientation (analogous to oriented-attachment in the solution-phase) is one mechanism to achieve a single-crystal structure. High-resolution imaging of such reorientation is shown in Figure 96 for the case of two 3-7 nm Au NCs supported on graphene.[252] An alternative mechanism applies when the initial coalescence event produces a grain boundary. Then, this grain boundary can migrate through the coalesced structure resulting in a single-crystal structure [cf. the above description of Cu NC deposition on Cu(100).[248] See Figure 97. This study of Au NCs on graphene also provided detailed imaging of mass transport during coalescence of crystallographically aligned Au NCs. See Figure 98.

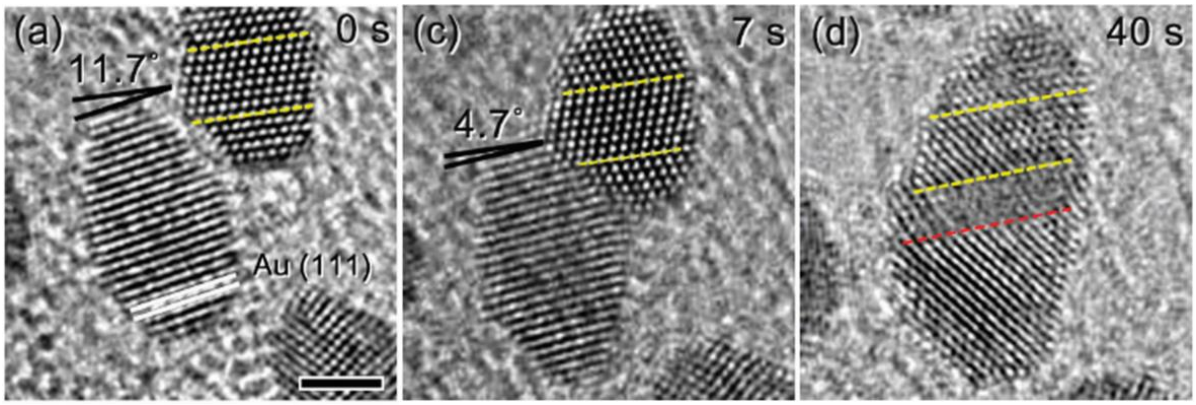

Figure 96. HRTEM study showing orientational alignment of Au NCs. Reprinted with permission from Ref. 252. Copyright 2013 Royal Society of Chemistry.

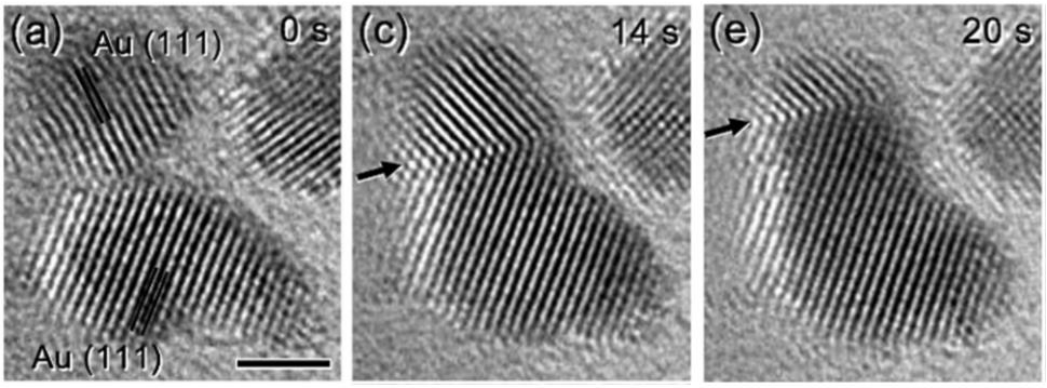

Figure 97. HRTEM study showing grain boundary elimination form a coalesced pair of Au NCs. Reprinted with permission from Ref. 252. Copyright 2013 Royal Society of Chemistry.

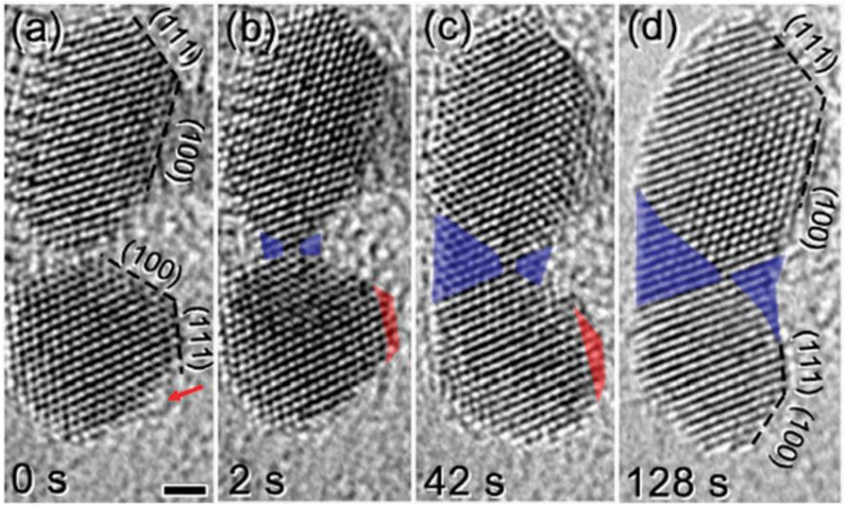

Figure 98. HRTEM study showing sintering of an aligned pair of Au NCs. Reprinted with permission from Ref. 252. Copyright 2013 Royal Society of Chemistry.

Multiple modeling studies of sintering or coalescence of unsupported NCs were in fact motivated by the above type of observations for supported NCs. Thus, it is natural to directly compare behavior in the supported and unsupported cases. To this end, we apply the model of Sec.3.4 with realistic surface diffusion kinetics to compare the sintering of two epitaxially supported Ag NCs on Ag(100) with corresponding behavior for the same unsupported NCs. Figure 99 shows simulations configurations of supported NCs during sintering at 600 °K for relatively weak adhesion with $\phi_s/\phi = \phi_1/\phi_0 = 0.05$. Note that the final NC configuration is significantly modified from that of the corresponding unsupported NC. Behavior is quantified in Figure 100 and compared against that for the unsupported case (showing little difference between the two).

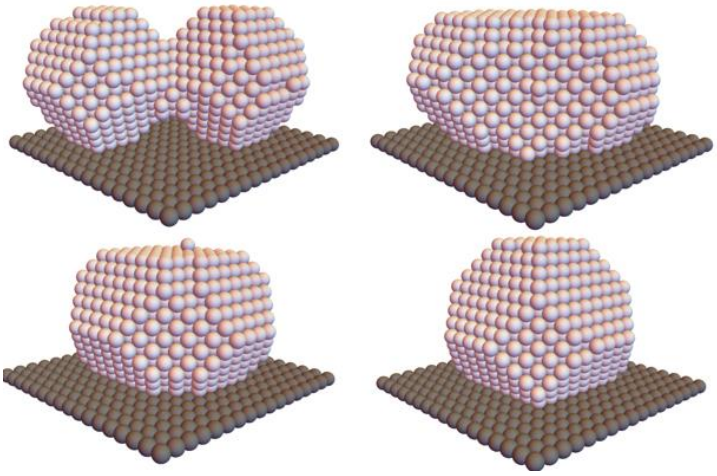

Figure 99: Sintering of homoepitaxially supported Ag NCs on Ag(100) at 600 °K with weak adhesion with $\phi_s/\phi = \phi_1/\phi_0 = 0.05$.

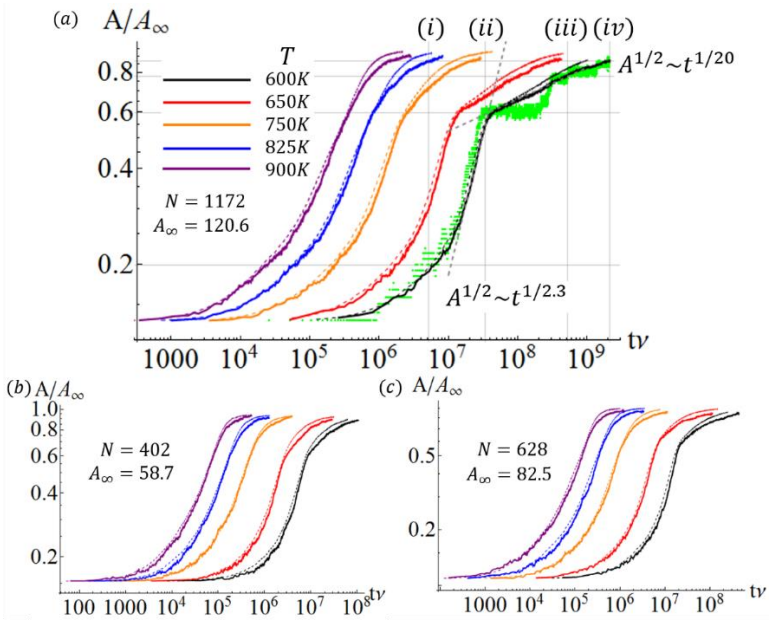

Figure 100: Supported sintering time sequence of different temperature. Only 40 samples of simulation for each line. Thin, dashed line is unsupported cases in previous section.

Finally, we describe observations of pinch-off or breakup phenomena which have in part motivated the modeling studies in Sec.6.4 for unsupported NCs. A Raleigh-Plateau type breakup instability is expected to be a general phenomenon for elongated 3D NCs where it is mediated by surface diffusion. Particularly high-resolution imaging of a single pinch-off event for an ultrathin 1.7 nm diameter Au nanowire (NW) deposited on a carbon-covered Cu support[253] is shown in Figure 101. We note however that the process is impacted by the electron beam. Breakup of NW involves asymmetric modification of apexes followed by formation of multi-atom chains (MACs) of 3-4 atoms and subsequently single-atom chains. Clearly, behavior is not described by the classic

continuum type modeling, and plausibly quantum size effects[254,255] are important. See Ref. 256 for another study of breakup of Au NW on carbon coated Cu support where larger scale images are provided.

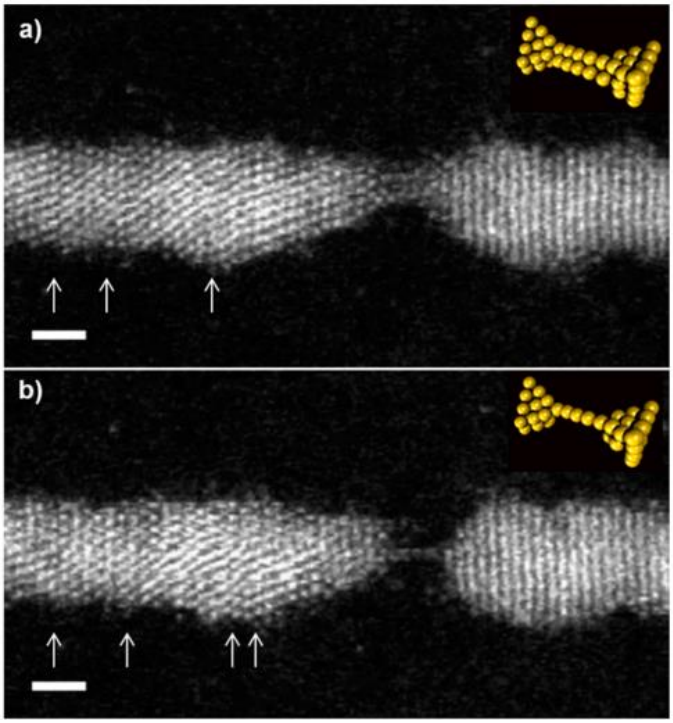

Figure 101. HREM of the pinchoff of an Au nanowire showing 3-4 atom chains, and then a 1 atom chain. Scale bar = 1.7 nm. Reprinted with permission from Ref. 253. Copyright 2014 American Chemical Society.

Next, we describe an analysis of the evolution of ultrathin silver nanowires grown in helium nanodroplets and then deposited onto an amorphous carbon TEM grid yielding irregular (bent) Ag NW morphologies[257] shown in Figure 102. The mean NW length is 500 nm, and the mean width is 5 nm. Images on left were exposed to e-beam which results in the rapid formation of a carbonaceous capping layer inhibiting the fragmented NW from reaching a collection of spherical NCs. However, imaging of a region of the substrate not exposed to the e-beam (image on the right) shows that such evolution is achieved. Quite similar morphological evolution was observed for Au NW with diameters 3 nm up to above 10 nm embedded in block copolymer cylindrical micelle where a detailed characterization of dependence on NP size and separation on NW diameter was also provided.[258]

To demonstrate the generality of pinch-off behavior, our final example illustrates the breakup of a fractal aggregate obtained by depositing Ag_{150} NCs on graphite at room temperature.[189] Figure 103 (a) corresponds to 6 ML of Ag with an arm thickness of 25 nm where pinch-off is limited to near the aggregate center. However, Figure 103 (b) corresponds to just 2 ML of Ag with thinner arms of width 15 nm where pinch-off occurs throughout the aggregate. This example constitutes an analogue for 3D fractal clusters of the experiment shown in Figure 59 for 2D fractal clusters of Ag.

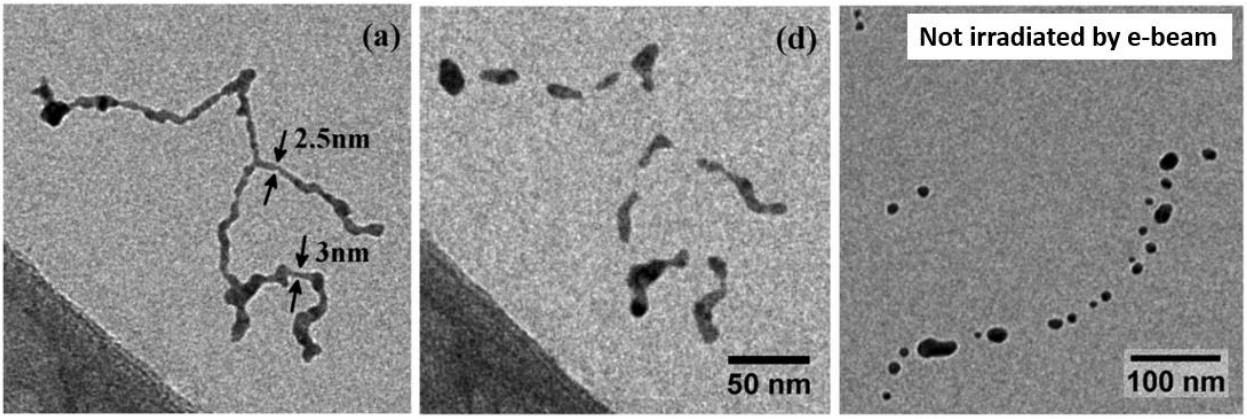

Figure 102. Pinch-off or an irregular Ag nanowire on an amorphous carbon support. The e-beam induced formation of a carbonaceous capping layer inhibits evolution in the middle frame, but not in the right frame. Reprinted with permission from Ref. 257. Copyright 2015 Royal Society of Chemistry.

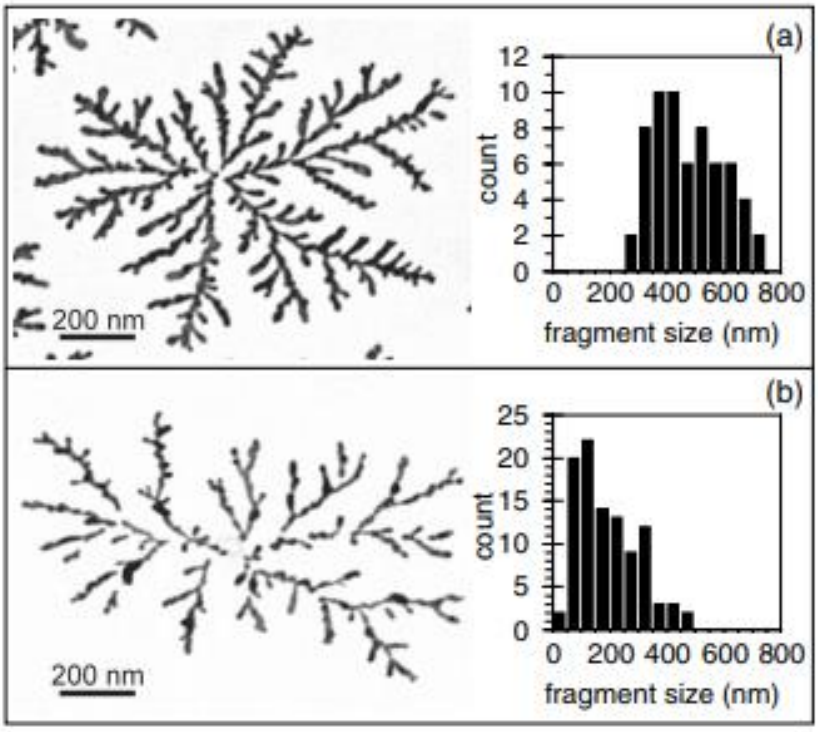

Figure 103. Pinchoff of fractal aggregate of Ag150 clusters on graphite: (a) 6 ML Ag with limited pinch-off; (b) 2 ML Ag with extensive pinch-off. Reprinted with permission from Ref. 189. Copyright 2002 American Physical Society.

7. COMPOSITIONAL EVOLUTION OF 2D AND 3D NCs

7.1. Intermixing and voiding: Basic concepts and theory

The basic concepts in a theoretical formulation of intermixing and related phenomena apply for both multi-component 3D crystalline bulk materials and NCs and 2D epitaxial layers. Since the former has been discussed extensively in contrast to the latter, we start with consideration of this case.

7.1.1. Mechanisms for intermixing and voiding. For intermixing in 3D bulk multi-component crystalline materials, two distinct paradigms have long been considered. Initially, the accepted mechanism was a concerted multi-atom exchange process involving either direct place exchange of two adjacent atoms (which would create very large localized distortions and thus have a high energy barrier), or ring diffusion where multiple atoms move simultaneously. However, subsequently the vacancy-mediated intermixing/diffusion picture of Kirkendall was begrudgingly recognized as a viable alternative.[259] In Kirkendall's picture, exchange of vacancy and adjacent atom positions can lead to intermixing (analogous to plastic letter shuffle games). Traditional studies considered a classic macroscopic "diffusion couple" geometry with a planar interface between two bulk materials, A and B, say. Then, the concerted mechanism imposes a constraint that the diffusion flux, $\mathbf{J}_B$, of B into A must be equal and opposite to the flux, $\mathbf{J}_A$, of A into B. This constraint is absent in the Kirkendall picture where a flux imbalance $|\mathbf{J}_A| \neq |\mathbf{J}_B|$ can be accommodated within the overall mass conservation constraint. Introducing a vacancy diffusion flux, $\mathbf{J}_V$, mass conservation implies that $\mathbf{J}_A + \mathbf{J}_B + \mathbf{J}_V = \mathbf{0}$. Thus, if A is more mobile than B in the sense that $|\mathbf{J}_A| > |\mathbf{J}_B|$, it follows that the vacancy flux $\mathbf{J}_V$ is non-zero and in the direction of $\mathbf{J}_B$ (and opposite to $\mathbf{J}_A$). If $|\mathbf{J}_V|$ is sufficiently large, then there is the possibility for nucleation of voids (vacancy clusters) on the A-side of the diffusion couple. This phenomenon is termed Kirkendall voiding.[54,55,259]

A nanoscale version of a diffusion couple is provided by NCs with a core-shell structure. For systems where the thermodynamically preferred state is an intermixed or alloyed NC, it is natural to assess the stability (i.e., the lifetime as a function of temperature) of the metastable core-shell structure, and the concentration profile evolution during intermixing. Furthermore, one might anticipate a nanoscale version of the above-mentioned voiding phenomena for this geometry. In fact, faster outward diffusion of the core material might lead to an optimum scenario for void formation given the confinement of the vacancy gas and the lack of defects in the crystalline core such as dislocations at which vacancies could be annihilated.[260] Voiding has been observed on nanoscale reaction-diffusion systems where an oxide or sulfide shell is formed around a single-component metallic NCs and also bimetallic core-shell NCs, and outward transport of fast moving cations is roughly counterbalanced by an inward transport of vacancies.[260-263] Voiding and associated formation of hollow and caged NCs have also been identified in various bimetallic systems (Au-Ag, Ni-Pt, Cu-Pt, etc.) as a result of post-synthesis evolution from core-shell structures.[264-267]

For our presentation below, it is appropriate to note that entirely analogous phenomena can be expected to occur for 2D epitaxial bimetallic core-ring NCs which

are readily synthesized by sequential deposition of the two components. In these cases, we just consider 2D vacancy-mediated diffusion within the epitaxial layer as being responsible for intermixing.

With respect to the studies of void formation or hollowing in 3D NCs, it should however be noted that an alternative has been proposed to the commonly adopted Kirkendall picture of vacancy-mediated bulk diffusion at least for room temperature (RT) systems.[268] This proposal was motivated by the recognition that vacancy formation energies can be high for 3D crystalline materials, so that the vacancy population can be extremely low, and consequently at any specific time it is almost certain that a NC contains no vacancies. This feature alone does not imply that intermixing is insignificant. If (short-lived) vacancies are created at a sufficiently high rate at the periphery, intermixing could still be efficient particularly accounting for the random walk nature of their trajectories within the NC. By detailed-balance, the barrier for vacancy formation will be given by the sum of that for bulk vacancy diffusion and the vacancy formation energy. Thus, the formation rate reflects the vacancy hop rate, the vacancy population, and the NC surface area (see below for more details). If the barrier for vacancy diffusion is high, then the vacancy creation rate will be low bring into question the viability of this picture. For a 3D Pt core, the vacancy formation energy is 1.15 eV, so the population of vacancies at RT is 1 per $3x10^{19}$ atoms, i.e., only one 10 nm Pt NC in $8x10^{14}$ NCs contains a vacancy at a given time. Since the barrier for vacancy diffusion in Pt is also high at ~1.5 eV, it was deemed that the Kirkendall mechanism was not viable.[268]

The alternative picture is based on the idea that shape fluctuations at the surface of the 3D core-shell NC lead to the formation of “pinholes” in the shell which survive for sufficiently long that the core can be etched away.[268] In principle, this problem can be analyzed in detail utilizing the Langevin formulation of Sec.4.2. However, a simpler analysis was performed considering the probability that shape fluctuations for given spherical harmonic modes exceed a required threshold to expose the core (where this probability increases with mode number reflecting the associated shorter distance for mass transport), and the characteristic time for relaxation of such modes (which decreases with mode number as shown in Sec.4.1.2). The picture was shown to be viable for Pt or PtO shell NCs. It was also shown that once a pinhole forms, it quickly closes consistent with the lack of experimental observation of such pinholes.

7.1.2. Theoretical formulation for vacancy-mediated intermixing. The general formulation applies for both 2D epitaxial and 3D crystalline NC systems. We start with discussion of vacancy diffusion in a single-component material (traditionally for a 3D bulk crystalline material). The key concept is that the effectiveness of vacancy diffusion depends on two components: the population of vacancies (which is controlled by thermodynamics and specifically the vacancy formation energy, E_{form}) and the rate (or barrier, E_{dv}) at which an atom adjacent to the vacancy hops to the vacancy position. The effective barrier for transport associated with vacancy diffusion is reasonably associated with the sum $E_{effv} = E_{dv} + E_{form}$.[269] E_{dv} is straightforwardly determined for either 2D epitaxial layers of 3D bulk systems just from the difference in energies (e.g., determined from DFT) for the initial configuration and the transition configuration if the latter is clear from symmetry considerations, or from a full Nudged Elastic Band (NEB) calculation.

The formation energy, E_{form}, corresponds to the energy change upon creating a vacancy in a semi-infinite cluster by shifting an atom from the interior to a kink site on the periphery. For a 2D epitaxial NC, this kink site should be at a straight extended step edge. For a 3D NC the kink should be at an extended straight step on a flat extended facet. See Figure 104. Note that a 2D epitaxial layer or 3D crystal can be grown indefinitely by repeatedly adding atoms to such sites. It is also clear that the formation energy corresponds to the lateral interaction energy per atom in interior of a 2D epitaxial layer, and the total interaction energy per atom in the interior of a 3D crystal. For DFT-level determination of E_{form}, the following formulation is utilized. We consider a cell with M sites and let E_{bulk} denote the energy where all sites are occupied by atoms, and E_{vac} denote the energy where M-1 sites are occupied and there is one vacancy. For plane-wave DFT analysis, the computational cell has periodic boundary conditions. The aforementioned energies involve just lateral interactions in the 2D case, and all interactions in 3D. Then, one has that[269]

$$E_{form} = E_{vac} - (M-1)E_{bulk}/M. \quad (79)$$

For a listing of E_{form} and E_{dv} for various pure metals, see Ref. 270. It should also be noted that corrections to account for "intrinsic surface error" are often required in DFT analysis of E_{form}.[269]

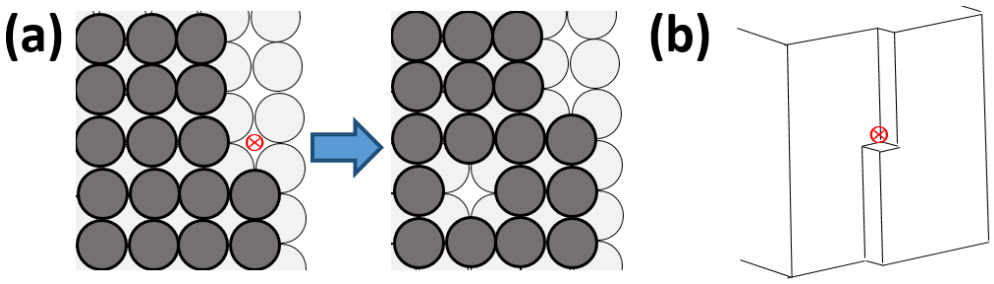

Figure 104. Vacancy formation moving an interior atom to a kink site ⊗: (a) 2D epitaxial layer; (b) 3D crystal.

Our main focus is on two-component systems, and specifically on the diffusion of B impurities in A. The description below applies to both 2D epitaxial NCs and 3D crystalline NCs. Here, the picture is that typically the B impurity is surrounded by A atoms. However, when a vacancy in the A-crystal diffuses to a site adjacent to the B impurity, then the B atom can hop to that vacancy site, and then an A atom can then hop to the vacancy position and subsequently the vacancy can diffuse through the A-crystal away from the B impurity. Thus, it is clear that beyond the formation energy and hopping barrier relevant for diffusion of vacancies through the pure A-crystal, additional energies should be considered (although this is not commonly the case).[25,271] The first of these is the hopping barrier, E_{dv}(B-V in A), for B to hop to the adjacent vacancy site, V. This barrier naturally is distinct from the barrier, $E_{dv} = E_{dv}$(A-V in A) for vacancy hopping in pure A. The second is the formation energy, E_{form}(B-V in A), to create a vacancy adjacent to the B-impurity in A. This energy is naturally distinct from $E_{form} = E_{form}$(A-V in A) for vacancy formation in pure A.

It is appropriate to comment in detail on the interpretation and also the evaluation of E_{form}(B-V in A).[25] Considering diffusion of a B impurity in an otherwise pure A NC, the formation energy corresponds to the energy change upon creating a vacancy by shifting an A atom from the site adjacent to B to a kink site. See Figure 105(a) providing an example for 2D epitaxial NCs. This is analogous to the discussion above for pure A illustrated in Figure 104. However, of more interest is the diffusion of a B impurity in the core of an A-core + B-shell NC. Here, the formation energy corresponds to the energy change upon creating a vacancy by shifting an A atom from the site adjacent to B to a kink site at the interface between the A-core and B-shell, and also moving a B-atom at this interface to a kink site on the outer periphery of the B-shell. See Figure 105(b). It is straightforward to show that E_{form}(B-V in A) is the same for both of these scenarios. For DFT-level determination of E_{form}(B-V in A), the following formulation is utilized. We consider a cell with M sites. Let E_{bulk}(B in A) denote the energy where M-1 sites are occupied by A and one site by B, E_{vac}(B-V in A) denote the energy with M-2 sites occupied by A, one site occupied by B, and a site adjacent to B vacant, and E_{bulk}(A) denote the energy where all M sites are occupied by A. For plane-wave DFT analysis, the computational cell has periodic boundary conditions. The aforementioned energies involve just lateral interactions in the 2D case, and all interactions in 3D.Then, one has that [271]

$$E_{form}(\text{B-V in A}) = E_{vac}(\text{B-V in A}) + E_{bulk}(\text{A})/M - E_{bulk}(\text{B in A}). \quad (80)$$

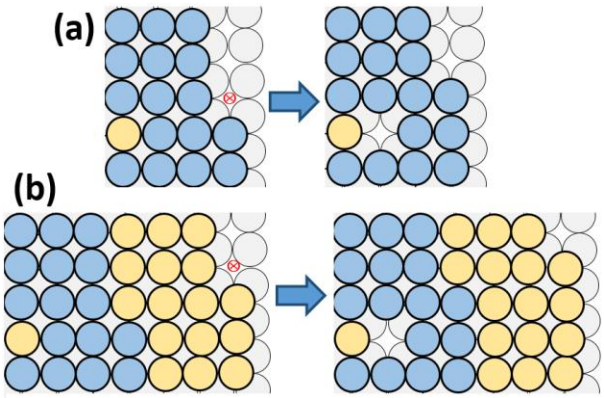

Figure 105. Formation of a vacancy next to a B impurity in an A region of a NC.

Finally, we consider the effective diffusion barrier for impurity diffusion, E_d(A in B). Since this requires the presence of a vacancy as well as hopping into a vacancy, E_d(A in B) is given by the sum of an appropriate E_{dv} and E_{form}. However, different regimes require different choices. First, consider the case where impurity hopping is slow compared to all other relevant rates, i.e., E_{dv}(B-V in A) is large. Then, one anticipates that the distribution of vacancies in the NC is equilibrated with respect to the quasi-static impurity. Impurity hopping is not limited by transport of vacancies to the impurity, but by hopping of the impurity itself to an adjacent vacancy, and by the population of such adjacent vacancies. The probability of an adjacent vacancy is controlled by E_{form}(B-V in A) rather than by E_{form}(A-V in A) and thus E_d(A in B) = E_{dv}(B-V in A) + E_{form}(B-V in A) (cf. Ref. 25). Second, consider the case where impurity

hopping is fast compared to other relevant rates. Then, once the vacancy is adjacent to the impurity, the impurity and the vacancy switch positions many times before the vacancy diffuses away from the impurity. Thus, there is a probability of ½ that the impurity is in a different position when the vacancy departs. In this case impurity diffusion is not limited by impurity hopping, but by transport of vacancies through A to the impurity. If E_{form}(B-V in A) < E_{form}(A-V in A), then it is also clear that impurity diffusion is limited by the formation of vacancies in A and that E_d(A in B) = E_{dv}(A-V in A) + E_{form}(A-V in A) (cf. Ref. 271).

7.1.3. Ab-initio kinetics for vacancy-mediated intermixing. In Sec.3.5.1, we have described modeling with ab-initio kinetics of formation and reshaping of Ag, Au, and Ag+Au 2D epitaxial NCs on Ag(100). The focus was on an accurate description of periphery diffusion for various local configurations and compositions of the typically convex step edge in the neighborhood of the diffusion edge atom. Unconventional ϕ interactions most relevant or prominent for such periphery diffusion processes are indicated in Figure 17 (right). These all ϕ's have the feature that all the atoms at adsorption sites (i.e., atoms in the NC) are "on one side" of the single atom at the bridge-site transition state or TS (which is diffusing at the periphery of the NC). In contrast, for vacancy mediated diffusion, the hopping atom at the TS has atoms at adsorption sites on "both sides". Thus, it is necessary to determine the corresponding additional unconventional trio interactions, ϕ_{t4} and ϕ_{t5}, shown in Figure 106. In addition, these interactions are relevant for evolution at concave step edges, e.g., the corner of pits where "atom sliding" out of the pit corner needs to be accurately described.[27] See Sec.5.2.

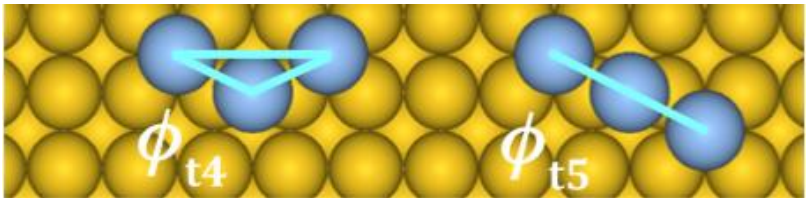

Figure 106. Additional unconventional interactions, ϕ_{t4} and ϕ_{t5}, for relevant for vacancy-mediated diffusion.

For the Au (= G) + Ag (= S) on Ag(100) system, there are 12 such interactions (SSS, GGG, SGS, GSG, SSG, GGS for each of ϕ_{t4} and ϕ_{t5}). These interactions are selected to precisely describe transition state energies for vacancy-mediated diffusion in various local environments, for extraction from straight steps for c(2x2) alloy structures (which is also relevant for intermixing), and also for atom sliding from pit corners. See Figure 107 which shows the configurations whose energies are used to determine ϕ_{t4} and ϕ_{t5} where the central atom at the bridge site TS is S. The results are listed in Table 6. Interchanging S and G in these configurations gives another 6 configurations whose energies used to get the 6 trios with G at the TS. This diversity of configurations is needed to obtain sufficient independent equations to determine all of these ϕ's.

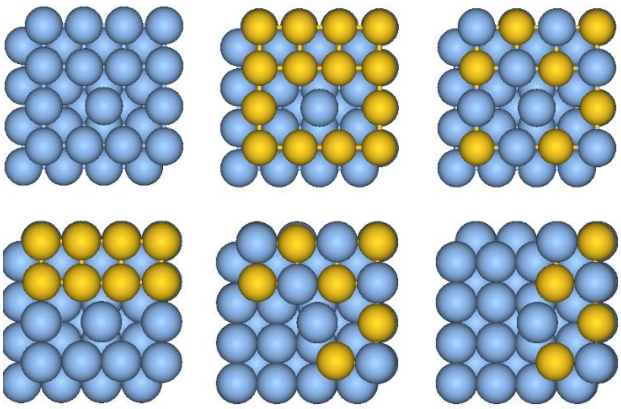

Figure 107. Configurations whose energies determine the six ϕ_{t4}(XSY) and ϕ_{t5}(XSY), with X,Y = S or G.

Table 6. ϕ_{t4} and ϕ_{t5} interactions for Ag(S) + Au(G) on Ag(100). The middle letter corresponds to the central atom at the TS. Values in eV. All interactions are repulsive.

	SSS	GSG	SSG	GGG	SGS	GGS
ϕ_{t4}	0.050	0.067	0.054	0.070	0.070	0.079
ϕ_{t5}	0.009	0.021	0.010	0.027	0.036	0.035

Finally, as an illustration of the ab-initio level determination of barriers for vacancy-mediated diffusion, consider Figure 108 showing hopping of an Au atom to an adjacent vacancy in the interior of an Au-Ag alloy island on Ag(100). The initial state energy, E_{init}, is determined from the sum of 3 ω_{1p}, 4 ω_{2p}, 4 ω_{lt}, and 3 ω_{lt} interactions. The transition state energy is determined from the sum of the terrace diffusion barrier for Au on Ag(100), E_d(Au), and 4 ϕ_{1p}, 2 ϕ_{2p}, 4 ϕ_{b1t}, 4 ϕ_{b2t}, and 2 ϕ_{tt} interactions, as well as 2 ϕ_{4t} and 2 ϕ_{5t} interactions determined as described above. The KMC simulation code which is applied below to describe the transition from bimetallic core-ring NCs to intermixed NCs automatically determines barriers for all such hops from pre-calculated and tabulated values of ω- and ϕ-interactions.

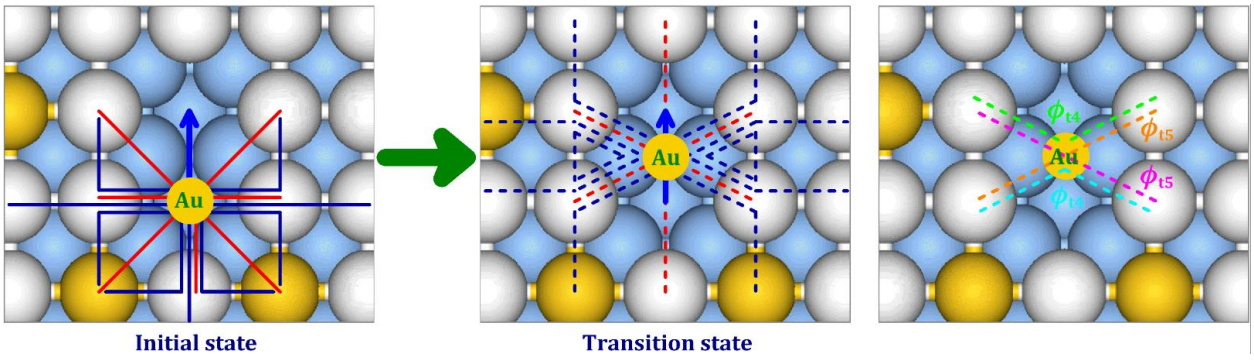

Figure 108. An example of the interactions in the initial state and at the TS for needed to determine the barrier for vacancy-mediated diffusion of Au within a specific Ag-Au alloy configuration on Ag(100).

One can anticipate an analogue for 3D crystalline NCs of the above formulation for 2D epitaxial NCs. However, this is predicted on being able to describe the TS as being located at a simple high-symmetry local-environment-independent position (analogous to the bridge site in the above 2D example). Such a formulation has yet to be implemented.

7.2. Evolution of 2D epitaxial core-ring NCs

Here, we apply the formulation in Sec.7.1.3 for the ab-initio treatment of intermixing kinetics in 2D epitaxial layers to consider the post-synthesis (i.e., post-deposition) evolution of core-ring NCs for two systems. Synthesis of these core-ring NCs is achieved simply by sequential deposition. Since these multicomponent systems have intermixed or alloy equilibrium structure, post-synthesis evolution naturally leads to destruction of the core-ring structure given sufficiently long times and/or sufficiently high temperatures.

Ag+Au on Ag(100): Our DFT analysis for the ab-initio thermodynamics of this system in Sec.3.5.1 indicates a weak preference for c(2x2) alloy ordering of Ag+Au NCs on Ag(100).[25] Thus, the equilibrium structure of these NCs is intermixed.

Our formulation for ab-initio kinetics described in Sec.7.1.3 recovers exactly the DFT value for E_{dv}(AgV in Au) = 0.578 eV as the associated configuration (upper middle frame in Figure 107) is used in our determination of ϕ_{t4}(AuAgAu) and ϕ_{t5}(AuAgAu). We also recover exactly the DFT value of E_{dv}(AuV in Au) = 0.750 eV as the associated configuration corresponding to vacancy diffusion in an Au alayer is used in our determination of ϕ_{t4}(AuAuAu) and ϕ_{t5}(AuAuAu). We also obtain E_{form}(Ag-V in Au) = 0.460 eV and E_{form}(Au-V in Au) = 0.474 eV from the ω-interactions provided in Ref. 25 which incorporates the same thermodynamics (i.e., the same ω's) as in the model utilized here, but not the same kinetics (i.e., we have added ϕ_{t4} and ϕ_{t5}). Consequently, based upon the discussion in Sec.7.1.2, one has that

$$E_d(\text{Ag in Au}) = E_{dv}(\text{Au-V in Au}) + E_{form}(\text{Au-V in Au}) = 1.22 \text{ eV}. \quad (81)$$

Similarly, our formulation for ab-initio kinetics recovers exactly the DFT values of E_{dv}(Au-V in Ag) = 0.562 eV and E_{dv}(Ag-V in Ag) = 0.470 eV. We also obtain E_{form}(Au-V in Ag) = 0.441 eV and E_{form}(Ag-V in Ag) = 0.428 eV from Ref. 25. Consequently, again based upon the discussion in Sec.7.1.2, one has that

$$E_d(\text{Au in Ag}) = E_{dv}(\text{Au-V in Ag}) + E_{form}(\text{Au-V in Ag}) = 1.00 \text{ eV}. \quad (82)$$

These analyses are relevant for interpretation of our simulation results below.

First, we present the results of simulations for the post-synthesis evolution of Ag core + Au ring NCs which were formed by first deposition 0.1 monolayers (ML) of Ag on Ag(100) at 325 K, and then depositing 0.3 ML of Au at 335 K. A typical initial core-ring configuration is shown on the left in Figure 109. Subsequent evolution at two different temperatures, 400 K and 500 K, is shown in the frames on the right. In both cases, intermixing is evident. However, there is a strong asymmetry in that Au atoms diffuse much more readily into the Ag core that Ag atoms diffuse into the Au ring. This

asymmetry is immediately explained by the above results showing that E_d(Ag in Au) > E_d(Au in Ag). Second, we present results for the post-synthesis evolution of Ag core + Au ring NCs formed by first deposition 0.1 ML of Au on Ag(100) at 360 K, and then depositing 0.3 ML of Ag at 300 K. A typical initial core-ring configuration is shown on the left in Figure 110. The same asymmetry in diffusion is seen as for the Ag core + Au ring NCs again explained by our DFT results for impurity diffusion barriers.

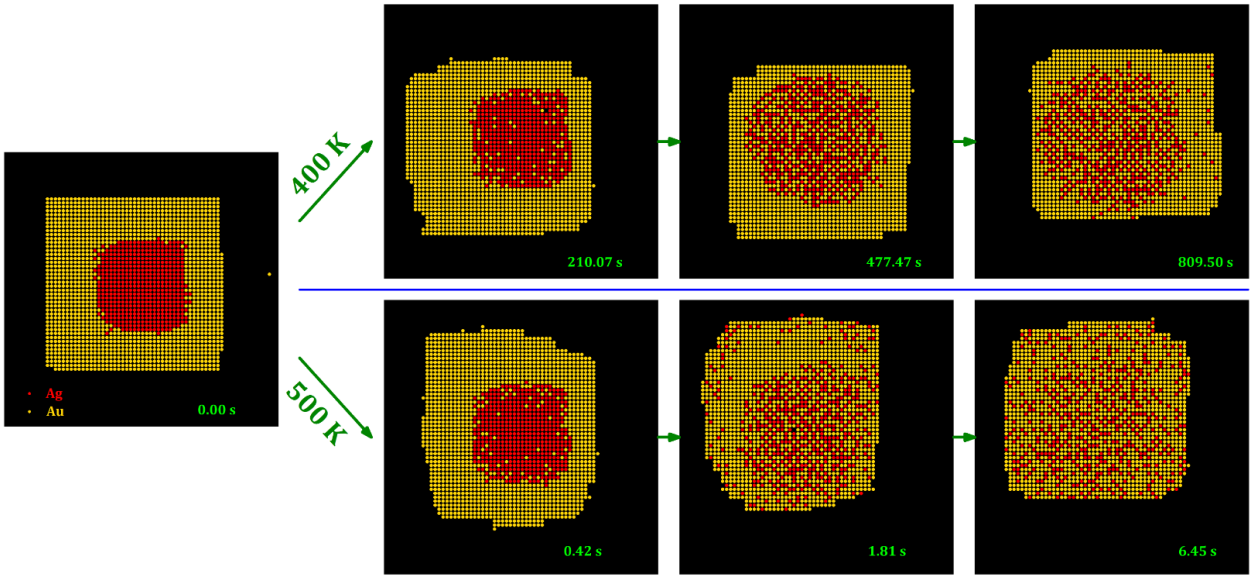

Figure 109: Post-synthesis evolution of Ag core + Au ring NCs on Ag(100) formed by sequential deposition of 0.1ML Ag @ 325 K then 0.3 ML Au @ 335 K.

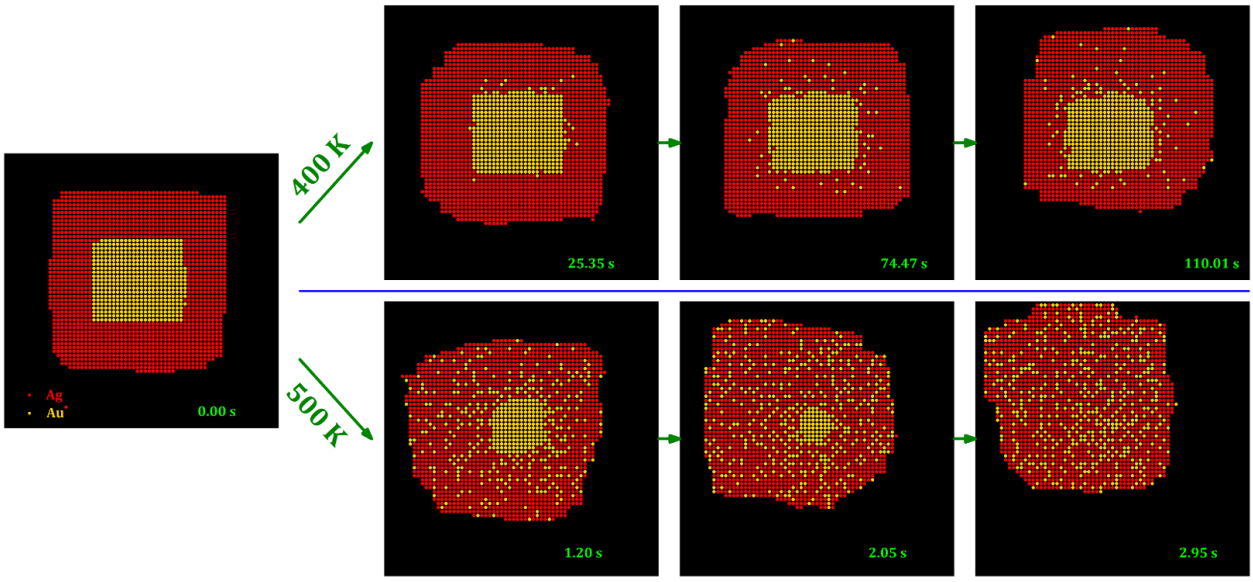

Figure 110: Post-synthesis evolution of Au core + Ag ring NCs on Ag(100) formed by sequential deposition of 0.1ML Au @ 360 K then 0.3 ML Ag @ 300 K.

Ni+Al on NiAl(110): Our second example for core-ring epitaxial NCs involves a more complex binary alloy substrate, NiAl(110). However, since we consider NCs composed of Ni and Al, the equilibrium structure of adlayers or NCs is clear at least for a 1:1 Ni:Al stoichiometry since these must propagate the perfect alloy ordering of the substrate. Thus, the equilibrium structure of 2D epitaxial NCs with 1:1 Ni:Al composition has alternating columns of Ni and Al (for our orientation of surface images). See Figure 18. For a 3:1 Ni:Al stoichiometry, perfectly ordered Ni_3Al structure is believed to correspond to the equilibrium ordering.[24]

Before discussing post-synthesis evolution, we first show a comparison of STM imaging and ab-initio KMC simulation of NC structure just after synthesis of core-ring NCs by sequential deposition at room temperature.[73] See Figure 111. For deposition of Al then Ni, a classic core-ring structure is realized in both experiment and simulation with little restructuring of the Al core during subsequent deposition of Ni and aggregation around the Ni core periphery to form a ring. This is understood since analysis of our ab-initio model reveals a high barrier of ~1.55 eV to extract Al from the periphery of the core even aided by nearby Ni atoms which can reduce the TS energy. For deposition of Ni then Al, STM imaging reveals a complex structure. This observation is explained by simulation which reveals that the Ni core is not robust, and that aggregation of Al at the periphery of this core facilitates extraction of Ni atoms at the core. As a results, voids form initially near the periphery of the core. This behavior which corresponds to a 2D nanoscale version of Kirkendall voiding is explained by model analysis revealing an Al-assisted Ni-extraction barrier of only ~0.55 eV. Finally, we note that sequential deposition at higher T leads to substantial intermixing.[24]

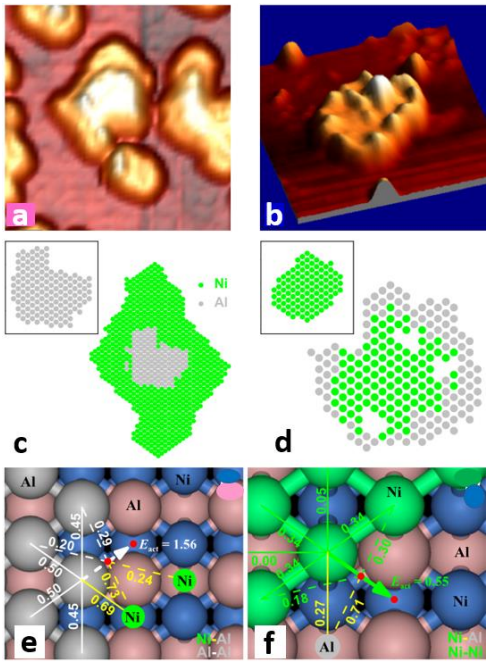

Figure 111. Sequential deposition at 300 K on NiAl(110) of: Al then Ni (a = STM; c = KMC); Ni then Al (b = STM; d = KMC). Barrier for extraction of: Al assisted by Ni (e); Ni assisted by Al (f). Reprinted with permission from Ref. 73. Copyright 2011 National Academy of Science.

Next, we analyze the post-synthesis evolution of the above core-ring NCs using our model from Sec.3.5.1 for ab-initio kinetics. We focus on Ni core – Al ring NCs which are more susceptible to substantial restructuring on time-scales accessible to simulation although this requires elevated temperatures. Figure 112 shows the evolution at both 1000 K and 1500 K of a Ni core – Al ring NC with 1:1 Ni:Al composition formed by room temperature deposition as described above. Outward diffusion of Ni into the surrounding Al shell leads to significant expansion of the small voids in the Ni core which were formed during synthesis. Partial development of perfect NiAl(110) order (with alternating rows of Ni and Al) is evident at 1000 K on the time scale of the simulation, and such perfect order is fully achieved at 1500 K on a much shorter time scale. It should be noted that during these simulations, there is significant diffusion of the NC, and the field of view in Figure 112 is adjusted to maintain the NC in the center. Next, in Figure 113, we track the evolution just at 1000 K of a Ni core – Al ring NC with 3:1 Ni:Al composition again formed by room temperature deposition. Similar to the case with 1:1 Ni:Al composition, there is a significant expansion of the void in the initial Ni core as Ni diffuses outward into the Al ring. However, there is limited development of perfect Ni_3Al/NiAl(110) structure with alternating columns of pure Ni and 1:1 Ni:Al (and where Ni and Al alternate in the latter)[24] over the time-scale of the simulation.

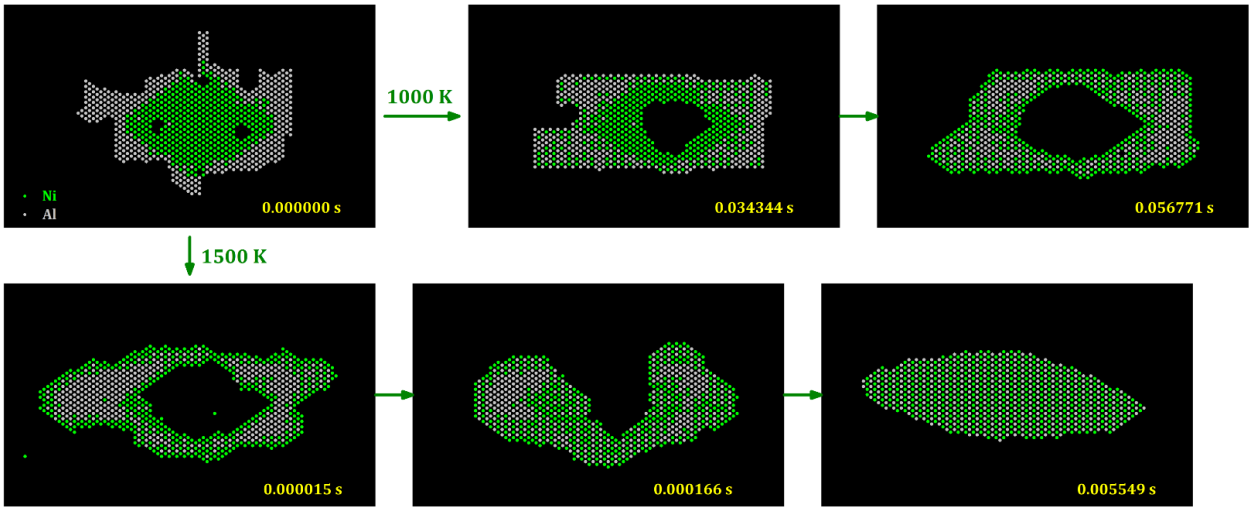

Figure 112: KMC analysis of annealing of a 1:1 Ni:Al Ni core – Al ring NC at 1000 K and 1500 K.

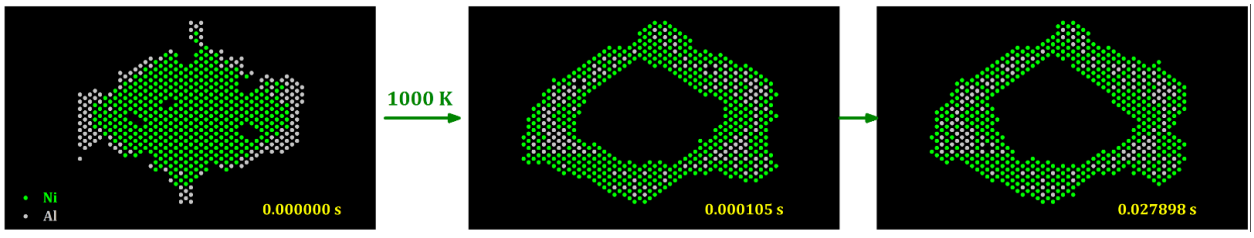

Figure 113: KMC analysis of annealing of 3:1 Ni:Al Ni core – Al ring NC at 1000 K.

Finally, ab-initio modeling was also used to analyze the evolution of Al core – Ni ring NCs. However, even at 1500 K, little evolution of the robust Al core was observed over the time scales accessible to simulation (which are short at ~10^{-3} s).

7.3. Evolution of unsupported 3D core-shell and sandwich or multi-shell NCs

Here we consider a few cases of the evolution of multi-component 3D NC which is mediated by intermixing describing both TEM imaging and associated theory.

Stability of shaped Pd core – Pt shell NCs. A fundamental question for the catalytic functionality of shaped core-shell NCs is stability against reshaping (cf. Sec.6.1) and intermixing (this Sec.7) at elevated temperatures. Pd nanocubes with well-defined {100} facets and also Pd octahedra with well-defined {111} facets have been used as a template for the initial formation of Pd core – Pt shell nanocubes with conformal shells of controlled thickness in the range 1-6 layers.[272] The thermal stability of such NCs with 4 layer shells was recently assessed through TEM analysis and theoretical modeling.[273] It was found that the nanocubes were less robust against reshaping, but more robust against intermixing. The behavior for nanocubes is shown in Figure 114 indicating a loss of cubic shape after heating to 500 °C and a loss of core-shell structure at 800 °C. For octahedra, the core-shell structure is lost after heating to 600 °C, and the shape is degraded after heating to 900 °C.

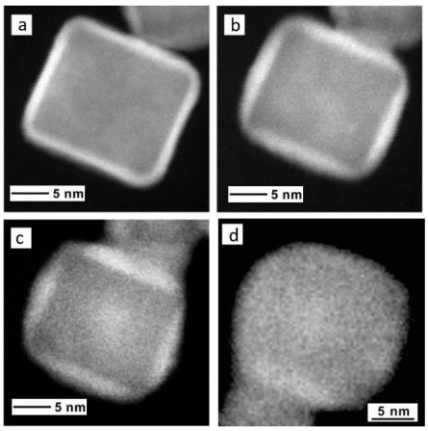

Figure 114. Pd core – Pt shell NC: (a) 400 °C 20 min; (b) 500 °C 60 min. (c) 700 °C 10 min. (d) Quick heating to 800 °C. Reprinted with permission from Ref. 273. Copyright 2017 American Chemical Society.

First, we discuss reshaping which involves the diffusion of atoms across the surface of the NCs. Diffusion of an isolated Pt adatom on {111} facets occurs via hopping (DFT matching the barrier of 0.26 eV extracted from the analysis of STM studies on extended surfaces[8]). Diffusion of Pt in {100} facets occurs via exchange (DFT matching the barrier of 0.47 eV obtained from FIM studies[150]). However, these do not correspond to the effective barriers for reshaping. Thus, Ref. 273 presented an instructive analysis of the barrier to move an atom on the edge of a perfectly shaped NC to a facet which is the initial step during reshaping of the NCs. For the structural model used for the Pt cube, the edge atom was 5-coordinated and the barrier was 0.60 eV (the

process is exothermic by ΔE = -0.15 eV). For the octahedron, the edge atom was 7-coordinated and the barrier was 1.99 eV (the process was endothermic by ΔE = +1.64 eV). This difference is consistent with the more facile reshaping of nanocubes. However, a different model for cubes with more heavily truncated edges as used in Sec.6.1 would make it harder to reshape cubes. Also prescription of the effective barrier for reshaping requires consideration of nucleation of new facts as also discussed in Sec.6.1.

Next, we discuss intermixing. Ref. 273 also presented a DFT analysis to provide insight into this behavior. Concerted ring-diffusion processes at the interface were ruled out given high barriers >5 eV. Thus, vacancy-mediated intermixing was proposed as the dominant mechanism. Figure 115 shows the results of an instructive DFT analysis of the energetics associated with an isolated vacancy in the surface layer of a 4 layer Pt shell diffusing to the Pt-Pd interface and thereby initiating intermixing. This process is more favorable for octahedral rather than cubes consistent with more facile intermixing for the former. Note that this is a kinetic picture where the initial "high energy" configuration with an isolated vacancy in the top layer is anticipated to be produced during shell growth. This corresponds to a high supersaturation of such vacancies. Equilibration would produce much lower densities, where effectively the vacancy would diffuse to a corner site in a surface facet on the NC lowering the energy of the initial state. This would correspond to higher effective barriers for the intermixing process.

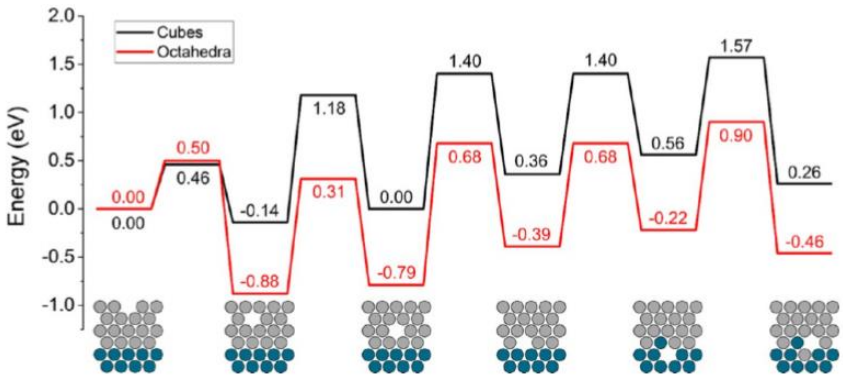

Figure 115. Energetics associated with an isolated surface-layer vacancy in the 4 layer Pt shell diffusing to the Pt-Pd interface and subsequent Pt-Pd intermixing. Reprinted with permission from Ref. 273. Copyright 2017 American Chemical Society.

Pd core – Pt shell NC evolution to Pt nanocages. Shaped Pd core – Pt shell NCs synthesized as described above with of 1-6 layers, when in a solution environment conducive to etching or removal of Pd from exposed Pd surfaces, transformed to create Pt nanocages.[272] The extremely high dispersion of Pt and also the facet selectivity is again appealing for catalysis applications[272]. See Figure 116(a,b). The focus of the analysis was on the mechanism for hollowing of the Pd core – Pt shell NCs. DFT analysis assessing the diffusion of Pd through a 4 layer Pt shell was performed (although not accounting for the Pd-Pt interface). Analysis of barriers for concerted 3-atom and 4-atom ring diffusion suggest a barrier of ~2 eV. The barrier for hopping of a Pd impurity to an adjacent vacancy in Pt was determined as E_{dv}(Pd-V in Pt) = 0.88 eV

versus E_{dv}(Pt-V in Pt) = 1.05 eV (which is lower than values in Ref. 269, 271). The value of E_{form}(Pd-V in Pt) is not available, but since E_{form}(Pt-V in Pt) = 1.2 eV,[269] it follows that a lower estimate for the barrier for vacancy-mediated diffusion of Pd in Pt of E_d(Pd in Pt) = 2.25 eV. Thus, these processes should not be active at the experimental temperature of 100 °C.

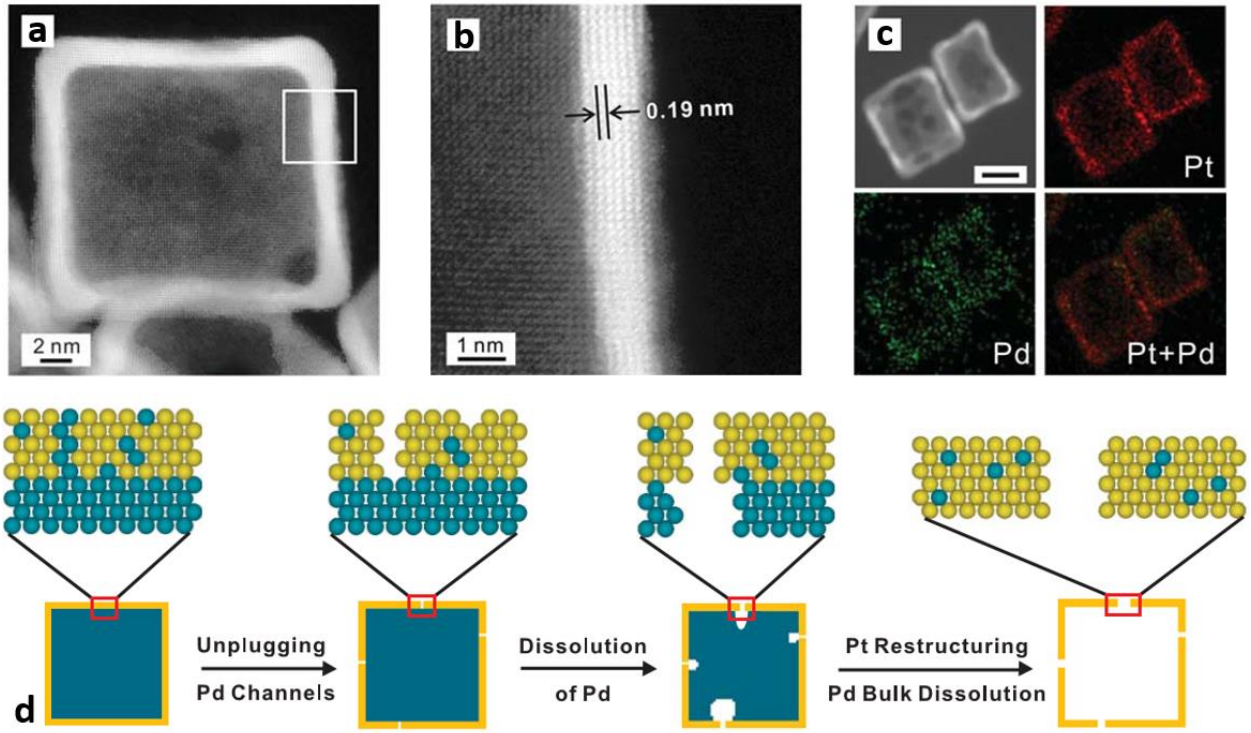

Figure 116. (a,b) Pd core - Pt shell nanocubes; (c) Pt nanocages; (d) mechanism for hollowing. Reprinted with permission from Ref. 272. Copyright 2015 American Association for the Advancement of Science.

Consequently, a different picture was developed for the hollowing process. DFT analysis using a 3x3 lateral unit cell for a Pt atom on a {100} Pd facet (in vacuum) finds a surface hopping barrier of E_d = 0.99 eV which should be contrasted with a significantly lower barrier of E_{ex} = 0.74 eV for the exchange of Pt with a surface Pd atom.[272] The latter process is exothermic by 0.38 eV. Thus, the exchange process is not only thermodynamically preferred, but also facile at experimental temperatures and thus should occur during synthesis of the Pd core – Pt shell NCs to form an intermixed Pt-Pd shell as shown in Figure 116(c). One expects some population of contiguous strings of Pd atoms which traverse the Pt shell. Then, etching of the top-most surface Pd, and subsequent diffusion through the opened channel to the surface and etching of the remaining Pd open a channel traversing the Pt shell. Over time, these channels may grow in size and reconstruct to allow direct corrosion of Pd from the core.

The Pd etching or corrosion of the pore is somewhat slow given the narrow nature of at least the initial channels formed. However, a control experiment where Pt and Pd are co-titrated during Pt (and Pd) deposition results in much faster etching. This

is consistent with the above pitcher since co-titration should produce a higher Pd content in the shell and thus form wider channels during etching.

As an aside, calculation of surface exchange barriers has been considered for various systems based upon early observations of exchange diffusion dominating surface hopping in homoepitaxial systems such as Pt/Pt(100).[150]. However, it has become clear that values obtain are sensitive to lateral unit cell size (small cells artificial constraining atom movement), and convergence to precise values can require cell sizes well above 3x3[274]. Indeed, DFT PBE analysis of the barrier for Pt exchange on a Pd(100) surface using a 4x4 unit cell yields a lower barrier of E_{ex} = 0.60 eV (whereas E_d and ΔE change little from values for the 3x3 unit cell).[27]

Finally, we note that octagonal Pt nanocages have also been synthesized starting with Pd core – Pt shell NC's with an octahedral Pd core. In this way, the surface of the nanocages was changed from {100} to {111} facets.

The facile and thermodynamically preferred exchange of Pt with the Pd(100) surface prompts consideration of the generality of this phenomenon which may be relevant for understanding the evolution of other transition metal bimetallic core-shell NC systems. A systematic DFT-based analysis has been performed for a large number of pairs of metals for both {100} and {111} facets.[275] Metals included Cu, Ag, Au, Ni, Pd, Pt, Rh, and Ir. See also Ref. 27. The general trend is that substitution of adatoms of more noble metals with lower bulk cohesive energies (to the right in the periodic table) into a substrate of less noble metals with higher bulk cohesive energies (to the left in the periodic table) is unfavorable (i.e., endothermic). Substitution of less noble atoms into more noble substrates is generally favored (i.e., exothermic). These trends are realized for the Pt-Pd pair with cohesive energies E_c(Pt) = 5.84 eV and E_c(Pd) = 3.89 eV.

Pt nanocube evolution to PtSn intermetallic NCs. Intermetallic NCs including PtSn have particular advantages for catalysis applications with more precise control of surface structure facilitating a better understanding of structure-property relationships.[276] Recent studies have explored the transformation of Pt nanocubes to PtSn NCs, including a characterization of the kinetics and in one case also the energetics.[271,277] One of these studies utilized in situ synchrotron XRD to track transformation kinetics of 6 nm Pt NC seeds under temperature ramping from 110 °C to 280 °C (at 15 °C/min) and maintaining 280 °C for 30 min.[277] The complete transformation was observed with a corresponding doubling in size as confirmed by HRTEM. See Figure 117. Kinetics was fit with a traditional constant-*T* macroscale Arvami model suggesting that transformation is controlled by diffusion of Sn into Pt.

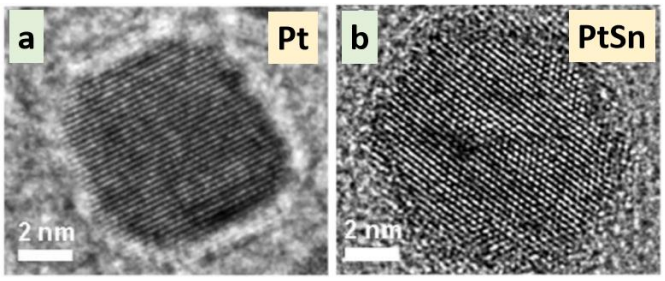

Figure 117. HRTEM images of 6 nm Pt seeds and the subsequent PtSn NCs. Reprinted with permission from Ref. 277. Copyright 2018 American Chemical Society.

We focus on another study which provided a detailed characterization of the transformation kinetics of both 5 nm and 14 nm Pt nanocubes for a range of temperatures, thereby enabling an Arrhenius analysis contingent of development of appropriate models for the transformation kinetics.[271] A schematic of the transformation process based on this study is shown in Figure 118 (top). There are two distinct stages. In the first "surface stage", a portion of the surface of the Pt nanocube remains exposed to the solution, and facilitates reduction of Sn and likely also intermixing and diffusion of Sn into the Pt NC. This surface stage ends when a PtSn shell (initially of variable thickness) has first formed around the entire Pt NC surface. It appears that Sn reduction is facile, so that an observable Sb shell does not form in the first stage of transformation (but it was observed in later stages). We focus on kinetics in this first stage which is modeled assuming that the fractional conversion, α = PtSn/(Pt + PtSn), satisfies d/dt α = A exp[-$E_{eff}/(k_BT)$] (α_{surf} - α)^m, and α_{surf} denotes the α-value at the end of this stage. Fitting data for 5 nm Pt nanocubes shows α_{surf} = 0.30, 0.57, 0.79 for 230, 240, 250 °C with m = 1.75 and E_{eff} = 2.54 eV. See Figure 118 (bottom left). A similar analysis for 14 nm Pt nanocubes yields m = 1.63 with E_{eff} = 2.33 eV and somewhat lower α_{surf}.

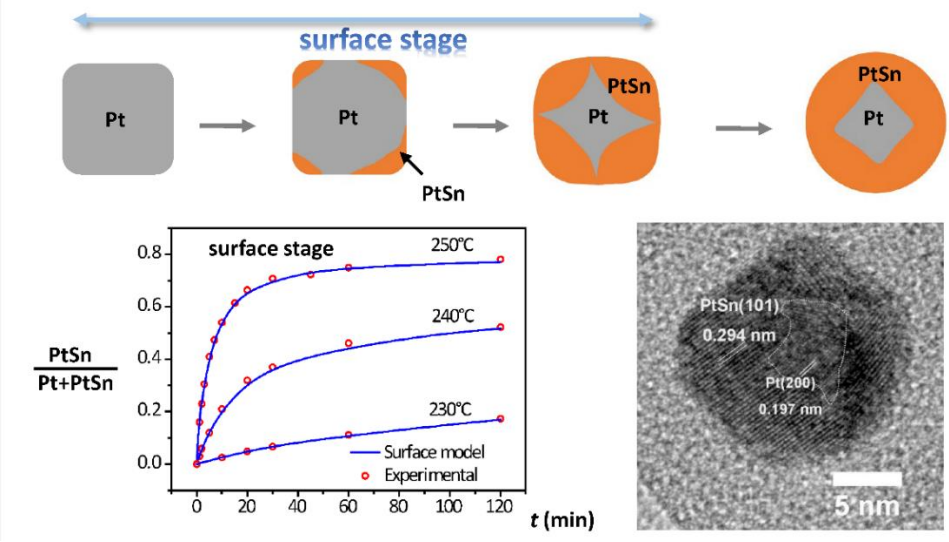

Figure 118. Conversion of Pt nanocubes into PtSn NCs. Reprinted with permission from Ref. 271. Copyright 2018 American Chemical Society.

To elucidate this behavior, we have performed DFT analysis of the energetics relevant to intermixing of Sn into Pt. We find that E_{dv}(Sn-V in Pt) = 0.68 (0.77) eV from PBE (PBEsol), compared with E_{dv}(Pt-V in Pt) = 1.23 (1.43) eV from PBE (PBEsol). We also find that E_{form}(Sn-V in Pt) = 0.44 (0.62) eV from PBE (PBEsol), compared with E_{form}(Pt-V in Pt) = 0.65 (0.84) eV from PBE (PBEsol) although corrections due in "intrinsic surface error" suggest a value of E_{form}(Pt-V in Pt) = 1.2 eV. Thus, based on the discussion in Sec.7.1.2, we conclude that

E_d(Sn in Pt) = E_{dv}(Pt-V in Pt) + E_{form}(Pt-V in Pt) = 2.4 (2.6) eV from PBE (PBEsol). (83)

This result appears consistent with the experimental E_{eff} = 2.5 eV indicating that the latter reflects vacancy-mediated diffusion of Sn through Pt.

Additional DFT analysis revealed that the diffusion barrier for Sn on Pt(100) is E_d = 0.76 eV, and that exchange of a Sn adatom with a Pt atom in at a Pt(100) surface is endothermic by ΔE = 0.46 eV.[271] This is consistent with the observations of Ref. 275 noting that Sn has a cohesive energy of E_c(Sn) = 3.14 eV which is much lower than that for Pt. We do find that surface alloys are thermodynamically stable, but the process of forming these likely involves concerted many-atom processes or is facilitated by defects (rather than occurring by exchange of isolated Sn adatoms).

The second stage of PtSn formation occurs once a complete intermetallic shell has formed. In Ref. 271, it is argued that this initially non-uniform shell should quickly develop a more uniform thickness, and then transformation kinetics can be reasonably described by adopting a refined version[271] of a Ginstling-Brounshtein model.[278,279]

Pd-Ni-Pt sandwich NCs and Au-Pd-Ni-Pt multi-shelled NCs. Richer structures than simple core-shell NCs (as described above for Pd core – Pt shell NCs) can be utilized as the starting point for studies of post-synthesis evolution. Figure 119 provides an example obtained by starting with a Pd nanocube and sequentially reducing first Ni and then Pt resulting in a sandwich structure.[82] Furthermore, it is possible to control the thickness of the various shells. Even more exotic structures such as a ternary Au-Pd-Ni-Pt multi-shelled NC can be synthesized replacing the Pd nanocubing seed in the above study with an Au core – Pd shell nanocube, and then subsequently reducing Ni and then Pt. See Figure 120. Of particular interest is the kinetics of intermixing at least of the outer Pt and Ni shells.

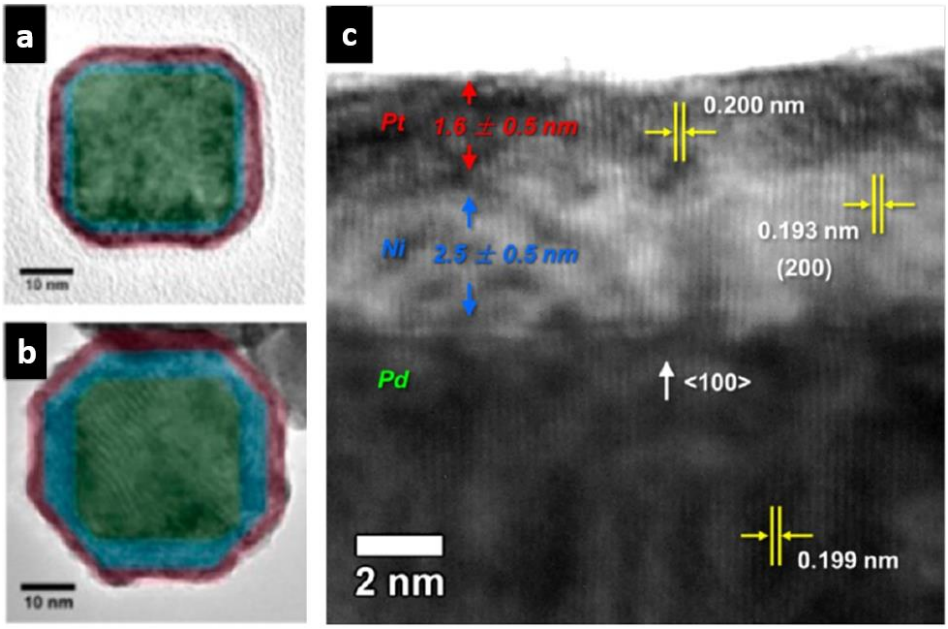

Figure 119. Pd-Ni-Pt sandwich NCs: colorized TEM for (a) 2.5 nm (n) 4.1 nm Ni shell; (c) HRTEM cross-section for 2.5 nm Ni shell. Reprinted with permission from Ref. 82. Copyright 2014 American Chemical Society.

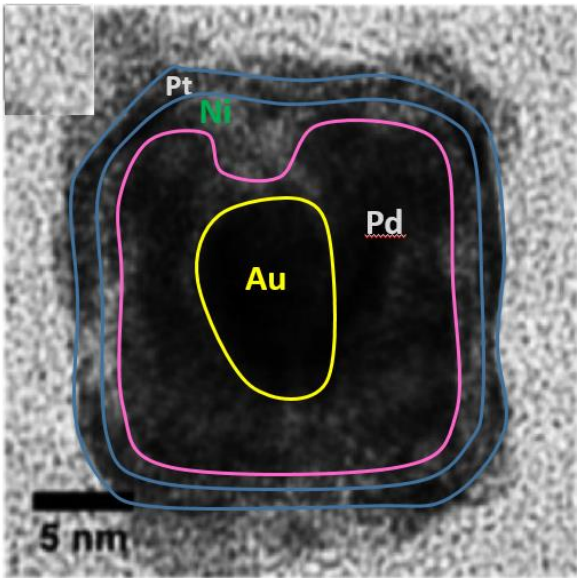

Figure 120. Multi-shelled Au-Pd-Ni-Pt NC. Curves approximately mark interfaces. Reprinted with permission from Ref. 82. Copyright 2014 American Chemical Society.

8. COARSENING OF ENSEMBLES OF 2D AND 3D NCs

8.1. Diffusion of 2D epitaxial NCs: Smoluchowski Ripening

Unexpected diffusion of large 2D epitaxial NCs of 100's to 1000's of atoms in metal(100) homoepitaxial systems was observed by STM in the early 1990's.[211] Analysis of the energetics in these systems indicates that cluster diffusion is mediated by periphery-diffusion (PD) of edge atoms. It was later shown that such cluster diffusion and resulting coalescence (i.e., Smoluchowski Ripening or SR) was the dominant mechanism for coarsening under typical conditions.[109] In Sec.4.4.2, we have noted that the key input to analysis of SR kinetics via the Smoluchowski equation is the dependence on size, N (in atoms), of the NC diffusion coefficient, D_N. Indeed, these early observations of cluster diffusion sparked intense experimental and theoretical interest in size-scaling of diffusivity, $D_N \sim N^{-\beta} \sim L^{-\beta^*}$ for $\beta^* = 2\beta$. Recall from Sec.4.4.2 that the size-scaling exponent, β, controls the coarsening kinetics in that the mean island size scales like $N_{av} \sim t^{1/(\beta+1)}$. In Sec.8.1, we focus on the N-dependence of D_N.

As noted in Sec.4.2, a continuum Langevin formulation (which should apply at least for sufficiently large NCs) predicts that $\beta = 3/2$ for PD-mediated diffusion.[174,193] The same scaling exponent results from a simplistic mean-field type analysis where the motion of periphery atoms is assumed to be uncorrelated. Here, one writes $D_N \sim M_{PD} (\delta R_{CM})^2$, where $M_{PD} \sim N^{1/2}$ gives the number of hopping periphery atoms and $\delta R_{CM} \sim 1/N$ is the shift in the center of mass upon each hop of a periphery atom.[14,280] However, an important STM study quantifying the size scaling found that $\beta \approx 1.14$ for Ag and $\beta \approx 1.25$ for Cu, for N from about 100-400 atoms at 300 K.[212] See Figure 121. These values are well below the continuum/mean-field value. Furthermore, this STM study[212] also quantified the coarsening kinetics finding that the mean NC size scaled like $N_{av} \sim t^n$ where n = 0.466 for Ag [versus $1/(\beta+1) = 0.467$] and n = 0.454 for Cu [versus $1/(\beta+1) = 0.444$]. Thus, the theoretical prediction for the connection between the size scaling of cluster diffusivity and coarsening kinetics is well satisfied.

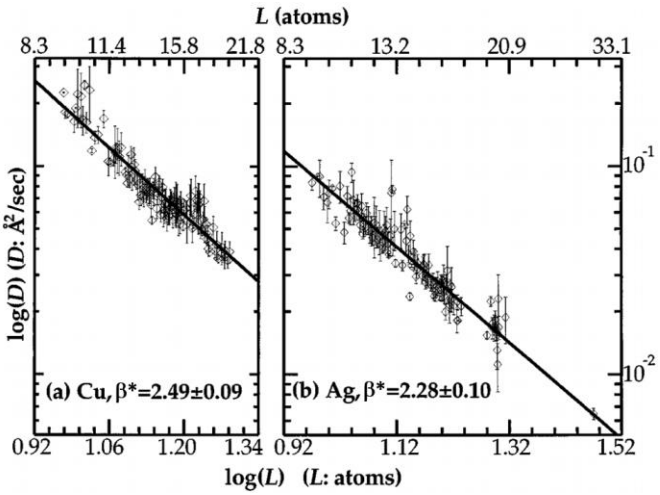

Figure 121. Size scaling of cluster diffusivity for: (a) Cu/Cu(100); (b) Ag/Ag(100). Reprinted with permission from Ref. 212. Copyright 1997 American Physical Society.

As noted above, the observed “anomalous” size scaling for cluster diffusivity prompted numerous theoretical analyses. Here, we first describe two studies utilizing generic models (cf. Sec.3.3) which provide insight into basic behavior in metal(100) homoepitaxial type systems rather than in describing specific systems. In the first, Heinonen et al.[151] use a refined Metropolis prescription (cf. Sec.3.3.2) of the activation barrier for hopping, $E_{act} = E_S + \min(0,\Delta_{NN})E_B$ where $E_S = 0.258$ eV when there is at least one atom diagonally adjacent to the TS for hopping (corresponding to edge diffusion) and $E_S = 0.399$ eV otherwise (e.g., for terrace diffusion). Also Δ_{NN} is the number of NN atoms in the final state minus that in the initial state. The energetic parameters are intended to correspond to Cu(100). Results of simulations for this model are shown in Figure 122. The basic picture presented was that a scaling exponent greater $\beta > 1$ associated with periphery diffusion was manifested for smaller N (ignoring the oscillatory behavior) crossing over to an exponent $\beta = 1$ for large N. The latter behavior was associated with cluster diffusion dominated by vacancy diffusion through the cluster interior. Thus, it was suggested that observed exponent of $\beta \approx 1.25$ observed for Cu(100) was proposed to correspond to crossover between these regimes. With regard to oscillatory behavior, it was noted that D_N for “perfect” sizes $N = L^2$ were significantly smaller than those for $N = L^2 + 1$ for lower temperatures.

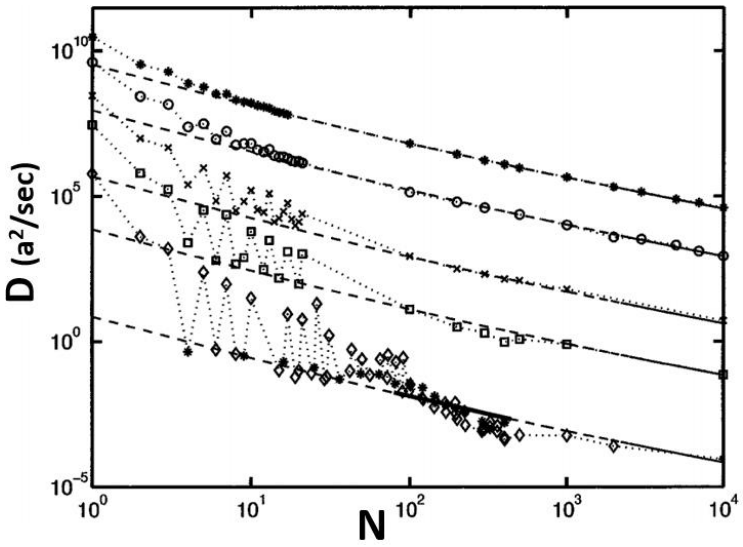

Figure 122. Refined Metropolis model for metal(100) homoepitaxial cluster diffusivity versus size (for selected sizes). Results are shown form T = 1000, 700, 500, 400, 300 K (from top to bottom). Stars for 300 K correspond to “perfect” sizes $N = L^2$. Reprinted with permission from Ref. 151. Copyright 1999 American Physical Society.

However, more recent analysis reveals that oscillatory behavior for small sizes is more subtle than suggested by the above study.[154,155] Also, it is not viable to assign a higher exponent to the small size regime associated with traditional theory for periphery-mediated diffusion. Finally, the crossover to vacancy-mediated diffusion for large sizes is likely a consequence of the feature that the refined Metropolis formulation assigns an

artificially small barrier for vacancy diffusion $E_{dv} = E_S \approx 0.26$ eV which is well below the adatom terrace diffusion barrier $E_d \approx 0.40$ eV. In fact, the vacancy diffusion barrier for most metal(100) systems including Cu is only slightly below E_d.[152]

It is natural to analyze predictions for periphery-diffusion mediated cluster diffusion from the tailored model for metal(100) homoepitaxial systems described at the end of Sec.3.3.2 and applied in Sec.5.2 and 5.4.[153-155] This model selects $E_{act} = E_e + (n-1)\phi$ for NN hops and $E_{act} = E_e + (n-1)\phi + \delta$ for 2NN hops for edge diffusion, and prohibits detachment of atoms from clusters. See Figure 12. Here E_e is the barrier for edge diffusion along close-packed step edges, δ is the additional kink or corner rounding barrier, and ϕ gives the strength of the NN attractive interactions.

Before presenting results for cluster diffusivity, it is appropriate to describe anticipated distinct classes of behavior for specific sizes of clusters. We identify perfect sizes $N_p = L^2$ and $L(L+1)$ with $L = 3,4,\ldots$ for which clusters have unique square or near square ground state shapes. Note that such uniqueness does not apply for sizes $N = L(L+n)$ with $n \geq 2$. For $N = N_p$, diffusion is nucleation-mediated in that after an atom is extracted from a corner in the ground state to an edge (raising the energy by $\Delta E = +\phi$), another atom must quickly detach from a corner or kink to join the first atom before the first atom returns to the corner. Such a pair of atoms nucleates a new edge. Long-range diffusion requires recovering ground state configurations with shifted center-of-mass (CM). The most direct pathway shifts atoms from kinks and corners of the opposite edge to complete this new edge. Shifting the second and subsequent atoms from one kink to another does not change the energy after each reattachment, so the system evolves through a series of first excited states with energy $\Delta E = +\phi$ above the ground state. Only shifting the last (isolated) edge atom to recover the ground state lowers the energy by $\Delta E = -\phi$. See Figure 123a. Note that diffusion of clusters with sizes N_p+3, N_p+4, etc. is also nucleation-mediated. Nucleation-mediated diffusion involves an atom breaking out of a kink (or corner) site with rate $h_k = \nu \exp[-(E_e+\phi)/(k_B T)]$ and aggregating with an isolated edge atom which has low quasi-equilibrium density $n_{eq} = \exp[-\beta\phi/(k_B T)]$. Thus, $D_N \sim n_{eq} h_k \sim \exp[-E_{eff}/(k_B T)]$ with effective barrier[281] $E_{eff} = E_e + 2\phi$ as confirmed by simulations.[154-155]

Next, we consider facile sizes N = N_p+1 and N_p+2, where edge nucleation is not necessary. For $N = N_p+1$, an isolated edge adatom on a perfect core, which we describe as a special ground state configuration, can readily diffuse around the cluster. For $N = N_p+2$, an edge dimer on a perfect core, a special ground state, can dissociate and reform on another edge. Neither process results in a net change of energy. After the isolated edge atom or dimer is transferred to a new edge, atoms can be transferred from the opposite edge of the core to complete the edge to which the adatom or dimer was moved. This recovers a special configuration with an adatom or dimer on the edge of a displaced perfect core. Shifting of atoms from one kink to another does not change the energy after reattachment, and in this case the system evolves through a set of ground state configurations. See Figure 123b. Facile diffusion just involves breaking atoms out of kink sites and subsequent edge diffusion, so that $E_{eff} = E_e + \phi$ as confirmed by simulations.[154,155]

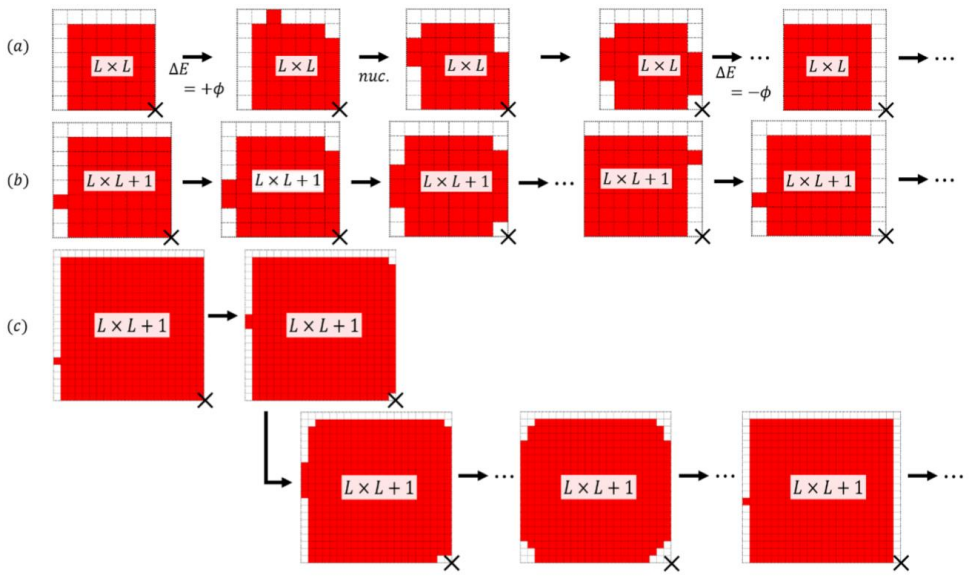

Figure 123. Direct diffusion pathways for (a) perfect; (b) facile sizes. (c) Indirect pathway for facile sizes. Reprinted with permission from Ref. 154. Copyright 2017 American Institute of Physics.

In addition to direct pathways, there are many indirect pathways for cluster diffusion with atoms removed from multiple corners. Here, the cluster wanders through a large phase space of configurations iso-energetic with the first excited state for perfect sizes, or with the ground state for facile sizes. See Figure 123c. However, for long-range diffusion by a sequence of transitions between ground states of the system, eroded corners must be rebuilt as the cluster must repeatedly pass through the unique ground state for perfect sizes, and the special ground state for facile sizes.

An overview of KMC results illustrating various regimes and branches of D_N behavior for $\phi = 0.24$ eV and $\delta = 0$ at 300 K is shown in Figure 124. Small sizes $N \leq 8$ all have the form $N_p + 1$ or $N_p + 2$ and exhibit facile diffusion with high D_N. For moderate sizes, $N = 9$ to $O(10^2)$, we just show four distinct branches: facile $N_p + 1$; facile $N_p + 2$; perfect N_p; and slow $N_p + 3$. Key features are as follows: **(i)** High values for smaller N and rapid decay of $D_N \sim N^{-\beta f}$ for facile sizes $N_p + 1$ with large $\beta_f \approx 2.6$ up to $N \sim 100$ and similar less regular decay for $N_p + 2$. **(ii)** Weak size-dependence of D_N for perfect sizes up to $N_p \approx 81$. **(iii)** Intermingling of D_N for perfect N_p with facile branches for $N_{mingle} \approx 81$. **(iv)** Lowest values of D_N for sizes $N_p + 3$ (not N_p) with slow decay $D_N \sim N^{-\beta s}$ where $\beta_s \approx 0.53$ for $N \sim 67$-200. N_p and $N_p + 3$ branches trivially merge at $N = 12 = 9+3$. **(v)** Analysis of D_N versus N for a full contiguous range of N shows quasi-periodic behavior. See Figure 124 (inset). **(vi)** Near-merging of all branches for $N \approx N_{merge} \approx 250$. For larger sizes $N > N_{merge}$, if we write $D_N \sim N^{-\beta eff}$, the effective exponent slowly varies from $\beta_{eff} \approx 0.75$ for N just above N_{merge}, to $\beta_{eff} \approx 1.12$ for N from 500-1000, to $\beta = 1.5$ (the continuum value) for $N \to \infty$. Here, the kink separation is $L_k \approx 52$, and the asymptotic regime $N >> (L_k)^2 \approx 2700$ is not achieved in our simulations. However, we have also performed simulations for $\phi = 0.20$ eV (and $\delta = 0$) where $L_k = 24$, and we do realize asymptotic scaling $N >> (L_k)^2 \approx 570$.

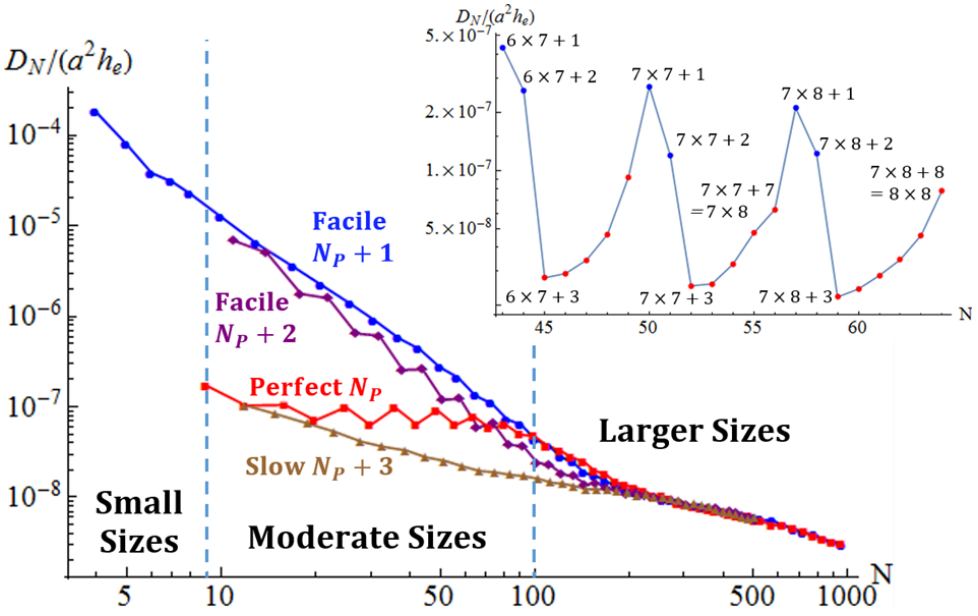

Figure 124. D_N versus N for the tailored model for metal(100 homoepitaxial systems. Reprinted with permission from Ref. 154. Copyright 2017 American Institute of Physics.

Deeper insight into the above diverse and subtle features of D_N versus N is desired. Various related comments are provided below. Of particular value is the application of combinatorial analysis assessing the number of cluster configurations in relevant ground states and excited states. Such an analysis exploits concepts from number theory. (We do not provide details here, but just note that possible configurations clusters associated with various ways of distributing vacancies in a corner of the cluster can be mapped onto Ferrer's or Young's diagrams developed in the theory of partitions of integers.) Below we let $\Omega_N(n)$ denote the number of configurations in the nth excited states for a cluster of size N. The basic conclusions are as follows.

(i). The number of ground state configurations, $\Omega_{Np+1}(0)$, for facile sizes $N = N_p+1$ scales like $\Omega_N(0) \sim N^{2.6}$ up to $N \sim 100$. Cluster diffusion requires repeatedly starting from the special configuration and wandering through a large ground state configuration space to return to a special configuration but with the cluster core is shifted by a lattice constant. $D_N \sim 1/\tau_{ret}$ should plausibly scale inversely with the return time, τ_{ret}, and random walk theory indicates that $\tau_{ret} \sim \Omega_N(0)$. Thus, the relation $D_N \sim 1/\Omega_N(0)$ explains the observed large size-scaling exponent $\beta \approx 2.6$.

(ii). The weak size dependence of diffusivity for perfect size clusters naturally reflects the feature that diffusion is limited by nucleation of new edges, a process which is not particularly sensitive to cluster size.

(iii). Perfect-sized clusters are only well-distinguished from facile clusters if there is a high probability that the cluster is in its unique ground state. The probability to be in an excited state scales like $\exp[-\phi/(k_BT)]\ \Omega_{Np}(1)$. Evaluation of $\Omega_{Np}(1)$ reveals that this probability is significant for $N \approx 81$ at 300 K with $\phi = 0.24$ eV.

(iv,v). Perhaps surprisingly for nucleation-mediated diffusion, D_N increases (rather than decreases) for increasing $N = N_p+3, N_p+4,\ldots,$ to N_{p+}, where N_{p+} denotes the perfect size above N_p. The inset to Figure 18 provides a few examples: $N_{p+} = 49$ for $N_p = 42$; $N_{p+} = 56$ for $N_p = 49$; and $N_{p+} = 64$ when $N_p = 56$. Nucleation-mediated diffusion requires excitation of the cluster to the first excited state. Thus, it is reasonable to speculate that diffusivity should be higher for higher probability to be in the first excited state relative to the ground state, and thus for higher $\Omega_N(1)/\Omega_N(0)$. Combinatorial analysis showed that indeed $\Omega_N(1)/\Omega_N(0)$ tracks well the cyclical behavior in D_N, and adopts local minima for $N = N_p+3$.

All the basic features described above apply upon introducing a finite kink rounding barrier $\delta > 0$. Naturally the actual value of D_N decreases upon increasing $\delta > 0$. Also, the effective barrier for cluster diffusion increases.[155]

Next, we briefly describe analysis of the diffusion of vacancy pits on metal(100) surfaces using the same tailored model as just applied for adatom cluster diffusion.[156] Results for $\delta = 0$ are shown in Figure 125. In this case, D_N for pits is lower than for adatom clusters or islands of the same size. For large enough N, these curves must merge since continuum theory does not distinguish between diffusion of islands and pits. However, for smaller N there are differences, e.g., pit diffusion is always nucleation-mediated. It is appropriate to note that for large δ, island diffusion must become slower than pit diffusion. The reason is that there are pathways for pit diffusion which avoid any corner or kink rounding.[156]

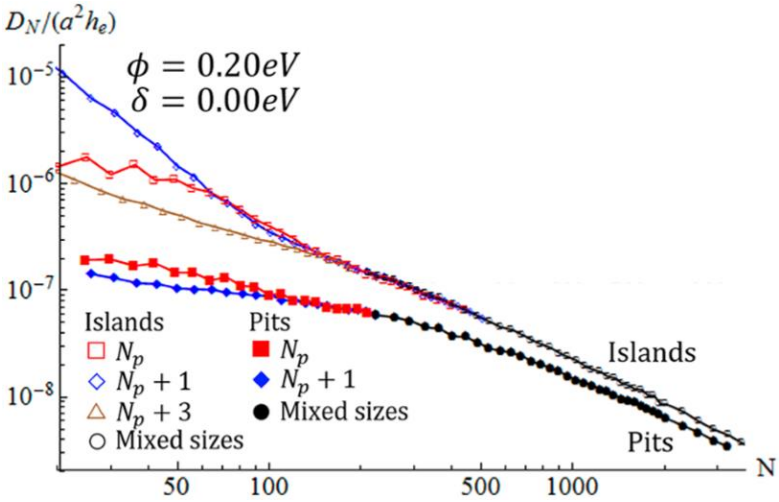

Figure 125. Comparison of vacancy pit and island diffusion for $\delta = 0$.

Returning to analysis of experimental data, the ISU[14] and Bochum groups[282] have compared vacancy pit and island diffusion for Ag(100) and both find similar D_N for the same N. It should be noted, however, that these studies are not fully consistent with the ORNL data in Figure 121. The ISU data has somewhat higher values for island diffusivity, and the Bochum data has much larger values.[156] At least the latter was suggested to be a consequence of significant surface strain associated with the extensive sputtering used to create pits. Thus, it was proposed that islands and pits have similar D_N and the magnitude is best described by the ORNL data. With this target,

the tailored model was shown to recover the proposed behavior upon choosing $E_e \approx$ 0.29 eV, $\delta \approx 0.18$ eV, $\phi \approx 0.27$ eV, and $\nu = 10^{13}$/s.[156]

Finally, we remark that experimental data is available for diffusivity of vacancy pits on Cu(111) and Ag(111),[243,283] and adatom islands in Ag/Ag(111) homoepitaxial systems.[243]

8.2. Decay of 2D epitaxial NCs: classic and unconventional Ostwald Ripening

8.2.1. OR for Ag/Ag(111). Perhaps the optimal 2D example of Ostwald Ripening (OR), for which there exists detailed information on the evolution of the island distribution, is provided by STM studies of the coarsening of Ag islands on an Ag(111) surface.[13,284] Since no additional barrier over that for terrace diffusion is expected for attachment to ascending steps on metal surfaces, OR should be terrace diffusion (TD)-limited rather than attachment-limited. Figure 126 (top) shows STM images of island evolution, and Figure 126(b) tracks the corresponding changes in sizes for a subset of islands. The characteristic non-linear decay in size for shrinking islands for TD-limited decay is evident. The feature that curves tracking island size versus time for different islands can cross is also indicative of TD-limited decay as it reveals that growth/decay rates depend not just on island size, but on the local environment of the island. For attachment-limited decay (or in mean-field type treatments of TD-limited decay), curves do not cross. See Figure 126(c).

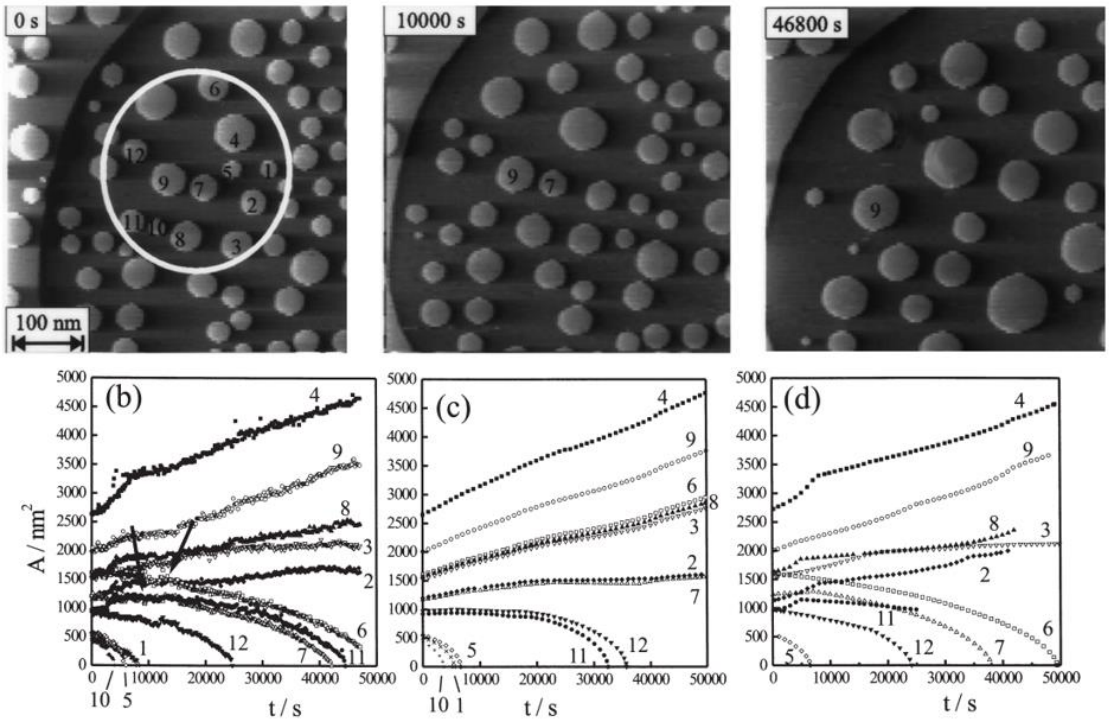

Figure 126. (a) OR of Ag islands on Ag(111) for 0.3 ML at 300K. (b) Experimental island sizes versus time. (c) Mean-field type prediction of island size evolution. (d) Prediction of island size evolution in the nearest-neighbor approach. Reprinted with permission from Ref. 284. Copyright 1999 Elsevier.

Selecting a finite ensemble of islands as shown in Figure 126, mass flow between those islands, and thus their rates of growth or decay, can be readily and precisely quantified in a continuum picture by adaptive mesh Finite Element Method (FEM) analysis. (See the discussion for Ag/Ag(110) below.) There is some approximation in treatment of the outer boundary. Nonetheless, by selecting a large enough ensemble, reasonable treatments should not significantly impact the evolution of islands in the center of the ensemble away from the boundary. However, rather than numerical analysis, development of an approximate analytic formulation to describe island growth/decay rates is perhaps more instructive. Such a formulation has been developed in Ref. 284 which emphasizes the local nature of evolution, specifically the dependence of the evolution of a specific island primarily on its nearest-neighbors. The formulation is based on the expression $J_{ij} = 2\pi D(\rho_i - \rho_j) / \ln(d_{ij}^2/r_i r_j)$ for the flux between an isolated pair of islands with radii $r_{i,j}$ and separation $d_{ij} >> r_{i,j}$. For a specific island, i, its nearest-neighbors are determined from a Voronoi construction. Then, the total flux between that island and all of its neighbors is assumed to have the form $J_i = \sum_{NN\ j} \alpha_{ij} J_{ij}$, where the weights, α_{ij}, are chosen as proportional to the opening angles, Φ_{ij}. See Figure 127. This approach, which is particularly successful for Ag/Ag(111) as shown in Figure 126(c), was motivated by earlier work in Ref. 285.

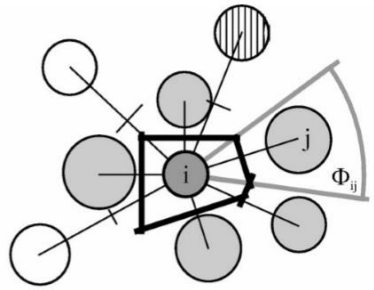

Figure 127. Construction of a nearest-neighbor model for TD-mediated OR. Reprinted with permission from Ref. 284. Copyright 1999 Elsevier.

In addition to traditional coarsening of island arrays for the Ag/Ag(111) systems, there are also studies focusing on the evolution of individual islands including those in "tailored" geometries, e.g., islands on islands, islands in pits, and also pits in pits[286-288]. The goal here was to extract key system energetics by applying traditional continuum models to analyze detailed data for island decay. Corresponding generic atomistic KMC simulation studies (i.e., not tailored to a specific system) recover key features of observed behavior.[289]

8.2.2. Anomalous OR for Ag/Ag(110). For the anisotropic Ag/Ag(110) system, Ag islands have an elongated rectangular form with aspect ratio, R, adopting an equilibrium value of $R_{eq} \approx 3$. For temperatures above about 220 K, coarsening of island arrays occurs via OR, with behavior described by conventional theory assuming equilibrated islands shapes with $R \approx R_{eq}$ and thus well-defined chemical potentials.

However, below 220 K, an unusual one-dimensional decay is observed by Morgenstern et al.[56] for “smaller” islands where these decrease in length with almost constant width so one can have initially $R \geq R_{eq}$ and finally $R < R_{eq}$. When islands become very small they do also shrink in width. An example of such decay at 190 K from the ISU group[57,112] with the initial $R \approx R_{eq}$ is shown in Figure 128 where the island decay rate is $K_{expt} = -dA/dt \approx 0.007$ nm^2/s.

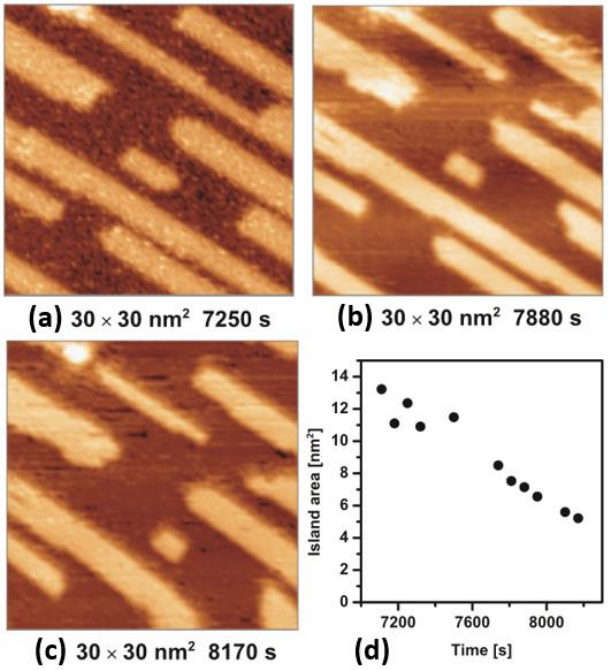

Figure 128. (a-c) STM data for one-dimensional decay of an Ag island on Ag(110) at 190 K. (d) Island area versus time. Reprinted with permission from Ref. 112. Copyright 2013 American Physical Society.

Suitable stochastic atomistic modeling can be applied to describe and potentially further elucidate behavior. However, such models should capture both system thermodynamics (i.e., the equilibrium aspect ratio) and kinetics. Key features of the kinetics (anisotropic terrace diffusion which is significantly more facile along the troughs in the x-direction than in the orthogonal y-direction; details of periphery diffusion including corner rounding) are described in Ref. 56 based on semi-empirical energetics. To this end, it is convenient to adopt the strategy described in Sec.3.5.1 developing models prescribing both conventional and unconventional interactions. However, we just include short-range pair interactions for both types as shown in Figure 129 which are tuned to recover the desired equilibrium island aspect ratio and the key features of terrace and periphery diffusion.[57,112]

This atomistic model was applied to simulate decay of island whose behavior is characterized above by incorporating the experimental distribution of islands surrounding the island of interest into the KMC simulation. See Figure 130. These simulations also apply atom-tracking KMC to follow the atoms (shown in white) initial in the island of interest.[57] Many of the atoms detaching from this shrinking island are

incorporated into the left end larger island to the right (as is already evident from the snap shot shown early in the decay process), and there is substantial attachment to the right end of island to the left (which due to PBC artificially corresponds to the right end of the island to the right). A key advantage of simulation relative to experiment is that one can repeat the simulation to assess the extent of fluctuations in island decay. As is clear from Figure 130, the spread in decay rates is large for the 99 trials shown from $K_{KMC} \approx 0.008$ nm^2/s to much smaller values, a range including the experimental value. The average initial decay rate from simulation is $K_{KMC} \approx 0.0026$ nm^2/s, although this increases to $K_{KMC} \approx 0.0033$ nm^2/s after 750 s.[112]

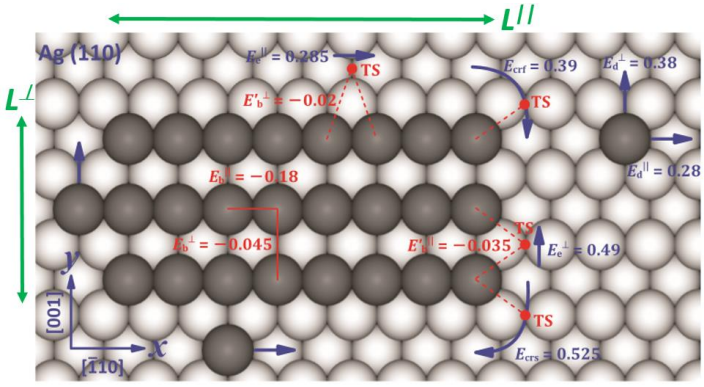

Figure 129. Energies for stochastic atomistic model describing Ag/Ag(110). Reprinted with permission from Ref. 57. Copyright 2013 American Physical Society.

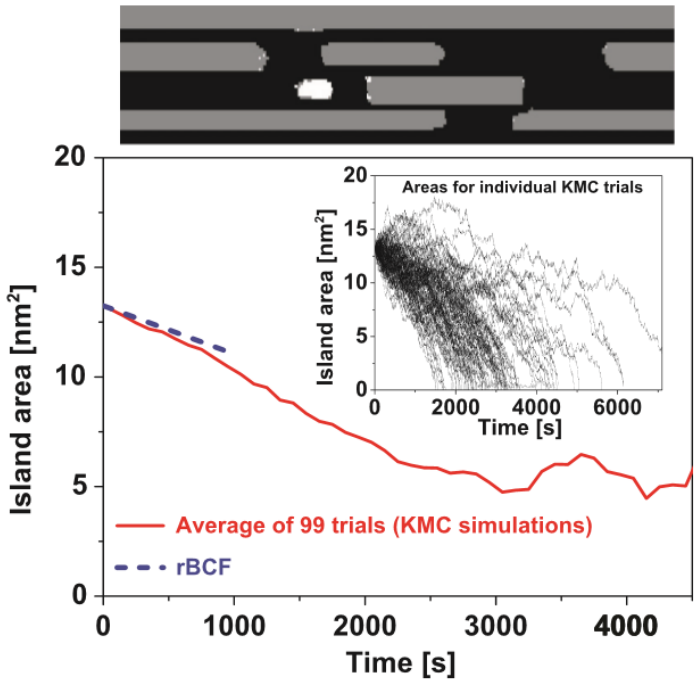

Figure 130. Atomistic model of the decay of the Ag island on Ag(110) shown in Figure 129. Results for area versus time for 99 trials and their average are shown. Also shown are the results of a refined BCF (rBCF) treatment. Reprinted with permission from Ref. 112. Copyright 2013 American Physical Society.

While stochastic modeling and simulation is instructive, deeper insight can be obtained by development of an appropriate analytical formulation (and from related numerical analysis). The first fundamental challenge is the lack of equilibration of island shapes during decay which precludes the assignment of a (standard) chemical potential for each island. However, particularly given the one-dimensional nature of decay, it is natural to introduce a partial chemical potential, $\mu_{<001>}$, describing the change in (free) energy for the "evolution mode" with varying island length, $L^{\parallel}$, for fixed width, $L^{\perp}$. One also assumes that adatoms at the <001> ends of the island with density $n_{<001>}$ are in equilibrium with the <001> steps and have the same chemical potential, $\mu^{\parallel}$. From the expression for the total island energy, it follows that[57,112]

$$\mu_{<001>} = \mu_{\infty} + 2\Omega\gamma_{110}/L^{\perp} \text{ and } n_{<001>} = n_{\infty} \exp[2\Omega\gamma_{110}/(k_B T L^{\perp})]. \quad (84)$$

Although it is not so relevant for our study, one can also define a partial chemical potential, $\mu_{<110>}$, for the evolution mode where the island changes width for fixed length. One obtains $\mu_{<110>} = \mu_{\infty} + 2\Omega\gamma_{001}/L^{\parallel}$ and a corresponding expression for the density, $n_{<110>}$, for the density of adatoms in equilibrium with <110> step edges. In these expressions, γ_{110} (γ_{001}) is the step energy for <110> (<001>) steps, and Ω demotes the unit cell area. For equilibrated island shapes, one has $\mu_{<001>} = \mu_{<110>}$ and thus $R_{eq} = L^{\parallel}_{eq}/L^{\perp}_{eq} = \gamma_{001}/\gamma_{110}$.

A standard continuum treatment of island evolution assuming facile attachment at ascending steps of Ag islands would solve a Dirichlet boundary value problem (BVP) for the steady-state (anisotropic) diffusion equation where adatom densities matched their appropriate partial equilibrium values at the different island edges. However, such a treatment leads to a decrease in island width as well as length for decaying islands. This problem is resolved by recognizing that <110> edges of islands are quite facetted with low or negligible kink populated, so that adatom attachment is effectively strongly inhibited. This behavior is quantified by a refined BCF (rBCF) treatment shows that the kinetic coefficient describing adatom attachment decreases like the square of kink density. Thus, we reasonably ignore adatom attachment/detachment at <110> step edges in which case this analytic formulation describes well observed behavior. Numerical analysis of the BVP using adaptive mesh FEM shown in Figure 131. This analysis predicts an initial decay rate of $K_{rBCF} \approx 0.0022$ nm^2/s quite consistent with the KMC result averaged over many trials.

There are other features of behavior in this system which differ from traditional OR in isotropic systems. The strongly anisotropic nature of diffusion leads to a quasi-1D flow of atoms between the <001> ends of neighboring islands. In this case, mass fluxes are more strongly dependent on the separation between islands than for an isotropic 2D systems with weaker logarithmic dependence. This impacts Arrhenius behavior of coarsening where the temperature-dependence of island separation now unconventionally plays a role. See Ref. 57 for further details.

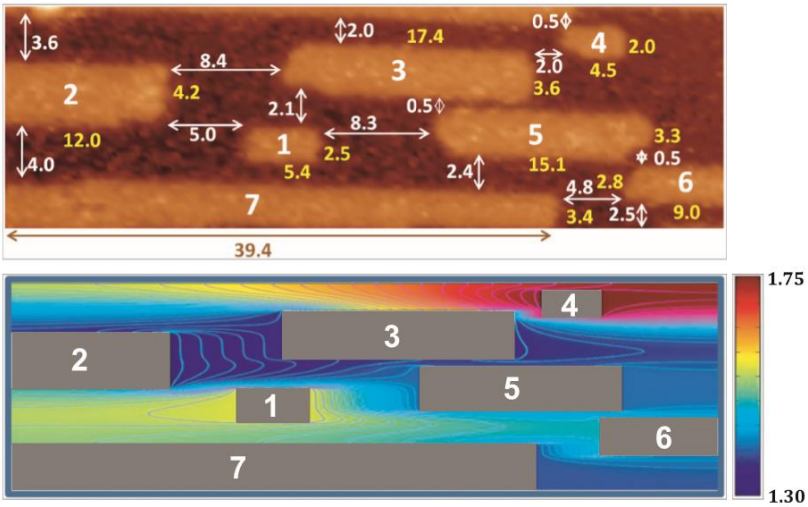

Figure 131. Adaptive mesh FEM analysis of mass transport between islands based upon partial chemical potentials and a rBCF treatment of boundary conditions. Reprinted with permission from Ref. 112. Copyright 2013 American Physical Society.

8.2.3. General comments. Traditional continuum OR theory has been particularly effective at characterizing behavior in traditional isotropic systems such as Ag/Ag(111). The theoretical framework requires equilibrated island shapes. The key concept is that islands with smaller area and higher chemical potential decay by transferring atoms to islands with larger area and lower chemical potential (locally for TD-limited decay, and globally for AD-limited decay). However, for the anisotropic Ag/Ag(110) system, islands do not have equilibrated shapes. It is necessary to introduce the concept of partial chemical potentials and also refined BCF boundary conditions accounting for inhibited attachment/detachment to steps with a low or negligible kink population. The conclusion is that coarsening is controlled by the relevant partial chemical potential, $\mu_{<001>} = \mu_\infty + 2\Omega\gamma_{110}/L^{\perp}$, so it is narrower islands (versus islands which are smaller in area) which decay. Consequently, one can have anti-coarsening behavior where islands with larger area shrink and those with smaller area grow provided that the larger islands are narrower than the smaller islands.

Numerical analysis of the relevant continuum BVPs with sophisticated adaptive-mesh FEM can precisely analyze mass flow between dozens of islands. Results facilitate interpretation of experimental observations. One caveat is that while such a procedure does precisely capture behavior even at sharp corners of islands with a fine mesh, the physical systems have a discrete array of adsorption sites. Thus, if the mesh is finer that the actual adsorption site grid, this analysis becomes artificial. An alternative to implement discrete diffusion equations where the grid corresponds to the actual adsorption sites.[112,207,208] Such formulations are quite versatile in that one can build in structure to the step edges and also higher-fidelity step edge kinetics. Consequently, further insight can be derived from traditional continuum treatments (and this approach provides a complementary strategy to stochastic atomistic modeling).

In Sec.4.4.3, we have discussed crossover possible crossover between OR and SR.[14,110] For example, based on this discussion, one anticipated a crossover from SR-dominated coarsening for Ag/Ag(100) or Cu/Cu(100) systems at 300 K to OR as the

mean island size becomes sufficiently large. It is appropriate to note that other more novel types of crossover behavior can also occur. STM studies reveal that coarsening for Cu/Cu(100) between 343 K to 413 K (rather than 300 K) is dominated by attachment-limited OR.[289] It was proposed that this coarsening process was mediated by diffusion of vacancies in the top Cu(100) surface layer rather than by adatoms, where the attachment-limited behavior is associated with an additional barrier for vacancies to diffuse between layers. It should be noted for this system that the diffusion barrier for vacancies is lower than for adatoms.[152] The viability of OR mediated by vacancy diffusion is discussed more generally in Ref. 14.

8.3. Diffusion and SR for supported 3D NCs

For decades, there has been debate as to whether the degradation of 3D supported catalysis NCs is dominated by OR or SR, where of course the latter is controlled by the diffusion of supported 3D NCs. There exist classic observations of 3D NC migration by Ruckenstein and coworkers[290] as well as more recent in-situ TEM studies.[30] There has also been extensive analysis of NC migration and coalescence on both amorphous C and SiO_2 substrates and crystalline substrates (MgO, KCl, NaCl, etc.) in the materials science literature.[20] A separate line of investigations assessed metallic NC diffusion of graphite (which is much more rapid than on amorphous C).[249] There has also been consideration of the mechanism of cluster diffusion with individual atom motion being ruled out in some cases for graphite and ionic substrates.[249] A key factor controlling diffusivity is suggested to be the degree of epitaxy with the substrate.

In terms of theory, a classic continuum analysis of 3D cluster diffusion mediated by surface diffusion suggested that the diffusion coefficient for NC of N atoms scaled like[291] $D_N \sim N^{-4/3}$. A prominent study by Reiss for non-epitaxial systems revealed a weak activation barrier for rotation (since some atoms move towards more stable positions as other move away).[292] Other models allowed for a partial rearrangement of the interface between the island and the substrate where there is substantial misfit.[20] Numerous other studies have utilized MD simulation to characterize 3D NC diffusion assessing the effects of mismatch and characterizing size-scaling if any.[249] A key general conclusion is that epitaxy of the NC with the substrate implies slow diffusion mediated by single-atom movements.[249]

Next, we consider in more detail a recent study by Abild-Pedersen and coworkers[157] of epitaxially-supported 3D Pt NC diffusion utilizing a stochastic atomistic model with ab-initio kinetics. As discussed in Sec.3.5.2, NC thermodynamics is described within a NN interaction model where the interaction strength is selected as ~0.35 eV based on DFT analysis. Interaction of the metallic NC with the substrate requires separate specification. In the study, it was assumed that a Pt NC was epitaxially supported on rutile SiO_2(001). The adhesion energy of Pt atoms in the lowest layer is assumed to depend on their coordination in the metal NC. Again DFT guides selection of these values: Pt(111) and Pt(100) slabs on SiO_2(001) gives values for 9- and 8-coordinated atoms respectively; nanowires supported by a 2-atom wide side give values for lower coordination 5, and 7. A single adatom gives the value for coordination 0. Values for other coordination numbers were obtained by interpolation with values vary from 0.25 eV for coordination 9 to 0.75 eV for coordination 0. Some account of

strain effect on these adhesion energies due to lattice mismatch was also included. As also noted in Sec.3.5.2, barriers for metal NC atom hopping to neighboring fcc sites were informed by DFT analysis.

Given the finite adhesion to the substrate, the equilibrium shape of the supported clusters differs from the unsupported case according to the Winterbottom construction. Simulated shapes are consistent with this construction and display overhanging {111} facets consistent with adhesion which is not extremely strong. See Figure 132(a) for a NC supported on a {100} facet. It is also noted that the equilibrium supported cluster shapes generally have lower symmetry that in the unsupported case. Note the 3x2 top {100} facet in Figure 132(a). Rotation of this facet without substantial diffusion of the cluster (see Figure 132(b)) leads to a shift in the center of mass (CM) and associated "fine-structure" in the CM trajectory at 1000 K as shown in Figure 132(c). The model was used to provide a comprehensive analysis of both the temperature and NC size dependence of cluster diffusivity. Figure 132(a) shows the activation barrier extracted from the T-dependence of diffusivity which tends to be fairly constant (as expected from our analysis of diffusion of 2D epitaxial NCs). However, there is a significant difference between the barrier for NCs supported on {100} versus {111} facets. This is not surprising as these cases have different effective adhesion to the substrate. Separate targeted studies of the influence of adhesion on cluster diffusivity show little difference between {100} and {111} supported NCs for weak adhesion and that the effective barrier for diffusion in both cases grows with increasing adhesion strength.

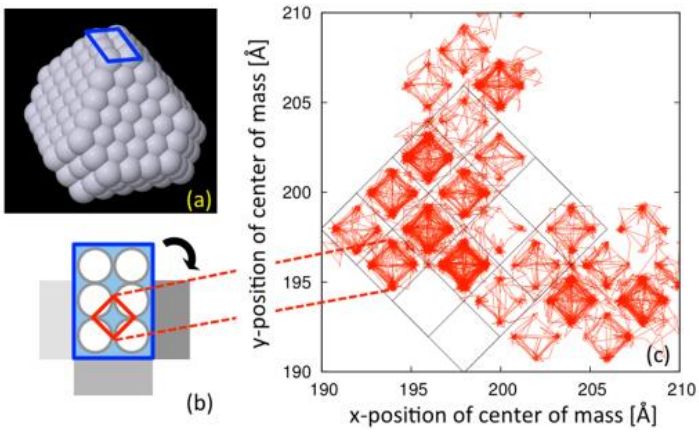

Figure 132. (a) Epitaxially-supported Pt_{309} NC; (b) rotation of the top 3x2 {100} facet; (c) simulated CM trajectory at 1000 K. Reprinted with permission from Ref. 157. Copyright 2017 American Chemical Society.

Finally, for this model, we present in Figure 133(b) predictions for the dependence on size, N (atoms), of cluster diffusivity, $D_{N,}$ of supported Pt NCs at 1400 K. Apart from an overall decrease with increasing size, strong quasi-periodic oscillations are also apparent somewhat reminiscent of the behavior shown in Sec.8.1 for 2D epitaxial NCs. It was suggested that the local minima in diffusivity correspond to situations where the cluster size corresponds to a closed shell configuration with all facets completely filled. This view anticipates that in clusters with partially filled facets, there are more atoms with lower coordination which are more mobile. However, we

have noted in Sec.8.1 for 2D epitaxial clusters that local minima in diffusivity do not correspond to close-shell sizes. Indeed, for the Pt system, *N* = 316 corresponds to a natural closed shell size which is not a minimum in local diffusivity. This issue could benefit from further analysis.

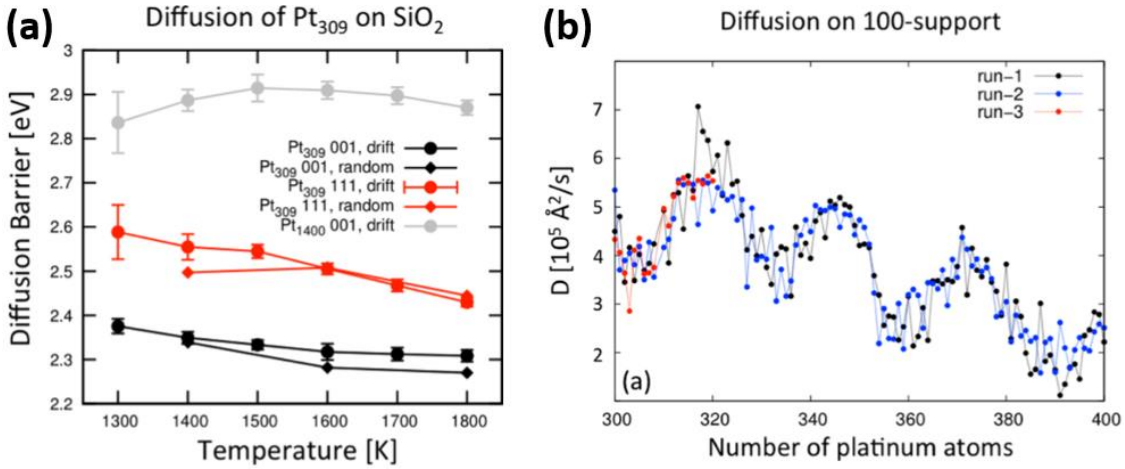

Figure 133. (a) Arrhenius barrier for epitaxially-supported Pt NC diffusion on SiO_2 for sizes N = 309 ({100} and {111}-supported) and N = 1400 ({100} supported). (b) Size-dependence of {100}-supported cluster diffusivity at 1400 K. Reprinted with permission from Ref. 157. Copyright 2017 American Chemical Society.

Next, we describe additional results for diffusion of epitaxially-supported 3D Ag NCs ignoring strain effects where now we utilize the tailored model to capture Ag atom hopping kinetics described in Sec.3.4. This model is adapted to treat epitaxially supported NCs by simply incorporating a separate NN interaction between NC atoms and substrate atoms where the NC is supported on a {100} facet, and atoms in the lowest NC layer reside at four-follow hollow sites on the substrate surface which has fcc {100} structure with lattice constant matching the NC. Figure 134 shows a trajectory for *N* = 52 at 700 K with strong adhesion with ϕ_S/ϕ = 0.75 (cf. Sec.3.5.2). The initial cluster configuration is flatter than the typical equilibrium configuration.

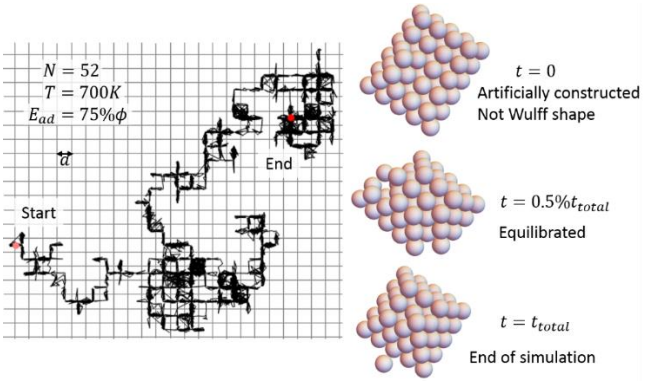

Figure 133. Diffusion trajectory for a size N = 52 epitaxially-supported Ag NC with adhesion 75% strength also showing snapshots at different times.

In addition, this model was applied to characterize the size (N) dependence of Ag NC diffusivity, D_N, for both strong and weak adhesion. Figure 134 shows behavior at 700 K for strong adhesion ($\phi_s/\phi = 0.75$). For the size range shown, natural discrete closed-shell Winterbottom-type configurations are 3-layer truncated pyramids (e.g., 5x5 base and 4x4 and 3x3 higher layers for N = 50; 5x6 base and 4x5 and 3x4 higher layers for N = 62; etc.). Strong oscillations occur in D_N versus N as for the Pt NCs. For contrast, behavior of the substantially higher D_N versus N for Ag NCs at 700 K is shown in Figure 135 for the case of weak adhesion ($\phi_s/\phi = 0.05$). In this case, equilibrium shapes should correspond closely to Wulff shapes for unsupported NCs, so that closed-shell sizes for truncated octahedral are N(3,3) = 201, N(3,4) = 314, etc.

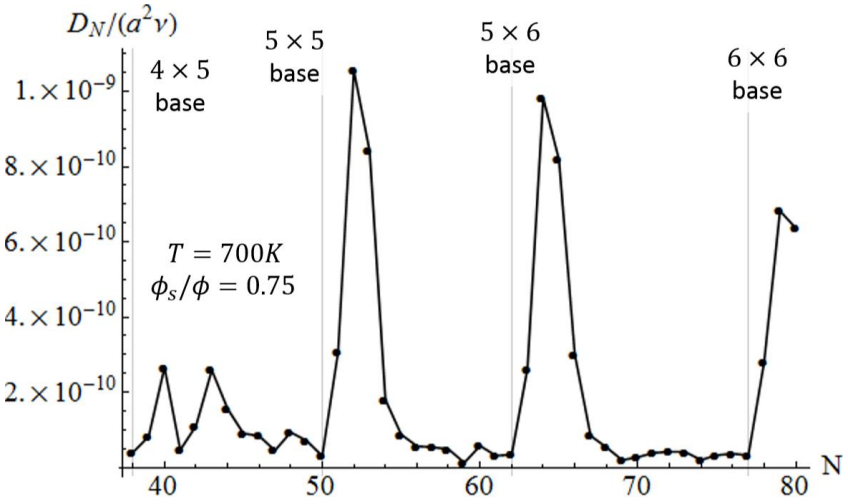

Figure 134. Diffusion coefficients for epitaxially-supported Ag NC for strong adhesion (ϕ_s/ϕ = 0.75) at 700 K.

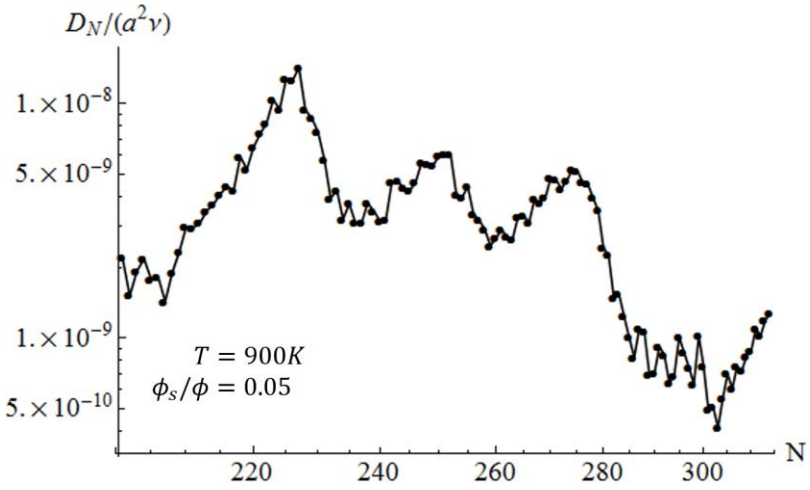

Figure 135. Diffusion coefficients for epitaxially-supported Ag NC for weak adhesion (ϕ_s/ϕ = 0.05) at 900 K for N =201-314.

8.4. Coarsening for supported and unsupported 3D NC

As noted above, there has been extensive historical speculation and discussion of the mechanism for degradation of catalysts: OR versus SR (where SR is often referred to as Particle Migration and Coalescence or PMC for these systems). Traditionally, an attempt was made to obtain insight into the mechanism from analysis of the particle size distribution, noting that different forms are predicted for OR and SR by theories of the type described in Sec.4.4. However, this strategy has proved inconclusive.[28] Instead, the issue can be resolved more directly and definitively exploiting recent advances in in-situ TEM allow direct observation of catalyst evolution at elevated temperatures under working conditions.[28,30,293] We briefly describe two such studies.

One study focused on Ni NC on $MgAl_2O_4$ divided the coarsening process into 3 stages: (i) rapid degradation; (ii) slower degradation; (iii) quasi-stabilization.[29] The study of Ni NC evolution was performed in an environment with 200 Pa H_2O and 200 Pa H_2 at 750 °C. The coarsening mechanism in stage (i) was identified as OR as validated by the in-situ TEM images shown in Figure 136. The decay in size of an individual island was tracked (analogous to the study of OR for 2D Ag/Ag(111) islands in Figure 126). In this case, behavior was described by theories for AD-limited decay of 3D islands as presented in Sec.4.4.1. For stage (ii), there is evidence for a combination of OR and SR. Figure 137 shows a sequence of TEM images revealing mobility and coalescence events.[30] In the first 13 s, NC I and a small nearby NC coalesce. NC II coalescences with a nearby small NC in the first 25 s. By 30 s, NC II has coalesced with a second nearby small NC. Significant mobility is also observed over 80 s with larger NCs more mobile than smaller ones. However, the authors note that such examples of mobility and coalescence are rare. It is difficult to assess general features such as the extent of SR, and also size-dependence of mobility (as different NC are in different environments and pinning is possible in some cases). For stage (iii), naturally no true steady-state is achieved and other effects such as support restructuring dominate behavior.

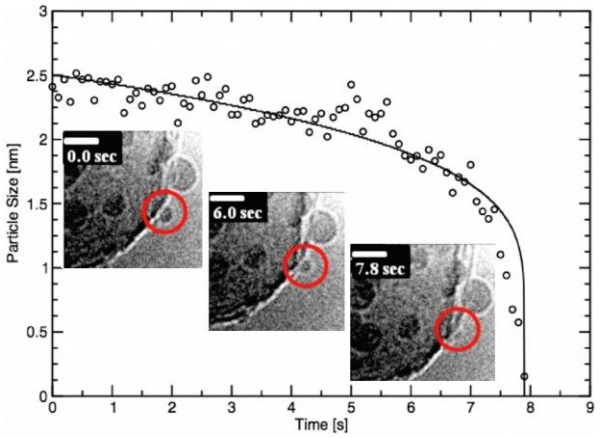

Figure 136. Early stage OR of Ni/ $MgAl_2O_4$ with 200 Pa H_2O and 200 Pa H_2 at 750 C. Decay of the small NC is described by mean-field type AD-limited decay. Reprinted with permission from Ref. 29. Copyright 2011 American Chemical Society.

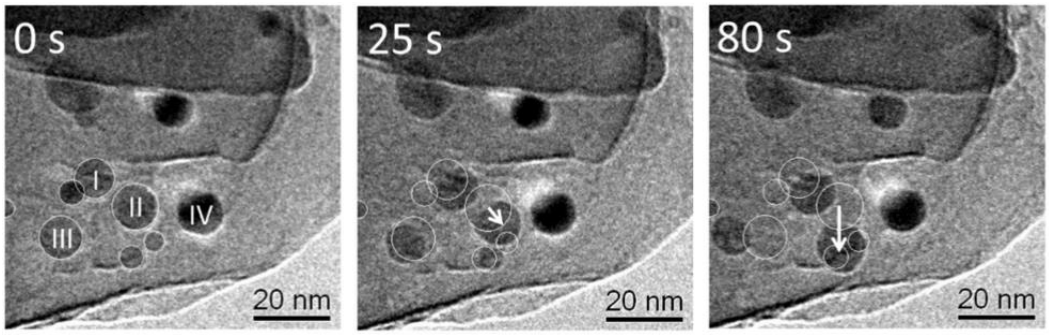

Figure 137. Early stage OR of Ni/$MgAl_2O_4$ with 200 Pa H_2O and 200 Pa H_2 at 750 C. Thin white circles denote initial NC positions. Reprinted with permission from Ref. 30. Copyright 2013 American Chemical Society.

Another study explored coarsening separately for small 2.2 nm Pt NC and for large 4.4 nm Pt NC, and for a mixture thereof, supported on Al_2O_3 in forming gas (5% H_2/N_2) at elevated temperature up to 800 C[293]. The particle size distribution evolved significantly for the small NC but not for the larger ones. However, the largest change occurred for an initial mixture indicating that coarsening was dominated by OR. Again, it was proposed that OR was AD-limited. In contrast, under conditions of low NC density, mobility of small 2.2 nm NCs was evident (see Figure 138), but not of the larger 4.4 nm NCs. Such a decrease in mobility with increasing size is consistent with traditional theories.[291].

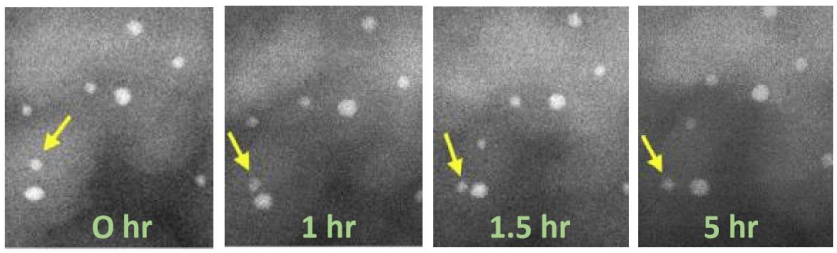

Figure 138. 2.2 nm Pt NC with low density ($14x10^{-4}$ nm^{-2}) on Al_2O_3 in forming gas (5% H_2/N_2) formed at 700 C evolving at 800 C. Reprinted with permission from Ref. 293. Copyright 2013 Elsevier.

A third study related to supported Pt NCs performed TEM analysis of coarsening on a simpler planar SiO_2 support and found OR as the dominant process with negligible NC mobility.[294,295] While the default expectation was AD-limited OR, sizes of individual decaying NCs were tracked and found to display deviations from a mean-field AD-limited picture, i.e., evolution depended to some extent on the local environment. However, rather than the TD-limited analysis described in Sec.8.1 for Ag/Ag(111), an AD limited picture was still adopted where the total flux to NC i was written as $J_i \propto 2\pi\, r_i \exp[-E_s/(k_B T)](\rho_{local} - \rho_i)$, where E_s is the energy barrier for a Pt atom to detach to the substrate, r_i is the radius of NC i, and critically ρ_{local} is the local equilibrium density associated with nearest-neighbor NCs to i. The nearest neighbors, j, are determined from a Voronoi construction, and ρ_{local} is determined from a weighted average of the ρ_j

utilizing the opening angles as defined in Sec.8.1. See Figure 139. This type of formulation has been applied for coarsening in semiconductor systems.[296]

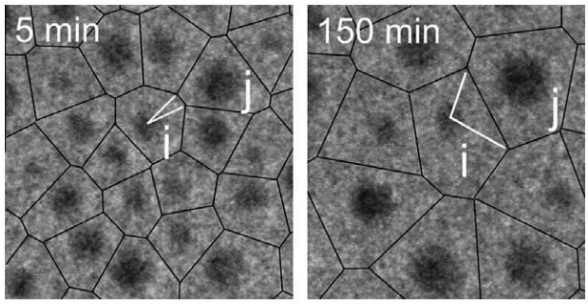

Figure 139. OR of Pt NC on SiO_2 with AD-limited behavior modified by local effects. Reprinted with permission from Ref. 295. Copyright 2011 Elsevier.

For a more comprehensive discussion of the sintering of NCs of various metals (Pt, Ir, Ag, Au, etc.) prepared in various ways (vapor deposition, micelle-synthesized) on various supports (TiO_2, SiO_2, Al_2O_3, etc.) under various conditions (oxidizing, reducing), see Ref. 297.

For solution-phase coarsening of 3D NCs, in general there is a challenge to deconvolute the classical nucleation and growth, aggregative growth (or SR), and Ostwald Ripening (OR) stages indicated in Figure 27. Studying subsequent growth of small preformed particles eliminates the first nucleation stage thereby reducing the challenge to distinguishing between aggregative growth and OR[44] (somewhat akin to the challenge described above for supported 3D NCs). Nucleation kinetics is often associated with a sigmoidal form for mean NC volume, $V(t)$, vs time, t, whereas (AD-limited) OR is associated with a linear increase of $V(t)$ with t. However, it has been suggested that aggregative growth can also display sigmoidal kinetics as illustrated in Figure 140 for thiolate-capped 1.7 nm gold nanocrystals.[298] Evidence for aggregative growth comes from observation of a bimodal NC size distribution (inset) at the end of the initial induction period. The smaller-size peak is assumed to correspond to the initial primary NCs and the larger-size peak with critical-sized aggregates.

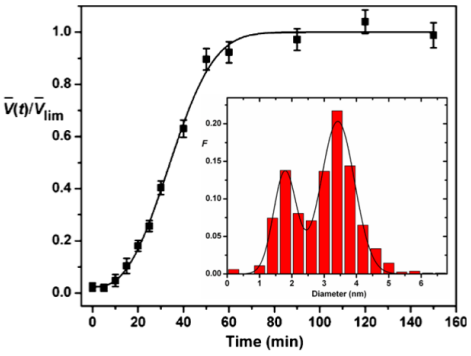

Figure 140. Mean size evolution during coarsening of 1.7 nm thiolate-capped Au NCs. The inset particle size distribution is taken just after the initial induction period. Reprinted with permission from Ref. 298. Copyright 2010 American Chemical Society.

Another example for which fairly detailed analysis of kinetics is available is for Ag NC growth by reaction of $(PPh_3)Ag(O_2CC_{13}H_{27})$ and AIBN in the presence of a PHD-co-PVP polymer stabilizer where primary nanocrystals of 1.8 nm diameter were observed to form within 3-4 min.[299] Again a bimodal distribution of NC sizes emerged after the first several minutes indicative of aggregative growth. However, in contrast to the above example for Au NCs, a clear long-time regime of OR emerges, i.e., classical nucleation occurs from 0-15 min, aggregative growth from 5-60 min., and OR from 60-100 min. See Figure 141.

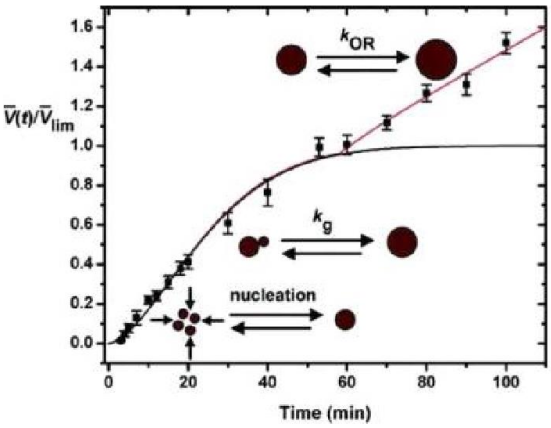

Figure 141. Mean size evolution during growth and coarsening of Ag NCs. Reprinted with permission from Ref. 299. Copyright 2010 American Chemical Society.

8.5. Accelerated complex-mediated Ostwald Ripening

It has long been speculated for complex systems involving supported 3D catalytic NCs,[70] and more recently for 2D epitaxial NCs, that coarsening can be accelerated through the formation of “volatile complexes” including the metal and some additional chemisorbed species.[59] For the former, facile formation of PtO_2 was proposed to facilitate metal mass transport, a process which was recently explored and confirmed by both HP-XPS experiment[300] and by theory.[301]

Here, we focus on analyses for 2D homoepitaxial systems where oxygen[302] and sulfur[303] have been shown to accelerate OR on Ag(100), and S has been shown to dramatically accelerate OR (by two orders of magnitude) on Cu(111)[304] and Ag(111).[113] Specifically, we describe in some detail the latter systems. A particularly comprehensive study was performed of the decay of Cu NCs on Cu(111) in the presence of trace amounts of S.[304] This study found three regimes of coarsening kinetics: **(i)** no significant change from TD-limited OR kinetics for S coverages up to 2 milli-monolayers (mML); **(ii)** a transition to apparent AD-limited OR with accelerated rate for 2-6 mML S; **(iii)** a second transition back to apparent TD-limited OR with further enhanced rates above 7 mML S. It was suggested that this enhancement in OR was due to mass transport facilitated by the formation of a Cu-sulfur surface complex, initially proposed by Feibelman[305] to be Cu_3S_3. The basic idea is similar to that for PtO_2 in catalytic systems that Cu_3S_3 is volatile in the sense that it has a low formation energy[305] associated with

extracting three Cu from the surface to form the complex with three terrace S. The fact that this formation energy is much lower than for atomic Cu on the terrace means that the equilibrium density of complexes is far higher than atomic Cu which more than compensates for their lower mobility.

Elucidation of the remarkable changes in OR kinetics with S coverage, θ_S, requires more sophisticated modeling. A simple but particularly effective and insightful strategy was adopted in Ref. 304 which replaced the standard steady-state diffusion equation $\partial\rho/\partial t = D\nabla^2\rho \approx 0$ with a coupled linear pair of diffusion equations for the M = Cu metal adatom density (or coverage), ρ_M, and the complex density, ρ_{Cx}. Assuming that Cu detaches from step edges and forms a complex on terraces with linear kinetics at rate α, and that the complexes decompose to atoms with linear kinetics at rate β, one has that

$$\partial/\partial t\ \rho_M = D_M\ \nabla^2\rho_M - \alpha\rho_M + \beta\rho_{Cx} \approx 0 \text{ and } \partial/\partial t\ \rho_{Cx} = D_{Cx}\ \nabla^2\rho_{Cx} - \beta\rho_{Cx} + \alpha\rho_M \approx 0. \qquad (85)$$

Here, D_M (D_{Cx}) denotes the surface diffusion coefficient for M (the complex). If $\rho_M(eq)$ [$\rho_{Cx}(eq)$] denotes the equilibrium density or coverage of adatoms [complexes] on terraces, then one has $\alpha/\beta = \rho_{Cx}(eq)/\rho_M(eq)$. Thus, for decreasing θ_S, one has that $\alpha/\beta \to 0$. There is a Dirichlet boundary condition for ρ_M at step edges which requires ρ_M to match the equilibrium density given by the Gibbs-Thompson condition. There is a zero flux boundary condition for ρ_{NC}.

Analysis of the solutions of these equations for simple geometries provides substantial insight into the observed distinct regimes of OR.[304] It is natural and instructive to introduce the characteristic "reaction length", $L_M \sim \sqrt{(D_M/\alpha)}$, which is the typical length that metal adatoms must diffuse before forming complexes. The above three regimes are elucidated as follows. **(i)** For very low θ_S and thus α, one has that $L_M >> L_c$, the typical separation between NCs. Then, atoms detaching from small NCs typically diffuse across terraces and are incorporated into larger NCs before reaction to form complexes. Coarsening behavior is dominated by TD-limited M adatom transport, as for the S-free system. Fluxes scale like $J \sim D_M\,\rho_M(eq)$ with a "small" magnitude reflecting the "large" distances of order L_c over which ρ_M varies significantly. **(ii)** For higher θ_S and α, one has that $L_M < L_c$. Now, ρ_M becomes uniform away from islands, specifically a distance greater than L_M from island edges. However, while ρ_{NC} is flat at step edges due to the boundary conditions, it varies away from step edges corresponding to mass transport mediated by complex diffusion away from NC edges. Fluxes still scale like $J \sim D_M\,\rho_{CM}(eq)$, but now with a "larger" magnitude reflecting the "smaller" distance, L_M, over which ρ_M varies significantly. These fluxes do not reflect distances between islands thereby producing AD-like behavior. **(iii)** For even higher θ_S and α with $L_M << L_c$, the complex density is essentially fully equilibrated with the adatom density, and both vary across terraces in a fashion reminiscent of standard TD-limited OR. Thus, fluxes scale like $J \sim D_{Cx}\,\rho_{Cx}(eq)$ with a magnitude again reflecting the larger distances of order L_c over which ρ_M and ρ_{CX} varies strongly, and which again produces TD-like behavior.

The above experimental and theoretical analysis for the S+Cu(111) system was limited in two respects. First, at the time there was no direct experimental observation or

evidence for the existence or nature of the complexes mediating mass transport. Second, the simple linear analytic theory could not be used make quantitative predictions of various contributions to mass transport needed to fully confirm the model.

Later similar accelerated coarsening was observed for the S+Ag(111) system with some differences in interpretation.[113] One of these is that there was a critical value, θ_S(crit), for θ_S such that for $\theta_S < \theta_S$(crit), all S on the surface is incorporated at step edges and does not participate in complex formation. Clearly, θ_S(crit) depends on the step density and thus the sample. It was θ_S(crit) $\approx$ 7 mML for the S+Ag(111) study[113]. It is expected that such a non-zero critical coverage also exists in the S+Cu(111) system, although evidently θ_S(crit) < 2 mML. Also, rather than using θ_S to characterize different regimes, it is more appropriate to use the excess coverage $\Delta\theta_S = \theta_S - \theta_S$(crit). In addition, for the S+Ag(111) system, it was not assumed that a single complex was involved in accelerated coarsening but rather various complexes. Furthermore, the above linear reaction-diffusion equations were replaced by an appropriate coupled non-linear set of reaction-diffusion equations involving relevant complexes.[113] Analysis of such complex equations is in fact viable by linearization considering small deviations in densities from their equilibrium values. In this way, explicit expressions for relevant complex formation and annihilation rates can be obtained.[113]

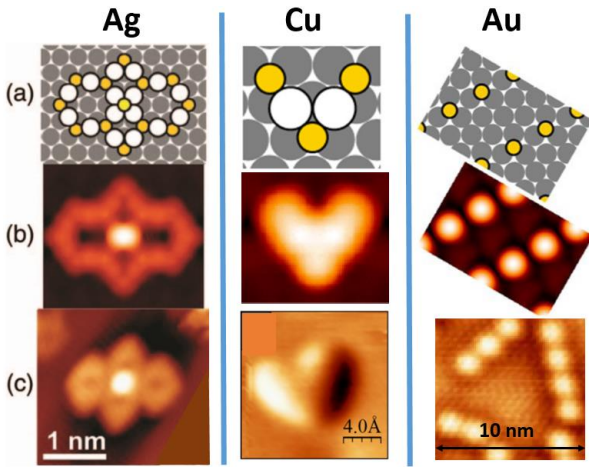

Figure 142. S-metal complexes observed by STM at 5 K on Ag and Cu, but not on Au. (a) proposed structural model; (b) simulated STM images; (c) actual STM image. Ag, Cu, Au image reprinted with permission from Ref. 306, 307, 308, respectively. Copyright 2013 American Institute of Physics, 2015 American Physical Society, 2015 American Institute of Physics, respectively.

With regard to the existence and identity of complexes, a systematic analysis has since been undertaken combining low-T STM studies and DFT analysis to identify adsorbed complexes in various S + metal systems.[306-308] The systems are dosed with S at higher temperature, but anticipated significant mobility of complexes means that these cannot be imaged at such temperatures and at the low coverages of interest. Consequently, for imaging, the system is quenched to 5 K where the complexes should be frozen. (Potentially, complexes can also be imaged at high temperatures for higher coverages if they become locked into an ordered pattern.[309,310]) Selected results are

shown in Figure 142 for S on Ag(111)[306], Cu(111)[307], and Au(111). [308] The lack of observation of M_3S_3 complexes are perhaps unexpected in that the Feibelman conjecture[305] prompted speculation of the existence of such complexes for several metals[311]. For Ag, the observed large $Ag_{16}S_{13}$ complex is presumably not stable at 300 K where coarsening is observed, and a range of smaller complexes were proposed to participate (see below). For Cu, Cu_2S_3 rather than Cu_3S_3 was observed, and indeed we propose that the former dominates mass transport for the S+Cu(111) system (see below). For Au, no complexes were observed, only S adatoms. S adatom ordering occurs at higher T were S is mobile results from a combination of linear trio attraction and long-range pairwise repulsions. It is "frozen in" in this 5 K image.

To develop an appropriate theory for enhanced coarsening in the S+Cu(111) and S+Ag(111) systems, it is necessary to first assess with DFT the stability of various metal-S complexes. Figure 143 shows such viable complexes, and also indicates for M = Cu their associated T=0 K S chemical potentials, μ_S. These μ_S reflects the energy per S atom to form the complex by extracting metal atoms from (kink sites at step edges on) the metal substrate. Thus, lower S implies higher relative stability. For Cu, one finds that the Cu_2S_3 complex is most stable (consistent with experimental observations), with CuS_3, CuS_2 and Cu_3S_3 all having similar slightly lower stability.[307] Table 7 shows these μ_S as well as corresponding diffusion barriers and formation energies $E_{form}(M_mS_n) = n[\mu_S(M_mS_n) - \mu_S(S)]$.

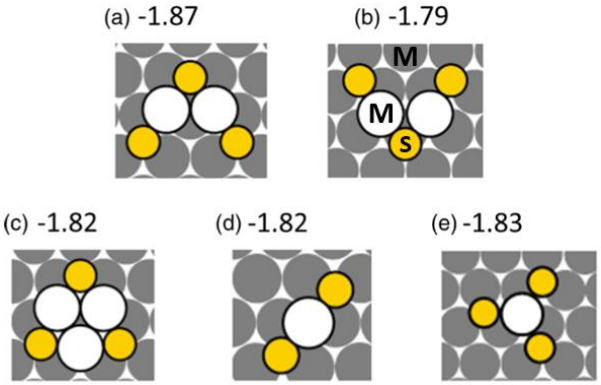

Figure 143. Viable small metal(M)-sulfur (S) complexes on metal(111) surfaces. S chemical potentials are shown for M = Cu indicating that Cu_2S_3 is the most stable. Reprinted with permission from Ref. 307. Copyright 2015 American Physical Society.

Table 7. S chemical potential, μ_S, diffusion barrier, E_d, and formation energy, E_{form}, for various Cu_mS_n complexes adsorbed on Cu(111).

Complex	μ_S (in eV)	E_d (in eV)	E_{form} (in eV)
Cu	n/a	0.05	+0.78
CuS	-1.24	0.33	+0.67
CuS_2	-1.82	0.34	+0.15
CuS_3	-1.83	0.36	+0.24
Cu_2S_3	-1.87	0.35	+0.11
Cu_3S_3	-1.82	0.36	+0.24

Comprehensive analysis of accelerated coarsening kinetics based on appropriate reaction-diffusion equations for complex formation. It is clear that not just complex thermodynamics (e.g., E_{form}) but also kinetics (as reflected in reaction lengths) is relevant. Said differently, the ease of complex formation is important as well as its stability. In fact, there are many possible mechanism or pathways involving different subsets of complexes which could be relevant. Suppose that mass transport is dominated by the complex C+ = M_2S_3 (or M_3S_3) which is formed by the reaction M + C- $\rightarrow$ C+ where C- = MS_3 (or M_2S_3). Then, if $K_{form}(M+C_- \rightarrow C_+)$ and $K_{diss}(C_+ \rightarrow M+C_-)$ denote corresponding forward and reverse rates, one has that

$$\partial/\partial t\ \theta_M = D_M \nabla^2\theta_M + K_{diss}(C_+ \rightarrow M+C_-) - K_{form}(M+C_- \rightarrow C_+) + \ldots \approx 0, \text{ and}$$

$$\partial/\partial t\ \theta_{C+} = D_{C+} \nabla^2\theta_{C+} - K_{diss}(C_+ \rightarrow M+C_-) + K_{form}(M+C_- \rightarrow C_+) + \ldots \approx 0, \qquad (86)$$

where dots indicates various other possible reaction mechanisms. Also, one has that $K_{form}(M+C_- \rightarrow C_+) = (D_M + D_{C-})\theta_M\,\theta_{C-}$ and $K_{diss}(C_+ \rightarrow M+C_-) = (D_M + D_{C-})\exp[-\Delta E/(k_BT)]\ \theta_{C+}$ where ΔE denotes the energy difference between separated M & C_- and C_+. Linearization writes $\theta_M = \theta_M(eq) + \delta\theta_M$, etc., and obtains

$$\nabla^2\,\delta\theta_M - \delta\theta_M/[L_M(C_-)]^2 \approx 0, \text{ where } L_M(C_-) = [D_M/k(M+C_- \rightarrow C_+)]^{1/2}, \qquad (87)$$

with $k(M+C_- \rightarrow C_+) = (D_M + D_{C-})\theta_{C-}(eq)$ and where we have used that the equilibrium values of K_{form} and K_{diss} are equal (so these terms cancel in the θ_M-equation).

As indicated above, one needs that $L_M(C_-) < L_c$ in order for the cluster C_+ to enhance mass transport. However, it was suggested that this is not the case for C_+ = Cu_2S_3 or Cu_3S_3 in the S+Cu(111) system, and that other possible pathways for enhanced coarsening might be considered, e.g., direct detachment of complexes from NC step edges.

9. SUMMARY

Stability of metallic NCs is a key issue for functionality in applications to catalysis and other areas. In this context, stability includes resistance to reshaping, e.g., from synthesized simple geometric shapes such as nanocubes, tetraheda, etc., to equilibrium Wulff polyhedral, or resistance to pinch-off of elongated nanorods. In addition, resistance to coarsening of ensembles of synthesized NCs via either Ostwald Ripening or Smoluchowski ripening is often desired. As the latter involves coalescence or sintering of pairs of NCs, the kinetics of this process is also of interest. For multi-component NCs, and particularly bimetallic NCs, stability of synthesized core-shell structures against intermixing is also of relevance. In this review, we have systematically described and compared these phenomena for 2D epitaxial NCs and for crystalline 3D NCs, where evolution for the former is typically observed by Scanning Tunneling Microscopy (STM) and for the latter by Transmission Electron Microscopy (TEM).

Our primary focus is on predictive atomistic-level stochastic modeling of the post-synthesis evolution of metallic NCs, although considerable additional insight is often also obtained from coarse-grained continuum modeling. Given the non-equilibrium nature of these phenomena, we emphasize the need for such modeling to include a realistic description of the kinetics (versus generic Metropolis, IVA, or even BEP prescriptions), as well as a realistic description of the system thermodynamics. This goal has been achieved traditionally for 2D epitaxial systems by crafting system-specific tailored models, and more recently by formulations incorporating ab-initio kinetics. Extensive success has been and continues to be achieved in providing detailed insight into behavior underlying experimental STM observations. Application of predictive atomistic-level modeling with realistic kinetics to elucidate the evolution of 3D NCs, either supported on substrates or unsupported, is relatively undeveloped field. However, we illustrate the potential of this approach with examples of relatively recent modeling efforts.

AUTHOR INFORMATION

Corresponding Author:

E-mail: evans@ameslab.gov (James W. Evans)

ORCID

King C. Lai: 0000-0003-2764-356X
Yong Han: 0000-0001-5404-0911
Wenyu Huang: 0000-0003-2327-7259
Patricia A. Thiel: 0000-0003-4195-0216
Da-Jiang Liu: 0000-0002-3019-9247
James W. Evans: 0000-0002-5806-3720

Notes

The authors declare no competing financial interest.

REFERENCES

(1) *Nanostructured Materials and Their Applications*, Logothedis, S. Eds.; Springer Series in Nanoscience and Technology (Springer): Berlin, 2012.
(2) Zaera, F. Nanostructured Materials for Applications in Heterogeneous Catalysis. *Chem. Soc. Rev*. **2013**, *7*, 2746-2762.
(3) Xia, Y.; Xiong, Y.; Lim, B.; Skrabalak, S. E. Shape-controlled Synthesis of Metal Nanocrystals: Simple Chemistry Meets Complex Physics? *Angew. Chem. Int. Ed.* **2009**, *48*, 60-103.
(4) Xia, Y.; Xia, X.; Wang, Y.; Xie, S. "Shape-controlled Synthesis of Metal Nanocrystals" *MRS Bulletin* **2013**, *38*, 335-343.
(5) Marks, L.D.; Peng, L. Nanoparticle Shape, Thermodynamics and Kinetics. *J. Phys. Condens. Matter* **2016**, *28*, 053001.
(6) Gilroy, K. D.; Ruditskiy, A.; Peng, H.C.; Qin, D.; Xia, Y. Bimetallic Nanocrystals: Syntheses, Properties, and Applications. *Chem. Rev.* **2016**, *116(18)*, 10414–10472.
(7) Brune, H. Microscopic View of Epitaxial Metal Growth: Nucleation and Aggregation. *Surf. Sci. Rep.* **1998**, *31*, 125-229.
(8) Michely, T; Krug, J. *Islands, Mounds, and Atoms;* Springer: Berlin, 2004.
(9) Evans, J.W.; Thiel, P. A.; Bartelt, M. C. Morphological Evolution during Epitaxial Thin Film Growth: Formation of 2D Islands and 3D Mounds. *Surface Science Reports* **2006**, *61*, 1-128.
(10) Ratke, L.; Voorhees, P.W. *Coarsening and Growth: Ostwald Ripening in Material Processes*; Springer: Berlin, 2001.
(11) Wang, K. G.; Glicksman, M. E. *Ostwald Ripening in Materials Processing, in Materials Processing Handbook*; Taylor & Francis: London, 2007.
(12) Zinke-Allmang, M.; Feldman, L. C.; Grabow, M. H. Clustering on Surfaces. *Surf. Sci. Rep.* **1992***, 16*, 377.
(13) Morgenstern, K. Fast STM as a Tool to Understand Changes on Metal Surfaces: from Nanostructures to Single Atoms. *Phys. Stat. Sol.* **2005**, *242*, 773-796.
(14) Thiel, P. A.; Shen, M.; Liu, D.-J.; Evans, J. W. Coarsening of 2D Nanoclusters on Metal Surfaces. *J. Phys. Chem. C* **2009**, *113*, 5047-5067.
(15) Thanh, N.T.K.; Maclean, N.; Mahiddine, S. Mechanisms of Nucleation and Growth of Nanoparticles in Solution. *Chem. Rev.* **2014**, *114*, 7610-7630.
(16) Kamat P.V. Photophysical, Photochemical and Photocatalytic Aspects of Metal Nanoparticles, *J. Phys. Chem. B* **2002** *106*, 7729-7744.
(17) Liu, X.; Wang, D.; Li, Y. Synthesis and Catalytic Properties of Bimetallic Nanomaterials with Various Architectures. *Nano Today* **2012**, *7 (5)*, 448-466.
(18) Freund, H.-J. Clusters and Islands on Oxides: from Catalysis via Electronics and Magnetism to Optics. *Surf. Sci. Rep.* **2002**, *500*, 271-299.
(19) *Metal Nanoclusters in Catalysis and Materials Science*, Corain, B., Schmid G., Toshima, N. Eds.; Elsevier: Amsterdam, 2008.
(20) Kern, R.; Le Lay, G.; Metois, J.J. *Basic Mechanisms in the Early Stages of Epitaxy.* In *Current Topics in Materials Science*, Vol.3; Kaldis, E. Eds; North Holland: Amsterdam, 1979; pp. 131-419.
(21) Appy, D.; Lei, H.; Wang, C. -Z.; Tringides, M. C.; Liu, D. -J.; Evans, J. W.; Thiel, P. A. Transition and Noble Metals on the (0001) Surface of Graphite: Fundamental Aspects of Adsorption, Diffusion, and Morphology. *Progress in Surface Science* **2014**, *89*, 219-238.
(22) Liu, X.; Han, Y.; Evans, J.W.; Engstfeld, A.; Behm, R.J.; Tringides, M.C.; Hupalo, M.; Lin, H.-Q.; Huang, L.; Ho, K.-M.; Appy, D.; Thiel, P.A.; Wang, C.Z.; Growth Morphology and Properties of Metals on Graphene. *Progress in Surf. Sci.* **2015**, *90*, 397-443.
(23) Han, Y.; Unal, B.; Jing, D.; Thiel, P.A.; Evans, J.W. Temperature-Dependent Growth Shapes of Ni Nanoclusters on NiAl(110). *J. Chem. Phys*. **2011**, *135*, 084706.

(24) Han, Y.; Ünal, B.; Evans, J. W. Formation of a Novel Ordered Ni3Al Surface Structure by Codeposition on NiAl(110). *Phys. Rev. Lett*. **2012**, *108*, 216102.
(25) Han, Y.; Liu, D.-J.; Evans, J. W. Real-Time Ab-initio KMC Simulation of the Self-Assembly and Sintering of Bimetallic Nanoclusters on fcc(100) Surfaces: Au+Ag on Ag(100), *Nano Letters* **2014***, 14*, 4646-4652.
(26) Han, Y.; Evans, J.W. Directing Anisotropic Assembly of Metallic Nanoclusters by Exploiting Linear Trio Interactions and Quantum Size Effects: Au Chains on Ag(100) Thin Films. *J. Phys. Chem. Lett.* **2015**, *6*, 2194-2199.
(27) Han, Y.; Stoldt, C. R.; Thiel, P. A.; Evans, J. W. Ab Initio Thermodynamics and Kinetics for Coalescence of Two-Dimensional Nanoislands and Nanopits on Metal (100) Surfaces. *J. Phys. Chem. C* **2016**, *120*, 21617-21630.
(28) Datye, A. K.; Xu, Q.; Kharas, K.C.; McCarty, J. M. Particle Size Distributions in Heterogeneous Catalysts: What Do They Tell Us about the Sintering Mechanism? *Catal. Today* **2006**, 111, 59-67.
(29) Challa, S. R.; Delariva, A. T.; Hansen, T. W.; Helveg, S.; Sehested, J.; Hansen, P. L.; Garzon, F.; Datye, A. K. Relating Rates of Catalyst Sintering to the Disappearance of Individual Nanoparticles during Ostwald Ripening. *J. Am. Chem. Soc. Comm.* **2011**, *133*, 20672-20675.
(30) Hansen, T. W.; DeLaRiva, A. T.; Challa, S. R.; Datye, A. K. Sintering of Catalytic Nanoparticles: Particle Migration or Ostwald Ripening? *Acc. Chem. Res.* **2013**, *46*, pp 1720–1730.
(31) Zheng, H.; Smith, R. K.; Jun, Y. –W.; Kisielowski, C.; Dahmen, U.; Alivisatos, A. P. Observation of Single Colloidal Platinum Nanocrystal Growth Trajectories, *Science* **2009,** *324*, 1309-1312.
(32) Lim, T. H.; McCarthy, D. N.; Hendy, S. C.; Stevens, K. J.; Brown, S. A.; Tilley, R. D. Real-time TEM and Kinetic Monte Carlo Studies of the Coalescence of Decahedral Gold Nanoparticles. *ACS Nano* **2009**, *3*, 3809-3813.
(33) Yuk, J. M.; Park, J.; Ercius, P.; Kim, K.; Hellebusch, D. J.; Crommie, M. F.; Lee, J. Y.; Zettl, A.; Alivisatos, A. P. High-Resolution EM of Colloidal Nanocrystal Growth Using Graphene Liquid Cells. *Science* **2012**, *336*, 61-64.
(34) Woehl, T. J.; Evans, J. E.; Arslan, I.; Ristenpart, W. D.; Browning, N. D.; Direct in Situ Determination of the Mechanisms Controlling Nanoparticle Nucleation and Growth. *ACS Nano* **2012**, *10*, 8599-8610.
(35) Liao, H. -G.; Zherebetskyy, D.; Xin, H.; Czarnik, C.; Ercius, P.; Elmlund, H.; Pan, M.; Wang, L. –W.; Zheng, H. Facet Development during Platinum Nanocube Growth. *Science* **2014**, *345*, 916-919.
(36) Ye, X.; Jones, M. R.; Frechette, L. B.; Chen, Q.; Powers, A. S.; Ercius, P.; Dunn, G.; Rotskoff, G. M.; Nguyen, S. C.; Adiga, V. P.; Zettl, A.; Rabani, E.; Geissler, P. L.; Alivisatos, A. P. Single-particle Mapping of Nonequilibrium Nanocrystal Transformations. *Science* **2016**, *354*, 874-877.
(37) Dubrovskii, V.C. *Nucleation Theory and Growth of Nanostructures*; Springer: Berlin, 2014.
(38) Shneidman, V.A. Nucleation Rates for High Supersaturations. *Phys. Rev. Lett.* **2005**, *95*, 115701.
(39) Shneidman, V.A. Universal Distributions Generated in a Nucleation Pulse. *Phys. Rev. Lett.* **2008**, *101*, 205702.
(40) Erdemir, D.; Lee, A. Y.; Myerson, A. S.; Nucleation of Crystals from Solution: Classical and Two-Step Models. *Acc. Chem. Res.* **2009**, *42 (5)*, 621–629.
(41) van Huis, M.A.; Kunneman, L.T.; Overgaag, K.; Xu, Q.; Pandraud, G.; Zandbergen, H.W.; Vanmaekelbergh, D. Low-Temperature Nanocrystal Unification through Rotations and Relaxations Probed by in Situ Transmission Electron Microscopy. *Nano Lett.* **2008**, *8*, 3959-3963.

(42) Li, D.; Nielsen, M. H.; Lee, J. R. I.; Frandsen, C.; Banfield, J. F.; De Yoreo, J. J. Direction-Specific Interactions Control Crystal Growth by Oriented Attachment. *Science* **2012**, *336,* 1014-1018.
(43) Zhang, H.; De Yoreo, J.J.; Banfield, J.F. A Unified Description of Attachment-Based Crystal Growth. *ACS Nano* **2014**, *8*, 6526-6530.
(44) Wang, F.; Richards, V. N.; Shields, S. P.; Buhro, W. E. Kinetics and Mechanisms of Aggregative Nanocrystal Growth. *Chem. Mat.* **2014**, *26*, 5-21.
(45) Seyed-Razavi, A.; Snook, I. K.; Barnard, A. S. Origin of Nanomorphology: Does a Complete Theory of Nanoparticle Evolution Exist? *J. Mater. Chem*. **2010**, *20*, 416-421.
(46) Seyed-Razavi, A.; Snook, I. K.; Barnard, A. S.; Surface Area Limited Model for Predicting Anisotropic Coarsening of Faceted Nanoparticles. *Crystal Growth & Design* **2011**, *11*, 158-165.
(47) Mpourmpakis G.; Vlachos, D. G. Growth Mechanisms of Metal Nanoparticles via First Principles. *Phys. Rev. Lett*. **2009**, *102*, 155505.
(48) Al-Saidi, W.; Feng, H.; Fichthorn, K. A. Adsorption of Polyvinylpyrrolidone on Ag Surfaces: Insight into a Structure-directing Agent. *Nano Letters* **2012**, *12*, 997-1001.
(49) Bealing, C. R.; Baumgardner, W. J.; Choi, J. J.; Hanrath, T.; Hennig, R. G. Predicting Nanocrystal Shape through Consideration of Surface-Ligand Interactions. *ACS Nano* **2012**, *6*, 2118-2127.
(50) Qi, X.; Balankura, T.; Zhou, Y.; Fichthorn, K. A. How Structure-Directing Agents Control Nanocrystal Shape: Polyvinylpyrrolidone-Mediated Growth of Ag Nanocubes. *Nano Lett.* **2015**, *15 (11)*, 7711–7717.
(51) Fichthorn, K. A.; Balankurab, T.; Qi, X.; Multi-scale Theory and Simulation of Shape-selective Nanocrystal Growth. *Cryst. Eng. Comm.* **2016**, *18*, 5410-5417.
(52) Newman, M.E.J.; Barkema, G.T. *Monte Carlo Methods in Statistical Physics*; Oxford University Press: Oxford, 1999.
(53) Landau, D.P.; Binder, K. *A Guide to Monte Carlo Simulations in Statistical Physics*; Cambridge University Press: Cambridge, 2000.
(54) Smigelskas, A.D.; Kirkendall, E.O. Zinc Diffusion in Alpha-brass. *Trans. AIME* **1947**, *171*, 130-142.
(55) Fan, H. J.; Gösele, U.; Zacharias, M. Formation of Nanotubes and Hollow Nanoparticles Based on Kirkendall and Diffusion Processes: A Review. *Small* **2007**, *3*, 1660–1671.
(56) Morgenstern, K.; Lægsgaard, E.; Stensgaard, I.; Besenbacher, F. Transition from One-Dimensional to Two-Dimensional Island Decay on an Anisotropic Surface. *Phys. Rev. Lett.* **1999**, *83*, 1613.
(57) Han, Y.; Russell, S. M.; Layson, A. R.; Walen, H.; Yuen, C. D. Thiel, P. A.; Evans, J. W. Anisotropic Coarsening: One-dimensional Decay of Ag Islands on Ag(110). *Phys. Rev. B* **2013**, *87*, 155420.
(58) Harris, P. J. F. Growth and Structure of Supported Metal Catalyst Particles. *Int. Mat. Rev.* **1995**, *40*, 97-115.
(59) Thiel, P.A.; Shen, M.; Liu, D.-J.; Evans, J.W. Adsorbate-enhanced Mass-transport on Metal Surfaces: Oxygen and Sulfur on Coinage Metals. *J. Vac. Science Technol. A* **2010**, *28*, 1285-1298.
(60) Whitesides, G.M.; Grzybowski, B. Self-assembly at All Scales. *Science* **2002**, *295*, 2418-2421.
(61) Witten Jr., T. A.; Sander, L. M.; Diffusion-Limited Aggregation, a Kinetic Critical Phenomenon. *Phys. Rev. Lett.* **1981**, *47*, 1400.
(62) Vicsek, T. *Fractal Growth Phenomena*; World Scientific: Singapore, 1992.
(63) Eden, M. *A Two-dimensional Growth Process.* In *Proceedings of Fourth Berkeley Symposium on Mathematics, Statistics, and Probability,* Vol. 4; University of California Press: Berkeley, 1961; pp. 223–239.

(64) Kardar, M.; Parisi, G.; Zhang, Y. -C. Dynamic Scaling of Growing Interfaces. *Physical Review Letters* **1986**, *56*, 889–892.
(65) Hwang, R. Q.; Schröder, J.; Günther, C.; Behm, R. J.; Fractal Growth of Two-dimensional Islands: Au on Ru(0001). *Phys. Rev. Lett.* **1991**, *67*, 3279-3282.
(66) Bartelt, M. C.; Evans, J. W. Dendritic Islands in Metal-on-Metal Epitaxy I: Shape Transitions and Diffusion at Island Edges. *Surf. Sci.* **1994**, *314*, 829-834.
(67) Hohage, M.; Bott, M.; Morgenstern, M.; Zhang, Z.; Michely, T.; Comsa. G. Atomic Processes in Low Temperature Pt-Dendrite Growth on Pt(111). *Phys. Rev. Lett.* **1996**, *76*, 2366-2369.
(68) Cox, E.; Li, M.; Chung, P.-W.; Ghosh, C.; Rahman, T.S.; Jenks, C.J.; Evans, J.W.; Thiel, P.A. Temperature-dependence of Island Growth Shapes in Submonolayer Deposition of Ag on Ag(111). *Phys. Rev. B* **2005**, *71*, 115414.
(69) Giesen, M. Step and Island Dynamics at the Solid/Vacuum and Solid/Liquid Interfaces. *Prog. Surf. Sci.* **2001**, *68*, 1-153.
(70) Henry, C.R. Morphology of Supported Nanoparticles. *Prog. Surf. Sci.* **2005**, *80*, 92-116.
(71) Bartelt, M. C.;Schmid, A. K.;Evans, J. W.;Hwang, R. Q. Island Size and Environment Dependence of Adatom Capture: Cu/Co Islands on Ru(0001). *Phys. Rev. Lett.* **1998**, *81*, 1901-1904.
(72) Brune, H.; *Creating Metal Nanostructures at Metal Surfaces Using Growth Kinetics*. In *Handbook of Surface Science*, *Vol. 3 Dynamics*; Hasselbrink, E. Eds; Elsevier: Amsterdam, 2008; pp. 761-786.
(73) Duguet, T.; Han, Y.; Yuen, C.; Jing, D.; Unal, B.; Evans, J.W.; Thiel, P.A. Self-assembly of Metal Nanostructures on Binary Alloy Substrates. *Proc. National Acad. Sciences*, **2011**, *108*, 989-994.
(74) Park, J. B.; Ratliff, J. S.; Ma, S.; Chen, D. A. In situ Scanning Tunneling Microscopy Studies of Bimetallic Cluster Growth: Pt–Rh on TiO2(110). *Surface Science* **2006**, *600 (14)*, 2913-2923.
(75) Park, J. B.; Conner, S. F.; Chen, D. A. Bimetallic Pt−Au Clusters on TiO2(110): Growth. Surfe Composition, and Metal−Support Interactions. *J. Phys. Chem. C* **2008**, *112 (14)*, 5490–5500.
(76) Galhenage, R. P.; Ammal, S. C.; Yan, H.; Duke, A. S.; Tenney, S. A.; Heyden, A.; Chen, D. A. Nucleation, Growth, and Adsorbate-Induced Changes in Composition for Co–Au Bimetallic Clusters on TiO2. *J. Phys. Chem. C* **2012**, *116 (46)*, 24616–24629.
(77) Galhenage, R. P.; Xie, K.; Yan, H.; Seuser, G. S.; Chen. D. A. Understanding the Growth, Chemical Activity, and Cluster–Support Interactions for Pt–Re Bimetallic Clusters on TiO2(110). *J. Phys. Chem. C* **2016**, *120 (20)*, 10866–10878.
(78) Han, Y.; Engstfeld, A. K.; Behm, R. J.; Evans, J.W. Atomistic Modeling of the Directed Assembly of Bimetallic Pt-Ru Nanoclusters on Ru(0001)-supported Monolayer Graphene. *J. Chem. Phys.* **2013**, *138*, 134703.
(79) Chaudhuri, R. G.; Paria, S. Core/Shell Nanoparticles: Classes, Properties, Synthesis Mechanisms, Characterization, and Applications. *Chem. Rev.* **2012**, *112 (4)*, 2373–2433.
(80) Wang, X.; He, B.; Hu, Z.; Zeng, Z.; Han, S.; Current Advances in Precious Metal Core–shell Catalyst Design. *Sci. Technol. Adv. Mater.* **2014**, *15*, 043502.
(81) Weiner, R. G.; DeSantis, C. J.; Cardoso, M. B. T.; Skrabalak, S. E.; Diffusion and Seed Shape: Intertwined Parameters in the Synthesis of Branched Metal Nanostructures. *ACS Nano* **2014**, *8 (8)*, 8625–8635.
(82) Sneed, B. T.; Young, A. P.; Jalalpoor, D.; Golden, M. C.; Mao, S.; Jiang, Y.; Wang, Y.; Tsung, C. –K.; Shaped Pd–Ni–Pt Core-Sandwich-Shell Nanoparticles: Influence of Ni Sandwich Layers on Catalytic Electrooxidations. *ACS Nano* **2014**, *8*, 7239-7250.
(83) Venables, J. A. Rate Equation Approaches to Thin Film Nucleation Kinetics. *Phil. Mag* **1973,** *27*, 697-738.

(84) Venables, J. A.; Spiller, G. D.; Handbuchen, M. Nucleation and Growth of Thin Films. *Rep. Prog. Phys*. **1984**, *47*, 399-459.
(85) Bales, G. S.; Chrzan, D. C. Dynamics of Irreversible Island Growth during Submonolayer Epitaxy. *Phys. Rev. B* ***1994***, *50*, 6057-6067.
(86) Bartelt, M. C.; Evans, J. W. Scaling Analysis of Diffusion-mediated Island Growth in Surface Adsorption Processes. *Phys. Rev. B.* **1992**, *46*, 12675-12687.
(87] Bartelt, M. C.; Evans, J. W. Nucleation and Growth of Square Islands during Deposition: Sizes, Coalescence, Separations & Correlations. *Surf. Sci.* **1993**, *298*, 421-431.
(88) Bartelt, M. C.; Evans, J. W. Exact Island Size Distributions for Submonolayer Deposition: Influence of Correlations between Island Size & Separation. *Phys. Rev. B (Rapid Comm.)* **1996**, *54*, 17359-17362.
(89) Stoyanov, S. *Nucleation Theory for High and Low Supersaturations*. In *Current Topics in Materials Science, Vol.3.* Kaldis, E. Eds.; North Holland: Amsterdam, 1979; pp. 421-462.
(90) Mulheran, P. A.; Blackman, J. A. Capture Zones and Scaling in Homogeneous Thin-film Growth. *Phys. Rev. B* **1996**, *53*, 10261-10267.
(91) Bartelt, M.C.; Stoldt, C.R.; Jenks, C.J.; Thiel, P.A.; Evans, J.W. Adatom Capture by Arrays of Two-Dimensional Ag Islands on Ag(100). *Phys. Rev. B* **1999**, *59*, 3125-3134.
(92) Bartelt, M.C.; Hannon, J.B.; Schmid, A.K.; Stoldt, C.R.; Evans, J.W.; Island Formation during Deposition and Etching. *J. Colloids and Surfaces A* **2000,** *165*, 373-403.
(93) Li, M.; Bartelt, M.C.; Evans, J.W. Geometry-based Simulation of Submonolayer Film Growth. *Phys. Rev. B* **2003**, *68*, 121401.
(94) Li, M.; Evans, J. W. Modeling of Island Formation during Submonolayer Deposition: A Stochastic Geometry-Based Simulation (GBS) Approach. *SIAM Multiscale Modeling & Simulation* **2005**, *3*, 629-657.
(95) Mulheran, P. A.; Robbie, D. A. Theory of the Island and Capture Zone Size Distributions in Thin Film Growth. *Euro. Phys. Lett*. **2000**, *49*, 617-623.
(96) Amar, J. G.; Popescu, M. N.; Family, F.; Rate-Equation Approach to Island Capture Zones and Size Distributions in Epitaxial Growth. *Phys. Rev. Lett.* **2001**, *86*, 3092-3095.
(97) Evans, J. W.; Bartelt, M.C.; Nucleation, Adatom Capture, and Island Size Distributions: Unified Scaling Analysis for Submonolayer Deposition. *Phys. Rev. B* **2001**, *63*, 235408.
(98) Evans, J. W.; Bartelt, M.C. Island Sizes and Capture Zone Areas in Submonolayer Deposition: Analysis via Scaling and Factorization of the Joint Probability Distribution. *Phys. Rev. B* **2002**, *66*, 235410.
(99) Rottman, C.; Wortis, M. Exact Equilibrium Crystal Shapes at Nonzero Temperature in Two Dimensions. *Phys. Rev. B* **1981**, *24*, 6274-6277.
(100) Winterbottom, W.L. Equilibrium Shape of a Small Particle in Contact with a Foreign Substrate. *Acta Metall.* **1967**, *15*, 303-310.
(101) Zhong, J.; Zhang, T.; Zhang, Z.; Lagally, M. G. Island-corner Barrier Effect in Two-dimensional Pattern Formation at Surfaces. *Phys. Rev. B* **2001**, *63*, 113403.
(102) Liu, S. J.; Huang, H.; Woo, C. H. Schwoebel-Ehrlich Barrier: from Two to Three Dimensions. *Appl. Phys. Lett*. **2002**, *80*, 3295-3297.
(103) Wang, J.; Huang, H.; Cale, T.S.; Diffusion Barriers on Cu Surfaces and near Steps. *Modelling Simul. Mater. Sci. Eng.* **2004**, *12*, 1209–1225.
(104) Xiang, S. K.; Huang. H. Ab initio Determination of Ehrlich–Schwoebel Barriers on Cu{111}. *Appl. Phys. Lett.* **2008**, *92*, 101923-101925.
(105) Zhao, Y. P.; Ye, D. X.; Wang, G. C.; Lu. T. M. Novel Nano-column and Nano-Flower Arrays by Glancing Angle Deposition. *Nano Lett.* **2002**, *2 (4)*, 351-354.
(106) Zhou, L. G.; Huang, H. Characteristic Length Scale of Nanorod Diameter during Growth. *Phys. Rev. Lett.* **2008**, *101*, 266102.
(107) Zhang, R.; Huang, H. Another Kinetic Mechanism of Stabilizing Multiple-layer Surface Steps. *Appl. Phys. Lett.* **2001**, *98*, 2219030-211905.

(108) Smoluchowski, M. Drei Vorträge über Diffusion, Brownsche Molekularbewegung und Koagulation von Kolloidteilchen. *Physik. Z* **1916**, *17*, 557–571, 585–599.
(109) Wen, J.-M.; Evans, J. W.; Bartelt, M. C.; Burnett, J. W.; Thiel, P. A. Coarsening Mechanisms in a Metal Film: From Cluster Diffusion to Vacancy Ripening. *Phys. Rev. Lett.* **1996**, *76*, 652-655.
(110) Shen, M.; Wen, J. M.; Jenks, C. J.; Thiel, P. A.; Liu, D. -J.; Evans, J. W. Ripening of Monolayer Vacancy Pits on Metal Surfaces: Pathways, Energetics, and Size-scaling for Ag(111) versus Ag(100). *Phys. Rev. B*, **2007**, *75*, 245409.
(111) Li, M.; Wang, C. Z.; Evans, J. W.; Hupalo, M.; Tringides, M.; Ho, K.-M. Competition between Area and Height Evolution of Pb Islands on a Si(111) Surface. *Phys. Rev. B* **2009**, *79*, 113404.
(112) Wang, C. -J.; Han, Y.; Walen, H.; Russell, S. M.; Thiel, P. A.; Evans. J. W. Analytic Formulations for One-dimensional Decay of Rectangular Homoepitaxial Islands during Coarsening on Anisotropic fcc(110) Surfaces. *Phys. Rev. B* **2013**, *88*, 155434.
(113) Shen, M.; Liu, D.-J.; Jenks, C.J.; Thiel, P.A.; Evans, J.W. Accelerated Coarsening of Ag Adatom Islands on Ag(111) due to Trace Amounts of S: Mass Transport Mediated by Ag-S complexes. *J. Chem. Phys.* **2009**, *130*, 094701.
(114) Stoldt, C.R.; Cadilhe, A.M.; Jenks, C.J.; Wen, J.-M.; Evans, J.W.; Thiel, P. A. Evolution of Far-From-Equilibrium Nanostructures Formed by Cluster-Step and Cluster-Cluster Coalescence in Metal Films. *Phys. Rev. Lett.* **1998**, *81*, 2950-2953.
(115) Frenkel, D.; Smit, B. *Understanding Molecular Simulation, Second Edition: From Algorithms to Applications*; Academic Press, 2001.
(116) Kelton, K.; Greer, A.; *Nucleation in Condensed Matter*, Vol. 15, 1st Edition, Applications in Materials and Biology; Elsevier: Amsterdam, 2010.
(117) De Yoreo, J.; Whitelam, S. *Nucleation in Atomic, Molecular, and Colloidal Systems*. *MRS Bulletin* **2016**, *41*, 5.
(118) Lee, J.; Yang, J.; Kwon, S. G.; Hyeon, T. Nonclassical Nucleation and Growth of Inorganic Nanoparticles. *Nature Rev. Mater.* **2016**, *1*, 16034.
(119) Watzky, M. A.; Finke, R. G. Transition Metal Nanocluster Formation Kinetic and Mechanistic Studies. A New Mechanism When Hydrogen Is the Reductant: Slow, Continuous Nucleation and Fast Autocatalytic Surface Growth. *J. Am. Chem. Soc.* **1997**, *119 (43)*, 10382–10400.
(120) van Kampen, N.G. *Stochastic Processes in Physics and Chemistry*, 3rd Edition; North Holland: Amsterdam, 2007.
(121) Combe, N.; Jensen, P.; Pimpinelli, A. Changing Shapes in the Nanoworld. *Phys. Rev. Lett.* **2000**, *85*, 110-113.
(122) McCarthy, D. N.; Brown, S. A. Evolution of Neck Radius and Relaxation of Coalescing Nanoparticles. *Phys. Rev. B* **2009**, *80*, 064107.
(123) Gorshkov, V.; Kuzmenko, V.; Privman, V. Nonequilibrium Kinetic Study of Sintering of Dispersed Nanoparticles. *Cryst. Eng. Comm.* **2013**, *15*, 7177-7191.
(124) Gorshkov, V.; Privman, V. Kinetic Monte Carlo Model of Breakup of Nanowires into Chains of Nanoparticles. *J. Appl. Phys.* **2017**, *122*, 204301.
(125) Mullins W.W. Flattening of a Nearly Plane Solid Surface due to Capillarity. *J. Appl. Phys.* **1959**, *30*, 77-83.
(126) Eggers, J. Coalescence of Spheres by Surface Diffusion. *Phys. Rev. Lett.* **1998**, *80*, 2634-2637.
(127) Herring, C. *Surface Tension as a Motivation for Sintering*. In *The Physics of Powder Metallurgy*; Kingston, W. E. Eds.; McGraw-Hill: New York, 1951; pp. 143-79.
Also in: *Fundamental Contributions to the Continuum Theory of Evolving Phase Interfaces in Solids.* Ball, J. M.; Kinderlehrer, D.; Podio-Guidugli P.; Slemrod M. Eds.; Springer: Berlin, Heidelberg, 1999.

(128) Nichols, F. A.; Mullins, W. W. Morphological Changes of a Surface of Revolution due to Capillarity-Induced Surface Diffusion. *J. Appl. Phys.* **1965**, *36*, 1826-1835.
(129) Khare, S.V. Einstein, T.L. Unified View of Step-edge Kinetics and Fluctuations. *Phys. Rev. B* **1998**, *57*, 4782-4797.
(130) Zia, R. K. P.; Avron, J. E. Total Surface Energy and Equilibrium Shapes: Exact Results for the d=2 Ising Crystal. *Phys. Rev. B* **1982**, *25*, 2042-2045.
(131) Zia, R. K. P. Exact Equilibrium Shapes of Ising Crystals on Triangular/Honeycomb Lattices. *J. Statist. Phys.* **1986**, *45*, 801–813.
(132) Stasevich, T. J.; Einstein, T. L.; Zia, R. K. P.; Giesen, M.; Ibach, H.; Szalma, F. Effects of Next-nearest-neighbor Interactions on the Orientation Dependence of Step Stiffness: Reconciling Theory with Experiment for Cu(001). *Phys. Rev. B*, **2004**, *70,* 245404.
(133) Stasevich, T. J.; Gebremariam, H.; Einstein, T. L.; Giesen, M.; Steimer, C.; Ibach, H. Low-temperature Orientation Dependence of Step Stiffness on {111} Surfaces. *Phys. Rev. B* **2005**, *71*, 245414.
(134) Stasevich, T. J.; Einstein, T. L. Analytic Formulas for the Orientation Dependence of Step Stiffness and Line Tension: Key Ingredients for Numerical Modeling. Multiscale Model. *Simul.* **2007**, *6*, 90-104.
(135) Stasevich, T. J.; Einstein, T. L.; Stolbov, S. Extended Lattice Gas Interactions of Cu on Cu(111) and Cu(001): Ab initio Evaluation and Implications. *Phys. Rev. B* **2006**, *73*, 115426.
(136) Tiwary, Y.; Fichthorn, K. A. Interactions between Al atoms on Al(110) from First-principles Calculations. *Phys. Rev. B* **2007**, *75*, 235451.
(137) Sathiyanarayanan, R.; Stasevich, T. J.; Einstein, T. L. Sensitivity of Short-Range Trio Interactions to Lateral Relaxation of Adatoms: Challenges for Detailed Lattice-Gas Modeling. *Surf. Sci.* **2008**, *602*, 1243−1249.
(138) Einstein, T. L.; Sathiyanarayanan, R. *Multisite Interactions in Lattice-Gas Models.* In *Nanophenomena at Surfaces;* Michailov, M., Eds.; *Springer Series in Surface Sciences 47*; Springer-Verlag: Berlin, Heidelberg, 2011; pp 19−37.
(139) Li, W.; Huang, L.; Evans, J. W.; Han, Y. Submonolayer Ag Films on Fe(100): A Frst-principles Analysis of Energetics Controlling Adlayer Thermodynamics and Kinetics. *Phys. Rev. B* **2016**, *93*, 155416.
(140) Sanchez, J. M. Cluster Expansion and the Configurational Theory of Alloys. *Phys. Rev. B* **2010**, *81*, 224202.
(141) Tiwary, Y.; Fichthorn, K. A. Connector Model for Describing Many-Body Interactions at Surfaces. *Phys. Rev. B* **2008**, *78*, 205418.
(142) Rottman, C.; Wortis, M. Equilibrium Crystal Shapes for (3D) Lattice Models with Nearest- and next-nearest-neighbor Interactions. *Phys. Rev. B* **1984**, *29*, 328-339.
(143) Wang, L. L.; Tan, T. L.; Johnson, D. D. Nanoalloy Composition-temperature Phase Diagram for Catalyst Design: Case Study of Ag-Au. *Phys. Rev. B* **2012**, *86 (3)*, 035438.
(144) Wang, L.L.; Tan, T.L.; Johnson, D.D. Configurational Thermodynamics of Alloyed Nanoparticles with Adsorbates. *Nano Lett.* **2014**, *14*, 7077-7084.
(145) Bronsted, J.N. Acid and Base Catalysis. *Chem. Rev.* **1928**, *5*, 231-338.
(146) Evans, M.G.; Polyani, M. Inertia and Driving Force of Chemical Reactions. *Trans. Faraday Soc.* **1938**, *34*, 11-24.
(147) Brown, G.; Rikvold, P. A.; Mitchell, S. J.; Novotny, M. A. *Interfacial Electrochemistry: Theory, Experiment, and Application*; Wieckowski, A., Eds.; Marcel Dekker: New York, 1999; pp. 47−61.
(148) Fichthorn, K. A.; Scheffler, M. Island Nucleation in Thin-Film Epitaxy: A First-Principles Investigation. *Phys. Rev. Lett.* **2000**, *84*, 5371− 5374.
(149) Yildirim, H.; Rahman, T. S. Diffusion Barriers for Ag and Cu Adatoms on the Terraces and Step Edges on Cu(100) and Ag(100): An Ab initio Study. *Phys. Rev. B* **2009**, *80*, 235413.

(150) Antczak, G.; Ehrlich, G. *Surface Diffusion: Metals, Metal Atoms, and Clusters.* Cambridge University Press: Cambridge, 2010.
(151) Heinonen, J.; Koponen, I.; Merikoski, J.; Ala-Nissila, T. Island Diffusion on Metal fcc (100) Surfaces. *Phys. Rev. Lett.* **1999**, *82*, 2733-2736.
(152) Liu, D.-J. Density Functional Analysis of Key Energetics in Metal Homoepitaxy: Quantum Size Effects in Periodic Slab Calculations. *Phys. Rev. B* **2010**, *81*, 035415.
(153) Liu, D.-J.; Evans, J.W. Sintering of 2D Nanoclusters in Metal(100) Homoepitaxial Systems: Deviations from Predictions of Mullins Continuum Theory. *Phys. Rev. B*. **2002**, *66*, 165407.
(154) Lai, K. C.; Evans, J. W.; Liu, D. -J. Communication: Diverse Nanoscale Cluster Dynamics: Diffusion of 2D Epitaxial Clusters. *J. Chem. Phys.* **2017**, *147*, 201101.
(155) Lai, K. C.; Liu, D. -J.; Evans, J. W. Diffusion of 2D Epitaxial Clusters on Metal(100) Surfaces: Facile versus Nucleation-mediated Behavior and Their Merging for Larger Sizes. *Phys. Rev. B* **2017**, *96*, 235406.
(156) Lai, K. C.; Liu, D. –J.; Thiel, P. A.; Evans, J. W. Modeling of Diffusivity for 2D Vacancy Pits and Comparison with 2D Adatom Islands on Metal(100) Surfaces Including Analysis for Ag(100). *J. Phys. Chem. C* **2018**, *122(21)*, 11334-11344.
(157) Li, L.; Plessow, P.N.; Rieger, M.; Sauer, S.; Sánchez-Carrera, R.S.; Schaefer, A.; Abild-Pedersen, F. Modeling the Migration of Platinum Nanoparticles on Surfaces Using a Kinetic Monte Carlo Approach. *J. Phys. Chem. C* **2017**, *121*, 4261-4269.
(158) Luke T. Roling, Lin Li, and Frank Abild-Pedersen, Configurational Energies of Nanoparticles Based on Metal−Metal Coordination. *J. Phys. Chem. C* **2017**, *121*, 23002-23010.
(159) Martin, T. P. Shell of Atoms. *Phys. Rep.* **1996**, *273*, 199-241.
(160) Lai, K.C.; Evans, J.W. Reshaping, Pinch-off and Sintering of 3D fcc metal Nanoclusters: Stochastic Atomistic Modeling with a Realistic Surface Diffusion Kinetics. *Phys. Rev. Letters* **2018**, submitted.
(161) Caspersen, K. J.; Stoldt, C. R.; Layson, A. R.; Bartelt, M. C.; Thiel, P. A.; Evans, J. W. Morphology of Multilayer Ag/Ag(100) Films versus Deposition Temperature: STM Analysis and Atomistic Lattice-Gas Modeling. *Phys. Rev. B* **2001**, *63*, 085401.
(162) Frank, S.; Wedler, H.; Behm, R. J.; Rottler, J.; Maass, P.; Caspersen, K. J.; Stoldt, C. R.; Thiel, P. A.; Evans, J. W. Approaching the Low Temperature Limit in Nucleation and Growth of fcc(100) Metal Films - Ag/Ag(100). *Phys. Rev. B* **2002**, *66*, 155435.
(163) Caspersen, K.J.; Layson, A.R.; Stoldt, C.R.; Fournee, V.; Thiel, P.A.; Evans, J.W. Development and Ordering of Mounds during Metal(100) Homoepitaxy. Phys. Rev. B **2002**, *65*, 193407.
(164) Li, M.; Chung, P.-W.; E. Cox, E.; Jenks, C.J.; Thiel, P.A.; Evans, J.W. Exploration of Complex Multilayer Film Growth Morphologies: STM Analysis and Predictive Atomistic Modeling for Ag on Ag(111). *Phys. Rev. B* **2008**, *77*, 033402.
(165) Yu, B. D.; Scheffler, M. Anisotropy of Growth of the Close-Packed Surfaces of Silver. *Phys. Rev. Lett.* **1996**, *77*, 1095-1098.
(166) Herder, L. M.; Bray, J. M.; Schneider. W. F. Comparison of Cluster Expansion Fitting Algorithms for Interactions at Surfaces. *Surf. Sci.* **2015**, *640*, 104-111.
(167) Busse, C.; Polop, C.; Müller, M.; Albe, K.; Linke, U.; Michely, T. Stacking-Fault Nucleation on Ir(111). *Phys. Rev. Lett.* **2003,** *91*, 056103.
(168) Li, M.; Han, Y.; Thiel, P. A.; Evans, J. W. Formation of Complex Wedding-cake-like Morphologies during Homoepitaxial Growth of Ag on Ag(111): Atomistic, Step-dynamics, and Continuum Modeling. *J. Phys. Cond. Matt.* **2009**, *21*, 084216.
(169) Kellogg, L.; Feibelman, P. J.; Surface Self-diffusion on Pt(001) by an Atomic Exchange Mechanism. *Phys. Rev. Lett.* **1990**, *64*, 3143-3147.
(170) Kellogg, G. L. Temperature Dependence of Surface Self-diffusion on Pt(001). *Surf Sci.* **1991**, *246*, 31-36.

(171) Henkelman, G.; Jonsson, H. Long Time Scale Kinetic Monte Carlo Simulations without Lattice Approximation and Predefined Event Table. *J. Chem. Phys.* **2001**, *115*, 9657-9666.
(172) Barkema, G. T.; Mousseau, N. Event-Based Relaxation of Continuous Disordered Systems. *Phys. Rev. Lett.* **1996**, *77*, 4358-4361.
(173) Trochet, M.; Sauvé-Lacoursière, A.; Mousseau, N. Algorithmic Developments of the Kinetic Activation-relaxation Technique: Accessing Long-time Kinetics of Larger and More Complex Systems. *J. Chem. Phys.* **2017**, *147*, 152712.
(174) Khare, S. V.; Einstein, T. L. Brownian Motion and Shape Fluctuations of Single-layer Adatom and Vacancy Clusters on Surfaces: Theory and Simulations. *Phys. Rev. B* **1996**, *54*, 11752.
(175) Krug, J.; Dobbs, H. T.; Majaniemi, S. Adatom Mobility for the Solid-on-solid Model. *Zeitschrift für Physik B Condensed Matter* **1995**, *97*, 281–291.
(176) Jensen, P.; Combe, N.; Larralde, H.; Barrat, J.L.; Misbah C.; Pimpinelli, A. Kinetics of Shape Equilibration for Two Dimensional Islands. *Eur. Phys. J. B* **1999**, *11*, 497-504.
(177) Pai, W. W.; Wendelken, J. F.; Stoldt, C. R.; Thiel, P. A.; Evans, J. W.; Liu, D.-J. Evolution of Two-Dimensional Worm-Like Nanoclusters on Metal Surfaces. *Phys. Rev. Lett* **2001**, *86*, 3088-3091.
(178) Liu, D. -J.; Stoldt, C. R.; Thiel, P. A.; Evans, J. W. *Sintering of Metal(100) Homoepitaxial Islands: Kink Rounding Barriers, Modified Size Scaling, and Experimental Behavior.* In *MRS Proceedings 749 on "Morphological and Compositional Evolution of Thin Films"*. Aziz, M. J.; Bartelt, N.C.; Berbezier, I.; Hannon, J. B.; Hearne S.J. Eds.; MRS: Pittsburgh, 2003; W.2.8.1-6.
(179) Dziuk, G.; Elliot, C. M. A Fully Discrete Evolving Surface Finite Element Method. *SIAM J. Numer. Anal.* **2012**, *50*, 2677-2694.
(180) Dziuk. G.; Elliot, C. M. Finite Element Methods for Surface PDEs. *Acta Numerica* **2013**, *22*, 289-396.
(181) Pierre-Louis, O.; Einstein, T.L. Electomigration of Single-layer Clusters. *Phys. Rev. B* **2000**, *62*, 13697.
(182) Grayson, M. A. The Heat Equation Shrinks Embedded Plane Curves to Round Points. *J. Diff. Geom.* **1987**, *26*, 285-314.
(183) Thouy, R.; Olivi-Tran, N.; Jullien, R. Fragmentation of Two-dimensional Mass Fractals by Surface-diffusion Sintering. *Phys Rev. B* **1997**, *56*, 5321-5327.
(184) Kuczynski, G.C. Study of the Sintering of Glass. *J. Appl. Phys.* **1949**, *20*, 1160-1163.
(185) Brailsford, A. D.; Gjostein, N. A. Influence of Surface Energy Anisotropy on Morphological Changes Occurring by Surface Diffusion. *J. Appl. Phys.* **1975**, *46*, 2390-2397.
(186) Strutt, J. W.; Lord Rayleigh. On the Instability of Jets. *Proc. London Math. Soc.* **1878**, *10*, 4–13.
(187) Plateau, J. *Experimental and Theoretical Statics of Liquids Subject to Molecular Forces Only;* Gauthier-Villars: Paris, 1973*;* Vol. 1.
(188) Nichols, F. A.; Mullins, W. W. Surface-(Interface-) and Volume Diffusion Contributions to Morphological Changes Driven by Capillarity. *Trans. Metall. Soc. AIME* **1965**, *233*, 1840–1947.
(189) Bréchignac, C.; Cahuzac, Ph.; Carlier, F.; Colliex, C.; Leroux, J.; Masson, A.; Yoon, B.; Landman, U. Instability Driven Fragmentation of Nanoscale Fractal Islands. *Phys. Rev. Lett.* **2002**, *88*, 196103.
(190) Mullins, W.W.; Rohrer, G.S. Nucleation Barrier for Volume-conserving Shape Changes of Faceted Crystals. *J. Am. Ceram. Soc.* **2000**, *83*, 214-216.
(191) T.D. Blake, The Physics of Moving Wetting Lines. *J. Colloid Interface Sci.* 2006, *299*, 1-13.
(192) Bonn, D.; Eggers, J.; Indekeu, J.; Meunier, J.; Rolley, E. Wetting and Spreading. *Rev. Mov. Phys.* **2009**, *81*, 739-805.

(193) Khare, S. V.; Bartelt, N. C.; Einstein, T. L. Diffusion of Monolayer Adatom and Vacancy Clusters: Langevin Analysis and Monte Carlo Simulations of their Brownian Motion. *Phys. Rev. Lett.* **1995**, *75*, 2148-2151.
(194) Pierre-Louis, O. Continuum Model for Low Temperature Relaxation of Crystal Steps. *Phys. Rev. Lett.* **2001**, *87*, 106104.
(195) Dufay, M.; Pierre-Louis, O. Model for Transient Elongation and Drift of Islands on Vicinal Substrates. *Phys. Rev. B* **2010**, *81*, 041407.
(196) Carter, W. C.; Roosen, A. R.; Cahn, J. W.; Taylor, J. E. Shape Evolution by Surface Diffusion and Surface Attachment Limited Kinetics on Completely Faceted Surfaces. *Acta Metallurgica et Materialia* **1995**, *43 (12)*, 4309-4323.
(197) Israeli, N.; Kandel, D. Novel Continuum Modeling of Crystal Surface Evolution. *Phys. Rev. Lett.* **2002**, *88*, 116103.
(198) Margetis,D.; Fok, P. -W.; Aziz, M. J.; Stone, H. A.; Continuum Theory of Nanostructure Decay Via a Microscale Condition. *Phys. Reb. Lett.* **2006**, *97*, 096102. (199) Politi, P. Villain, J. Ehrlich-Schwoebel Instability in Molecular-beam Epitaxy: A Minimal Model. *Phys. Rev. B* **1996**, *54*, 5114-5129.
(200) Li, M.; Evans, J. W. Theoretical Analysis of Mound Slope Selection during Unstable Multilayer Growth. *Phys. Rev. Lett.* **2005**, *95*, 256101.
(201) Provatas, N.; Elder, K. *Phase-Field Methods in Materials Science and Engineering*; Wiley-VCH: Weinheim, 2010.
(202) Wang, Y. U. Computer Modeling and Simulation of Solid-state Sintering:
A Phase Field Approach. *Acta Materialia* **2006**, *54*, 953–961.
(203) Chockalingam, K.; Kouznetsova, V.G.; van der Sluis, O.; Geersa, M. G. D. 2D Phase Field Modeling of Sintering of Silver Nanoparticles. *Comput. Methods in Appl. Mech. and Eng*. **2016**, *312*, 492-508.
(204) Biswas, S.; Schwen, D.; Wang, H.; Okuniewski, M.; Tomar, V. Phase Field Modeling of Sintering: Role of Grain Orientation and Anisotropic Properties. *Comput. Mater. Sci.* **2018**, *148*, 307-319
(205) Elder, K. R.; Grant, M. Modeling Elastic and Plastic Deformations in Nonequilibrium Processing using Phase Field Crystals. *Phys. Rev. E* **2004**, *70*, 051605.
(206) Margetis, D.; Caflisch, R. E. Anisotropic Step Stiffness from a Kinetic Model of Epitaxial Growth. *Multiscale Model. Simul.* **2008**, *7(1)*, 242–273.
(207) Ackerman, D.; Evans, J. W. Boundary Conditions for Burton-Cabrera-Frank Type Step Flow Models from Coarse-graining of Discrete 2D Deposition-diffusion Equations. *SIAM Multiscale Modeling & Simulation* **2011**, *9*, 59-88.
(208) Zhao, R.; Ackerman, D. M.; Evans, J. W.; Refined BCF-type Boundary Conditions for Mesoscale Surface Step Dynamics. *Phys. Rev. B* **2015**, *91*, 235441.
(209) Zhao, R.; Evans, J. W.; Oliveira, T. J. Permeability and Kinetic Coefficients for Mesoscale BCF Surface Step Dynamics: Discrete 2D Deposition-diffusion Equation Analysis. *Phys. Rev. B* **2016**, *93*, 165411.
(210) Hausser, F.; Voigt, A. Ostwald Ripening of Two-dimensional Homoepitaxial Islands. *Phys. Rev. B* **2005**, *72*, 035437.
(211) Wen, J.-M.; Chang, S.-L.; Burnett, J. W.; Evans, J. W.; Thiel, P. A. Diffusion of Large Two-Dimensional Ag Clusters on Ag(100). *Phys. Rev. Lett. **1994**, 73*, 2591-2594.
(212) Pai, W. W.; Swan, A. K.; Zhang, Z.; Wendelken, J. F. Island Diffusion and Coarsening on Metal (100) Surfaces. *Phys. Rev. Lett.* **1997**, 79, 3210-3213.
(213) Ruckenstein, E.; Pulvermacher, B. Kinetics of Crystallite Sintering during Heat Treatment of Supported Metal Catalysts. *AiChE Journal* **1973**, *19*, 356-364.
(214) Ruckenstein, E.; Pulvermacher, B. Growth Kinetics and Size Distributions of Supported Metal Crystallites. *J. Catal.* **1973**, *29*, 224-245.

(215) Kandel, D. Selection of the Scaling Solution in a Cluster Coalescence Model. *Phys. Rev. Lett.* **1997**, *79*, 4238-4241.
(216) Niethammer, B.; Pego, R. L. Non-self-similar Behavior in the LSW Theory of Ostwald Ripening. *J. Statist. Phys.* **1999**, *95(5-6)*, 867–902.
(217) Pego, R. L. *Lectures on Dynamics in Models of Coarsening and Coagulation. Dynamics in Models of Coarsening, Coagulation, Condensation and Quantization*; Boo, W.; Liu, J. -G., Eds.; Lect. Notes Ser. Inst. Math. Sci. Natl. Univ. Singap., 9; World Sci. Publ.: Hackensack, NJ, 2007; pp. 1-61.
(218) Menon, G.; Pego, R. L. Dynamical Scaling in Smoluchowski's Coagulation Equations: Uniform Convergence. *SIAM Review* **2006**, *48*, 745-768.
(219) Stoldt, C. R.; Jenks, C. J.; Thiel, P. A.; Cadilhe, A. M.; Evans, J. W. Smoluchowski Ripening of Ag Islands on Ag(100). *J. Chem. Phys.* **1999**, *111*, 5157-5166.
(220) Shneidman, V.A. Early Stages of Ostwald Ripening. *Phys. Rev. E* **2013**, *88*, 010401.
(221) Mattsson, T. R.; Mills, G.; Metiu, H. A New Method for Simulating the Late Stages of Island Coarsening in Thin Film Growth: The Role of Island Diffusion and Evaporation. *J. Chem. Phys.* **1999**, *110*, 12151-12160.
(222) Sugimoto, T.; Preparation of Monodispersed Colloidal Particles. *Adv. Colloid Interface Sci.* **1987**, *28*, 65-108.
(223) Shneidman, V.A. Transformations of the Distribution of Nuclei Formed in a Nucleation Pulse: Interface-limited Growth. *J. Chem. Phys.* **2009**, *131*, 164115.
(224) Dubrovskii, V. G.; Nazarenko, M. V. Nucleation Theory Beyond the Deterministic Limit. I. The Nucleation Stage. *J. Chem. Phys.* **2010**, *132*, 114507.
(225) Dubrovskii, V. G.; Nazarenko, M. V. Nucleation Theory Beyond the Deterministic Limit. II. The Growth Stage. *J. Chem. Phys.* **2010**, *132*, 114508.
(226) Gunton, J.D.; Droz, M. *Introduction to the Theory of Metastable and Unstable States*; Lecture Notes in Physics Vol. 183; Springer: Berlin, 1983.
(227) Weitz, D. A.; Huang, J. S.; Lin, M. Y.; Sung, J. Limits of the Fractal Dimension for Irreversible Kinetic Aggregation of Gold Colloids. *Phys. Rev. Lett.* **1985**, *54*, 1416-1419.
(228) Meakin, P. Formation of Fractal Clusters and Networks by Irreversible Diffusion-Limited Aggregation. *Phys. Rev. Lett.* **1983**, *51*, 1119−1122.
(229) Kolb, M.; Botet, R.; Jullien, R. Scaling of Kinetically Growing Clusters. *Phys. Rev. Lett.* **1983**, *51*, 1123−1126.
(230) Meakin, P. The Effects of Random Bond Breaking on Diffusion Limited Cluster-cluster Aggregation. *J. Chem. Phys.* **1985**, *83*, 3645-3649.
(231) Kolb, M.; Jullien. R. Chemically Limited versus Diffusion Limited Aggregation. *Journal de Physique Lettres* **1984**, *45 (20)*, 977-981.
(232) Weitz, D. A.; Lin, M. Y. Dynamic Scaling of Cluster-Mass Distributions in Kinetic Colloid Aggregation. *Phys. Rev. Lett.* **1986**, *57*, 2037-2040.
(233) van Dongen, P. G. J.; Ernst, M. H. Dynamic Scaling in the Kinetics of Clustering. *Phys. Rev. Lett.* **1985**, *54*, 1396-1399.
(234) Ball, R. C.; Weitz, D. A.; Witten, T. A.; Leyvraz, F. Universal Kinetics in Reaction-limited Aggregation. *Phys. Rev. Lett.* **1987**, *58*, 274-277.
(235) Combe, N.; Larralde, H. Low-temperature Shape Relaxation of Two-dimensional Islands by Edge Diffusion. *Phys. Rev. B* **2000**, *62*, 16074-16084.
(236) Ulman, A. Formation and Structure of Self-Assembled Monolayers. *Chem. Rev.* **1996**, *96*, 1533−1554.
(237) Min, B. K.; Alemozafar, A. R.; Biener, M. M.; Biener, J.; Friend, C.M. Reaction of Au(111) with Sulfur and Oxygen: Scanning Tunneling Microscopic Study. *Top. in Catalysis* **2005**, 36, 77-90.
(238) Friend, C. M. Dynamic Restructuring of Gold Surfaces during Chemical Reactions. *Actualite Chimique* **2008**, *320-21*, 75-80.

(239) Chauraud, D.; Durinck, J.; Drouet, M.; Vernisse, L.; Bonneville, J.; Coupea C. Influence of Terrace Widths on Au(111) Reconstruction. *Phys. Rev. B* **2017**, *96*, 045410.
(240) Brune, H.; Röder, H.; Bromann, K.; Kern, K.; Jacobsen, J.; Stoltze, P.; Jacobsen, K.; Norskov, J. Anisotropic Corner Diffusion as Origin for Dendritic Growth on Hexagonal Substrates. *Surf. Sci.* **1996**, *349*, 115-122.
(241) Eßer, M.; Morgenstern, K.; Rosenfeld, G.; Comsa, G. Dynamics of Vacancy Island Coalescence on Ag(111). *Surf. Sci.* **1998**, *402–404*, 341–345.
(242) Rosenfeld, G.; Eßer, M.; Morgenstern, K.; Comsa, G. Ripening Mechanisms in Ultrathin Metal Films. *Mat. Res. Soc. Symp. Proc.* **1998**, *528*, 111-124.
(243) Schloesser, D. C.; Morgenstern, K.; Verheij, L. K.; Rosenfeld, G.; Besenbacher, F.; Comsa, G. Kinetics of Island Diffusion on Cu(111) and Ag(111) Studied with Variable-temperature STM. *Surf. Sci.* **2000**, *465*, 19–39.
(244) Wendelken, J.F.; Swan, A.K.; Pai, W.-W., Zuo, J.-K. Morphology and Energy Barriers in Homoepitaxial Growth and Coarsening: A Case Study for Cu(100). In *Morphological organization in Epitaxial Growth and Removal*; Zhang, Z.; Lagally, M.G. Eds.; World Scientific: Singapore, 1998; pp.320-348.
(245) La Magna, A. Nanoisland Shape Relaxation Mechanism, *Surf. Sci.* **2007**, *601*, 308-314.
(246] Lü, B.; Almyras, G. A.; Gervilla, V.; Greene, J. E.; Sarakinos, K. Formation and Morphological Evolution of Self-similar 3D Nanostructures on Weakly Interacting Substrates. *Phys. Rev. Mater.* **2018**, *2*, 063401.
(247) Li, M.; Wendelken, J. F.; Liu, B.-G.; Wang, E. G.; Zhang, Z. Decay Characteristics of Surface Mounds with Contrasting Interlayer Mass Transport Channels. *Phys. Rev. Lett.* 2001, *86*, 2345-2348.
(248) Yeadon, M.; Yang, J. C.; Averback, R. S.; Bullard, J. W.; Olynick, D. L.; Gibson, J. M.; In-situ Observations of Classical Grain Growth Mechanisms during Sintering of Copper Nanoparticles on (001) Copper. *Appl. Phys. Lett.* **1997**, *71*, 1631-1633.
(249) Jensen, P. Growth of Nanostructures by Cluster Deposition: Experiments and Simple Models. *Rev. Mod. Phys.* **1999**, *71*, 1695-1735.
(250) Iijima, S.; Ajayan, P. M. Substrate and Size Effects on the Coalescence of Small Particles. *J. of Appl. Phys.* **1991**, *70*, 5138.
(251) Asoro, M. A.; Ferreira, P.J.; Kovar, D. In situ Transmission Electron Microscopy and Scanning Transmission Electron Microscopy Studies of Sintering of Ag and Pt Nanoparticles. *Acta Mat.* **2014**, *81*, 173-183.
(252) Yuk J.M.; Jeong, M.; Kim, S.Y.; Seo, H.K.; Kim, J.; Lee, J.Y. In situ atomic imaging of coalescence of Au nanoparticles on graphene: rotation and grain boundary migration. ChemComm 2013, 49, 11479-11481
(253) Lacroix, L. -M.; Arenal, R.; Viau, G.; Dynamic HAADF-STEM Observation of a Single-Atom Chain as the Transient State of Gold Ultrathin Nanowire Breakdown. *J. Am. Chem. Soc*. **2014**, *136(38)*, 13075–13077.
(254) Zhang, C.-H.; Kassubek, F.; Stafford, C. A. Surface Fluctuations and the Stability of Metal Nanowires. *Phys. Rev. B* **2003**, 68, 165414.
(255) Han, Y.; Liu, D. -J. Shell Structure and Phase Relations in Electronic Properties of Metal Nanowires from an Electron-gas Model. *Phys. Rev. B* **2010**, *82*, 125420.
(256) Takahata, R.; Yamazoe, S.; Warakulwit, C.; Limtrakul, J.; Tsukuda, T. Rayleigh Instability and Surfactant-Mediated Stabilization of Ultrathin Gold Nanorods. *J. Phys. Chem. C* **2016**, *120 (30)*, 17006–17010.
(257) Volk, A.; Knez, D.; Thaler, P.; Hauser, A. W.; Grogger, W.; Hofer, F.; Ernst, W. E. Thermal Instabilities and Rayleigh Breakup of Ultrathin Silver Nanowires Grown in Helium Nanodroplets. *Phys. Chem. Chem. Phys.* **2015**, *17*, 24570-24575.

(258) Xu, J.; Zhu, Y.; Zhu, J.; Jiang, W. Ultralong Gold Nanoparticle/Block Copolymer Hybrid Cylindrical Micelles: a Strategy Combining Surface Templated Self-assembly and Rayleigh Instability. *Nanoscale* **2013**, *5*, 6344-6349.
(259) Nakajima, H. The Discovery and Acceptance of the Kirkendall Effect: The Result of a Short Research Career. *JOM - TMS* **1997**, *46*, 15-19.
(260) Yin, Y.; Rioux, R. M.; Erdonmez, C. K.; Hughes, S.; Somorjai, G. A.; Alivisatos, A. P. Formation of Hollow Nanocrystals Through the Nanoscale Kirkendall Effect. *Science* **2004**, *304*, 711-714.
(261) Ha, D. -H.; Moreau, L. M.; Honrao, S.; Hennig, R. G.; Robinson, R. D. The Oxidation of Cobalt Nanoparticles into Kirkendall-Hollowed CoO and Co3O4: The Diffusion Mechanisms and Atomic Structural Transformations. *J. Phys. Chem. C*, **2013**, *117 (27)*, 14303–14312.
(262) Yang, Z.; Yang, N.; Pileni, M. -P. Nano Kirkendall Effect Related to Nanocrystallinity of Metal Nanocrystals: Influence of the Outward and Inward Atomic Diffusion on the Final Nanoparticle Structure. *J. Phys. Chem. C* **2015**, *119 (39)*, 22249–22260.
(263) Dai, S.; You, Y.; Zhang, S.; Cai, W.; Xu, M.; Xie, L.; Wu, R.; Graham G. W.; Pan, X. In situ Atomic-scale Observation of Oxygen-driven Core-shell Formation in Pt3Co Nanoparticles. *Nature Comm.* **2017**, *8*, 1-7.
(264) González, E.; Arbiol, J.; Puntes, V. F. Carving at the Nanoscale: Sequential Galvanic Exchange and Kirkendall Growth at Room Temperature. *Science*, **2011**, *334*, 1377-1380.
(265) Wang, J. X.; Ma, C.; Choi, Y. M.; Su, D.; Zhu, Y.; Liu, P.; Si, R.; Vukmirovic, M. B.; Zhang, Y.; Adzic, R. R. Kirkendall Effect and Lattice Contraction in Nanocatalysts: A New Strategy to Enhance Sustainable Activity. *J. Am. Chem. Soc.* **2011**, *133 (34)*, 13551–13557.
(266) Han, L.; Liu, H.; Cui, P.; Peng, Z.; Zhang, S.; Yang, J. Alloy Cu3Pt Nanoframes through the Structure Evolution in Cu-Pt Nanoparticles with a Core-shell Construction. *Scientific Reports* **2014**, *4*, 6414.
(267) Chen, C.; Kang, Y.; Huo, Z.; Zhu, Z.; Huang, W.; Xin, H. L.; Snyder, J. D.; Li, D.; Herron, J. A.; Mavrikakis, M.; Chi, M.; More, K. L.; Li, Y.; Markovic, N. M.; Somorjai, G. A.; Yang, P.; Stamenkovic V. R. Highly Crystalline Multimetallic Nanoframes with Three-Dimensional Electrocatalytic Surfaces. *Science* **2014**, *343*, 1339-1343.
(268) Erlebacher, J.; Margetis, D. Mechanism of Hollow Nanoparticle Formation Due to Shape Fluctuations. *Phys. Rev. Lett.* **2014**, *112*, 155505.
(269) Mattsson, T. R.; Mattsson, A. E. Calculating the Vacancy Formation Energy in Metals: Pt, Pd, and Mo. *Phys. Rev. B* **2002**, *66*, 214110.
(270) Angsten, T.; Mayeshiba, T.; Wu, H.; Morgan, D. Elemental Vacancy Diffusion Database from High-throughput First-principles Calculations for fcc and hcp Structures. *New J. Phys,* **2014**, *16*, 015018.
(271) Chen, M.; Han, Y.; Goh, T. W.; Sun, R.; Maligal-Ganesh, R. V.; Pei, Y.; Tsung, C. -K.; Evans, J. W.; Huang, W. Kinetics, Energetics, and Size dependence of the Transformation from Pt to Ordered PtSn Intermetallic Nanoparticles. *ACS Nano* **2018**, submitted.
(272) Zhang, L.; Roling, L. T.; Wang, X.; Vara, M.; Chi, M.; Liu, J.; Choi, S.-I.; Park, J.; Herron, J. A.; Xie, Z.; Mavrikakis, M.; Xia, Y., Platinum-based Nanocages with Subnanometer-thick Walls and Well-defined, Controllable Facets. *Science* **2015**, *349*, 412-416.
(273) Vara, M.; Roling, L. T.; Wang, X.; Elnabawy, A. O.; Hood, Z. D.; Chi, M.; Mavrikakis, M.; Xia, Y. Understanding the Thermal Stability of Palladium−Platinum Core−Shell Nanocrystals by In Situ Transmission Electron Microscopy and Density Functional Theory. *ACS Nano* **2017**, *11*, 4571−4581.
(274) Li, W.; Huang, L.; Pala, R. G. S.; Lu, G. -H.; Liu, F.; Evans, J. W.; Han, Y. Thickness-dependent Energetics for Pb Adatoms on Low-index Pb Nanofilm Surfaces: First-principles Calculations. *Phys. Rev. B* **2017**, *96*, 205409.
(275) Roling, L. T.; Mavrikakis, M., Toward Rational Nanoparticle Synthesis: Predicting Surface Intermixing in Bimetallic Alloy Nanocatalysts. *Nanoscale* **2017**, *9*, 15005-15017.

(276) Yan, Y.; Du, J.S.; Gilroy, K. D.; Yang, D.; Xia, Y.; Zhang, H. Intermetallic Nanocrystals: Syntheses and Catalytic Applications. *Adv. Mater.* **2017**, *29 (14)*, 1605997.
(277) Wu, L.; Fournier, A. P.; Willis, J. J.; Cargnello, M.; Tassone, C. J., In Situ X-ray Scattering Guides the Synthesis of Uniform PtSn Nanocrystals. *Nano Lett.* **2018**, *18*, 4053-4057.
(278) Ginstling, A. M.; Brounshtein, B. I., O Diffuzionnoi Kinetike Reaktsiiv Sfericheskikh Chastitsakh. *Zhurnal Prikladnoi Khimii* **1950**, *23*, 1249-1259.
(279) Khawam, A.; Flanagan, D. R., Solid-state Kinetic Models: Basics and Mathematical Fundamentals. *J. Phys. Chem. B* **2006**, *110*, 17315-17328.
(280) Binder, K.; Kalos, M. H. "Critical Clusters" in a Supersaturated Vapor: Theory and Monte Carlo simulation. *J. Stat. Phys.* **1980**, *22*, 363-396.
(281) Mills, G.; Mattsson, T. R.; Møllnitz, L.; Metiu, H. Simulations of Mobility and Evaporation Rate of Adsorbate Islands on Solid Surfaces. *J. Chem. Phys.* **1999**, *111*, 8639-8650.
(282) Ge, X.; Morgenstern, K. Ehrlich-Schwoebel Barrier and Interface-limited Decay in Island Kinetics on Ag(100). *Phys. Rev. B* **2012**, *85*, 045417.
(283) Morgenstern, K.; Rosenfeld, G.; Poelsema, B.; Comsa, G. Brownian Motion of Vacancy Islands on Ag(111). *Phys. Rev. Lett.* **1995**, *74*, 2058-2061.
(284) Morgenstern, K.; Rosenfeld, G.; Comsa, G. Local Correlation during Ostwald Ripening of Two-dimensional Islands on Ag(111). *Surf. Sci.* **1999**, *441*, 289–300.
(285) Zheng, X.; Bigot, B. Ostwald Ripening on a Substrate: Modeling Local Interparticle Diffusion. *Journal de Physique II* **1994**, *4 (5)*, 743-750.
(286) Morgenstern, K.; Rosenfeld, G.; Comsa, G. Decay of Two-Dimensional Ag Islands on Ag(111). *Phys. Rev. Lett.* **1996**, *76*, 2113-2116.
(287) McLean, J. G.; Krishnamachari, B.; Peale, D. R.; Chason, E.; Sethna, J. P.; Cooper, B. H. Decay of Isolated Surface Features Driven by the Gibbs-Thomson Effect in an Analytic Model and a Simulation. *Phys. Rev. B* **1997**, *55*, 1811-1823.
(288) Morgenstern, K.; Rosenfeld, G.; Lægsgaard, E.; Besenbacher, F.; Comsa, G. Measurement of Energies Controlling Ripening and Annealing on Metal Surfaces. *Phys. Rev. Lett.* **1998**, *80*, 556-559.
(289) Hannon, J. B.; Klünker, C.; Giesen, M.; Ibach, H.; Bartelt, N. C.; Hamilton, J. C. Surface Self-Diffusion by Vacancy Motion: Island Ripening on Cu(001). *Phys. Rev. Lett.* **1997**, *79*, 2506-2509.
(290) Sushumna, I.; Ruckenstein, E. Events Observed and Evidence for Crystallite Migration in Catalysts. *J. Catalysis* **1988**, *109*(2), 433-462.
(291) Wynblatt, P.; Gjostein, N. A.; Supported Metal Crystallites. *Progress in Solid State Chem.* **1975**, *9*, 21-58.
(292) Reiss, H., Rotation and Translation of Islands in the Growth of Heteroepitaxial Films. *J. Appl. Phys.* **1968**, *39*, 5045-5061.
(293) Zhang, S.; Cargnello, M.; Cai, W.; Murray, C. B.; Graham, G. W.; Pan, X. Revealing Particle Growth Mechanisms by Combining High-surface-area Catalysts Made with Monodisperse Particles and Electron Microscopy Conducted at Atmospheric Pressure. *J. Catalysis* **2016**, *337*, 240–247.
(294) Simonsen, S. B.; Chorkendorff, I.; Dahl, S.; Skoglundh, M.; Sehested, J.; Helveg, S. Direct Observations of Oxygen-induced Platinum Nanoparticle Ripening Studied by In Situ TEM. *J. Am. Chem. Soc.* **2010**, *132 (23)*, 7968–7975.
(295) Simonsen, S. B.; Chorkendorff, I.; Dahl, S.; Skoglundh, M.; Sehested, J.; Helveg, S. Ostwald Ripening in a Pt/SiO2 Model Catalyst Studied by In situ TEM. *J. Catalysis* **2011**, *281*, 147–155.
(296) Theis, W.; Bartelt, N. C.; Tromp, R. M.; Chemical Potential Maps and Spatial Correlations in 2D-Island Ripening on Si(001). *Phys. Rev. Lett.* **1995**, *75*, 3328-3331.
(297) Behafarid, F.; Cuenya, B. R.; Towards the Understanding of Sintering Phenomena at the Nanoscale: Geometric and Environmental Effects. *Top Catal* **2013**, *56*, 1542-1559.

(298) Shields, S. P.; Richards, V. N.; Buhro, W. E. Nucleation Control of Size and Dispersity in Aggregative Nanoparticle Growth. A Study of the Coarsening Kinetics of Thiolate-Capped Gold Nanocrystals. *Chem. Mater.* **2010**, *22 (10)*, 3212–3225.
(299) Richards, V. N.; Rath, N. P.; Buhro, W. E. Pathway from a Molecular Precursor to Silver Nanoparticles: The Prominent Role of Aggregative Growth. *Chem. Mater.* **2010**, *22 (11)*, 3556-3567.
(300) Porsgaard, S.; Merte, L. R.; Ono, L. K.; Behafarid, F.; Matos, J.; Helveg, S.; Salmeron, M.; Cuenya, B. R.; Besenbacher, F. Stability of Platinum Nanoparticles Supported on SiO2/Si(111): A High-Pressure X-ray Photoelectron Spectroscopy Study. *ACS Nano*, **2012**, *6 (12)*, 10743-10749.
(301) Plessow, P. N.; Abild-Pedersen, F. Sintering of Pt Nanoparticles via Volatile PtO2: Simulation and Comparison with Experiments. *ACS Catal.* **2016**, *6 (10)*, 7098–7108.
(302) Layson, A. R.; Evans, J. W.; Thiel, P. A. Use of Adsorbates to Manipulate Nanostructure Formation: O+Ag/Ag(100). *J. Chem. Phys.* **2003**, *118*, 6467-6472.
(303) Shen, M.; Russell, S. M.; Liu, D.-J.; Thiel, P. A. Destabilization of Ag Nanoislands on Ag(100) by Adsorbed Sulfur. *J. Chem. Phys.* **2011**, *135(15)*, 154701.
(304) Ling, W. L.; Bartelt, N. C.; Pohl, K.; de la Figuera, J.; Hwang, R. Q.; McCarty, K. F. Enhanced Self-Diffusion on Cu(111) by Trace Amounts of S: Chemical-Reaction-Limited Kinetics. *Phys. Rev. Lett*. **2004**, *93*, 166101.
(305) Feibelman, P. J. Formation and Diffusion of S-Decorated Cu Clusters on Cu(111). *Phys. Rev. Lett.* **2000**, *85*, 606-609.
(306] Russell, S.; Kim, Y.; Liu, D. -J.; Evans, J. W.; Thiel, P. A. Structure, Formation, and Equilibration of Ensembles of Ag-S Complexes on an Ag Surface. *J. Chem. Phys.* **2013**, *138*, 071101.
(307) Walen, H.; Liu, D. -J.; Oh, J.; Lim, H.; Evans, J. W.; Aikens, C.; Kim, Y.; Thiel, P. A. Cu2S3 Complex on Cu(111) as a Candidate for Mass Transport Enhancement. *Phys. Rev. B* **2015**, *91*, 045426.
(308) Walen, H.; Liu, D.- J.; Oh, J.; Lim, H.; Evans, J. W.; Kim, Y.; Thiel, P. A. Self-Organization of S Adatoms on Au(111): √3R30◦ Rows at Low Coverage. *J. Chem. Phys.* **2015**, *143*, 014704.
(309) Wahlström, E.; Ekvall, I.; Kihlgren, T.; Olin, H.; Lindgren, S. -A.; Walldén, L. Low-temperature Structure of S/Cu(111). *Phys. Rev. B* **2001**, *64*, 155406.
(310) Shen, M.; Liu, D. -J.; Jenks, C. J.; Thiel, P. A. Novel Self-Organized Structure of a Ag-S Complex on the Ag(111) Surface below Room Temperature. *J. Phys. Chem. C* **2008**, *112*, 4281-4290.
(311) Liu, D. -J.; Lee, J.; Windus, T. W.; Thiel, P. A.; Evans, J. W. Stability of M3S3 Complexes on fcc M(111) Surfaces: M = Au, Ag, Cu, and Ni. *Surf, Sci.* **2018**, *676*, 2-8.

Biographies

King (Alex) C. Lai is currently a graduate student in the Department of Physics & Astronomy at Iowa State University and at the Ames Laboratory – USDOE in the Division of Chemical and Biological Sciences. He obtained his B.Sc. and M. Phil. degrees in Physics at the Chinese University of Hong Kong in 2012 and 2014, and is performing his Ph.D. research in Condensed Matter Physics under the supervision of Jim Evans on modeling of the evolution of 2D and 3D metal nanoclusters. His research interests include non-equilibrium statistical physics and nanophysics.

Yong Han is a Scientist at Iowa State University and is also partially supported by the Ames Laboratory – USDOE Division of Materials Sciences and Engineering. He obtained his M.S. in Physics and Ph.D. in Materials Science & Engineering at the University of Utah in 2007 under the supervision of Feng Liu. His research interests include quantum effects in metal nanostructures, and predictive ab-initio level modeling of self-assembly and coarsening processes for surface nanostructures.

Peter Spurgeon is currently a graduate student in the Department of Chemistry at Iowa State University. He obtained his B.S. in Chemistry at Eastern Washington University in 2014. He is performing his Ph.D. research in Chemistry under the supervision of Patricia Thiel exploring coarsening on metal surfaces including enhancement by additives. His research interests are in using Scanning Tunneling Microscopy to study the effects of sulfur on gold island coarsening on Au(111).

Wenyu Huang is an Associate Professor of Chemistry at Iowa State University. He obtained his B.S. in Chemistry at Nanjing University in 2000, and a Ph.D. in Chemistry from Georgia Institute of Technology in 2007 under the supervision of Mostafa El-Sayed. He performed postdoctoral research at the University of California Berkeley and at Lawrence Berkeley National Laboratory with Gabor A. Somorjai and Peidong Yang. His research interests include development of well-defined heterogeneous catalysts based on intermetallics, MOF-confined nanoclusters, and mesoporous silica nanomaterials.

Patricia A. Thiel is a Distinguished Professor of Chemistry and of Materials Science & Engineering at Iowa State University and a Faculty Scientist in the Ames Laboratory – USDOE Division of Materials Sciences and Engineering. She obtained her B.A. at Macalaster College in 1975, and a Ph.D. from Caltech in 1980 under the supervision of W. Henry Weinberg. She performed postdoctoral research at the University of Munich with Gerhardt Ertl. Her research interests include surface structures and properties of complex intermetallics, interaction of chalcogens with metal surfaces, and metal adsorption and intercalation on and in layered materials such as graphite.

Da-Jiang Liu is a Scientist at the Ames Laboratory – USDOE in the Division of Chemical and Biological Sciences. He obtained a B.Sc. in Physics at the University of Science

and Technology, China, in 1991, and a Ph.D. in Physics at the University of Maryland in 1998 under the supervision of John D. Weeks. His research interests include predictive modeling of surface processes related to chemistry and materials. This includes chemisorption and catalytic surface reactions, formation of metal-chalcogenide complexes on surfaces, and the stability of metal nanostructures.

Jim Evans is a Professor Physics & Astronomy and of Mathematics at Iowa State University, and a Project Leader at Ames Laboratory – USDOE, Division of Chemical and Biological Sciences. He obtained a B.Sc.(Hons) in Mathematics at the University of Melbourne in 1975, and a Ph.D. in Mathematical Physics at the University of Adelaide in 1979 under the supervision of Herbert S. Green. His research interests include modeling and simulation of the self-assembly and stability of nanostructures (especially those formed by deposition), epitaxial thin film growth and relaxation, catalytic reaction-diffusion processes in 1D nanoporous and 2D surface systems, and fundamental statistical mechanical analysis of far-from-equilibrium systems.

ACKNOWLEDGEMENTS

Studies related to 2D epitaxial NCs by KCL, YH, JWE (theory) and PS, PAT (experiment) were supported by NSF Grant CHE-1507223. YH and JWE were supported for theoretical analysis of intermixing in 2D and 3D bimetallic NCs by NSF Grant CHE-1507223. DJL was supported for theoretical studies related to coarse-grained continuum modeling of reshaping and related to additive-enhanced coarsening by the USDOE, Office of Science, Basic Energy Sciences, Chemical Sciences, Geosciences, and Biosciences Division. KCL and JWE were supported for theoretical modeling of the reshaping of 3D NCs by the USDOE, Office of Science, Basic Energy Sciences, Chemical Sciences, Geosciences, and Biosciences Division. USDOE supported research by KCL, DJL, and JWE was performed at the Ames Laboratory, which is operated by Iowa State University under contract number DE-AC02-07CH11358. JWE and WH also acknowledge support from a Presidential Interdisciplinary Research Seed (PIRS) grant at Iowa State University for modeling of 3D NCs.

DFT calculations by DJL used resources of the National Energy Research Scientific Computing Center (NERSC), a U.S. DOE Office of Science User Facility operated under Contract No. DE-AC02-05CH11231. DFT calculations by YH used resources of the National Energy Research Scientific Computing Center (NERSC), a U.S. DOE Office of Science User Facility operated under Contract No. DE-AC02-05CH11231. DFT calculations by YH also used the Extreme Science and Engineering Discovery Environment (XSEDE), which is supported by National Science Foundation grant number ACI-1548562.

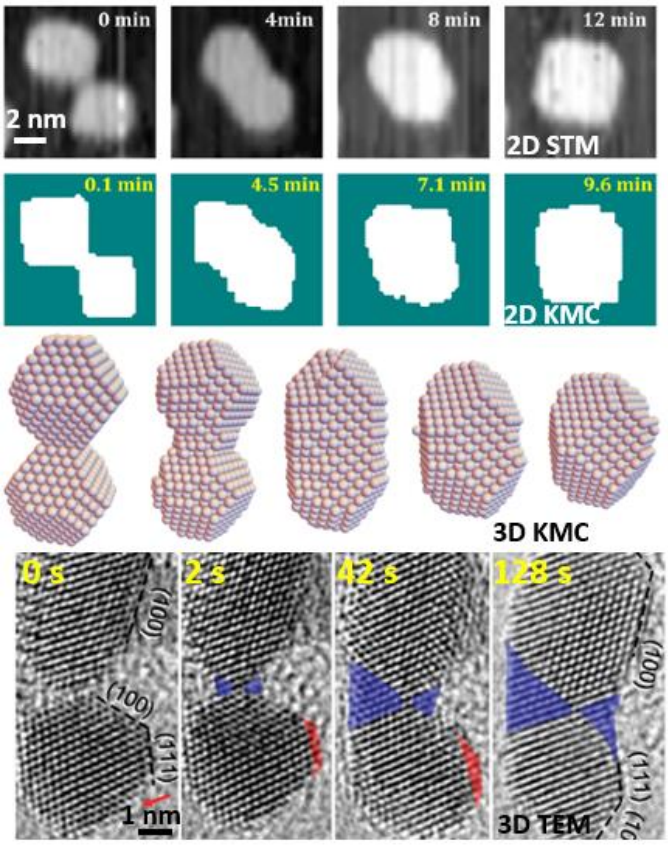
0 min
4min
8 min
12 min
2 nm
2D STM
0.1 min
4.5 min
7.1 min
9.6 min
2D KMC
3D KMC
0 s
2 s
42 s
128 s
(100)
(111)
1 nm
3D TEM

TOC figure